UNIVERSITÉ DE LIÈGE

DOCTORAL THESIS

Seismicity and Seismological Models of the Virunga Volcanic Province and Kivu Rift, Democratic Republic of Congo

Author:
Josué SUBIRA

Supervisors:
Aurélia HUBERT-FERRARI (Uliège)
Julien BARRIERE (ECGS)
Corentin CAUDRON (ULB)
François KERVYN (RMCA)

A thesis submitted in fulfillment of the requirements for the degree in Doctor of Sciences

in the

Department of Geography

July 26, 2024

UNIVERSITÉ DE LIÈGE

Abstract

Faculty of science
Department of Geography

Doctor of Sciences

Seismicity and Seismological Models of the Virunga Volcanic Province and Kivu Rift, Democratic Republic of Congo

by Josué SUBIRA

The monitoring of geological hazards, such as earthquakes and volcanic eruptions, is the primary and most important task of volcano observatories. These hazards are observed and studied from a wide range of scientific disciplines. The work presented in this thesis is principally based on a local seismic network, which is often viewed as an essential monitoring infrastructure. While such monitoring is not an easy task for any observatory worldwide, it remains a major challenge for those in developing countries for a number of reasons, including recurrent socio-political instabilities. The Goma Volcano Observatory (GVO) is one of these.

The GVO is located in the Kivu Rift region in the bordering region of the Democratic Republic of Congo (DRC) and Rwanda, in the Western branch of the East African Rift. The active volcanoes Nyamulagira and Nyiragongo in the Virunga Volcanic Province (part of the Kivu) threaten the city of Goma (DRC) and neighbouring agglomerations. Urbanisation in the direct vicinity of the volcano undergoes sustained rapid growth, and the region counts more than 1 million inhabitants today. Recent Nyiragongo's flank eruptions, which occurred in 1977, 2002 and 2021, caused major disasters and casualties. Moreover, destructive earthquakes of moderate magnitude can also affect this tectonically active region.

After several attempts to set up an operational seismic network in the region, an initiative involving local and international scientific institutions was successful over the past decade. For the first time, a dense and telemetered broadband seismic network, called KivuSNet, provided real-time data in the region. This local network became the main seismic network of the GVO for daily routine monitoring work between 2013 and 2022. This work presents the lessons learned from about 7 years (July 2015 – June 2022) of continuous seismic monitoring in the Kivu rift.

In the first part of this thesis, we have investigated the relevance of using the recorded seismic amplitude at each available station to assess the seismic activity in the Virunga volcanic Province (VVP). Under certain conditions, the spatio-temporal variability of volcanic seismicity can be monitored from the analysis of the seismic amplitude recorded across the network. The chosen approach is based on the amplitude at each station as well as the amplitude ratios between pairs of stations, which has proved to be efficient to

track high-frequency volcano-tectonic seismicity (> 2Hz) at other volcanoes. In our case, we took advantage of the existence of shallow tremor sources (i.e., continuous seismic pertubations) of volcanic origin at low frequency (< 2 Hz) to successfully apply this technique for the first time in this context. Coupled with other geophysical datasets, the same approach was also well suited over the period 2018-2022 for interpreting the variations of seismic amplitudes in terms of volcano-related processes before, during and after the 2021 flank eruption at Nyiragongo. These results have direct implications in the monitoring of the Virunga volcanoes since they can provide guidance to GVO on the use of similar amplitude-based tools, which are easy-to-implement and relevant to use in case of seismic data scarcity using only a few stations.

In the second part, our aim was to fill the gap in the poor knownledge of the seismic velocity structure and seismicity patterns in the region. We used the seismological information derived from KivuSNet to obtain robust 1D seismic (P- and S-wave) velocity models for the Kivu Rift region. A first local magnitude scale was also proposed using the same data set. We recommend the use of these models as new routine models at GVO and as starting point for further works in the region. Both the methodology and the results were extensively detailed, which allowed a comprehensive comparison between this new model and existing ones. Then, a seismic catalogue of nearly 50,000 detected events (volcanic and tectonic) over 7 years (2015-2022) was located. The main characteristics (spatial distribution, count, magnitude, spectral frequency) were discussed with a special emphasis on Nyiragongo and Nyamulagira and how this new knowledge can help the Goma Volcano Observatory in improving its monitoring tasks. This analysis must be seen as a first promising outcome, which should encourage further research in the region on this large topic.

UNIVERSITÉ DE LIÈGE

Résumé

Faculté des Sciences
Département de Géographie

Docteur en Sciences

Sismicité et modèles sismologiques dans la Province Volcanique des Virunga et dans le Rift du Kivu, République Démocratique du Congo

par Josué SUBIRA

La surveillance des risques géologiques, tels que les tremblements de terre et les éruptions volcaniques, est la tâche principale et la plus importante des observatoires volcanologiques. Ces risques sont observés et étudiés à partir d'un large éventail de disciplines scientifiques. Les travaux de cette thèse s'appuie essentiellement sur un réseau sismique local, qui est souvent considéré comme une infrastructure de surveillance essentielle. Si une telle surveillance n'est pas une tâche facile pour tout observatoire au monde, elle reste un défi majeur pour ceux des pays en voie de développement pour de nombreuses raisons, notamment l'instabilité socio-politique récurrente. L'Observatoire Volcanologique de Goma (OVG - GVO en anglais) est l'un d'eux.

L'OVG est situé dans la région du Rift du Kivu, à la frontière de la République démocratique du Congo (RDC) et du Rwanda, dans la branche occidentale du Rift Est-Africain. Les volcans actifs Nyamulagira et Nyiragongo dans la province volcanique des Virunga (qui fait partie dudu Kivu) menacent la ville de Goma (RDC) et les agglomérations voisines. L'urbanisation à proximité directe du volcan connaît une croissance rapide et soutenue, et la région compte aujourd'hui plus d'un million d'habitants. Les récentes éruptions de flanc du Nyiragongo, qui se sont produites en 1977, 2002 et 2021, ont provoqué des catastrophes et des pertes en vie humaines importantes. De plus, des tremblements de terre destructeurs de magnitude modérée peuvent également affecter cette région tectoniquement active.

Après plusieurs tentatives de mise en place d'un réseau de surveillance sismique dans la région, une initiative impliquant des institutions scientifiques locales et internationales a été réussie au cours de la dernière décennie. Pour la première fois, un réseau sismique dense à large bande et télémétré, s'appelant KivuSNet, a fourni des données en temps réel dans la région. Ce réseau local est devenu le réseau sismique principal de l'OVG pour la surveillance quotidienne entre 2013 et 2022. Ce travail présente les leçons tirées d'environ 7 ans (juillet 2015 – juin 2022) de surveillance sismique continue dans le Rift du Kivu.

Dans la première partie de cette thèse, nous avons étudié la pertinence d'utiliser l'amplitude sismique enregistrée à chaque station disponible pour évaluer l'activité sismique dans la Province Volcanique des Virunga (PVV - VVP en anglais). Sous certaines conditions,

la variabilité spatio-temporelle de la sismicité volcanique peut être suivie à partir de l'analyse de l'amplitude sismique enregistrée à travers le réseau. L'approche choisie est basée sur l'amplitude à chaque station ainsi que sur les rapports d'amplitude entre paires de stations, ce qui s'est avéré efficace pour suivre la sismicité volcano-tectonique à haute fréquence (> 2 Hz) sur d'autres volcans. Dans notre cas, nous avons profité de l'existence de sources superficielles de trémor (c-à-d une perturbation sismique continue) d'origine volcanique à basses fréquences (< 2 Hz) pour appliquer avec succès cette technique pour la première fois dans ce contexte. Couplée à d'autres données géophysiques, la même approche a également été été efficace sur la période 2018-2022 pour interpréter les variations des amplitudes sismiques en termes de processus volcaniques avant, pendant et après l'éruption de 2021 sur les flancs du Nyiragongo. Ces résultats ont des implications directes dans la surveillance des volcans des Virunga puisqu'ils peuvent guider l'OVG sur l'utilisation d'outils similaires basés sur l'amplitude sismique, faciles à mettre en œuvre et pertinents à utiliser en cas de pénurie de données sismiques en utilisant seulement que quelques stations.

Dans la deuxième partie, notre objectif était de combler les lacunes dans les faibles connaissances de la distribution des vitesse sismiques en profondeur et de la répartition de la sismicité dans la région. Nous avons utilisé les informations sismologiques dérivées du KivuSNet pour obtenir des modèles 1D robustes de vitesse sismique (ondes P et S) pour la région du Rift du Kivu. Une première échelle de magnitude locale a également été proposée en utilisant les mêmes données. Nous conseillons l'utilisation de ces modèles comme nouveaux modèles de routine à utiliser à l'OVG et comme point de départ pour d'autres travaux dans la région. La méthodologie et les résultats ont été largement détaillés, ce qui a permis une comparaison exhaustive entre ce nouveau modèle et les modèles existants. Ensuite, un catalogue sismique de près de 50.000 événements détectés (volcaniques et tectoniques) sur 7 ans (2015-2022) a été localisé. Les principales caractéristiques (répartition spatiale, comptage, magnitude, fréquence spectrale) ont été discutées avec un accent particulier sur le Nyiragongo et le Nyamulagira et comment ces nouvelles connaissances peuvent aider l'Observatoire Volcanologique de Goma à améliorer ses tâches de surveillance. Cette analyse doit être considérée comme un premier résultat prometteur qui devrait encourager la poursuite de travaux de recherche dans la région sur ce vaste sujet.

Acknowledgements

First of all, I would like to thank my supervisor, Prof. Aurélia Hubert-Ferrari (Univ. Liège), for her constant support during the thesis. I would also like to thank my co-supervisor, Dr. Julien Barrière (ECGS). This whole adventure was possible because he has always believed in me and in my vocation for seismo-volcanology. He has encouraged and guided me to succeed. My sincere thanks also go to all the members of my thesis committee, Dr. François Kervyn (RMCA), who gave me the opportunity to obtain this PhD grant under the project HARISSA (natural HAzards, RISks and Society in Africa: developing knowledge and capacities), and Dr. Corentin Caudron (ULB) for his guidance.

The research was carried out at the Royal Museum for Central Africa (RMCA) in Tervuren (Belgium) and in the facilities of the European Center for Geodynamics and Seismology (ECGS) and National Museum of Natural History (NMNH) in Walferdange (Luxembourg). I wish thus to thank RMCA's managing director Mr. Bart Ouvry, NMHN's director Mr. Patrick Michaely and ECGS's general secretary Mr. Eric Buttini and ECGS's chairman of the administrative board Mr. Michel Feider for their welcome, which enabled me to carry out my research at their institutions.
I thank people at ECGS (Maxime Jaspard, Gilles Celli, Marie-Jo Maciel, Yannick Breh) for their support and their daily collaboration during my stay in Luxembourg. Many thanks to Muriel Van Nuffel (RMCA's coordinator for work placements and study visits) for the organization of our trips in Europe. This was done with a professionalism that demonstrated her exceptional experience in this field.

I am deeply grateful to the technician team of the Goma Volcano Observatory (GVO) for their implication in the maintenance of the KivuSNet network, of which data are exploited in this thesis. Thanks to Prof Katcho, the GVO authorities and the colleagues in the GVO's department of seismology.
I would like to thank Dr. Nicolas d'Oreye (NMHN, Luxembourg) for many useful scientific discussions and his passion for the Kivu region. Many thanks to Dr. Adrien Oth (ECGS's scientific director) for his help and fruitful discussions about seismology and to Dr. Benoît Smets (RMCA and Vrije Universiteit Brussel, Belgium) for discussions on the regional geology and for providing some shapefiles of his work in the region.

Finally, I would like to acknowledge the love and support of my family and friends who have stood by me during the most challenging phases of this academic endeavour, namely Naomi Kazingufu, my wife, and my children Helena Kasaba and Gad Kasereka. These people have helped to keep my spirits high and my mind focused and I would not be here without them.

Contents

List of Figures

List of Tables

List of Abbreviations

EARS	**E**ast **A**frican **R**ift **S**ystem
VVP	**V**irunga **V**olcanic **P**rovince
SKVP	**S**outh **K**ivu **V**olcanic **P**rovince
DRC	**D**emocratic **R**epublic of **C**ongo
GVO	**G**oma **V**olcano **O**bservatory
OVG	**O**bservatoire **V**olcanologique de **G**oma
INGV	**I**stituto **N**azionale di **G**eofisica e **V**ulcanologia
CRSN	**C**entre de **R**echerche en **S**ciences **N**aturelles
UB	**U**niversity of **B**urundi
ULB	**U**niversité **L**ibre de **B**ruxelles
RNRA	**R**wanda **N**atural **R**esources **A**uthority
ECGS	**E**uropean **C**enter for **G**eodynamics and **S**eismology
RMCA	**R**oyal **M**useum for **C**entral **A**frica
SARA	**S**eismic **A**mplitudes **R**atios **A**nalysis
UN	**U**nited **N**ations
FDSN	International **F**ederation of **D**igital **S**eismograph **N**etworks
NCF	**N**oise **C**ross-correlation **F**unction
PSD	**P**ower **S**pectral **D**ensity
HF	**H**igh-**F**requency (or **H**autes **F**réquences)
LF	**L**ow-**F**requency
BF	**B**asses-**F**réquences
FI	**F**requency **I**ndex
USGS	**U**.**S**. **G**eological **S**urvey
EDT	**E**qual **D**ifferential **T**ime

General introduction

THE Kivu Rift is located in the middle part of the West Branch of East African Rift System (EARS) and bordering region of the DRC, Rwanda and Uganda. It is covering the Virunga Volcanic Province (VVP), the South Kivu Volcanic Province (SKVP) and the Lake Kivu Basin in between. This region is seismicaly and volcanically active within the geodynamic context of a continental rift system. The active volcanoes Nyamulagira and Nyiragongo, standing at 3058 m and 3470 m respectively in the VVP, threaten the cities of Goma (DRC), Gisenyi (Rwanda) and neighbouring agglomerations. Urbanisation in the direct vicinity of the volcano is undergoing sustained rapid growth, and the region counts more than 1 million inhabitants (Syavulisembo Muhindo et al., 2021). The successive eruptions of Nyiragongo in 1977 (Tazieff, 1977), 2002 (Komorowski et al., 2002) and 2021 (Smittarello et al., 2022) caused major disasters and casualties. Moreover, destructive earthquakes also affect the region, such as the 2002 Kalehe earthquake (Mw 6.2) along the western shore of Lake Kivu (Wauthier et al., 2015), or the 2008 Bukavu earthquake (Mw 5.9) (D'Oreye et al., 2011), south of Lake Kivu.

The Goma Volcano Observatory (GVO, or OVG for Observatoire Volcanologique de Goma in French) was created after the catastrophic eruption of Nyiragongo in 1977. The role of GVO is to monitor volcanoes and earthquakes in the region using the recommended panel of geophysical measurements (seismology, geodesy, geochemistry), as recommended for example in the US by Moran et al. (2008). Seismology is especially important and considered as the backbone of any volcanological observatory, providing real-time continuous and high-sample-rate data linked to the internal state of the volcano (Thompson et al., 2015). It is also the oldest discipline developed within this institution, and the relationship between magmatic and seismic activities at the Nyiragongo and Nyamulagira volcanoes is already well established (e.g., Hamaguchi et al., 1982; Kavotha et al., 2002; T. Mavonga et al., 2010; T. Mavonga et al., 2006). However, deploying and maintaining such monitoring infrastructure in developing countries remains problematic. This leads to limited knowledge of the area and the associated geological hazards, which has a negative impact on theirs monitoring, as in the case of the Kivu Rift region. The main reason for the limited study of the Kivu Rift is the difficulty of developing a ground-based monitoring network in the context of poor governance, political instability and recurring armed conflicts (F. Kervyn, 2022). Thus, the space-based InSAR (Interferometric Synthetic-Aperture Radar) approach appears as a good alternative for studying the geological processes and associated hazard in the region (e.g., M. Kervyn et al., 2007; Wauthier, 2011), but it has a limited temporal resolution and its full applicability is hampered in tropical zones by the presence of dense vegetation (Ebmeier et al., 2013).

The main challenge in setting up a ground-based monitoring network involves not only the scientific or technical constraints of installing equipment (e.g. site selection, signal transmission), but also factors dependent on local conditions (e.g. security, lack of infras-

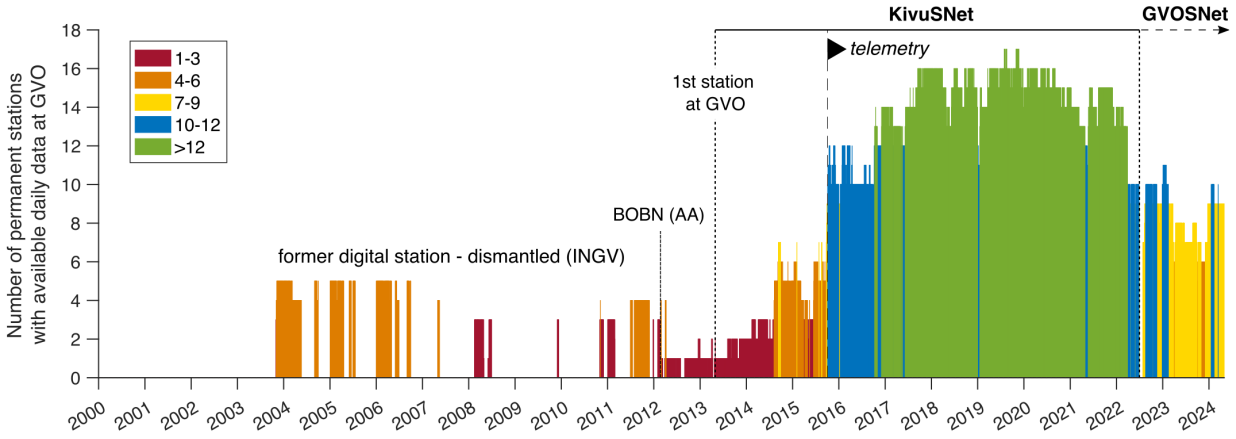

FIGURE 1: Timeline of the development of seismic networks in the VVP over the last 24 years (number of stations with daily data availability). The acronym AA for the station BOBN means the station was installed in the framework of the AfricaArray network in 2012. In 2016, BOBN was repaired (Oth et al., 2017) and included in the KivuSNet network.

tructure, cost). Finding good sites for deploying stations is a compromise between the advantages of the site in terms of providing a good signal and ensuring security. These choices result in a rather sparse network around the volcanoes (distance between stations on the order of tens of km) and some stations in areas contaminated by high levels of anthropogenic noise, limiting the analyses that can be conducted compared to other well-instrumented observatories (e.g., Hawaii, Etna, Piton de la Fournaise).

Numerous initiatives have been underway to equip the Goma Observatory with a real-time seismic monitoring system (Figure 1). The first digital seismic network of the Goma Volcano Observatory (GVO), in collaboration with the Istituto Nazionale di Geofisica e Vulcanologia (INGV), was deployed in the VVP between 2004 and 2012 with up to 7 stations (Pagliuca et al., 2009). Unfortunately, these data, shared between GVO and INGV, were underutilized due to insufficient data completeness caused by technical and transmission issues (T. Mavonga et al., 2010). Between 2013 and 2022, the first dense real-time telemetered broadband seismic network in the Kivu Rift region (KivuSNet) (Oth et al., 2017) was gradually deployed in the frame of several research projects and became fully operational with sufficient station coverage ($>$ 10 stations) and telemetry in October 2015 (Figure 1). The KivuSnet was a research-based initiative developed in the partnership with the local institutions, namely the Goma Volcano Observatory (GVO/DRC), the Centre de Recherche en Sciences Naturelles (CRSN/DRC), University of Burundi (UB/Burundi), the Rwanda Natural Resources Authority (RNRA/Rwanda) and international institutions, the European Center for Geodynamics and Seismology (ECGS/Luxembourg) and the Royal Museum for Central Africa (MRAC/Belgium). Due to the fundamental importance of monitoring the seismicity in this region, substantial efforts were made for setting up this network permanent with real-time data acquisition, which rapidly became the main seismic network of the Goma Volcano Observatory for daily routine monitoring work. In July 2022, GVO decided to replace the KivuSNet network by a new seismic network, GVOSNet operated by GVO under the government support, to perpetuate the achievements.

Recent studies (Barrière et al., 2018, 2019, 2022; Oth et al., 2017; Smittarello et al., 2022; Subira et al., 2023) based on data collected by the KivuSnet network have provided new insights into the seismic activity in the Kivu Rift, particularly the magmatic processes in the VVP. On this basis, the May 2021 eruption of Nyiragongo was well understood, unlike the last two eruptions (1977, 2002) where the reported facts could have been either exaggerated or misinterpreted due to lack of field data.(Smets et al., 2015)

This thesis presents the lessons learned from approximately 7 years (2015 - 2022) of continuous seismic data acquisition in the Kivu Rift. The aim is to understand the seismicity associated with the rifting process in the Kivu Rift and its impact on the evolution of magmatism in the VVP. We also provide important seismological knowledge such as a new 1D velocity model, a new local magnitude scale and the 2015-2022 tectonic and magmatic events catalog to improve the seismic monitoring in the region. The thesis is structured into 4 Chapters subdivided in two parts, with a first part concerning the analysis of continuous seismic amplitude measurements and the second part describing the seismological models and seismicity patterns.

- **PART 1: Analysis of continuous seismic amplitude measurements**
  Chapter 1 is dedicated to the study of seismic tremor sources encountered in the Kivu Rift and relies on the use of continuous seismic data recorded between December 2015 and March 2018. We investigated the potential of using seismic amplitude measurements and their ratios at available stations as a good indicator of volcanic seismic activity in the context of seismic monitoring at the GVO. This work began with Subira et al. (2023), who highlighted the potential of using seismic amplitudes ratios analysis in the low frequency domain $[0.3 - 1]Hz$ to monitor the magmatic activities at Nyiragongo and Nyamulagira volcanoes. **Chapter 2** is a logical continuation of Chapter 1 using seismic data recorded in the next 4 years from April 2018 to July 2022 and provide a complete benchmark to assess the use of seismic amplitude-based analysis for monitoring Nyiragongo.

- **PART 2: Seismological models and seismicity patterns**
  In the second part of this thesis, we used the data from the first dense network (KivuSNet) over a 6-year time period (October 1, 2015 - October 1, 2021) to derive, in **Chapter 3**, a robust 1D seismic velocity model dedicated to the Kivu Rift region. The new local magnitude scale will be also presented at the end of this Chapter. We used about 300 well-constrained local earthquakes for this purpose, aiming to improve hypocenter and magnitude estimates in the VVP region. **Chapter 4** presented the complete new 2015-2022 seismicity catalogue (volcanic and tectonic events) during over 6 years of analysis, discussing the main seismic patterns with a special emphasis on how this new knowledge can help the Goma Volcano Observatory in improving its monitoring tasks.

Part I

Analysis of continuous seismic amplitude measurements

Chapter 1

Detecting sources of shallow tremor at neighboring volcanoes in the VVP using seismic amplitude ratio analysis

THis Chapter was published as a research article in Bulletin of Volcanology : *Subira, J., Barrière, J., Caudron, C., Hubert-Ferrari, A., Oth, A., Smets, B., d'Oreye, N., Kervyn, F. Detecting sources of shallow tremor at neighboring volcanoes in the Virunga Volcanic Province using seismic amplitude ratio analysis (SARA). Bull Volcanol 85, 27 (2023). https://doi.org/10.1007/s00445-023-01640-5*. It provides a suitable introduction to the study area and the specificities of the ambient seismic wavefield in the Kivu region and Virunga Volcanic Province (VVP).

1.1 Introduction

Due to their location in the western branch of the East African Rift in the Kivu rift and Virunga Volcanic Province (VVP), the cities of Goma and Gisenyi are threatened by several geological hazards (volcanic eruptions, earthquakes, floods, etc.). With more than 1 million inhabitants (Syavulisembo Muhindo et al., 2021) Goma and its surrounding areas are permanently exposed to Nyiragongo volcano, located at $15km$ distance, and, to a lesser extent, Nyamulagira volcano at $30km$ distance (Figure 1.1). Nyiragongo, an open-vent stratovolcano, hosts one of the largest permanent lava lake on Earth at its summit. This lava lake was drained during each of the three known historical eruptions, i.e., in 1977 (Tazieff, 1977), 2002 (Komorowski et al., 2002), and 2021 (Smittarello et al., 2022). The three eruptions were characterized by fast basaltic lava flows erupting from fissures on the volcano's flanks. These flows reached the city of Goma in 2002 and 2021, and Lake Kivu in 2002 (Komorowski et al., 2002). Nyamulagira is a very active shield volcano characterized by about 30 eruptions during the twentieth century (Smets, 2015), the last one occurring in 2012. These eruptions are also effusive and start either in the large $2km$ wide caldera or on the flanks through vents and fissures (Figure 1.1c) (Wauthier et al., 2015).

In such a context, capacity reinforcement of volcanic earthquake monitoring by a permanent and telemetered network is of the utmost importance. Abnormal seismicity (e.g., increase of the number of events, appearance of tremor) is often among the first signs of a resurgence or a change of volcanic activity which can lead up to an eruption (Tilling, 2008). Following the 2002 Nyiragongo flank eruption, the first digital seismic network of the Goma Volcano Observatory (GVO) has been deployed in the VVP between 2004 and 2012 with up to 7 stations (Pagliuca et al., 2009). Unfortunately, these data have been little exploited due to insufficient data completeness caused by technical and transmission issues (T. Mavonga et al., 2010). Since mid-2013 to June 2022, a new telemetered broadband seismic network called KivuSNet has been progressively developed in the area under the initiative of international and cross border local institutions (Oth et al., 2017), leading, since October 2015, to the densest seismic network ever installed in the Kivu region (up to 20 stations), thus offering opportunities to better understand the seismicity in the VVP (Figure 1.2a).

Alongside recent research-based developments and findings in the VVP (e.g., Barrière et al., 2017, 2018, 2019; Oth et al., 2017), it is also of primary importance that low computational cost and user-friendly methods become general practice at GVO. Notably, techniques consisting in computing the variation of seismic amplitude through a network have become a standard approach since the pioneering study by Endo and Murray (1991) (Wassermann, 2012). Since then, the RSAM, which stands for real-time seismic amplitude measurement, and related calculations, are commonly implemented at volcano observatories worldwide, including GVO. Here we intend to apply the SARA method (seismic amplitude ratio analysis), which is based on the calculation of amplitude ratios between station pairs (Taisne et al., 2011). Originally developed for detecting magma migration, SARA relies on the decay of seismic wave amplitude along the source-receiver travel path. Because magma movement to the surface is often accompanied by seismicity known as volcano-tectonic (i.e., a fracturing of the surrounding rock), the SARA technique has been generally used in a rather high-frequency band (e.g., 2 to $15Hz$), which is

typical of this kind of source processes (Caudron et al., 2015). Recently, Tan et al. (2019) set up the so-called Red-flag SARA to track magma migration in the context of real-time volcano monitoring without event locations. Compared to the original study at Piton de la Fournaise by Taisne et al. (2011), the KivuSNet is a local network with a large interstation distance (10 to 100km). Due to the unstable political situation in the region, stations cannot be deployed between the volcanoes. Their locations are restricted to secure places (e.g., GVO, UN military compounds, etc.). As a consequence, most of the seismic records exhibit a strong anthropogenic noise level at high frequency (above 2Hz, see the "Overview of the 2-year-long seismic data used" section). Put together, the sparse geometry of the network and the high level of human-induced seismic noise hamper the classical use of the SARA approach for locating high-frequency seismic sources.

Here, we test the applicability of the SARA technique within a different context. The main goal is the assessment of this method in a particular range of low frequencies corresponding to the shallow volcanic signal observed in the time period between flank eruptions at both volcanoes. One of the particularities of the VVP is the dominant, permanent background seismic signal generated by Nyiragongo's lava lake at low frequency ($< 2Hz$) within its central crater and propagating as surface waves that are detectable throughout the entire network (Barrière et al., 2018). Tracking changes of this dominant seismic source in the VVP may therefore be relevant to monitor Nyiragongo's activity. Moreover, Barrière et al. (2017) have shown that Nyamulagira exhibits a similar low-frequency signature during intra-caldera eruptive activity (lava lake and fountaining). We thus explore in this paper if this alternative application of SARA at low frequency could be an efficient monitoring solution of the long-lasting summit effusive activity at Nyiragongo and/ or Nyamulagira. The advantage of the proposed approach is its capability for detecting and interpreting changes of eruption dynamics in the Virunga with limited field records and minimal data processing. The main limitation of the method is, however, the overlap with non-volcanic signals at similar low frequencies caused by Lake Kivu's microseisms that can temporarily hamper the straight- forward interpretation of continuous (real-time) seismic amplitude time series.

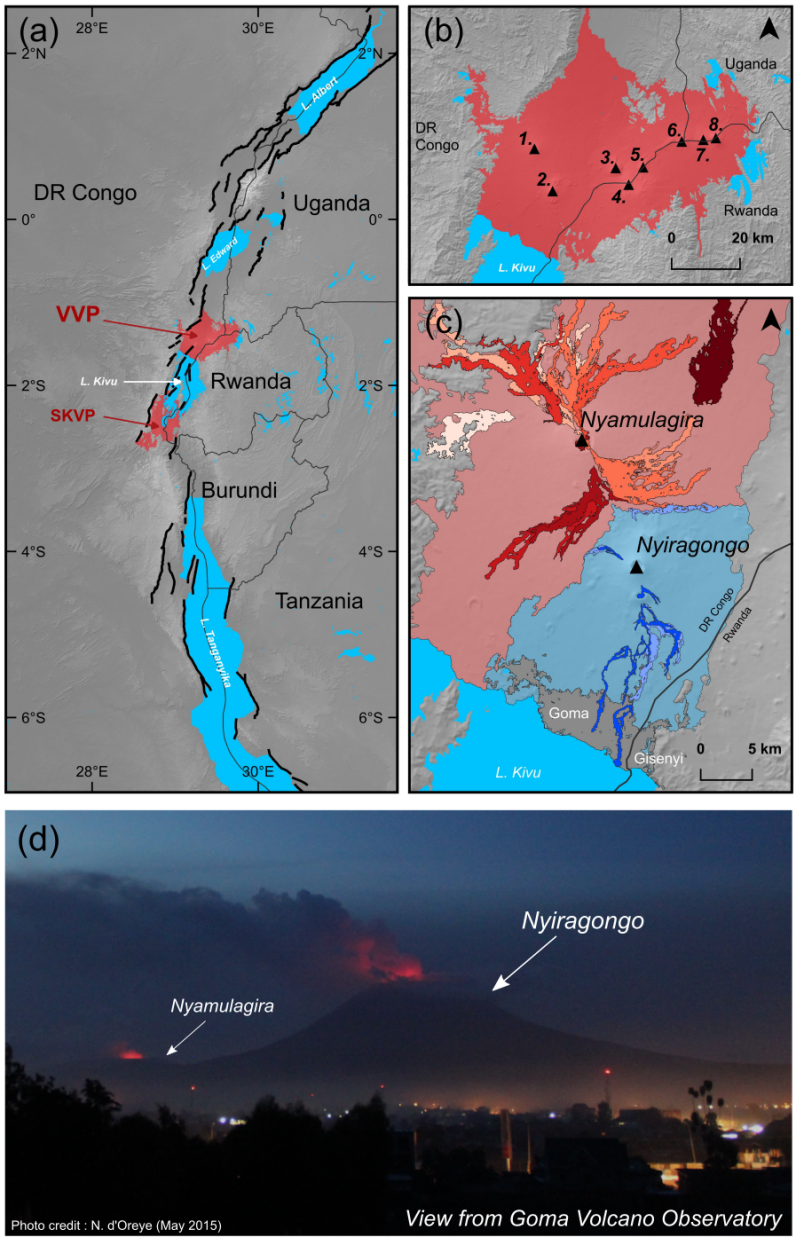

FIGURE 1.1: **(a)** The Virunga Volcanic Province (VVP) and the South Kivu Volcanic Province (SKVP) within the East African Rift system (EARS). It borders many different countries: Rwanda, Burundi, the East of the Democratic Republic of Congo (DRC), the south-west of Uganda, and the north-west of Tanzania, and it is located in the middle of a topographical uprising called the Kivu Dome. **(b)** Zoom in the VVP (red color) with the eight main volcanic edifices (1: Nyamulagira, 2: Nyiragongo, 4: Karisimbi, 3: Mikeno, 5: Visoke, 6: Sabinyo, 7: Gahinga, 8: Muhavura). The two major active ones are Nyiragongo and Nyamulagira. **(c)** The different volcanic fields and some recent eruptions (lava flows are shown) are associated with the two volcanoes, the ones from Nyiragongo in lavender and magenta colors affecting the cities of Goma and Gisenyi at the north of the lake Kivu. All shape files of the lava flow are from Smets et al. (2010). The background hillshade topography is derived from the SRTM 3 arc seconds (NASA/ USGS), which is made available from the US Geological Survey. **(d)** Picture of Nyiragongo and Nyamulagira taken from the Goma Volcano Observatory in May 2015 by N. d'Oreye. At that time, there was two active lava lakes in the Virunga

1.2 The VVP and its seismicity

1.2.1 General context

The VVP is a transition zone between the Lake Kivu and Lake Edward rift basins, in the central part of the western branch of the East African Rift System (EARS) (Figure 1.1a) (Ebinger, 1989; Smets et al., 2016). In this part of the EARS, the extension rate reaches $2.8 mm/year$ (Ji et al., 2017; Saria et al., 2013). The VVP comprises eight main volcanic edifices, with two major active ones, which are Nyiragongo and Nyamulagira (Figure 1.1b, c). These two volcanoes are among the most active in Africa, and even on Earth (Wright et al., 2015) (Figure 1.1d).

Nyiragongo (1.53°S, 29.25°N) has the shape of a stratovolcano and culminates at $3470m$ with a 1200-m-wide main crater (Smets et al., 2017). The main edifice is also characterized by two satellite cones: Baruta on the northern flank and Shaheru on the southern flank. Its eruptive activity is mostly characterized by persistent lava lake activity in its summit crater, sometimes becoming the largest lava lake surface on Earth (Smets et al. 2016). Only three flank eruptions have been documented since the arrival of the first European explorers in the nineteenth century. These eruptions occurred in January 1977 (Tazieff, 1977), January 2002 (Komorowski et al., 2002), and May 2021 (Smittarello et al., 2022) Nyiragongo lavas have the lowest viscosity ever observed for terrestrial silicate lavas (Dawson et al., 1990; Morrison et al., 2020).

Nyamulagira (1.41°S, 29.20°E) is a shield volcano located about 15 km to the north-west of Nyiragongo and is mostly characterized by phases of summit eruptive activity (1913-1938, 2014-present) and phases made of flank eruptions (before 1912, 1938-2012) occurring every 1-4 year(s) (Smets et al., 2015). The main edifice culminates at 3058m above sea level and is topped by a $2 \times 2.3 km$ wide caldera. The characteristics of flank eruptions of Nyamulagira mostly vary according to their location (Smets et al., 2015). The Nyamulagira lava flows have a low viscosity and can cover long distances of up to several tens of kilometers (Smets et al., 2015; Smets, D'Oreye, & Kervyn, 2014a).

1.2.2 Characteristics of the seismicity

The group of seismic signals encountered in the VVP are similar to those commonly detected at other volcanoes (Chouet & Matoza, 2013).
They are classified into four families based on their waveform characteristics: short- period (or high-frequency, often classified as volcano-tectonic), long-period (or low-frequen cy), hybrid events (i.e., low-frequency event with high-frequency onset), and tremors (Lukaya et al., 1992; Tanaka, 1983). Long- period (LP) earthquakes, also called low-frequency (LF), are generally interpreted as the consequence of fluid migration in the magmatic plumbing system while low- frequency volcanic tremors are indicators of sustained magma movement (Chouet & Matoza, 2013). However, no manual classification has been routinely performed at GVO, notably due to the lack of modern instruments maintained operational in the region in the past decades. A first long-term seismic monitoring database at GVO, obtained from the deployment of the telemetered seismic network KivuSNet in the Kivu rift region, has been available since late 2015. To date, this new

insight into the Virunga volcanoes' seismicity has allowed to highlight a persistent background tremor source with a dominant frequency below 1 Hz (Barrière et al., 2017; Oth et al., 2017). This continuous low-frequency signal is attributed to the lava lake spattering activity (Barrière et al., 2018, 2019), which is recorded at a long-distance range (up to 100 km) across the local seismic network. Barrière et al., 2022 showed that seismic activity at Nyiragongo is often associated with swarm sequences associated with magmatic intrusion (i.e., deeper than 10 km below sea level). These swarms are synchronous with large lava lake drops and contain many events with characteristics similar to hybrid events (i.e., high-frequency onset up to 10 Hz and low-frequency wavetrains). Additionally, seismic activity at this volcano is characterized by a cluster of daily repetitive events (more than 5000 between September 2015 and 2018) that suggest a non-destructive source beneath Nyiragongo (Barrière et al., 2019). These events are located at large depths (11-15 km) and are characterized by higher frequencies $[2-10]$Hz) than the low-frequency content generally observed for repetitive events attributed to magmatic movements. However, brittle failure can hardly explain their highly repetitive nature. Fluid-related movement is thus the probable source mechanism of such high-frequency excitation, as observed for instance by Caplan-Auerbach and Petersen (2005) at Shishaldin volcano. The last May 2021 eruption was also the first eruption at Nyiragongo well monitored by numerous broadband instruments, which allowed drawing a clear seismic picture of the flank eruption and the shallow dyke intrusion beneath the city of Goma (Smittarello et al., 2022). At Nyamulagira, the detected seismicity has been mostly characterized by a dominant long-period signature (LP events, tremors) in the 0 to 20 km depth range, either inferred from recent observations during intra-crater lava lake/fountaining activity (Barrière et al., 2017) or using available pre- and syn-eruptive digital data from a dismantled network (G. T. Mavonga, 2010; T. Mavonga et al., 2006).

1.2.3 Overview of the 2-year-long seismic data used

We used data from the KivuSNet seismic stations (FDSN network code KV), which was a recent broadband seismic network installed in the region (Oth et al., 2017), comprising seismic and infrasound stations. The network was gradually deployed and operational between September 2013 and June 2022, the first station installed being GOM located in the GVO grounds. Our study is based on data collected from late 2015 coinciding with the main deployment phase of the KivusNet and the start of the operational telemetry (Oth et al., 2017). The data are both telemetered (sampled at $50Hz$) and stored locally on a hard drive (sampled at $200Hz$). Six key stations with long-lasting records are selected around the volcanoes. They are all located between approximately 6 to $35km$ away from both active volcanoes. Hereafter, we discuss the results from analyses based on seismic amplitude variations recorded between December 2015 and March 2018. The locations of the selected stations are plotted in Figure 1.2a. Power spectral density (PSD) between 0.1 and $10Hz$ obtained from the entire records (Dec. 2015–Mar. 2018) at 3 stations are plotted in Figure 1.2. These 3 stations depict site properties typical of those encountered in the VVP:

- The station GOM is located close to the shore of Lake Kivu in an urban environment. Nyiragongo's and Nyamulagira's summits are located respectively around 17 and 30 km away toward the north.

- Station KBTI is located in a rural place affected by human activities (main road and villages), but it is also the closest station to one of the active volcanoes ($\sim 6km$ away from Nyiragongo's inner crater).
- The station TGO is located in a military compound (UN base camp) in a remote place though affected by the nearby military activity. Its location to the North of the Virunga remains highly strategic in terms of volcano monitoring despite its distant location (23 to $35km$ from Nyamulagira and Nyiragongo, respectively), its difficult accessibility and its location in a region affected by strong insecurity.

In light of the above mentioned site descriptions, one can better gauge the 2-year-long PSDs obtained as these three stations plotted in Figure 1.2b (represented as probability density functions, further called pdf). The processing follows the one described in McNamara and Buland (2004) using a main time window of 2^{19} samples with a sampling rate of $50Hz$ ($\approx 175min$), overlapped by 50% and subdivided into 13 segments overlapping by 75%, thus resulting in sub-windows of 2^{17} samples ($\approx 44min$). The final PSDs are smoothed along $1/16^{th}$ octave intervals. The only similar pattern between the three PSDs is the oceanic secondary microseism peak $(0.15 - 0.2Hz)$ recorded everywhere on Earth (with regional and seasonal amplitude variations depending on the source properties) (McNamara & Buland, 2004). Above $0.3Hz$, strong dB level differences between the three stations (spaced by $\approx 50km$ at maximum between GOM and TGO) point out local source and/or site effects. According to Barrière et al. (2018), the peak between 0.3 and $2Hz$ at KBTI is due to the Nyiragongo lava lake activity nearby, generating a stable and persistent tremor. Available records at the summit during expeditions or from a station deployed on the crater rim in the course of the year 2018 (not shown here) depict a lava-lake tremor with a broadband signature up to 10 Hz (Barrière et al., 2018). In the $[0.3 - 2]Hz$ frequency range, this lava lake signal does not clearly stand out at stations GOM and TGO. At both stations, the power increase above $1Hz$ is mainly due to human activity (so-called cultural noise) where the spreading of the pdf is mainly due to diurnal variations (McNamara & Buland, 2004). For all stations, anthropogenic noise sources are dominant above $2Hz$. At GOM, another peak is noticeable between 0.3 and $2Hz$, which do not correspond to the maximum mode (black line). We will see later in the "Variations of low-frequency seismic amplitudes in the VVP" section that this signal overlapping the volcanic tremor band is mostly due to short-period microseisms from Lake Kivu. The term "short-period," in accordance with the study of Xu et al. (2017) analyzing several lake microseisms signatures across the globe, refers to the $[0.5 - 2]Hz$ frequency band, higher than the one characterizing the oceanic microseisms.

We conclude that analyzing the continuous amplitude of the seismic signals above $1Hz$ at relatively large distances (i.e., tens of kilometers away from both volcanoes) could be too strongly affected by unwanted noise sources. Selecting a band between $0.3Hz$, above the ocean microseismic band, and $1Hz$, below the dominant anthropogenic noise sources, would successfully highlight seismic amplitude variations generated, at least partially, by volcanic tremor sources. This frequency band also corresponds to the one chosen by Barrière et al. (2017) for detecting and locating Nyiragongo's and Nyamulagira's tremor across the network (up to $100km$ away from the edifice) based on seismic interferometry principles. In this case, the amplitude information is lost due to pre-processing proce-

dures such as time-domain normalization and spectral whitening.

Thus, for the specific analysis presented in this paper, we bandpass filter the data in the $[0.3-1]Hz$ frequency band. The obtained amplitude variations either correspond to magmatic processes at one or both volcanoes, or to other unknown sources. The 2-year-long seismic amplitude records from GOM, KBTI, and TGO, whose calculation details are provided in the "Variations of low-frequency seismic amplitudes in the VVP" section, are plotted in Figure 1.2c. Between December 2015 and March 2018, we identified two categories of variations. The first ones are short-term changes associated with rapid variation of seismic amplitudes (1 day to few weeks) possibly indicative of fast changes in volcanic tremor activity or other phenomena in the region. The second ones are long-term changes, more prominent for GOM records, that extend over several months. This long-term trend of the GOM timeseries, which appears to be seasonal, is discussed in Figure 1.4. Five short-term changes are analyzed separately in five figures (gray boxes in Figure 1.2c), corresponding either to the largest amplitude variations (Figures. 1.7, 1.8, and 1.9) or to repetitive amplitude peaks (Figures 1.5 and 1.6) clearly noticeable between April and October at GOM and KBTI. We already note that the overall low-frequency seismic amplitude at TGO (located in the countryside) is significantly lower than at KBTI (close to Nyiragongo) and GOM (close to Lake Kivu).

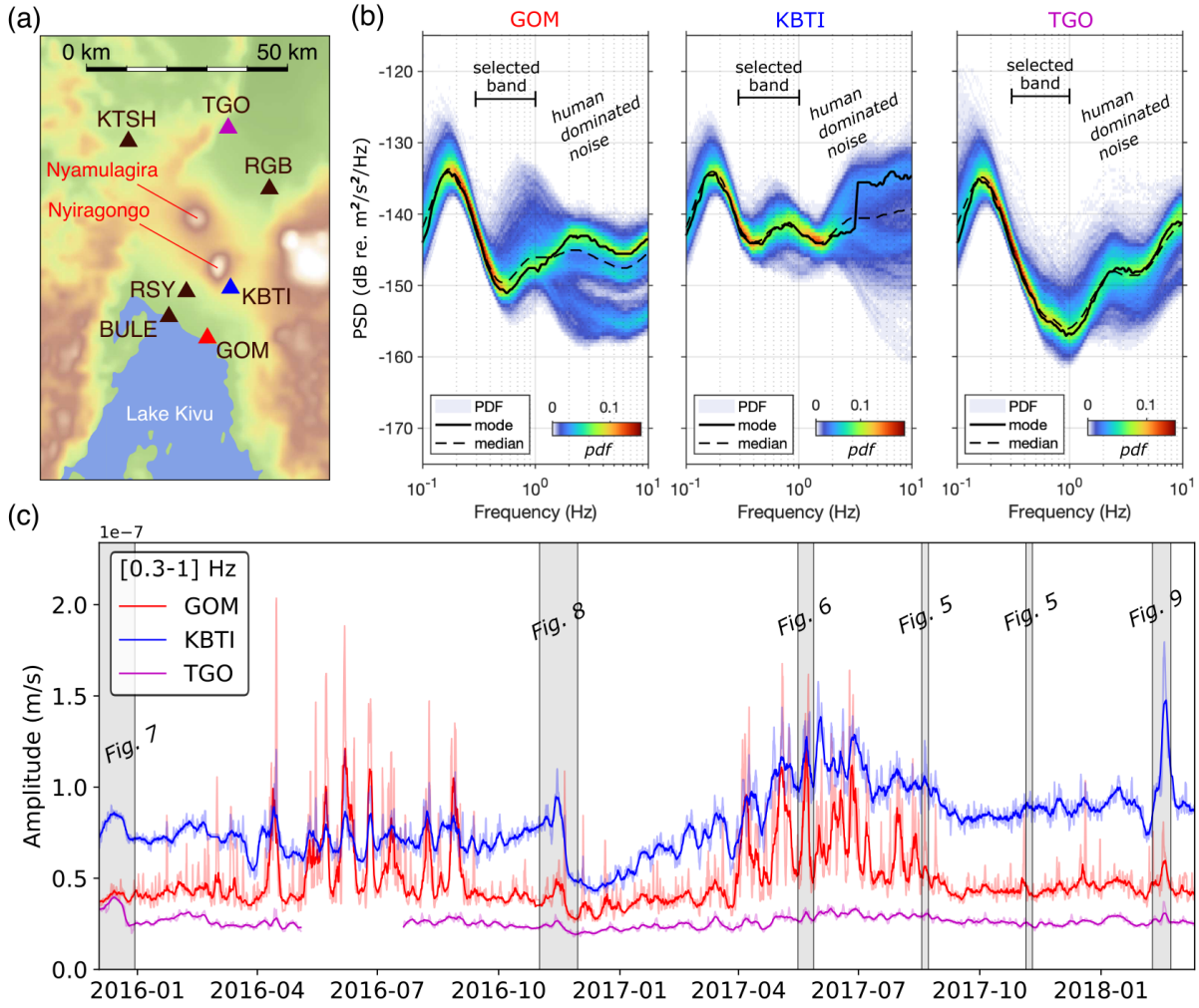

FIGURE 1.2: **(a)** Seismic stations used in this study displayed on a topographic map of the Virunga Volcanic Province. The colored triangles (GOM, KBTI, and TGO) show the locations of the seismic stations close to Lake Kivu, Nyiragongo, and Nyamulagira respectively on which we performed the power spectral density (PSD).**(b)** Evaluation of the seismic background noise level using PSD (in dB re $m^2/s^2/Hz$) analysis at GOM, KBTI, and TGO stations. **(c)** Two-year-long time-series of the seismic amplitudes (in $10^{-7}m/s$ after correction of the instrumental response) smoothed using $1day$ (light colored lines) and $7days$ (dark colored lines) rolling median calculated between 0.3 and $1Hz$ at GOM, KBTI, and TGO stations. The grey bands represent the short-term variation on the seismic amplitudes associated with magmatic or non-magmatic events discussed in Figure 1.5, 1.6, 1.7, 1.8 and 1.9. The map has been generated with the GMT software using the ETOPO Global relief Model, which is made available from the NOAA

1.3 Applicability of the SARA method in the VVP

The SARA method was defined by Taisne et al. (2011) for characterizing and locating the seismic signature of magmatic intrusion at the Piton de la Fournaise. The method requires defining the theoretical decay of seismic wave amplitudes along the source-receiver travel path. Such an amplitude-based location approach was originally proposed by Battaglia and Aki (2003) for seismic events and eruptive fissures on the same volcano. After assuming that velocity and attenuation remain constant during the migration and based on a simple attenuation law, Taisne et al. (2011) used the following expression for the seismic amplitude ratio between two stations i and j:

$$\frac{A_i}{A_j} = (\frac{r_j}{r_i})^n - exp(-B(r_i - r_j)) \tag{1.1}$$

With :

$$\frac{\pi f}{Q\beta} \tag{1.2}$$

where r is the distance of the stations i and j from the source, A is the amplitude at the stations i and j, n = 0.5 for surface waves or 1 for body waves, β is the shear wave velocity, Q is the quality factor for attenuation, and f is the frequency.

Johnson and Aster (2005) pointed out the difficulty of estimating the radiated seismic energy in heterogeneous volcanic systems, where the seismic wavefield is constituted by both body and surface waves and where near-surface Earth structures can create strong local site responses. Thus, the SARA technique may be affected by site amplification factors and a non isotropic wave radiation pattern. Taisne et al. (2011) have hypothesized that the radiation pattern is isotropic for a body wave propagation regime, which allowed them to invert for the depth of the magma propagation based on simple modeling (Eq. 1.1). They also indicated to be able to locate shallow volcanic tremor after assuming surface wave propagation. In addition, Battaglia and Aki (2003) successfully detected volcanic tremor sources after assuming an amplitude decay of either surface or body waves in a homogeneous medium. More recently, Caudron et al. (2018) applied the SARA approach for tracking the $2014 - 2015$ Holuhraun dike propagation. They analyzed high-frequency body waves ($> 2Hz$) because the assumption of an isotropic radiation pattern only holds at sufficiently high frequency due to path effects (Takemura et al., 2009).

Here, we do not indent to locate the tremor sources using the amplitude-based method applied in SARA (i.e., the "full" SARA methodology described in Taisne et al. (2011). Instead, when considering the characteristics of the ambient seismic noise in the VVP ("Overview of the 2-year-long seismic data used" section 1.2.3) and the sparse geometry of the KivuSNet, we rather follow the simpler SARA approach of Caudron et al. (2015) or Tan et al. (2019). The method basically consists of computing ratios of seismic amplitude between station pairs to qualitatively infer temporal and spatial variations of the volcano-related seismicity. This procedure does not correct for potential site amplification factors at each station and therefore implies that the variations of the seismic amplitude ratios can only be discussed qualitatively. Interpreting spatial amplitude variations at low frequency ($< 1Hz$) cannot rely on the aforementioned assumption of an isotropic radiation pattern due to path effects and can be affected by the possible source anisotropy.

Defining which type of waves dominates the recorded seismic amplitude remains essential for better interpreting the results from SARA and assessing their reliability. Our seismic recordings exhibit low $[0.3-1]$Hz frequency signals triggered by coherent shallow volcanic tremor sources from Nyiragongo and Nyamulagira, generating a wavefield dominated by surface waves (Barrière et al., 2017, 2018). These signals can be compared for instance with the ones observed at Masaya volcano by Métaxian et al. (1997a), who detected a continuous and dominant surface waves signature from a shallow seismic source located close to its lava lake conveying a superficial magmatic activity at this volcano at that time. At Piton de la Fournaise, Aki and Ferrazzini (2000) observed low-frequency tremor below 2.5 Hz whose amplitude decay with distance can be fitted by the theoretical decay of surface waves (after correction of site factors).

We illustrate the motivation behind the chosen approach by analyzing a long-period (LP) "lava lake's event" at Nyiragongo occurring on June 22, 2017 (Figure 1.3). At that time, only the station RGB was unavailable. Barrière et al. (2018) showed that this seismic signal has a dominant frequency around $0.5Hz$ and elliptical particle motion typical of Rayleigh surface wave. It also has an acoustic counterpart and comes from Nyiragongo's crater, thus having all characteristics of a very shallow source generated at the lava lake such as a large explosion. This event can be seen as a discrete form of the shallow tremor from Nyiragongo's lava lake. This continuous tremor is detected across the entire KivuSNet network and is adequately located after assuming a lateral propagation velocity model defined by a simple power-law equation (Barrière et al., 2017). The theoretical traveltimes obtained from this velocity model explain the observed arrival times of the LP event (blue dashed lines in Figure 3), confirming the common origin of the lava-lake tremor and this single LP event. As expected, we observe a pronounced decay of the surface wave amplitude between the closest station to the lava lake (KBTI, $6.1km$ away from Nyiragongo's crater), GOM $(17.5km)$, TGO $(35km)$, and KTSH $(38.6km)$. However, we do also note important site effects at RSY and BULE, which are both located in a subsiding area affected by significant CO_2 degassing (Wauthier et al., 2018). It is therefore important to keep in mind these two strong site-dependent effects when analyzing amplitudes from RSY and BULE. Yet, analyzing amplitude ratios in the frequency band $[0.3-1]Hz$ as a function of source-receiver distance remains relevant and should be useful for detecting temporal and spatial variations of magmatic activity in the Virunga. The SARA processing is performed using the python based software MSNoise (Lecocq et al., 2014) following the procedure described by Taisne et al. (2011). The continuous seismic amplitudes (envelopes) were computed by taking the absolute value of the analytic signal of the traces filtered between 0.3 and $1Hz$ after removing the instrumental response and using a bandpass, 4-poles zero-phase Butterworth filter. The obtained envelopes were then decimated to 1 min using a median filter in order to remove the transient spikes, and smoothed using a centered moving median of one day. The amplitude ratios for each station pair were computed from the 1-min decimated amplitude time series and smoothed using a centered moving median of 1 day. The choice of the window length for the smoothing operation (i.e., 1 day in this study) depends on targeted sources. The network characteristics (in terms of stations distribution and performance) control the strength of the temporal smoothing needed. For example, with a dense network around the main edifice allowing high temporal/spatial resolution, Taisne et al. (2011) took 5 min for reducing the influence of big earthquakes in the amplitude ratios before the signal inversion for tracking

magma propagation. On another hand, in a more qualitative approach using a sparser network, Caudron et al. (2015) chose a value of $6h$ to capture the main characteristics of stress migration at the Klyuchevskoy volcano group. In our study, we tested several window sizes to better gauge the influence of this critical smoothing operation on the final result and interpretation. It appears that a 1-day smoothing window is needed to better visualize and understand significant changes in seismic amplitude ratio across the VVP. A 1-day window allows to capture the main fluctuations of the continuous tremor activity in the VVP while shorter windows (e.g., 10 min) emphasize erratic, non-volcanic amplitude variations, such as the Lake Kivu's microseisms discussed later. For the 2-year-long time series plotted in Figure 2c, an additional 7-day moving median filter is applied to capture the main amplitude variations over this long-time frame, which are analyzed in more detail in Figs. 1.5, 1.6, 1.7, 1.8 and 1.9.

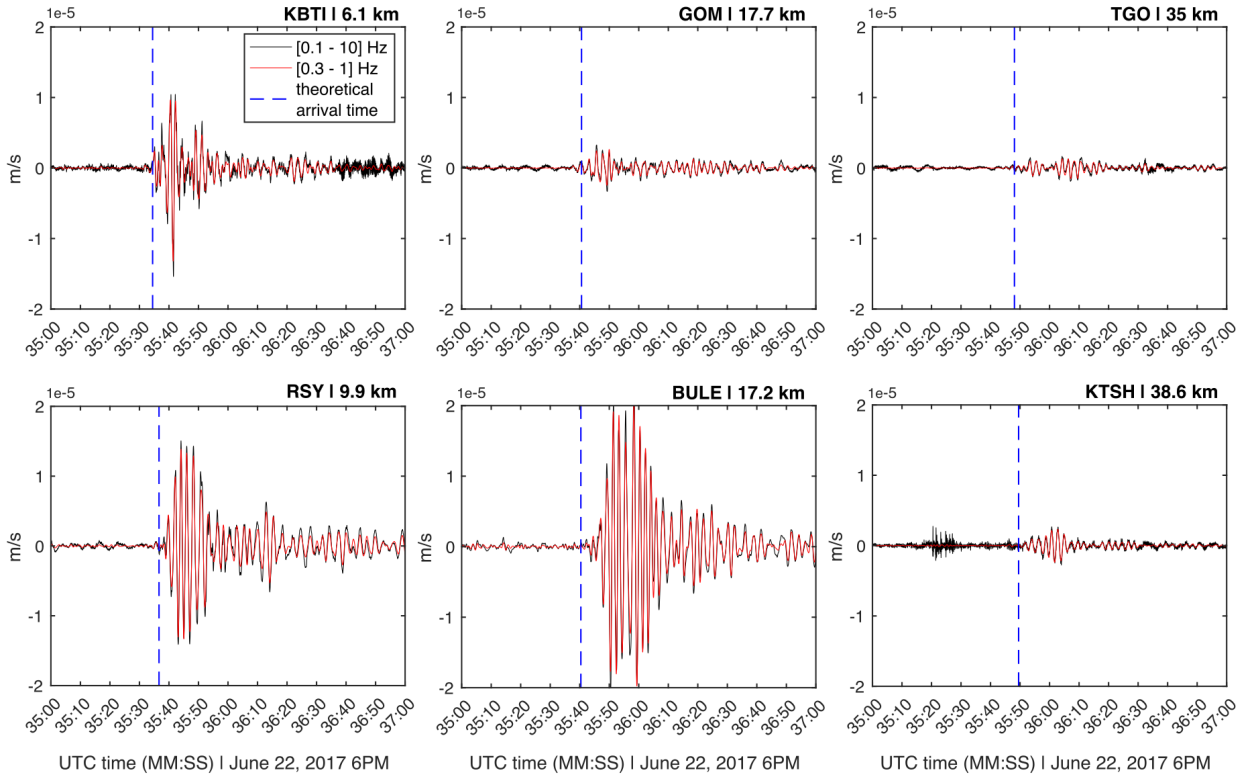

FIGURE 1.3: Two-minute-long seismograms (in $10^{-5}m/s$) at KBTI, GOM, TGO, RSY, BULE, and KTSH starting on June 22, 2017, at 6 PM (UTC time) depicting a shallow LP seismic event originating from Nyiragongo's crater. The seismic traces plotted in black are the broadband traces filtered between 0.1 and $10Hz$ and the ones plotted in red are obtained with a bandpass filtering between 0.3 and $1Hz$. The dashed blue lines represent the theoretical arrival times of a seismic signal originating from Nyiragongo's lava lake using the surface wave velocity model obtained by Barrière et al. (2017) and KBTI as reference station (i.e., the theoretical arrival time is set to the observed arrival time at this station)

1.4 Variations of low-frequency seismic amplitudes in the VVP

1.4.1 Long-term (seasonal) variations due to Lake Kivu microseisms

Figure 1.4 a shows the 4-year-long GOM time series (7-day median) plotted in Figure 1.2c. In Figure 1.4b and 1.4c, we provide monthly wind speed and monthly cumulative rainfall retrieved from a meteorological station also located at GVO. The wind speed dataset is split into winds coming from the south (mostly Lake Kivu) and from the north (inland). In order to only highlight the highest wind speeds, we selected the 97.5th percentile per month. The highest wind speeds occur during low rainfall periods, in accordance with observations at Lake Kivu (Kranenburg et al., 2020) or at another African Great Lake, Lake Tanganyika, located about 200 km southward from Goma (Docquier et al., 2016). The dry season in the Lake Kivu region generally starts in June and ends in September (Thiery 2015), which is confirmed by the local rainfall data obtained at Goma (Figure 1.4). This bimodal seasonal cycle is also obvious through the fluctuations of wind speed associated with the lake breeze (i.e., from south) starting to increase in April, which is 2 months earlier than the start of the dry season inferred from the rainfall. On a monthly basis (Figure 1.4b), the winds coming from the South are also stronger than those coming from the North (i.e., land breeze) all year long. Kranenburg et al. (2020) pointed out strong variations of the preferential wind speed direction depending on the location in the Lake Kivu region. From this study based on 2013–2016 data from a measurement station off the coast of the city of Gisenyi (Rwanda) next to Goma, the dominant wind direction is from the north and the wind speed range of the lake breeze (from south) is overall higher. Comparing Figure 1.4a and 1.4b, we observe here that the long-term variations of the seismic amplitude follows at first order the seasonality of the Lake breeze, thus being potentially at the origin of unwanted seismic noise in the considered frequency range.

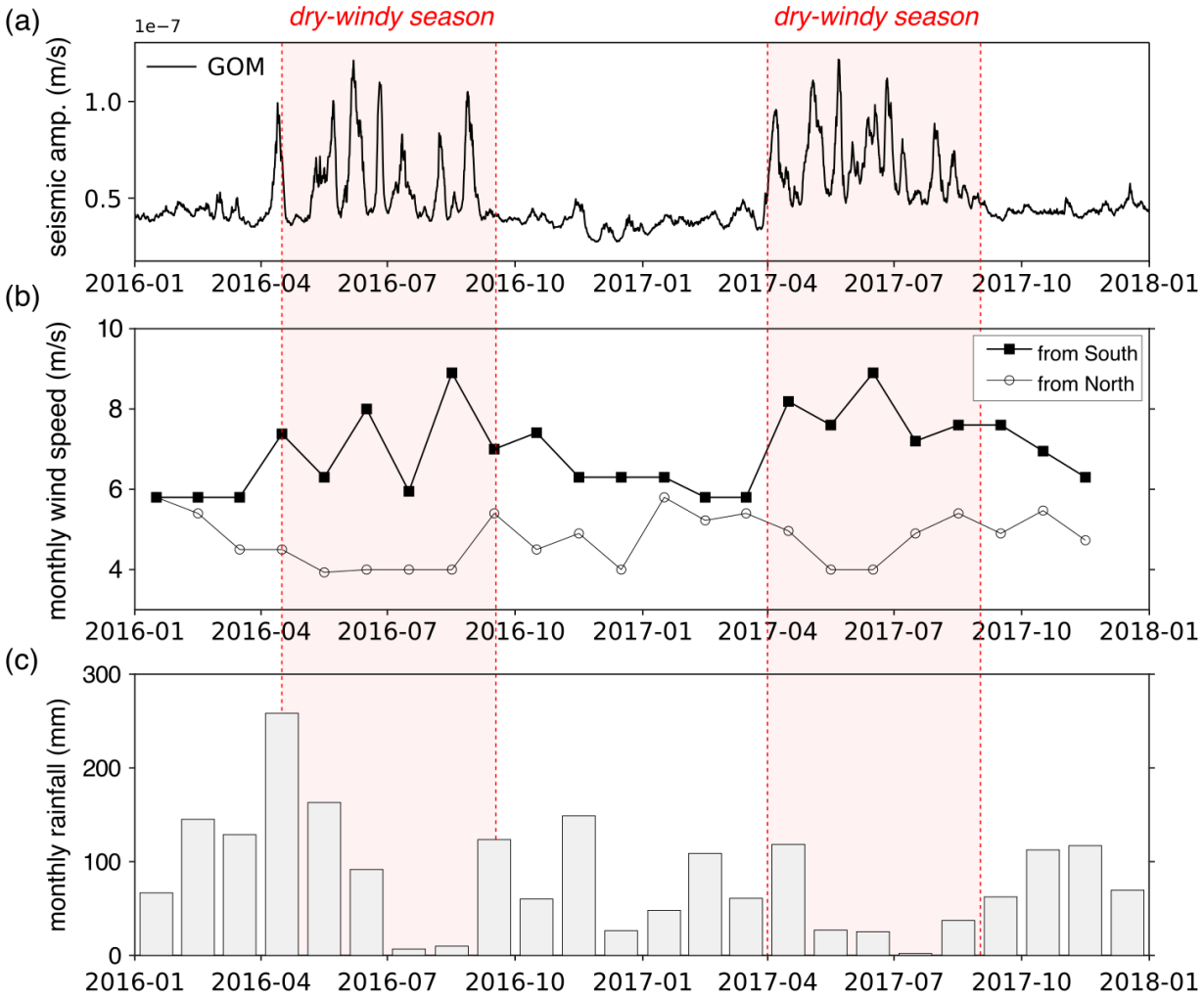

FIGURE 1.4: **(a)** Two-year-long seismic amplitudes timeseries (7-day median) at GOM seismic station (in $10^{-7} m/s$). **(b)** Monthly wind speed (97.5th percentile per month) split in two dominant wind directions, i.e., coming from the south (black line and squares) and from the north (grey line and circles). **(c)** Monthly cumulative rainfall data. Meteorological data are collected from a station located at GVO. The red dashed box corresponds to the maximum extent of the dry-windy season inferred from wind and rainfall data

Wind is known to be an important factor affecting the seismic noise at frequencies above 2Hz (Smith & Tape, 2019). Tan et al. (2019) noted that this spurious noise source can hamper the use of SARA at high frequencies. However, in the frequency band of interest $[0.3 - 1Hz]$, this effect should be mitigated. A strong local site effect might be an explanation but these marked long-term patterns are also observed at KBTI station (Figure 1.2c). Barrière et al. (2019) also pointed out such seasonal variability of the seismic noise below 2Hz after analyzing data from the station BULE located on the shore of Lake Kivu, close to the station GOM (see stations map in Figure 1.2a). Following recent studies about the generation of microseisms from Great Lakes across the globe (Anthony et al., 2018; Xu et al., 2017), we assumed that this seasonality in the frequency band $[0.5 - 2]Hz$ was most likely due to nearby Lake Kivu. Despite some potential similarity with the shoaling process of the primary ocean microseisms or the wave-wave interaction process of the secondary ocean microseisms, it is still unclear what exact mechanisms generate such

short-period microseisms (Anthony et al., 2018) and this question remains beyond the scope of this paper. The key role of wind speed variations in modulating the amplitude of the Lake microseisms appears however obvious, similarly to the ocean microseisms (Kerman & Mereu, 1993). Moreover, as evidenced in Figure 1.4b, 1.4a surface wind speed coming from the south with respect to GVO (lake breeze) higher than from the north (land breeze) could enhance the coupling into seismic energy during swell periods in Lake Kivu.

In order to support this hypothesis, we bring in the following section a new detailed investigation between wind speed and seismic amplitude data in the Virunga. Beyond the observed seasonal fluctuations, it is well known that the wind speed variations are also diurnal (Thiery 2015) (Kranenburg et al., 2020). Thus, we analyze two selected periods of a few days when seismic amplitude and wind speed can be compared with high temporal resolution. These specific periods are plotted in Figures 1.5 and 1.6.

1.4.2 Short-term (diurnal) variations due to Lake Kivu microseisms

Figure 1.5 compares two 5-day periods during the dry season (18-23 August 2017) and the following wet season (5-10 November 2017). Figure 1.5a represents the wind speed with a temporal resolution of 30 min coming from the south (lake breeze) and from the north (land breeze). The seismic amplitude at GOM is plotted against these histograms. A striking observation is that the seismic amplitude peaks in August 2017 coincide with the highest wind speed from the south. As described in the "Applicability of the SARA method in the VVP" section, the sliding window used is 1 day and the resulting seismic amplitude time series are strongly smoothed. Therefore, it is also interesting to plot the full seismic records and their corresponding spectrograms to better gauge the temporal relation between the wind speed and the level of seismic noise. In Figure 1.5b, we plot the spectrograms for the stations GOM, KBTI, and TGO for the two selected periods, pre-filtered in the frequency band $[0.3 - 2]Hz$. Seismic traces (in m/s) and spectrograms (in dB/Hz) at GOM, KBTI, and TGO are plotted with the same scale. The continuous (background) seismic tremor from Nyiragongo's lava lake is seen on all records, notably at KBTI across the full frequency range $[0.4 - 2]Hz$. On top of that, numerous transients are detected, which are due to the anthropogenic activity in most cases (see TGO above $1.5Hz$). Some local and regional earthquakes simultaneously recorded at all stations are also detected. Finally, the Lake Kivu microseisms are obvious on the August 2017 spectrograms and form bursts of seismic energy lasting a few hours between 0.5 and 2Hz and concentrated around $[0.5 - 0.7]Hz$ at KBTI and TGO. The reduced frequency range and amplitude for stations further away from the Lake Kivu (KBTI and TGO) confirm a source region closer to GOM. Such patterns are recorded all year long and are more prominent during the dry season, being responsible for the seasonal amplitude increase at GOM observed in Figure 1.4a. The case of November 2017 illustrates an example of low wind speed from both directions (north and south). Some weak microseisms decorrelated from the wind speed measured at GVO are recorded at GOM only, thus conveying again a source region closer to this station.

The seismic records at BULE, which is also on the shore of Lake Kivu close to the station GOM (see Figure 1.2a), often exhibits similar signature of lake microseisms (Barrière et al.,

2019). In Figure 1.6, we compare the seismic amplitude ratio between BULE and TGO and the wind speed obtained at GVO. A time period of 12 days is selected between May 16 and 28 at the beginning of the 2017 dry season. Here, the seismic traces and the spectrograms are filtered between 0.3 and 10 Hz, which allows for a better visualization of the influence of the anthropogenic noise above 1.5 Hz. Once more, we observe an excellent temporal agreement between the strongest wind speed from the south and the low $[0.3 - 1]Hz$ frequency seismic amplitude peaks related to the lake microseisms. The amplitude ratio BULE/TGO (Figure 1.6a) shows clear diurnal variations synchronous with the occurrence of strong southerly winds while the attenuation of the signal between BULE and TGO is obvious, thus conveying a source region closer to BULE. Only the strongest microseisms (between May 19 and 25) are detected at TGO between 0.5 and 0.7 Hz. The correlation observed between the seismic records at BULE and the wind speed measured at GVO implies that the microseisms recorded at GOM and BULE share the same source, though the variability of the wind speed along the shore of the Lake Kivu can be significant (Kranenburg et al., 2020). It also emphasizes that the wind speed recorded at GVO is well representative of the lake breeze at the origin of the Lake Kivu microseisms recorded by the seismometers deployed on its shore. Nonetheless, other minor microseismic events observed at BULE are not clearly associated with variations of the wind speed measured at GVO (see before May 19 and after May 26), similarly to the observations of weak microseisms at GOM in November 2017 (Figure 1.5). Thus, the source at the origin of the lake microseisms cannot be explained solely by an increasing lake breeze even if the highest wind speed from the lake region appears to play a fundamental role. The source of these signals appears to be a complex process and its mechanism remains elusive, though our analysis paves the way for further investigations comparing the atmospheric changes and the lake dynamics with seismic records around the Lake Kivu.

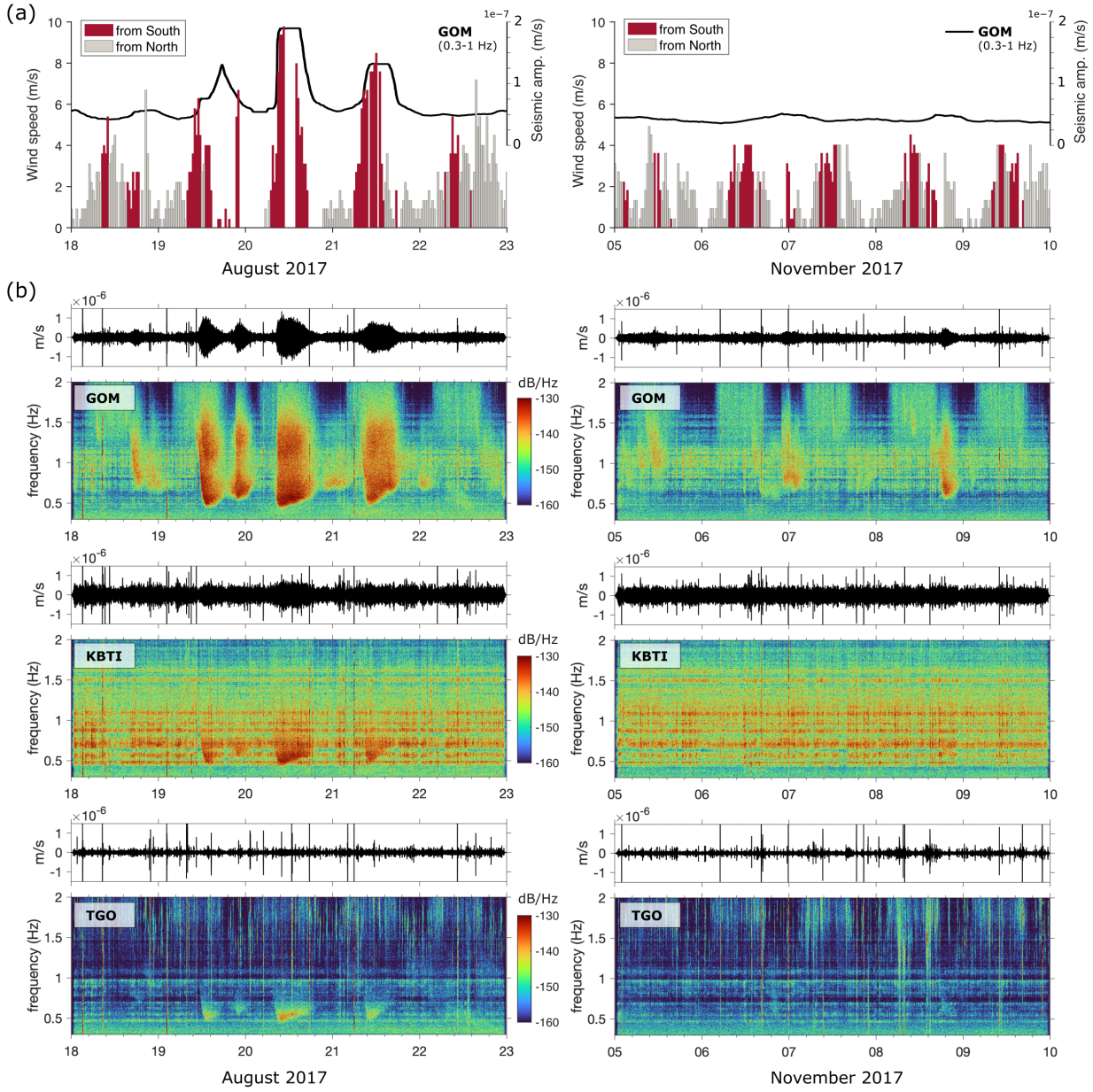

FIGURE 1.5: **(a)** Wind speed and seismic amplitudes in $10^{-7} m/s$ (GOM station) comparison at GVO between two 5-day periods during the dry season (18–23 August 2017; left) and the wet season (5–10 November 2017; right). The wind speed data (in m/s) has a temporal resolution of 30 min and are split in two dominant wind directions, i.e., coming from the south (red histograms) and from the north (grey histograms). **(b)** Filtered seismic traces (in $10^{-6} m/s$) in the frequency band $[0.3 - 2] Hz$ and corresponding spectrograms (in dB/Hz) at GOM, KBTI, and TGO stations for the same time periods depicted in **(a)**

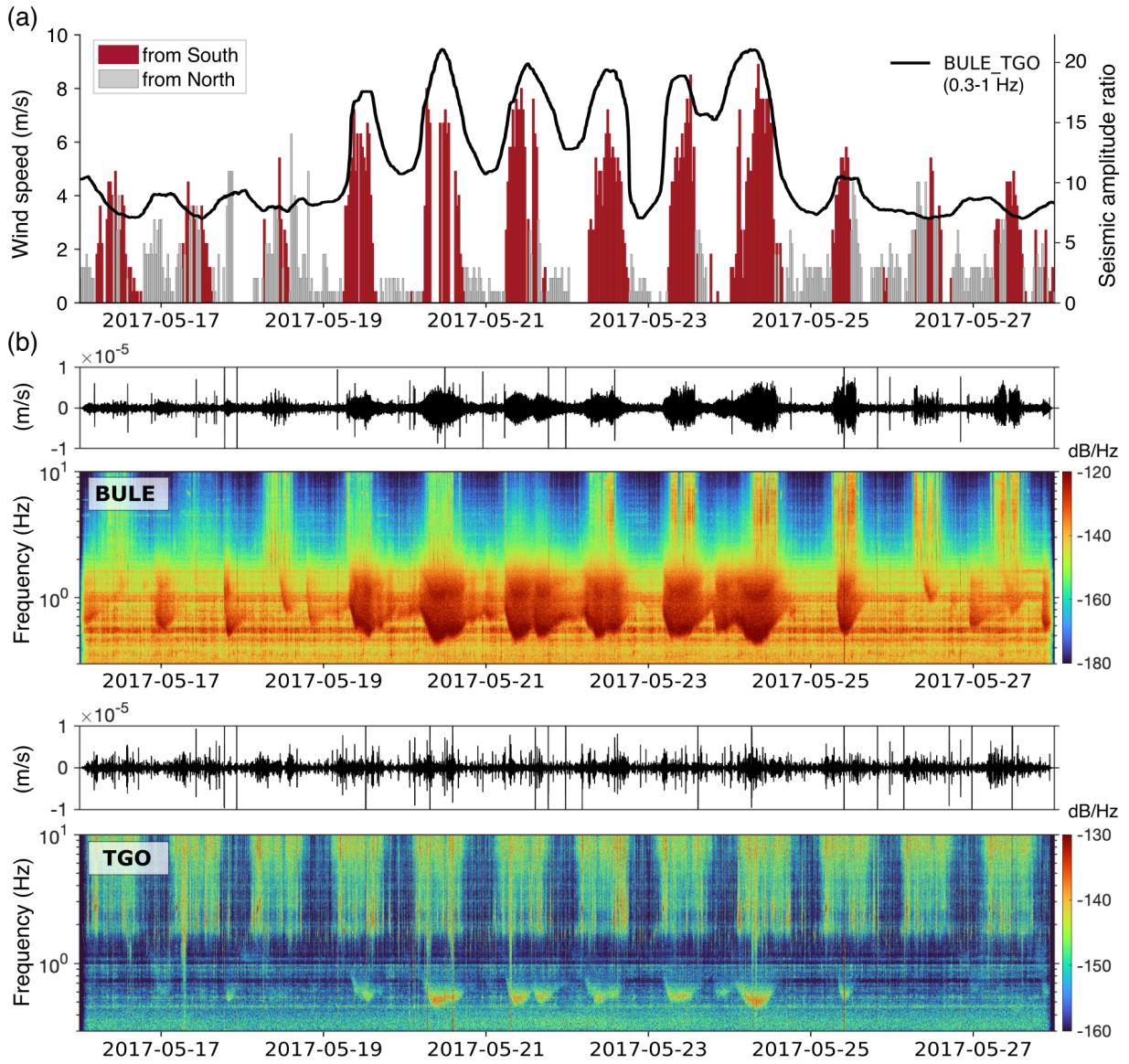

FIGURE 1.6: **(a)** Comparison between the seismic amplitude ratios for a station pair (BULE/TGO) and wind speed (red histograms for wind coming from the south and grey histograms from the north) obtained at GVO at the beginning of the 2017 dry season. **(b)** Filtered seismic traces in the frequency band $[0.3 - 10] Hz$ and corresponding spectrograms (in dB/Hz) at BULE and TGO stations for the same time periods depicted in **(a)**

1.4.3 Detecting the intermittent sources of tremor at Nyamulagira

A typical case of magmatic movements detected by SARA in the low-frequency band is presented in Figure 1.7. This kind of short-term event lasting approximately 1 day took place from 22 to 23 December 2015. Amplitudes at stations to the north of VVP near the Nyamulagira volcano (RGB, TGO, KTSH) have decreased much more than at the southern stations (KBTI, GOM). For example, the amplitude at RGB decreased about twice as much as at KBTI (Figure 1.7a). Hence, the amplitude ratios for pairs using the northern stations as reference (denominator) clearly increased (Figure 1.7b) while the ratio between two northern stations (RGB/TGO for instance) does not exhibit any significant variation.

In that case, one can only observe that the amplitude decay is slightly stronger at TGO than at RGB. On another hand, the ratio KBTI/TGO shows a stronger decay at TGO. Since all stations recorded an amplitude decrease, stronger in the north than in the south, this suggests that a persistent source in the northern part of the region, possibly associated to Nyamulagira, stopped around 23 December.

This hypothesis is further supported by other independent observations suggesting changes in the Nyamulagira eruptive activity. The volcanic tremor location obtained by Barrière et al. (2017) in the VVP following the interferometry approach of Ballmer et al. (2013) helps to refine the observations made with SARA (Figure 1.7c). On these daily location maps, the maximum location likelihood for the sources of continuous shallow tremor is highlighted in red. Since we applied a grid-search strategy assuming tremor sources as point sources, multiple active sources during a day could result in multiple regions colored in red. The accuracy of the final solution is constrained by the network layout and the ability to detect coherent noise sources at each station, enhanced by specific pre-processing procedures of the continuous records (see Barrière et al., 2017 for more details). Thus, in Figure 1.7c, the exact location (grid point) of the global maximum is not relevant. Instead, these daily location maps mainly tell us if the dominant tremor source region in the VVP is predominantly located at Nyamulagira, Nyiragongo or both. Hence, on 21 December, continuous tremors were both detected at Nyamulagira and Nyiragongo. Between 22 and 23 December, we observed a dominant source region toward Nyiragongo, reflecting the lava lake activity. After this date, the background persistent signature of Nyiragongo's lava lake, as illustrated by the tremor location on 23 December 2015 in Figure 1.7c, persisted up to the 22 May 2021 when the lava lake drained during the last flank eruption at Nyiragongo (Smittarello et al., 2022).

A wrong interpretation of the tremor location maps depicted in Figure 1.7c would be a shift of the tremor source due to magmatic movement from Nyamulagira to Nyiragongo. Instead, the SARA analysis indicates that a shut-down of the powerful shallow tremor source occurred at Nyamulagira. The surface effusive activity at Nyamulagira persisted a few months after this event in December 2015. Barrière et al. (2017) showed that this shallow signal was replaced by the occurrence of deeper LP events having similar frequency content. However, in the $[0.3 - 1]Hz$ frequency band considered, the continuous amplitude ratio time series across the network did not exhibit this deeper seismic signature. Activity depicted in the time series is rather dominated by the Nyiragongo shallow persistent tremor due to its lava lake activity. Because these shallow tremor sources are very energetic when active lava lakes are present both at Nyiragongo or Nyamulagira, a change in depth as high-lighted at Nyamulagira with a tremor-LP transition requires complementary methods to be detected (e.g., detection/location of single events, template matching of repetitive clustered events). Together with the SARA-based results, these complementary observations can be interpreted as a sudden decrease in magmatic activity in the shallow part of the Nyamulagira edifice.

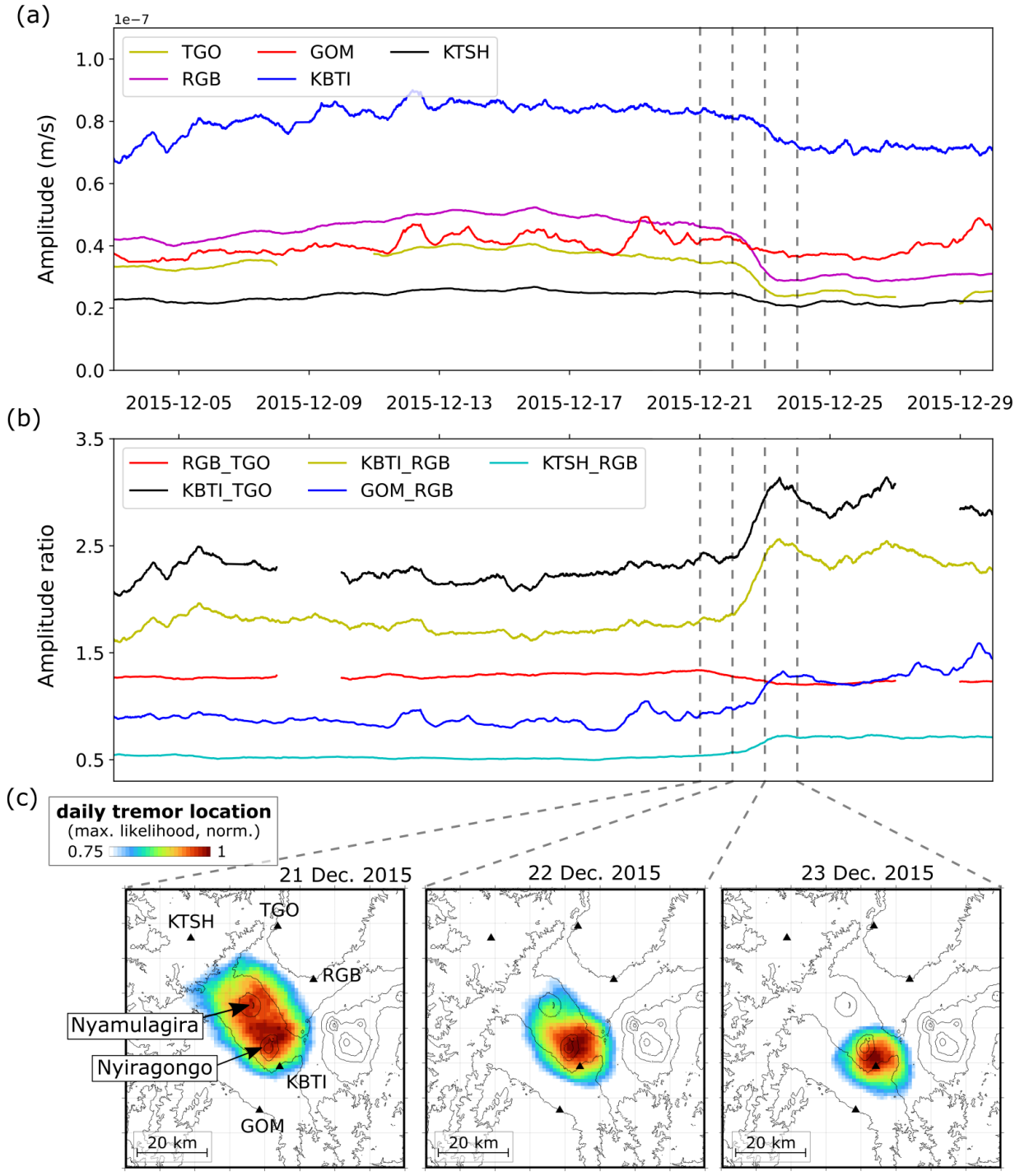

FIGURE 1.7: **(a)** Seismic amplitude (in 10^{-7} m/s) at TGO, RGB, GOM, KBTI, and KTSH between 3 and 30 December 2015. **(b)** Amplitude ratios for the station pairs RGB/TGO, KBTI/TGO, KBTI/RGB, GOM/RGB, and KTSH/RGB. **(c)** Daily location maps of the dominant continu- ous shallow volcanic tremor sources in the VVP between 21 and 23 December 2015. Both seismic amplitude timeseries **(a, b)** and location maps **(c)** are obtained from seismic signals filtered in the same frequency band $[0.3 - 1]Hz$ (see text for details)

1.4.4 Monitoring the background lava-lake tremor at Nyiragongo

Figures 1.8 and 1.9 are related to magmatic events evidenced by SARA in November 2016 and February 2018, respectively. Looking at Figure 1.2, these two amplitude variations are the strongest ones recorded at KBTI during the selected 2-year-long period. An interesting pattern in Figure 1.2c between KBTI, GOM, and TGO is the clear amplitude decay between these three stations, corresponding to an increasing distance from Nyiragongo. We focus in this section on these two specific events to support the hypothesis that we detect some relevant changes at Nyiragongo.

The November 2016 event (Figure 1.8) lasted approximately 9 days. At the beginning of the event on November 12, we observe increasing amplitudes at the southern (GOM, RSY, KBTI) and northern (RGB and TGO) stations further away from Nyiragongo. The largest amplitudes are observed at the two stations near Nyiragongo (RSY and KBTI) (Figure 1.8a). From November 14 to 21, all amplitude timeseries decrease, then stabilize. The overall level of seismic amplitude at all stations is significantly lower after than before November 21 (up to twice lower than the maximum reached a few days before). There is also a large peak the day before November 21, which is much stronger at GOM and RSY than at KBTI while it is barely noticeable at northern stations RGB and TGO.

The amplitude ratio between stations located close and far from Nyiragongo help to better understand the overall trend of amplitude variations over the whole month as well some changes more limited in time such as the large peak on November 20. Three amplitude ratios plotted in Figure 8b compare stations close to Nyiragongo (KBTI, RSY) and further away (TGO, RGB). A fourth ratio compares GOM on the shore of Lake Kivu with KBTI on the flank of Nyiragongo. The three ratios between "Nyiragongo's stations" (KBTI, RSY) and "northern stations" (TGO, RGB) depict roughly the same pattern, though more prominent for the station pair RSY-TGO: a rather constant trend during the week before November 12, a smooth increase and decrease between the 12th and 19th, then a marked peak ending with a significant decay reaching a new lower constant level. This new seismic amplitude level is the lowest one ever recorded during the full 2-year period (see Figure 1.2). Since these ratios closely follow the trend of the seismic amplitude curves at KBTI and RSY, we can infer that the main amplitude variations are due to changes close to these stations, that is close or at Nyiragongo. The ratio GOM-KBTI brings another piece of information where the most prominent feature is the large peak on November 20. It is clear that this sharp increase of amplitude ratio between GOM and KBTI indicates a source predominantly located to the south toward Lake Kivu, thus suggesting amplitude of this large peak compared to the background level over an increasing distance from the Lake Kivu (i.e., GOM > RSY > KBTI). In turn, we can conclude that the main amplitude change of magmatic origin only occurred on November 12-13 and that the following days exhibited a progressive decrease of the seismic tremor amplitude overlapped on November 20 by a non-magmatic event.

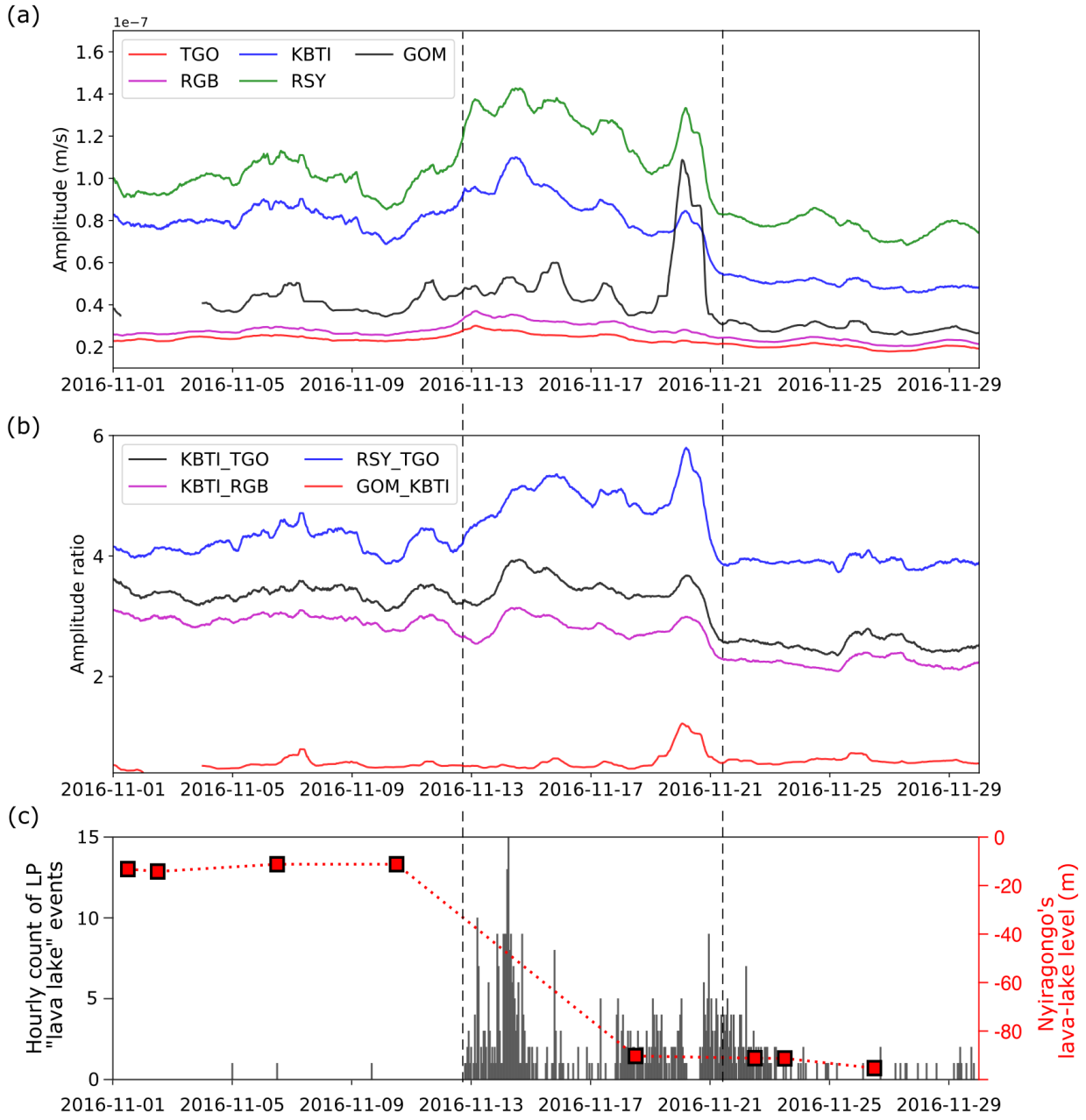

FIGURE 1.8: **(a)** Seismic amplitude (in $10^{-7} m/s$) at GOM, KBTI, RGB, RSY, and TGO between 1 and 30 November 2016. **(b)** Amplitude ratios for the station pairs KBTI/TGO, KBTI/RGB, GOM/KBTI, and RSY/TGO. **(c)** Left, hourly count of LP events originating from Nyiragongo's lava lake from Barrière et al. (2018). Right, lava lake level with regards to the lava lake rim (red squares connected by a dashed line) estimated from SAR space-based measurements (Barrière et al., 2022). The magmatic event corresponding to the drop of the lava lake level is encompassed between the two black vertical dashed lines (12-21 November)

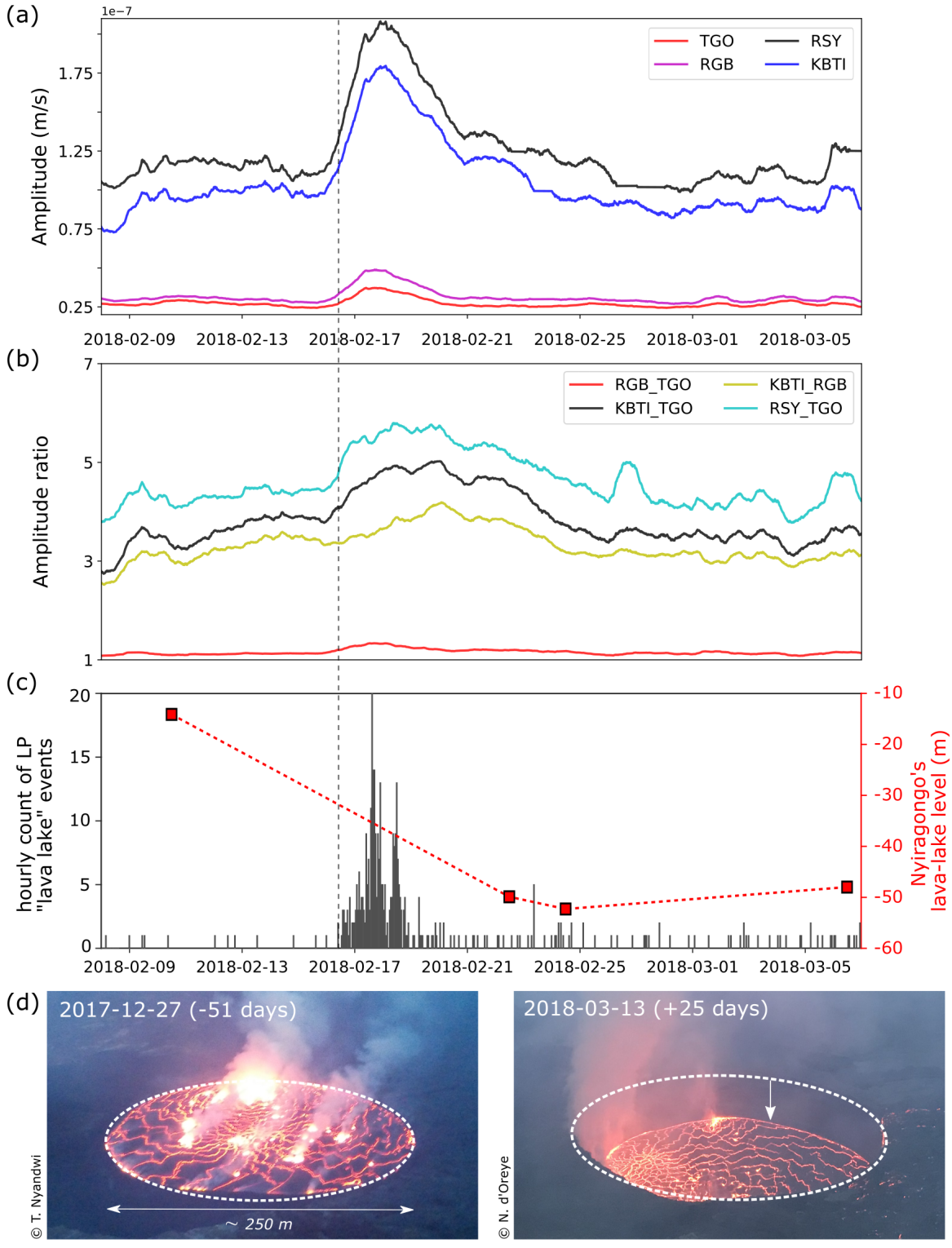

FIGURE 1.9: **(a)** Seismic amplitude (in $10^{-7} m/s$) at TGO, RGB, KBTI, and RSY between 8 February and 7 March 2018. **(b)** Amplitude ratios for the station pairs KBTI/TGO, KBTI/RGB, RSY/TGO, and RGB/TGO. **(c)** Left axis and grey bars: hourly count of LP events originating from Nyiragongo's lava lake. Right axis and red squares: lava lake level (with regards to the lava lake rim) estimated from SAR space-based measurements (Barrière et al., 2022). The start of the magmatic event corresponding to the drop of the lava lake level is identified by the black vertical dashed line on 16 February 2018. **(d)** Two pictures of Nyiragongo's lava lake before (-51 days) and after (+25 days) the lava lake drop on 16 February 2018.

1.5 Conclusion and perspectives

Former studies using the SARA method, either through qualitative (i.e., trend of the amplitude ratios) or quantitative (i.e., source location) approaches, generally focused on volcano-tectonic signals in a high frequency band (above $2Hz$) during magmatic migration (e.g., Caudron et al., 2015, 2018; Tan et al., 2019). Considering the specificities of the ambient seismic noise sources in the Virunga, we provided here a benchmark to assess the application of the SARA technique in monitoring Nyamulagira and Nyiragongo volcanoes at low frequency ($[0.3 - 1]Hz$). We show how we can use it to highlight temporal changes of shallow tremor sources at long distance (several tens of kilometers).

We identified that the nature of the volcanic seismicity in the VVP and the distribution of the available stations in the region (i.e., no dense network in close vicinity to both volcanic edifices) are best suited to detect magma movements using seismic amplitude ratios under 1 Hz, this low-frequency band being rich in information related to the superficial magmatic activity. The seismic wavefield below 1 Hz is dominated by the propagation of surface waves from persistent volcanic sources conveying summit eruption dynamics at both volcanoes. We qualitatively discuss the temporal and spatial variations of the seismic amplitude ratios in the VVP assuming isotropic radiation pattern and neglecting site effects. We showed that this simple approach applied in the low frequency range remains relevant since the decay of amplitude from the source (i.e., Nyiragongo, Nyamulagira, Lake Kivu) is well noticeable at the considered stations. However, strong site effects at two stations (RSY, BULE) are also noticed, which hamper the straightforward analysis of amplitude ratios involving one of these stations. We used more than two years of seismic data recorded by telemetered stations from the KivuSNet broadband seismic network. The technique seems sensitive to the intermittent sources of tremor at Nyamulagira volcano and to amplitude variations of the background tremor at Nyiragongo volcano. The six stations used in the present study correspond to the best ones available at that time in terms of station performance, data availability and distance to the volcanoes (see Oth et al., 2017). To date, in addition to a station deployed at the summit in early 2018, these stations remain among the most relevant for the monitoring of Virunga volcanoes. KBTI station best tracks the large level fluctuations in the lava lake at Nyiragongo. For Nyamulagira, RGB and TGO stations can be used to track tremor changes. However, it is noteworthy that TGO does not exist anymore (withdrawal of UN camp where the station has been installed since September 2015), which leaves a gap at the North of the Virunga.

Records at GOM and BULE stations located on the shore of Lake Kivu can be largely influenced by microseisms originating from Lake Kivu. As observed for other Great Lakes around the world (Xu et al., 2017), this effect decreases as the distance to the lake increases. The dominant non-magmatic source detected by SARA in this low-frequency band (i.e., $< 1Hz$) is related to the seasonal patterns of lake-generated microseisms, which are studied here in detail for the first time at an African Great Lake [1]. On this particular

[1] We would like to stress here the important work by Carchedi et al. (2022), who published an in-depth analysis of lake microseisms at lake Malawi with a dense network of instrument (including lake-bottom seismometers). While we wrote this sentence in our manuscript before the publishing date of this article, we should have mentionned "to the best of our knowledge". Thus, our study is not stricly-speaking the first detailled analysis of microseisms at an African Great Lake, though Carchedi et al. (2022) did not use comparative weather data.

aspect, this study brings additional clues about the source mechanisms as being strongly related to the lake breeze and swell periods. One should note that analog records (from Kinemetrics instrument) at BULE station were claimed to exhibit volcanic tremors for several months prior to 2002 Nyiragongo eruption while synchronous records from the other available station located at the North of Nyiragongo did not record any tremor (Kavotha et al., 2002). In light of the results presented here, one can question whether diurnal to seasonal variations of short-period Lake Kivu microseisms were also potentially recorded at that time at BULE station.

In the context of real-time monitoring, we thus identify the main limitation of the method in this frequency band as being influenced by lake microseisms, which are associated predominantly to southerly winds over Lake Kivu. This effect is more pronounced during the dry season and is dominant for stations deployed close to the shore of Lake Kivu. These seasonal to diurnal seismic amplitude variations can mask volcanic signals since the microseismic signature can remain significant for stations closer to the volcanic edifices like RSY and KBTI, both located less than 15 km away from the Lake Kivu. This also implies that interpreting signal at a single station during these unfavorable periods should be done with caution. The SARA approach combining records at different locations is of particular interest in this case. Having several stations located over an increasing distance to the lake allows gauging easily the most likely source region between Lake Kivu's microseisms and Nyiragongo/Nyamulagira's volcanic tremors. The main advantage of this method is thus its ease of implementation and interpretation. In this context, it offers the possibility of detecting changes in the volcanic tremors caused by unrest at Nyamulagira or Nyiragongo. It is also efficient in detecting major variations related to eruptive dynamics at both volcanoes and can provide decisive real-time information from limited field records (i.e., a few station pairs), as it may happen for volcanoes monitored with ground sensors deployed in remote areas. Considering its simplicity, computing continuously the seismic amplitude ratios between relevant pairs of stations constitutes an interesting complementary tool to the Goma Volcano Observatory for monitoring the summit effusive activity at both volcanoes, alongside other monitoring solutions.

Finally, it is worth noting that the work presented here was completed before the intense seismic crisis associated with the dyke intrusion occurring during the last May 2021 flank eruption at Nyiragongo and remarkably well recorded by the seismic network KivuSNet network over an entire week (Smittarello et al., 2022). In turn, we did not analyze in this paper this particular period, which will be dedicated to further investigations. In that case, the more standard approach of the SARA technique focusing on high-frequency volcano-tectonic signals could be well suited to track the progression of this major dyke intrusion with the KivuSNet available at that time. If possible, in the future, a denser deployment of stations around the edifices would be obviously beneficial for applying the full SARA methodology for tracking magma movement in the VVP.

Chapter 2

Seismic amplitude measurements prior, during and after the May 2021 Nyiragongo flank eruption

THe next 4-year period analyzed in the present Chapter between 2018 and 2022 encompasses the May 2021 flank eruption at Nyiragongo, which was a major volcanic and humanitarian crisis in the region. This Chapter is thus a logical continuation of the previous Chapter as we will now provide a complete benchmark to assess the use of seismic amplitude-based analysis for monitoring Nyiragongo during "stable" eruptive activity within its summit crater (i.e, lava lake, spatter cone) and rare crisis periods marked by flank eruption and dyke intrusion (i.e., lava flows, fracturing, high-rate tectonic seismicity).

2.1 Preliminary considerations

In Chapter 1, we qualitatively analyzed the variations of seismic amplitudes at several stations and their ratios (SARA method) across the Virunga up to early 2018. We demonstrated that variations in seismic amplitudes within a narrow low frequency band ($[0.3 - 1]Hz$) could be interpreted as directly related to changes at Nyiragongo's lava lake, though sometimes contaminated by lake microseisms from nearby lake Kivu. This straithforward processing can provide decisive near real-time information from limited field records.

During volcanic crisis, like the 2021 flank eruption at Nyiragongo, applying the full SARA methodology at high frequency ($> 2Hz$) to track magma movements in the edifices could be considered. This approach involves locating seismic sources based on seismic amplitude ratio. However, it requires a dense network of stations not available in the Virunga despite the recent monitoring efforts. Over the past few years, Nyiragongo has been instrumented with only two seismometers (one at the summit and one on its flank), while no permanent seismic station has never been deployed near Nyamulagira volcano. Due to numerous impediments in this region (i.e., civil war, political instability, difficult access to remote areas, etc.), it remains unlikely that denser deployments of permanent, broadband, telemetered seismometers around the volcanic edifices could be achieved in the near future. As pointed out in the conclusion of Chapter 1, the sparse network configuration is more suited to follow the subsequent $\approx$ 20-km dyke intrusion from Nyiragongo to lake Kivu. Nevertheless, we have not yet tested the full SARA methodology to this particular case study.

In light of the above-mentioned restrictions and with the aim of testing and providing a seismic product that is easily interpretable in terms of volcanic unrest, we maintain the same approach applied in Chapter 1: directly analyzing seismic amplitudes and ratios between available stations at key locations. This approach still allows a first-guess location of the dominant seismic source(s) using only a few station pairs. To characterize both low-frequency shallow volcanic tremor generated at Nyiragongo's lava lake and the high-rate hybrid/tectonic seismicity during fracturing and dyke propagation, we further refine our approach by analyzing spectrograms in detail at different time scales and by processing seismic amplitudes in different frequency bands with various smoothing operators. To confirm (or refute) interpretations based solely on the observed seismic amplitudes, we incorporate results from complementary tools, such as seismic event locations in the Virunga during the flank eruption, long-term tremor location at Nyiragongo, and infrasound measurements near Nyiragongo before, during, and after the eruption.

This Chapter 2 is fully written in French and the title can be translated as followed "Amplitudes sismiques avant, pendant et après l'éruption de flanc du Nyiragongo en mai 2021".

2.2 Introduction

Le volcan Nyiragongo reste le plus fascinant et le plus dangereux de la province volcanique des Virunga. Il culmine à 3470 m d'altitude et il a été l'hôte du plus grand lac de lave au monde pendant plusieurs décennies; sa surveillance est cruciale pour la population environnante et plus particulièrement pour la ville de Goma et sa population de plus d'un million d'habitants dont il n'est distant que d'environ 15 km. (Figure 2.1a). En général, l'activité volcanique du Nyiragongo est dominée par des éruptions effusives dans le cratère sous la forme d'un lac de lave persistant (jusqu'à plusieurs décennies), alimenté par un réservoir superficiel sous-jacent (Smets, 2015).

Le 22 mai 2021, sans précurseurs apparents (sismicité, déformation, dégazage) hormis une augmentation de l'activité sismique au sommet environ 40 minutes avant, une éruption se déclare sur le flanc sud du Nyiragongo, drainant rapidement un volume estimé de 10 à $15 Mm^3$ de lave qui envahit les quartiers nord de la ville (Smittarello et al., 2022). Cette éruption a créé une crise humanitaire sans précèdent dans cette zone qui peine à sortir des conflits armés. Les éruptions sur les flancs du Nyiragongo sont rares; seulement trois ont été répertoriées au cours des cent dernières années, en 1977 (Tazieff, 1977), 2002 (Komorowski et al., 2002) et 2021 (Smittarello et al., 2022), ce qui limite par conséquent l'étude et la compréhension de leurs dynamiques. Ces trois éruptions effusives (écoulement de laves sur les flancs) partagent des traits communs dans leur déroulement. Avant l'éruption, le cratère possédait un lac de lave actif à une altitude supérieure ou égale à 3200 m (surtout en 1977 et 2021, le fond du cratère en 2002 étant encroûté depuis 1995, avec la présence d'hornitos) (Figure 2.1). Les coulées de lave à travers un réseau de fractures sur les flancs ont été synchrones avec le drainage du lac de lave (en 1977 et 2021) et un effondrement progressif du fond du cratère s'étalant sur plusieurs jours. La sismicité co- et post-éruptive a été très forte et soutenue pendant plusieurs jours (Hamaguchi et al., 1982; Kavotha et al., 2002; Smittarello et al., 2022). La composition pétrographique du magma des coulées de 2021 est également similaire à celle de l'éruption de 2002 soit un magma très fluide sous-saturé en silice avec des traces d'olive primitive témoignant un apport d'un magma profond lors l'éruption (Smittarello et al., 2022).

Sur base d'une révision de la littérature par Smets (2015), les éruptions fissurales du Nyiragongo de Janvier 1977 et Janvier 2002 ont été précédées par certains évènements sismiques liés à la géodynamique du rift du Kivu et pouvant être apparentés comme des signaux précurseurs. En 1977, les faits les plus notables sont un séisme régional superficiel de magnitude modérée (Mb 5.2) ayant eu lieu 4 jours avant l'éruption, suivi d'une augmentation d'amplitude et de la fréquence de signaux trémor (Hamaguchi et al., 1982). En 2002, Kavotha et al. (2002) mentionnent la détection de trémors inhabituels jusqu'à 11 mois avant l'éruption. Des séismes ressentis par la population avant ces éruptions de 1977/2002 et des changements d'activité de surface dans le cratère ou sur les flancs en 2002 (panache de cendres, fumerolles, augmentation de température dans des fissures) sont d'autres observations perçues comme précurseurs et relevées par Komorowski et al. (2002).

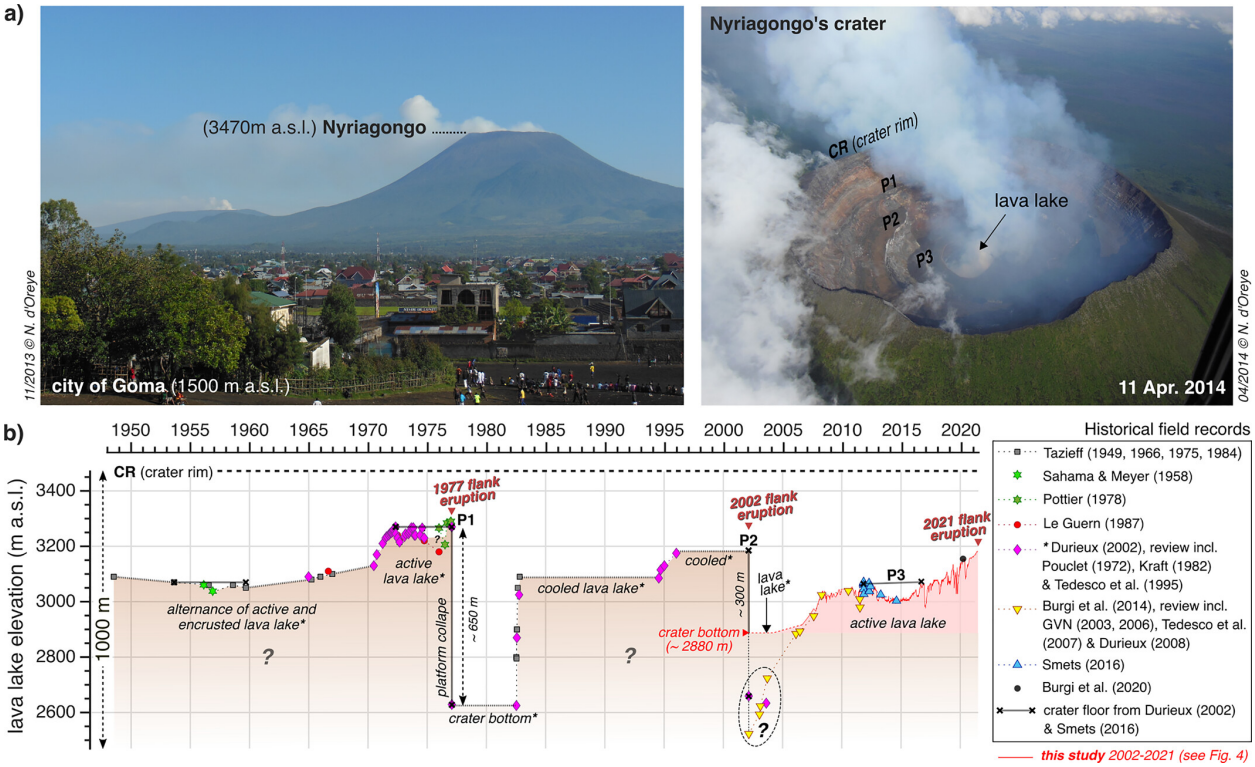

FIGURE 2.1: Le lac de lave du Nyiragongo (Figure extraite de Barrière et al., 2022). **(a)** Volcan Nyiragongo situé à 3470m d'altitude vu de la ville de Goma. **(b)** Vue aérienne du cratère de Nyiragongo avec ses différentes plates-formes. P1 représente la première plateforme proche du bord du cratère suivi de la P2 et en fin de la P3 plus profonde et proche du lac de lave. **(c)** Mesure de l'élévation du lac de lave et de son évolution de 1950 à 2021.

Notre but n'est pas ici de ré-analyser ces éléments et certains observations rapportées dans ces études semblent probantes. Cependant, concernant la sismicité, il convient de mentionner que ces études reposent sur un nombre très restreint de sismomètres "analogiques" c'est-à-dire desenregistrements sur papier ou film. En 1977, il n'y avait qu'un seul sismomètre situé à 100 km du volcan (station LWI, site ré-utilisé dans le réseau KivuSNet) et en 2002, deux stations situées pour la première à une vingtaine de kilomètres au sud du Nyiragongo (station BULE ou BLG, site ré-utilisé dans le KivuSNet) et et pour la seconde au nord du Nyiragongo (station KTL, site non utilisée dans le KivuSNet). Les mécanismes sources et les localisations de ces trémors restent donc incertains et sujets à débat. Par exemple, nous avons montré dans le chapitre précédant que les trémors journaliers enregistrés à la station de BULE (et non détectés à celle de KTL) avant l'éruption de 2002 pourraient être également induits par des microséismes du Lac Kivu et non au processus magmatique du volcan Nyiragongo.

Le Nyiragongo est un volcan dit à "conduit ouvert" où le dégazage est continu. Détecter l'apport de magma frais en mesurant des variations de déformation du sol (par GNSS, InSAR) ou des changement de la sismicité est bien moins évident que pour des volcans dits fermés, c'est-à-dire avec un/des conduit(s) solidifié(s) (Lesage et al., 2018). Dans le cas de conduits fermés, la mise sous pression du système magmatique se traduit par une augmentation notable de la sismicité et de la déformation lors de la fracturation de l'édifice (Kilburn, 2018). Une caractéristique notable et récurrente des systèmes ouverts, comme

en Islande, au Piton de la Fournaise, à l'Etna, ou au Kīlauea, est un déclenchement de l'éruption qui survient de manière beaucoup plus inattendue que dans les systèmes fermés, parfois quelques minutes après les premiers signaux géophysiques alarmants, car le magma est déjà proche de la surface (Acocella et al., 2024).

Certains volcans très bien instrumentés sur de longues périodes d'observations tels que l'Etna ou le Piton de la Fournaise ont un historique de nombreuses éruptions très bien étudiées, permetant un taux de prévision excellent des éruptions (Acocella et al., 2024) ce qui n'est pas le cas du volcan Nyiragongo. Par définition, lorsqu'il possède un lac de lave (ce qui est souvent le cas, cf. Figure 2.1), le Nyiragongo peut être considéré comme constamment en éruption. La quantité de signaux géophysiques (sismicité, infrasons, émissions de gaz, niveau du lac de lave) témoigne de cette activité continue et sont alors détectés quotidiennement (Barrière et al., 2017, 2018; Oth et al., 2017; Subira et al., 2023). En l'absence de mesures géophysiques historiques denses et reproductibles lors des précédentes éruption de 1977 et 2002, la dernière éruption de 2021 a mis en évidence la difficulté de qualifier les changements de ces signaux géophysiques quelques jours, semaines ou mois avant l'éruption comme des précurseurs avérés d'une éruption de flanc imminente (Barrière et al., 2022, 2023b; Smittarello et al., 2022).

Avec ce chapitre, notre but est d'aborder la sismicité avant, pendant et après cette éruption de flanc par une analyse multi-fréquentielle des variations de l'amplitude sismique à diverses échelles de temps (année, mois, jour). Sur base de l'ensemble des stations sismiques disponibles pendant la période considérée, cette analyse exhaustive vise ainsi à établir une étude référence sur les niveaux de sismicité dans les périodes inter-éruptives et les périodes de crise, c'est-à dire d'éruption de flanc. En complément du chapitre 1, nous pourrons ainsi juger des atouts et inconvénients de la technique SARA simple à metre en oeuvre dans le cadre d'un monitoring quasi temps-réel du Nyiragongo à l'OVG.

2.3 Chronologie de l'éruption du 22 mai 2021

Les détails sur le déroulement l'éruption de mai 2021 de Nyiragongo ont été décrits par Smittarello et al. (2022) et sont illustrés par la Figure 2.2. L'éruption commence le soir du samedi du 22 mai 2021 sans précurseurs apparents (sismique, déformation, dégazage) moins d'une heure avant l'apparition de lave sur les flancs, surprenant à la fois la population de la ville de Goma et le personnel de l'Observatoire Volcanologique de Goma. Ce jour-là, l'activité volcanique semblait normale d'après l'analyse des données sismiques du réseau KivuSNet. Cependant, à $15h57(UTC)$, une augmentation de l'activité sismique est observée sous forme d'un essaim de séismes enregistré uniquement par la station du sommet. Le premier évènement sismique localisé au niveau de l'édifice est détecté par le réseau à $16h15(UTC)$. L'activité sismique s'est ensuite intensifiée, couplée à une augmentation du niveau infrason à partir de $16h30(UTC)$ mais la source des infrasons restait contrainte au cratère principal. Entre $16h46$ et $16h56(UTC)$, il y a eu l'ouverture des premières fissures sur le flanc du volcan. Entre $17h00$ et $17h10(UTC)$, le pic d'intensité infrason associé aux fontaines de laves s'est produit (Barrière et al., 2023a). Six fractures se sont ouvertes séquentiellement du nord au sud, formant deux fronts de coulées de lave (Figure 2.2c). Une coulée a progressé vers l'est en direction du Rwanda, s'arrêtant à quelque kilomètres de la frontière, tandis qu'une autre s'est dirigée vers la ville de Goma, s'arrêtant à environ 1,3 km de l'aéroport. La fin de l'éruption de flanc déduit des données infrasons est estimée autour de $22h30(UTC)$ (Barrière et al., 2023a), soit environ 6 heures après les premières laves.

Bien qu'elle ait couvert une faible superficie de la ville de Goma, l'impact de l'éruption de mai 2021 a été importante. Smittarello et al. (2022) reportent 220 personnes décédées directement ou indirectement dans cette catastrophe et de nombreuses infrastructures de base détruites, notamment huit écoles, trois centres de santé, des lignes électriques hautes tension, des antennes de télécommunication, etc. En 1977, 61 personnes étaient décédées directement et 554 personnes étaientdevenues sans-abris (Smets et al., 2015). En 2002, 70 à 100 personnes ont été tués directement ou indirectement, et 13% de la ville couverte ont été par la lave (Smets et al., 2015). L'éruption de 2021 reste la plus catastrophique en raison de l'expansion de la ville et de la forte pression démographique qui a poussé les habitants à occuper des zones jadis utilisées pour l'agriculture près du volcan (Nyandwi et al., 2023).

Concernant la surveillance des enregistrements sismiques, comme pour d'autres observations (GPS, InSAR, géochimie), cette éruption n'a montré aucun signe précurseur évident de regain d'activité magmatique. Aucune déformation du sol ni une augmentation significative de l'activité sismique n'avait été rapporté quelques mois, quelques jours et voir même quelques heures avant l'éruption. L'intense activité du lac de lave et d'un cône actif à l'intérieur du cratère étaient les seuls faits connus particuliers depuis 2016 sur ce volcan. Au fil des années, le fond du cratère s'est rempli du fait de débordements successifs du lac de lave. Avant l'éruption, son niveau était équivalent à celui estimé avant l'éruption de 2002 et environ 85 m plus bas que le niveau de 1977 (Barrière et al., 2022).

La combinaison de toutes les données disponibles a mis en évidence différentes phases de l'éruption de mai 2021 décrite par Smittarello et al. (2022) et résumée par la Figure 2.2.

La première phase fait référence aux événements ayant conduit à la rupture de l'édifice au niveau des flancs, suivie d'une vidange rapide du lac de lave (Barrière et al., 2023a). Bien que l'activité effusive ait duré environ 6 heures, l'activité sismique associée à une intrusion magmatique superficielle a persisté dans le temps sur environ dix jours avec des milliers de séismes de faible magnitude et des centaines de séismes de magnitude modérée (M_L 3 à 5) ressentis dans la ville de Goma et ses environs. Le motif de déformation du sol observé (GNSS, InSAR) et la répartition de la sismicité sont typiques de l'ouverture d'un dyke accompagné de la formation d'un graben en subsidence. La deuxième phase éruptive est la propagation de la sismicité durant l'intrusion magmatique se propageant vers le sud. La sismicité illumine ainsi la propagation d'un dyke depuis le sommet de l'édifice en direction du sud. Cette seconde phase commence dès les premières heures de l'éruption le soir du 22 mai. L'activité sismique a migré du sommet du Nyiragongo vers la ville de Goma jusqu'au 24 mai. Un fort dégazage de SO_2 et l'apparition d'une colonne de cendres au sommet du volcan le 23 ont été d'autres évènements notables. La troisième phase a commencé avec un large panache de cendres le 25 mai au sommet à $4H30(UTC)$, accompagnée d'une augmentation brutale du taux de sismicité et de la magnitude des évènements de 1 à 2 unités. Cette phase correspond également à une reprise de la migration de sismicité vers le sud qui restait particulièrement concentrée sous la ville de Goma le 24 mai. Cette dernière séquence sismique s'est étendu sur plusieurs jours et, spatialement, a couvert le nord du bassin du Lac Kivu jusqu'à la faille de Nyabihu, où la sismicité associée au dyke n'a plus progressé.

Ces séquences résument dans le temps la migration magmatique progressive d'un dyke subvertical estimé, par inversion d'interférogrammes radar, d'une épaisseur de 2,5 mètres et d'un volume de 240 Mm^3, depuis le sommet de Nyiragongo jusqu'au bassin du Lac Kivu au niveau de la faille de Nyabihu (Figure 2.2c) (Smittarello et al., 2022).Ces observations seront discutées dans la suite de ce chapitre afin d'analyser l'évolution de la sismicité par simple analyse des amplitudes sismiques et de leurs rapports.

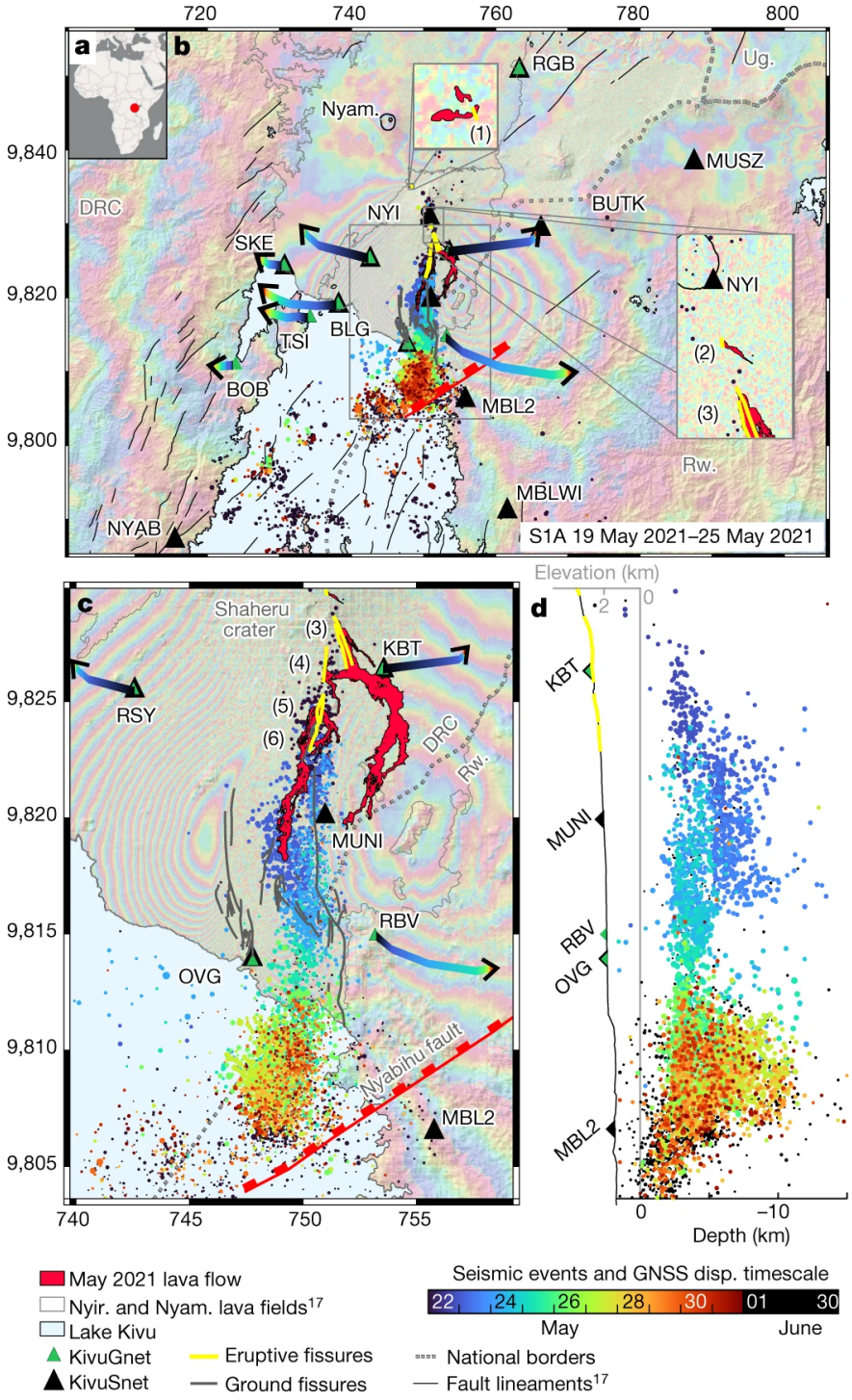

FIGURE 2.2: Observations relatives à l'éruption de mai 2021 du Nyiragongo (figure extraite de Smittarello et al., 2022). **(a)** Localisation du Nyiragongo sur une carte politique d'Afrique. **(b)** Observations d'interferométrie radar (franges interférométriques issues de Sentinel-1 en arrière plan, couleurs bleu à rouge), de sismologie (hypocentres avec code couleur correspondant au temps d'origine) et de géodésie (déplacements GNSS avec code couleur correspondant au temps de mesure) de l'éruption de mai 2021 du Nyiragongo. Les triangles noirs représentent les stations sismiques et les triangles verts représentent les stations GPS (parfois co-localisés avec les stations sismiques). Les lignes jaunes représentent les fissures éruptives etles coulées de lave sont représentées en rouge. **(c)** Zoom de la carte représentée en **(b)**. **(d)** Une coupe nord-sud des hypocentres correspondant au zoom de la sous-figure (c).

2.4 Données et méthodes

2.4.1 Données sismiques: KivuSNet

Les données utilisées dans ce nouveau chapitre proviennent du réseau KivuSNet majoritairement déployées en R.D. Congo et au Rwanda pour deux d'entre elles (BUTK et SAHA) (Oth et al., 2017). Une station au Burundi (BUJA) environ 200 km au sud de Goma n'est pas utilisée car trop éloignée. La majorité des stations du réseau, représentées sur la Figure 2.3, ont été utilisées à l'exception de quelques unes, en fonction de la disponibilité des données indiquée dans la Figure 2.4. Ainsi, les stations MUSK, MUNI, LBGA n'ont pas été considérées. La station MUSK a été démantelée très tôt pour éviter des problèmes de perte d'équipement et n'aura fonctionné que pendant moins d'un an. Cette station était localisée dans la base de la mission des Nations Unies au Congo (MONUSCO) qui avait été fermée peu de temps seulement après son implantation. La station de MUNI est aussi localisée dans une base à proximité d'une route nationale très fréquentée (unique route/piste majeure reliant Goma au nord des Virunga passant par KBTI). Elle avait été démantelée en raison de la mauvaise qualité des données due au très haut niveau de bruit d'origine anthropogénique (route, activité humaine dans le camps). Il est cependant à noter qu'un sismomètre y a été redéployé juste après l'éruption pour le suivi de l'activité post-éruptive. Quant à la station LBGA, télémétrée mais difficile d'accès pour l'équipe de maintenance, n'a pas fourni de données avec une continuité satisfaisante et n'est donc pas adéquate pour une analyse SARA. Au total, nous avons traité plus de quatre ans de données sur un ensemble de 16 stations sismiques durant la période allant de 2018 (fin de l'analyse du chapitre 1) jusqu'à juillet 2022 (fin d'opération du KivuSNet).

2.4.2 Paramétrisation des calculs d'amplitudes sismiques

Spectrogrammes à différentes échelles de temps

La détection d'un trémor à basses fréquences ($[0.3-1]Hz$) liée à l'activité effusive au Nymalugira et au Nyiragongo (Barrière et al., 2017) a motivé l'analyse des amplitudes sismiques et de leurs rapports dans la VVP comme réalisée dans le chapitre 1. Suivre notamment l'évolution du "trémor de fond" ("background tremor") associé au Nyiragongo a permis de comprendre la dynamique de son lac de lave (Barrière et al., 2019; Subira et al., 2023). Cela constitue un paramètre important à suivre pour l'observatoire basée à Goma.

Pour les stations et la période d'étude considérées, nous avions établi que la bande de fréquence ($[0.3-1]Hz$) était adaptée à la caractérisation des différentes sources de trémors dans le VVP, dont Barrière et al. (2017) obtient la localisation dans la même bande fréquentielle par cross-corrélation du bruit ambiant. Barrière et al. (2019) montrent que la bande de fréquence optimale pour la détection du trémor du lac de lave au Nyiragongo est variable suivant qu'on soit proche ou non de Nyiragongo (effet d'atténuation du signal sismique) et suivant le niveau de bruit antropogénique à la station. Par exemple, la signature fréquentielle de ce trémor est claire jusqu'à 2 Hz à la station KBTI au pied du Nyiragongo (au delà, l'activité humaine est dominante durant la journée) tandis qu'au sommet (station NYI) le trémor excite une large bande jusqu'à 10 Hz. Il nous semble donc important de réévaluer les bornes des bandes de fréquence qui pourraient être per-

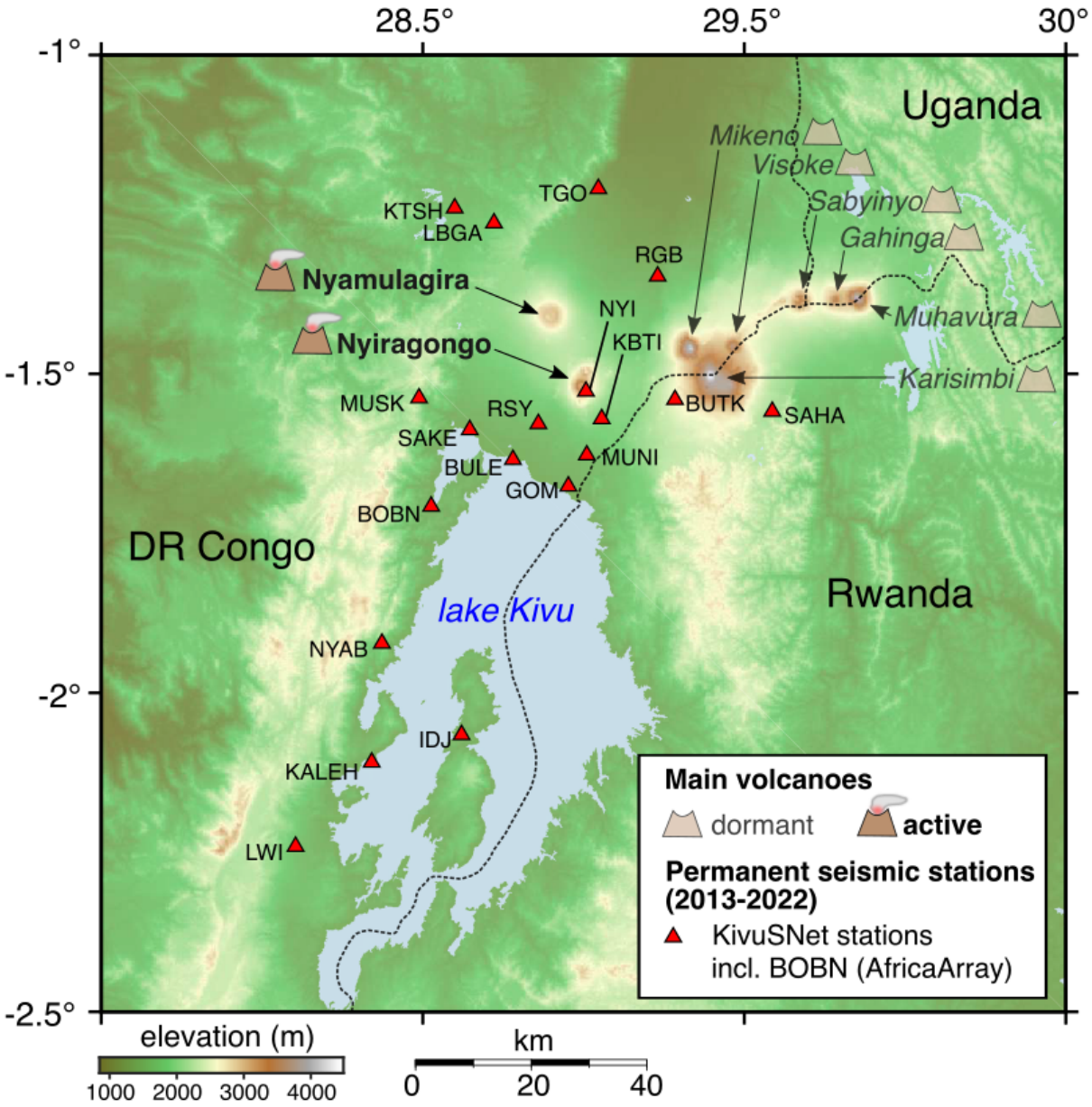

FIGURE 2.3: Stations du réseau KivuSnet (triangles rouges) sur une carte topographique répertoriant les principaux volcans actifs et dormant de la province volcanique des Virunga. La station BOBN appartient au réseau AfricaArray, mais a été réparée et remplacée intégralement par des équipements du réseau KivuSNet.

tinentes au delà de la simple détection de ce trémor basse-fréquence.

Pour cela, avant les calculs des amplitudes et de leur rapports, nous avons opté pour une analyse temps-fréquence (spectrogramme) couvrant une longue période afin d'évaluer les signatures sismiques des différentes sources dans la PVV. L'intérêt d'une analyse temps-fréquence (c'est-à-dire, une "image 2D" du signal) est de mieux cerner les variations fréquentielles du signal en fonction du temps aux différentes stations. Bien que l'intérêt des calculs d'amplitudes soit de résumer l'information en une représentation compacte sous forme de séries temporelles 1D, l'analyse temps-fréquence permettra dans

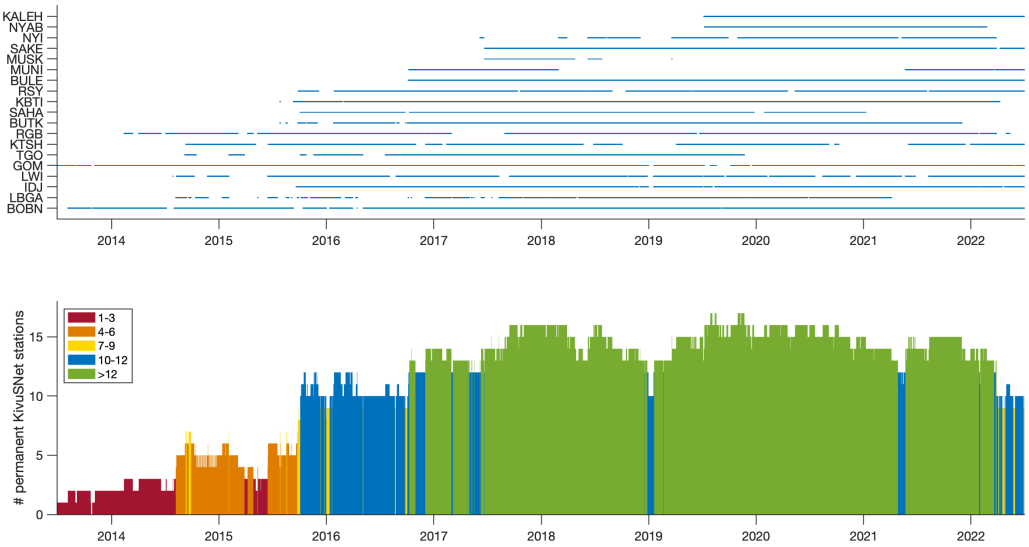

FIGURE 2.4: Disponibilité des données sur l'ensemble des stations de KivuSnet depuis 2013 (déploiement de la première station KivuSNet à l'OVG). En haut, données disponibles par stations. Un point est indiqué si au moins un fichier journalier de données est disponible. En bas, représentation de la densification du réseau (nombre de stations permanentes, télémétrées) dont la couleur des barres reflète le nombre quotidien des stations opérationnelles.

un premier temps de discerner les bandes de fréquences pertinentes à choisir suivant le mécanisme source ciblé et les stations utilisées.

Tenant compte de la propagation de la sismicité lors de l'éruption de Nyiragongo de mai 2021, nous avons calculé une série de spectrogrammes sur 4 stations du nord au sud: NYI, KBTI, GOM et IDJ (Figures 2.5, 2.6 et 2.7). Les stations RSY et BULE n'ont pas été choisies pour ces calculs (et d'une manière générale peu utilisées par la suite) car fortement affectées par une amplification locale associée à une géologie complexe dans cette zone (voir Chapitre 1). Une anomalie de vitesse sismique sera également détectée pour ces deux stations dans le Chapitre 3. Il est cependant à noter que Barrière et al. (2019) a pu utiliser des anciens enregistrements de 2011 à BULE et y déceler un lien évident entre les variations d'amplitudes observées en dessous de 2 Hz et les variations d'activité du lac de lave (gas pistonning et spattering) capturées par caméra.

Les spectrogrammes ont été obtenus pour la période janvier 2018 à Juillet 2022 entre $[0.02 - 20]Hz$. Généralement représentées sous formes de PDF (Probability Densisty Functions) comme dans le Figure 1.2 du Chapitre 1, nous donnons ici une représentation temps-fréquence de calculs de spectres obtenus suivant la méthode de McNamara and Buland (2004), qui est adaptée à l'analyse de longue période de temps. La fenêtre principale d'analyse glissante est constituée de 2^{19} échantillons avec une fréquence d'échantil lonage de 50 Hz (≈175 minutes), chevauchée ("overlapped") de 50%, sous-divisée en 13 segments constitués de 2^{17} échantillons (≈43.5 minutes) avec un chevauchement de 75%. Le lissage est effectué en moyennant dans des bandes successives d'1/3 d'octave avec un pas d'1/16 d'octave. Une autre série de spectrogrammes est faite à l'échelle de

deux semaines sur cinq stations (RGB, NYI, KBTI, GOM et IDJ) centrée sur l'éruption de Nyiragongo de mai 2021 (Figure 2.11). Ces spectrogrammes sont calculés de la même façon que les précédents avec une fenêtre principale d'analyse glissante constituée de 2^{16} échantillons avec une fréquence d'échantillonage de 50 Hz (≈22 minutes), chevauchée de 50%, sous-divisée en 13 segments constitués de 2^{14} échantillons (≈5.5 minutes) avec un chevauchement de 75%. Le lissage est effectué en moyennant dans des bandes successives d'1/3 d'octave avec un pas d'1/16 d'octave.

Séries temporelles dans des bandes de fréquences distinctes

Comme pour le chapitre 1, les calculs sur 16 stations ont été effectués en utilisant le plugin SARA incorporé dans le package python MSNoise. Après détermination des bandes de fréquences adéquates (suite à l'analyse de spectrogramme), l'analyse des amplitudes et de leurs rapports seront présentés à différentes échelles de temps (année, mois et jour)(voir par exemple les Figures 2.9, 2.10, 2.12,) afin de suivre dans le détail les différentes phases de l'évolution magmatique sur l'ensemble de la PVV, mais principalement sur le volcan Nyiragongo. L'objectif principal est de connaître l'état du volcan à partir de la variations dans les courbes des amplitudes sismiques et de leurs rapports et parvenir à utiliser cette information dans sa surveillance. Les valeurs moyennes centrées glissantes de lissage des amplitudes sismiques et de leurs rapports ont été fixées à 7 jours, 1 jour et 6 heures.

2.4.3 Analyses complémentaires

Pour comprendre les résultats issus des analyses des amplitudes sismiques et de leurs rapports plusieurs analyses complémentaires ont été nécessaires et sont incluses dans ce chapitre :

Sismicité dans le champ volcanique du Nyiragongo :
Les solutions d'hypocentres utilisées proviennent de l'étude de Smittarello et al. (2022). La méthode de localisation est basée sur le principe de balayage de sources (source-scanning) sur une grille à 3 dimensions (longitude, latitude, profondeur). C'est une méthode totalement automatique dite "waveform-based" utilisant les signaux continues enregistrés aux stations au contraire de méthodes plus classiques ("picking-based") basées sur l'inversion des temps d'arrivées d'ondes aux stations (et donc nécessitant un pointé manuel ou automatique des temps d'arrivées aux stations). Il existe de nombreuses méthodes et variantes apparentées à ce type de technique de recherche sur grille (e.g. Grigoli et al., 2018). Une description de la méthode employée ici (appelée XCLoc, e.g., Barrière et al., 2022) va au-delà du propos de ce chapitre, mais cet aspect sera abordé au chapitre 4 de cette thèse. Le catalogue de Smittarello et al. (2022) utilisé consiste en 6856 évènements couvrant la période allant d'avril à juin 2021.

Détection et localisation du trémor dominant au Nyiragongo :
Pour comprendre le comportement magmatique du Nyiragongo, nous avons aussi fait une localisation journalière 2D (longitude-latitude) du trémor volcanique continu comme l'avaient fait Subira et al. (2023), en se basant sur l'approche décrite par Barrière et al. (2017) (voir Figures 2.21 et 2.23). Le principe de cette localisation a déjà été évoquée dans

le Chapitre 1, mais nous donnons ci-dessous un peu plus de détails sur cette technique. Cette méthode de localisation repose sur l'interférométrie du bruit sismique ambiant entre paires de stations dans une bande de fréquence donnée. On parle souvent de corrélation de bruit, car l'idée première est d'approcher la fonction de Green entre chaque paire de stations au travers de la fonction de corrélation croisée (Noise Cross-correlation Function, NCF), qui sera ensuite utile pour réaliser une tomographie de vitesses sismiques (Bensen et al., 2007). Pour un résultat optimal, l'hypothèse la plus importante est d'avoir une distribution de sources de bruit isotropique et diffuse pour que la fonction de corrélation croisée se rapproche au mieux de la fonction de Green. Cependant, si une source locale focalisée génère des signaux continus enregistrés aux stations, comme ça peut être le cas avec du trémor volcanique, la corrélation croisée de ces signaux entre plusieurs paires de stations va plutôt mettre en évidence cette source au détriment de la fonction de Green (Ballmer et al., 2013). En combinant les NCFs à toutes les paires de stations, on peut imager la cohérence spatiale du champs d'ondes généré par cette source à travers le réseau et ainsi détecter la région source la plus probable. Cette carte de localisation du trémor peut être appelée "network response" ("réponse du réseau") en référence à l'étude de Droznin et al. (2015) (voir Figure A.1). Il est possible de corréler les signaux sur différentes durées (minute, heure, jour, etc.) pour évaluer la variabilité temporelle des sources trémors. S'agissant de mettre en évidence des sources continues, nous employons ici un calcul journalier de la fonction de corrélation croisée pour maximiser la détection de signaux trémors à travers le réseau tout en gardant une résolution temporelle satisfaisante pour la période d'analyse (4 ans). L'amplitude du signal n'a pas d'influence sur la localisation mais aucune information sur l'amplitude à la source n'est donc dérivée de cette technique. Étant une localisation 2D de sources trémor assumées superficielles, un éventuel approfondissement significatif de la source n'est pas considéré.
De cette méthode, nous avons aussi dérivé deux séries temporelles permettant de juger la qualité de la solution:

1. "Distance to Nyiragongo" : la distance entre la région source la plus probable et le cratère de Nyiragongo (Figure 2.23). En considérant que la cohérence du signal peut fluctuer et que la résolution spatiale reste limitée par le nombres et l'espacement entre stations, une valeur en dessous de quelques kilomètres peut être associée au Nyiragongo.

2. "Max-Min" : Le résultat de la localisation étant une carte limitée par une valeur maximale (source probable) et minimale, nous calculons l'écart entre ces deux valeurs extrêmes pour gagner une information sur la qualité de la localisation (voir Figure A.1). En d'autres termes nous vérifions la variabilité temporelle de la "réponse du réseau" et détectons pour chaque journée la présence ou non d'un maximum clair, indicatif d'une source probable ou non. Le nombre de paires de stations utilisées (paramètre "Nb XCorr") est aussi important à indiquer car il permet de détecter un éventuel biais de localisation due à un nombre de stations qui varie.

Enfin, issu du même traitement du signal, la représentation graphique de la fonction de corrélation croisée entre seulement deux stations est possible (sous forme de matrice 2D "date vs. time lag"). Il est alors bien sûr impossible de localiser une source, mais cela permet de juger de l'intérêt d'appliquer une analyse interférométrique du bruit sismique ambiant si seulement deux stations sont disponibles. Par exemple, nous montrerons ici le

résultat pour la paire de stations la plus pertinente, celle du Nyiragongo NYI-KBTI.

Enregistrement des infrasons à proximité du Nyiragongo :
Nous avons utilisé les données infrasons de la station KBTI située au pied de Nyiragongo de 2018 à 2022 (Figure 2.20). Le traitement du signal reprend celui effectué par Barrière et al. (2023b), qui montrent que le niveau d'amplitude acoustique dans la bande de fréquence [0.4-2] Hz à la station KBTI est un marqueur fiable de l'activité effusive au sein du cratère du Nyiragongo. Un calcul d'amplitude RMS (root-mean-square) toutes les 10 minutes est d'abord effectuée. Ensuite on applique une médiane glissante centrée d'une journée par incrément d'une heure afin de détecter les variations les plus évidentes à comparer avec les autres séries temporelles mentionnées dans cette section, elles aussi filtrées par médiane ou moyenne sur des échelles de temps variant de quelques heures à quelques jours.

Niveau du lac de lave du Nyiragongo :
Les fluctuations du lac de lave fournissent des informations sur les conditions de pression du magma et constituent un paramètre clé dans la surveillance volcanique (Vergniolle & Métrich, 2022). En effet, comme ceux d'autres volcans à conduit ouvert tel que le Kīlauea à Hawaii (Patrick et al., 2015), le lac de lave du Nyiragongo peut-être vu comme un piézomètre naturel du système magmatique car certaines larges fluctuations du niveau du lac de lave reflètent des variations de pression en profondeur (Barrière et al., 2022; Walwer et al., 2023). La série temporelle du niveau de lac de lave de Nyiragongo utilisée ici provient de l'étude de Barrière et al. (2023b) compilant les résultats obtenus depuis des observations spatiales SAR (Synthetic Aperture Radar) par Barrière et al. (2022) et Smittarello et al. (2023) (Figure 2.23). La résolution temporelle de ces mesures est de l'ordre de quelques jours, dépendant de la période de retour des satellites utilisés (voir les études citées pour plus de détails).

2.5 Analyse des spectrogrammes et des calculs d'amplitudes sismiques

2.5.1 Aperçu général des variations de janvier 2018 à juin 2022

Nous représentons les stations NYI, KBTI, GOM et IDJ localisées suivant un axe nord-sud du Nyiragongo à l'île d'Idjwi. L'analyse des spectrogrammes (PSD) entre 0.1 et 20 Hz sur les Figures 2.5, 2.6, 2.7 et 2.8 couvrant la période 2018-2022 nous permet d'identifier plusieurs bandes de fréquences distinctes pour lesquelles nous pouvons assumer des mécanismes sources dominants. Une échelle de couleur commune aux quatre spectrogrammes pour représenter les valeurs de PSD permet de mieux jauger les différences entre chaque station.

Comme attendu, la bande de microséismes océaniques montre une activité dominante en dessous de $0.3Hz$ à toutes les stations (voir aussi Chapitre 1). Nous décidons de masquer cette gamme fréquentielle sur ces Figures (avec un bandeau transparent) afin de mettre en évidence les signaux locaux/régionaux à plus haute fréquence avec une borne inférieure à 0.4Hz afin de bien séparer la bande microsismique du reste du spectre.

L'analyse des fréquences supérieures à $0.4Hz$ montre l'existence d'un trémor continu du lac de lave au sommet de Nyiragongo. Cette activité du lac de lave est visible sur l'ensemble des quatre spectrogrammes et couvre des intervalles de fréquences très variées d'une station à une autre, en fonction de la proximité avec le Nyiragongo. A la station NYI (Figure 2.5), par exemple, elle couvre une large bande pouvant aller jusque à 10Hz, tandis qu'à la station KBTI au pied du volcan, elle est décelable jusqu'à environ $5Hz$ (Figure 2.6). A la station GOM (environ 15 km du Nyiragongo), cette signature trémor est contenue en dessous de $2Hz$ (Figure 2.7). De plus, nous observons clairement à cette station la présence de microséismes de lac mis en évidence par Subira et al. (2023) (Chapitre 1) dans la même bande fréquentielle sous la forme de paquets plus énergétiques. Sur cette échelle de temps de plusieurs années, nous mettons en évidence l'apparition saisonnière de ces signaux pendant la période sèche/venteuse (d'avril-mai à août-septembre). Comme montré dans le chapitre 1, il est possible que cet effet soit notable même à KBTI. Les microséismes de lac sont également discernable sur l'île d'Idjwi au centre du lac (station IDJ), mais sans variations saisonnières évidentes. Bien que l'échelle de couleur choisie puisse jouer un rôle sur la perception de ces variations à IDJ, Barrière et al. (2019) avaient déjà noté que l'amplitude et la variabilité saisonnière des microséismes de lac au niveau de la station IDJ était moins notable qu'au nord du lac comme aux stations GOM ou BULE.

Comme évoqué dans le chapitre 1, les mécanismes sources des microséismes de lac semblent proches, mais plus complexes, que ceux observés pour les microséismes globaux (processus simple et double fréquence, se référer par exemple à Stutzmann et al. (2012)). D'après de récentes études, une complexité plus importante de la géométrie du rivage, de la bathymétrie et de la dynamique des vagues en serait la cause (Anthony et al., 2018; Carchedi et al., 2022; Farrell et al., 2023). La bathymétrie plus importante au nord du lac Kivu, excédant 400 m au nord de l'île d'Idjwi (Kranenburg et al., 2020), et la linéarité du rivage nord (axe BULE-GOM) couplées avec un vent de lac sud-nord ("lake breeze")

pourraient ainsi avoir un rôle important dans la génération et l'amplification de ces signaux enregistrés dans le VVP. Une analyse plus détaillée de ces signaux au lac Kivu reste cependant un sujet qui va au-delà de l'objectif de cette thèse.

Barrière et al. (2019) ont étudié en détail la signature du trémor de lac de lave et ont conclu que l'analyse appropriée du trémor de lac de lave serait optimale en se situant au-dessus de la bande des microséismes océaniques et en dessous des fréquences influencées par les bruits anthropogéniques. En combinant leur conclusion avec nos observations, nous choisissons la bande de fréquence $[0.4 - 2]Hz$ pour notre étude puisqu'elle convient le mieux pour l'analyse des amplitudes et leurs rapports à basses fréquences.

Au dessus de $2Hz$, une signature diurne typique d'une activité sismique d'origine humaine est détectée à toute les stations, hormis NYI au sommet du Nyiragongo. IDJ est également une station moins influencée par le bruit anthropogénique, mais l'absence de variations diurnes sur la Figure 2.8 est aussi le fait de l'échelle de couleur commune à toutes les stations. Cependant, malgré l'activité humaine enregistrés sur la plupart des stations, la bande de fréquence au-dessus de 2 Hz montre des variations notables qui sont très probablement liées à l'activité magmatique du Nyiragongo.

C'est à la station NYI (Figure 2.5) que sont observées les plus fortes variations dans cette partie haute du spectre. En plus du trémor du lac de lave qui couvre une large bande spectrale au sommet, de significatifs démarrages et interruptions de signaux de haute énergie sont détectés depuis 2019. En 2019, on y voit principalement un enchaînement de signaux larges bandes dont la signature fréquentielle change avec le temps. A cheval sur 2019 et 2020, le signal le plus notable est l'apparition d'une intense signature trémor avec une fréquence dominante autour de $5Hz$ qui s'arrête brutalement en avril 2020. En 2021, la période éruptive de mai sature complètement l'échelle de couleur à toutes les fréquences, témoignant de la plus forte activité sismique mesurée au Nyiragongo depuis le déploiement du KivuSNet et liée aux changements drastiques de l'activité magmatique au Nyiragongo (drainage du lac de lave, intrusion d'un dyke superficiel). Enfin, entre fin 2021 et 2022, une signature trémor inédite, de très forte amplitude et intermittente, est enregistrée au sommet dans une bande de fréquence haute au dessus de 1 à 2 Hz. La signature trémor du lac de lave entre 0.4 et $2Hz$ est complètement perdue après l'éruption.

Les principaux changements à haute fréquence que nous venons de répertorier à la station NYI sont également visibles à la station KBTI (Figure 2.6). De la même manière, la signature du lac de lave a clairement disparu après l'éruption. Aux stations GOM et IDJ, hormis pendant la période éruptive de mai 2021, les spectrogrammes ne dépeignent pas aussi clairement ces changements notables de sismicité associés au Nyiragongo au dessus de 2 Hz (Figures 2.7 et 2.8). Cependant, sur des échelles de temps plus courtes, il reste possible de détecter des signaux associés au Nyiragongo au delà de 2 Hz à ces stations plus lointaines. Ainsi, avant l'éruption de 2021, la détection et la localisation de séismes aux formes d'ondes similaires se répétant chaque jour (ayant donc pour origine un processus non destructif) ou de swarms associés à des intrusions profondes ($> 10km$) au Nyiragongo avaient déjà été mis en évidence à ces stations (Barrière et al., 2019, 2022). Suite à l'ensemble de ces observations, et en accord avec d'autres études utilisant la méthode SARA pour mieux comprendre l'activité volcano-tectonique au Piton de la Fournaise

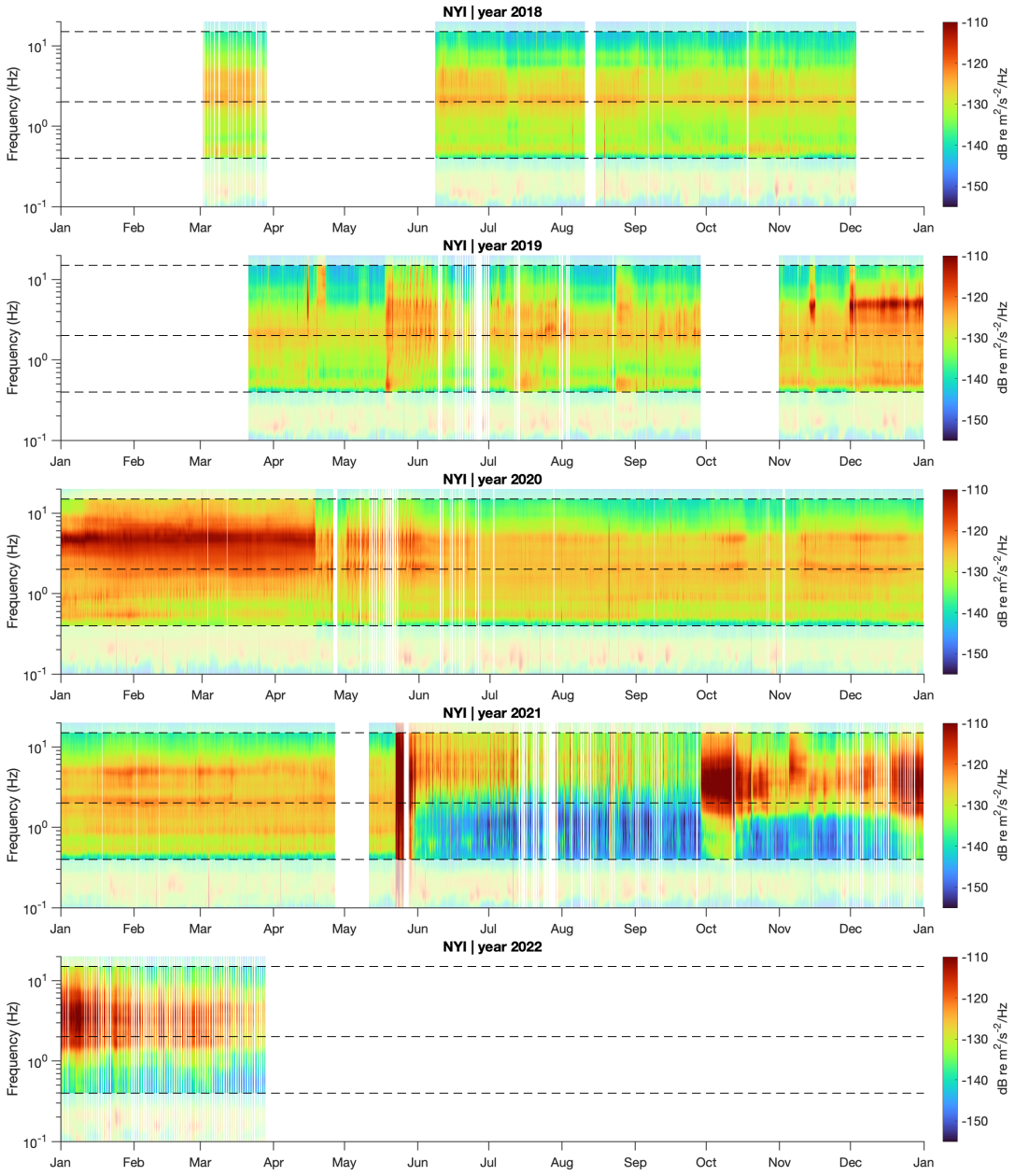

FIGURE 2.5: Pour la station NYI, Spectrogrammes annuels entre 0.1 et 20 Hz pour la période janvier 2018 à Juillet 2022 en suivant le traitement du signal décrit par McNamara and Buland (2004). PSD ou DSP en français représente la densité Spectrale de Puissance, exprimé en dB re $m^2/s^{-2}/Hz$. La fenêtre principale d'analyse glissante est constituée de de 2^{19} échantillons avec une fréquence d'échantillonage de 50 Hz ($\approx$ 175 minutes), chevauchée ("overlapped") de 50%, sous-divisée en 13 segments constitués de 2^{17} échantillons ($\approx$ 43.5 minutes) se chevauchant de 75%. Le lissage est effectué en moyennant dans des bandes successives d'1/3 d'octave avec un pas d'1/16 d'octave. Les bandes fréquentielles non utilisées ($< 0.4Hz$ et $> 15Hz$) sont opaques. Les lignes pointillées noires délimitent les deux bandes LF ("Low-Frequency") et HF ("High-Frequency") utilisées dans l'analyse. Les périodes sans donnée disponible sont représentées en blanc. L'échelle de couleur est ajustée manuellement entre -110 et -150 dB pour laisser apparaître les principales variations et conserver la même gamme pour les Figures 2.7, 2.6 et 2.8.

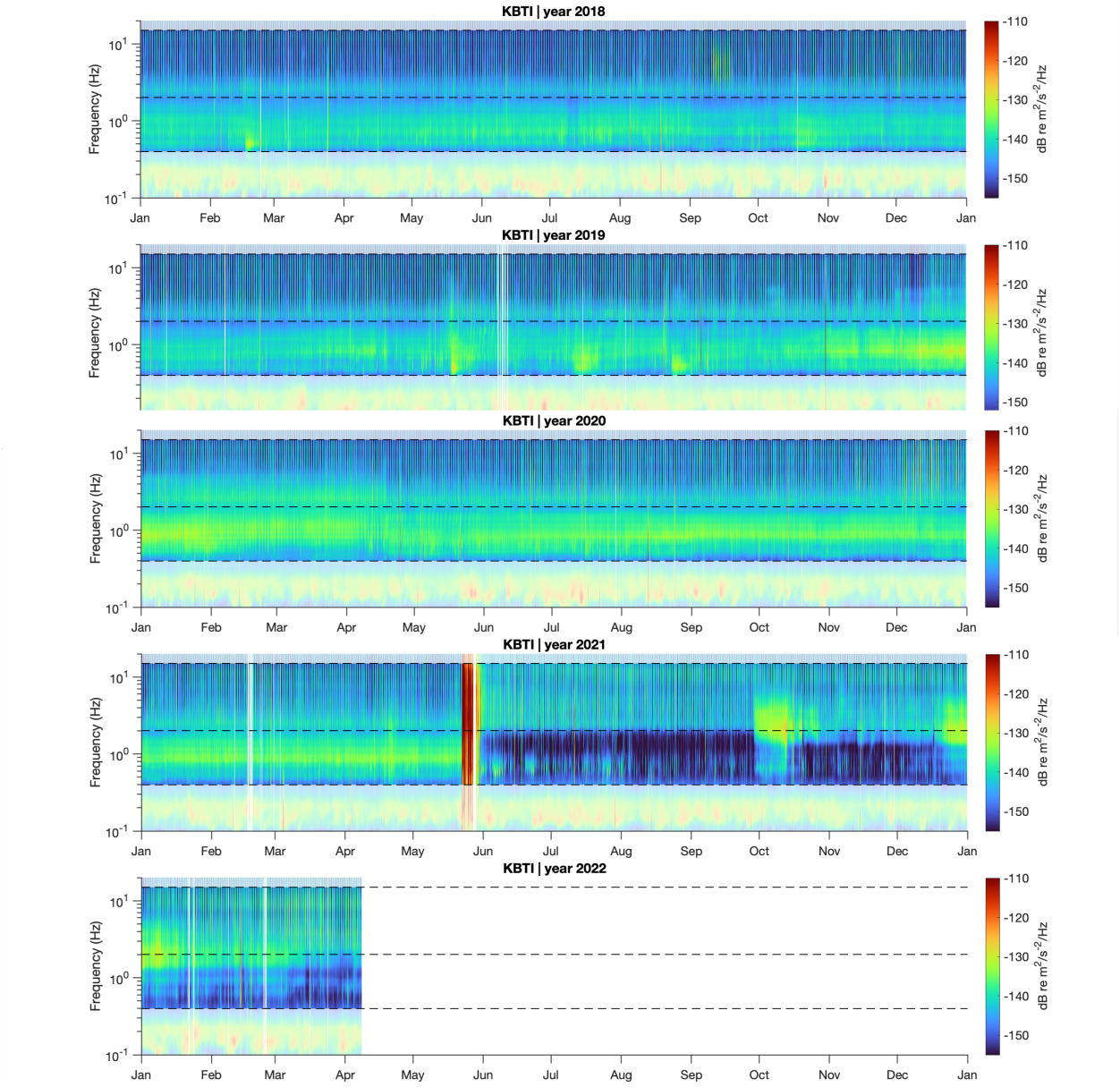

FIGURE 2.6: Pour la Station KBTI, Spectrogrammes annuelles entre 0.1 et 20 Hz pour la période janvier 2018 à Juillet 2022 en suivant le traitement du signal décrit par McNamara and Buland (2004). PSD ou DSP en français représente la densité Spectrale de Puissance, exprimé en dB re $m^2/s^{-2}/Hz$. La fenêtre principale d'analyse glissante est constituée de de 2^{19} échantillons avec une fréquence d'échantillonage de 50 Hz ($\approx$ 175 minutes), chevauchée ("overlapped") de 50%, sous-divisée en 13 segments constitués de 2^{17} échantillons ($\approx$ 43.5 minutes) se chevauchant de 75%. Le lissage est effectué par moyennage dans des bandes successives d'1/3 d'octave avec un pas d'1/16 d'octave. Les bandes fréquentielles non utilisées ($< 0.4Hz$ et $> 15Hz$) sont opaques (on peut distinguer le microséisme global de forte amplitude à basses frequences). Les lignes pointillées noires délimitent les deux bandes LF ("Low-Frequency") et HF ("High-Frequency") utilisées dans l'analyse. Les périodes sans donnée disponible sont représentées en blanc. L'échelle de couleur est ajustée manuellement entre -110 et -150 dB pour laisser apparaître les principales variations et conserver la même gamme pour les Figures 2.7, 2.5 et 2.8.

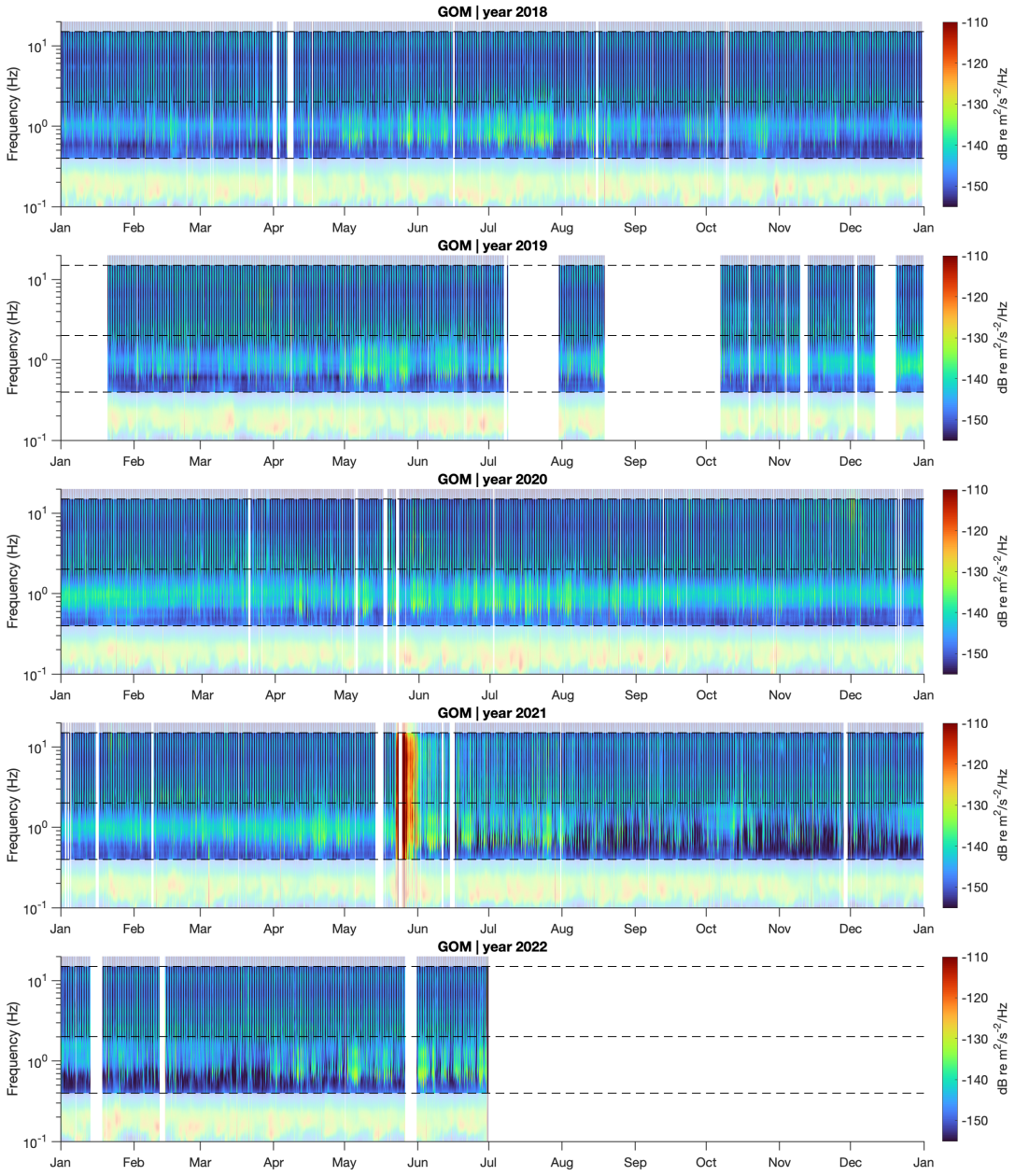

FIGURE 2.7: Pour la Station GOM, Spectrogrammes annuelles entre 0.1 et 20 Hz pour la période janvier 2018 à Juillet 2022 en suivant le traitement du signal décrit par McNamara and Buland (2004). PSD ou DSP en français indique la densité Spectrale de Puissance, exprimée en dB re $m^2/s^{-2}/Hz$. La fenêtre principale d'analyse glissante est constituée de de 2^{19} échantillons avec une fréquence d'échantillonage de 50 Hz ($\approx$ 175 minutes), chevauchée ("overlapped") de 50%, sous-divisée en 13 segments constitués de 2^{17} échantillons ($\approx$ 43.5 minutes) se chevauchant de 75%. Le lissage est effectué par moyennage dans des bandes successives d'1/3 d'octave avec un pas d'1/16 d'octave. Les bandes fréquentielles non utilisées ($< 0.4Hz$ et $> 15Hz$) sont opaques (on peut distinguer le microséisme global de forte amplitude à basses fréquences). Les lignes pointillées noires délimitent les deux bandes LF ("Low-Frequency") et HF ("High-Frequency") utilisées dans l'analyse. Les périodes sans donnée disponible sont représentées en blanc. L'échelle de couleur est ajustée manuellement entre -110 et -150 dB pour laisser apparaître les principales variations et conserver la même gamme pour les Figures 2.6,2.5 et 2.8.

.

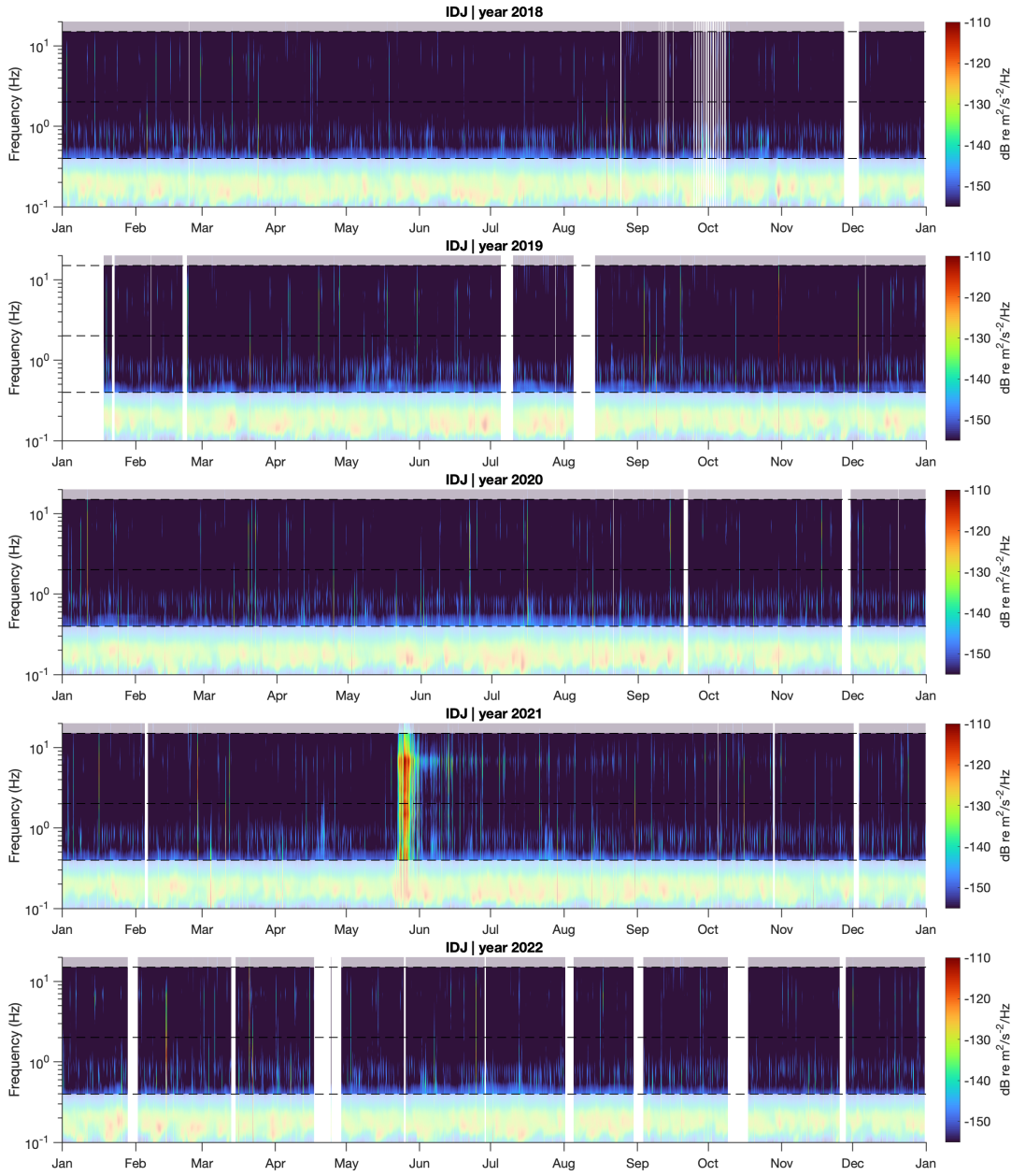

FIGURE 2.8: Pour la Station IDJ, Spectrogrammes annuelles entre 0.1 et 20 Hz pour la période janvier 2018 à Juillet 2022 en suivant le traitement du signal décrit par McNamara and Buland (2004). PSD ou DSP en français indique la densité Spectrale de Puissance, exprimée en dB re $m^2/s^{-2}/Hz$. La fenêtre principale d'analyse glissante est constituée de de 2^{19} échantillons avec une fréquence d'échantillonage de 50 Hz ($\approx$ 175 minutes), chevauchée ("overlapped") de 50%, sous-divisée en 13 segments constitués de 2^{17} échantillons ($\approx$ 43.5 minutes) se chevauchant de 75%. Le lissage est effectué par moyennage dans des bandes successives d'1/3 d'octave avec un pas d'1/16 d'octave. Les bandes fréquentielles non utilisées ($< 0.4Hz$ et $> 15Hz$) sont opaques (on peut distinguer le microséisme global de forte amplitude à basses fréquences). Les lignes pointillées noires délimitent les deux bandes LF ("Low-Frequency") et HF ("High-Frequency") utilisées dans l'analyse. Les périodes sans donnée disponible sont représentées en blanc. L'échelle de couleur est ajustée manuellement entre -110 et -150 dB pour laisser apparaître les principales variations et conserver la même gamme pour les Figures 2.5, 2.6 et 2.7

(La Réunion), au Mont Gede (Indonésie) ou au Tolbachik (Russie)(Caudron et al., 2015; Tan et al., 2019), nous choisissons $([2-15]Hz)$ Hz comme bande fréquentielle d'analyse en haute fréquence.

Suivant le traitement du signal SARA décrit dans la section 2.4.2, les Figures 2.9 et 2.10 montrent l'évolution des amplitudes dans la province volcanique des Virunga à basse $([0.4-2]Hz)$ et haute fréquence $([2-15]Hz)$ de janvier 2018 à juin 2022 avec une médiane glissante centrée à 7 jours. Les calculs basses et hautes fréquences pourront être par la suite appelés BF ou LF ("Low-frequency") et HF, respectivement. Pour faciliter la lecture des Figures, les stations sont classées du nord au sud en fonction de leur latitude. Les amplitudes sismiques sont normalisées entre 0 et 1. Avec trois bandes grisées, nous mettons en évidence trois périodes distinctes où l'amplitude sismique à la station du sommet du Nyiragongo (NYI) est la plus élévée : au début 2020, pendant l'éruption de mai 2021 et à la fin de cette même année. Ces deux dernières périodes seront particulièrement analysées par la suite. Il est à noter que les séries temporelles pour les stations non opérationnelles pendant l'éruption de mai 2021 (TGO, KTSH, NYAB et LWI) sont normalisées par rapport à un maximum plus faible et mises à une échelle différente.

A basses fréquences: $[0.4-2]Hz$

L'éruption est l'événement le plus marquant sur toutes les stations sismiques du réseau. Avant cela un maximum est obtenu au début de l'année 2020, mais uniquement pour les stations déployées dans le VVP (de RGB à GOM). Nous verrons plus tard que cette augmentation est liée à l'activité dans le cratère du Nyiragongo. De même, les multiples pics avant cette date détectés en 2019 sur l'ensemble des stations des Virunga indique un lien avec le Nyiragongo et cela sera évoqué par la suite. Par contre, les oscillations autour de mai-août 2020 uniquement visibles sur les stations entourant le nord du lac Kivu (BULE à KALEH) sont très probablement dues aux microséismes de lac pendant la période sèche et venteuse. Cela est potentiellement le cas aussi pour les pics plus importants observés sur ces stations en 2018 pendant la même période de l'année. On constate que le niveau moyen d'amplitude avant l'éruption baisse nettement après l'éruption. Cela traduit la perte du trémor volcanique qui est continue lorsque qu'un lac de lave est présent au sommet du Nyiragongo, comme cela est également visible sur les spectrogrammes. Il est intéressant d'observer ensuite des pics sur les stations autour du lac Kivu, ce qui semble témoigner encore de l'influence des microséismes de lac dans cette bande de fréquence. La période de réactivation du trémor au Nyiragono (troisième bande grisée sur la droite), bien que plus haute fréquence comme observé sur les spectrogrammes, reste clairement décelable dans cette bande de fréquence pour les stations des Virunga.

A hautes fréquences: $[2-15]Hz$

Il est frappant d'observer que l'éruption domine très nettement dans cette bande de fréquence. La station du sommet est singulière, notamment au début de l'année 2020 où l'amplitude suit une comportement "on/off" (bien visible dans le spectrogramme) qu'on ne retrouve pas aux autres stations. Cela indique alors une source à l'édifice probablement superficielle. A cause de son contenu fréquentiel élevé, ce signal est fortement rapidement atténué; il est donc moins bien détecté aux autres stations. Ceci est aussi vrai pour

la période post-éruptive dans la deuxième moitié de l'année 2021 où seules les stations les plus proches du Nyiragongo détectent une augmentation d'activité sismique.

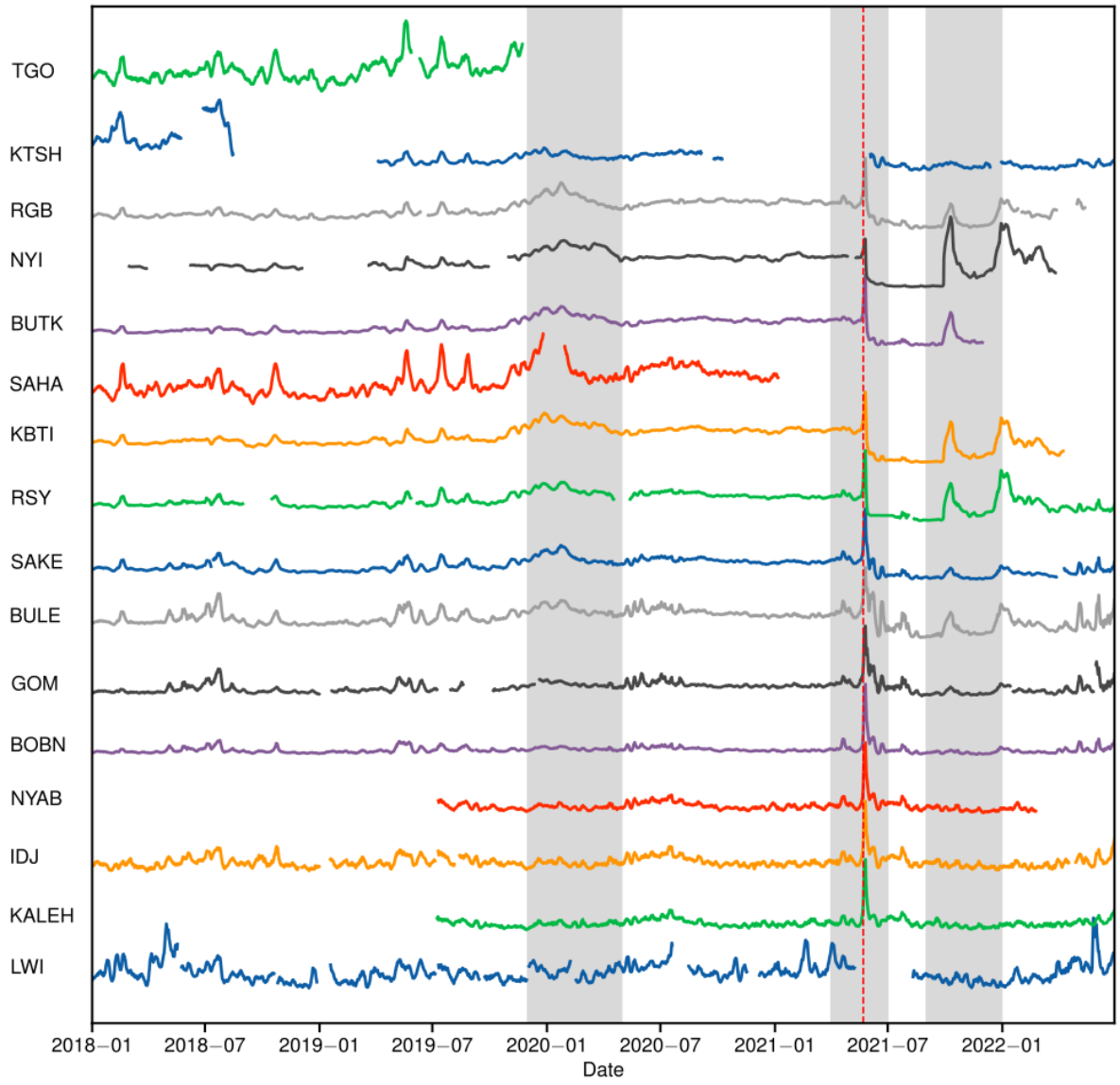

FIGURE 2.9: Amplitudes sismiques filtrées entre $[0.4 - 2] Hz$ lissées en utilisant sept jours de médiane centrée glissante, de janvier 2018 à juin 2022. Elles sont corrigées de la réponse instrumentale et normalisées. Les bandes grises représentent les périodes pendant lesquelles les niveaux d'amplitude à la station NYI sont les plus élevés. La ligne en pointillé rouge marque l'éruption de Nyiragongo

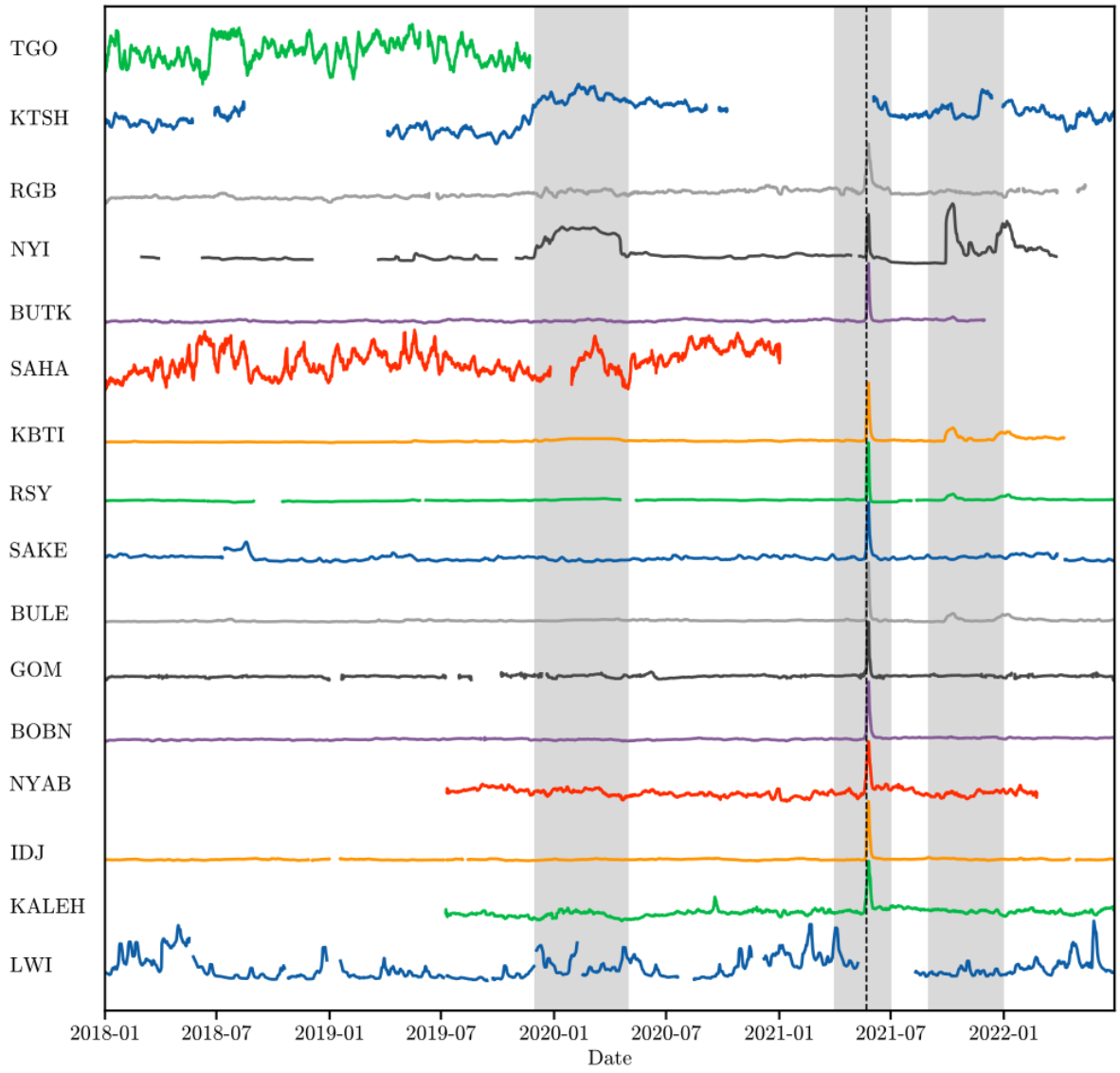

FIGURE 2.10: Amplitudes sismiques entre $[2-15]Hz$ lissées en utilisant sept jours de médiane glissante, de janvier 2018 à juin 2022. Elles sont corrigées de la réponse instrumentale et normalisées. Les bandes grises représentent les périodes pendant lesquelles les niveaux d'amplitude à la station NYI sont les plus élevés. La ligne en pointillé rouge marque l'éruption de Nyiragongo

2.5.2 Zoom sur l'éruption de flanc du Nyiragongo, mai 2021

L'analyse pluri-annuelle des spectrogrammes, combinée au calcul des amplitudes sismiques sur toutes les stations du réseau, nous a permis de bien cerner les principales variations significatives de l'activité sismique volcanique du Nyiragongo. Ainsi pour la suite de notre analyse, nous nous concentrons sur les stations, du nord au sud, RGB, NYI, KBTI, GOM et IDJ. Nous avons également identifié l'importance stratégique de la station située au sommet du volcan Nyiragongo car elle capte de nombreux processus magmatiques non enregistrés ou enregistrés avec une très faible intensité sur les autres stations. Nous avons opté pour une valeur de six heures pour la médiane glissante centrée pour des fenêtres d'analyse de plusieurs semaines à plusieurs mois. Comme expliqué auparavant, ce choix est dicté à la fois par le souhait d'améliorer la résolution temporelle de nos

calculs SARA, mais également de mitiger les variations d'origine non-magmatique qui peuvent contaminer le signal.

L'activité humaine est toujours visible sur les spectrogrammes entre 0.02 et $20Hz$ zoomant sur l'éruption de 2021 pour les stations sélectionnées à l'exception de la station de NYI (Figure 2.11). Une forte activité humaine est visible aux stations RGB, KBTI et GOM. Les microséismes de lac sont aussi fortement marqués à GOM et également nettement décelables à la station IDJ. On devine aussi par moment leurs signatures dans la bande de fréquence $[0.4 - 2]Hz$ aux autres stations, notamment après l'éruption (voir entre le 29 et le 31 mai). Nous avons élargi la bande fréquentielle jusqu'à $0.02Hz$, ce qui permet de mettre en évidence les signaux très longues périodes, comme plusieurs téléséismes avant l'éruption. Il est également intéressant de noter une signature très large bande pendant et après l'éruption. La complexité des enregistrements pendant cette période d'environ une semaine, combinant les signaux liées aux changements à l'édifice (drainage du lac de lave, effondrement) et l'intrusion magmatique du Nyiragongo à Goma, sera analysée plus en détail par la suite avec l'analyse multi-paramétrique.

La Figure 2.12 couvre la période allant du 1^{er} avril au 1^{er} juillet 2021 pour les basses fréquences. Les variations des amplitudes LF mettent en évidence le début de la crise éruptive le 22 mai et sa fin probable autour du 28 mai. Le terme "crise éruptive" ici englobe l'éruption de flanc de courte durée (6 heures) et l'intrusion magmatique qui a suivi pendant environ une semaine. Avant cette date, les amplitudes ne montrent aucune anomalie significative pouvant être attribuée à une activité magmatique inhabituelle du Nyiragongo. On observe par contre les fluctuations en amplitude des microséismes sur les enregistrements sismiques des stations localisées dans le bassin du Lac Kivu comme à la station de GOM localisée sur la côte nord du Lac. Lors de l'éruption, les amplitudes sismiques des stations proches du Nyiragongo (NYI et KBTI) sont dix fois plus élevées que les amplitudes des stations localisées dans le bassin du Lac Kivu (GOM, IDJ) et RGB localisées respectivement plus de 20 km au sud et au nord du sommet. Pour la station GOM, les microséismes nettement visibles avant l'éruption se superposent au signal de l'éruption. Aux stations NYI et KBTI, les amplitudes montrent deux pics nets. Le premier pic correspond au début de l'éruption du 22 mai et est suivi d'une chute drastique de l'amplitude jusqu'au 25 mai, date du second pic de plus faible amplitude. A la station RGB à 20 km au nord du sommet Nyiragongo les deux pics ont une amplitude similaire alors que le deuxième pic à la station IDJ est le plus important des deux. Ces variations d'amplitudes dominées par deux pics majeurs correspondent parfaitement aux différentes séquences sismiques comme décrites par Smittarello et al. (2022), c'est-à-dire une sismicité importante au sommet, puis une sismicité dominante plus au sud associée à la propagation de l'intrusion magmatique jusqu'au lac Kivu.

L'analyse à haute fréquence présentée à la Figure 2.13 revèle d'autres aspects intéressants non clairement visibles à basse fréquence. Les séquences sismiques deviennent plus fortes en amplitude et sont globalement plus marquées que pour les amplitudes LF, notamment à la station GOM où l'influence des microséismes est filtrée. Néanmoins, on note toujours la présence de variations diurnes liées à l'activité humaine. La baisse de la sismicité associée à la propagation du dyke autour du 28 mai est synonyme d'une cyclicité diurne qui devient à nouveau visible sur les stations situées au sud du réseau. Les

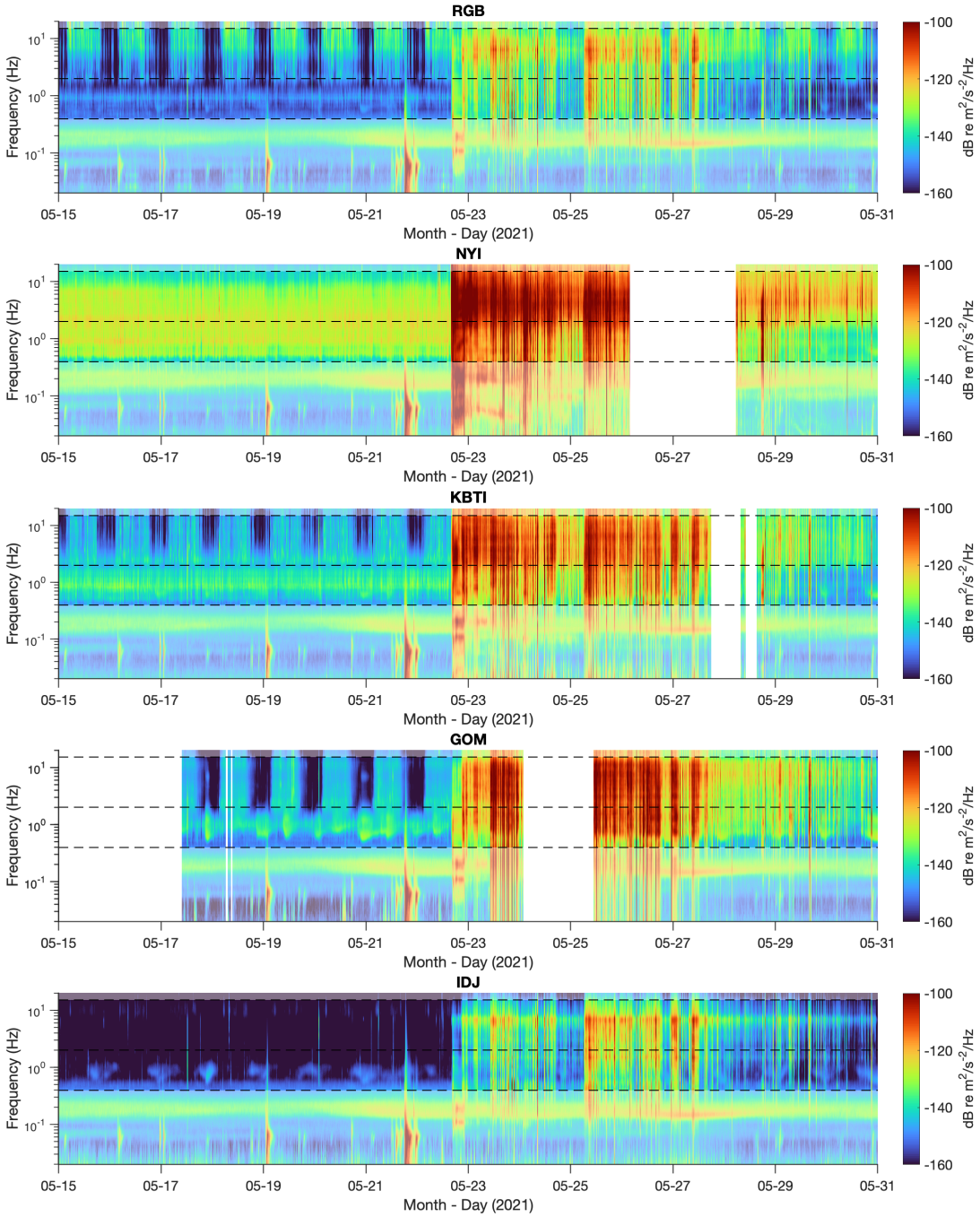

FIGURE 2.11: Spectrogrammes entre 0.02 et 20Hz pour la période 15-31 mai 2021 (éruption du Nyiragongo du 22 au 28 mai) en suivant le traitement du signal décrit par McNamara and Buland (2004). De haut en bas, classées du nord au sud, les stations RGB, NYI, KBTI, GOM et IDJ. PSD ou DSP en français indique la Densité Spectral de Puissance, exprimée en dB re $m^2/s^{-2}/Hz$. La fenêtre principale d'analyse glissante est constituée de de 2^{16} échantillons avec une fréquence d'échantillonage de 50 Hz ($\approx$ 22 minutes), chevauchée ("overlapped") de 50%, sous-divisée en 13 segments constitués de 2^{14} échantillons ($\approx$ 5.5 minutes) se chevauchant de 75%. Le lissage est effectué par moyennage dans des bandes successives d'1/3 d'octave avec un pas d'1/16 d'octave. Les bandes fréquentielles non utilisées ($< 0.4Hz$ et $> 15Hz$) sont opaques. Les lignes pointillées noires délimitent les deux bandes LF ("Low-Frequency") et HF ("High-Frequency") utilisées dans l'analyse. Les périodes sans donnée disponible sont représentées en blanc. L'échelle de couleur est ajustée manuellement entre -100 et $-160dB$ pour laisser apparaître les principales variations et conserver la même gamme pour les 5 stations.

stations plus éloignées du Nyiragongo montrent une évolution de la sismicité différente de celles proches, NYI et KBTI. Par rapport au premier pic de l'éruption (22-23 mai), les pics d'amplitude à GOM et IDJ à partir du 25 mai sont comparativement plus importants qu'à NYI ou KBTI. Ces observations correspondent avec la migration vers le sud de la sismicité le long du dyke lors de sa propagation. Comme pour l'analyse LF, les pics du 22-23 et après le 25 mai sont d'amplitudes comparables à RGB. Il est par conséquent plus difficile de relier ces observations à un simple effet de distance entre la station et la source pour cette station.

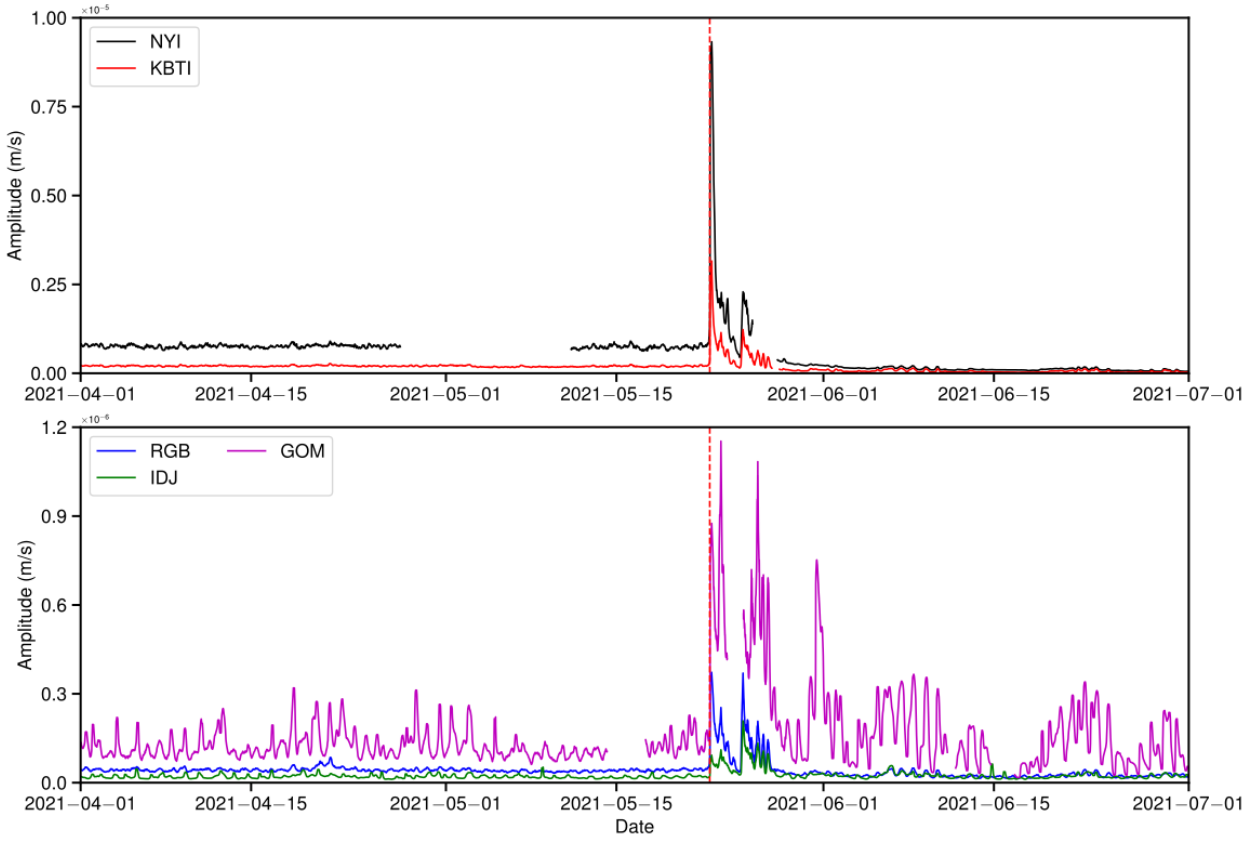

FIGURE 2.12: Amplitudes sismiques corrigées de la réponse instrumentale à basse fréquence du 1^{er} avril au 1^{er} juillet 2021. En haut, amplitudes aux stations de NYI et KBTI de l'ordre de $10^{-5}m/s$; en bas, amplitudes aux stations de RGB, IDJ et GOM de l'ordre $10^{-6}m/s$. La ligne rouge en pointillé marque le début de l'éruption.

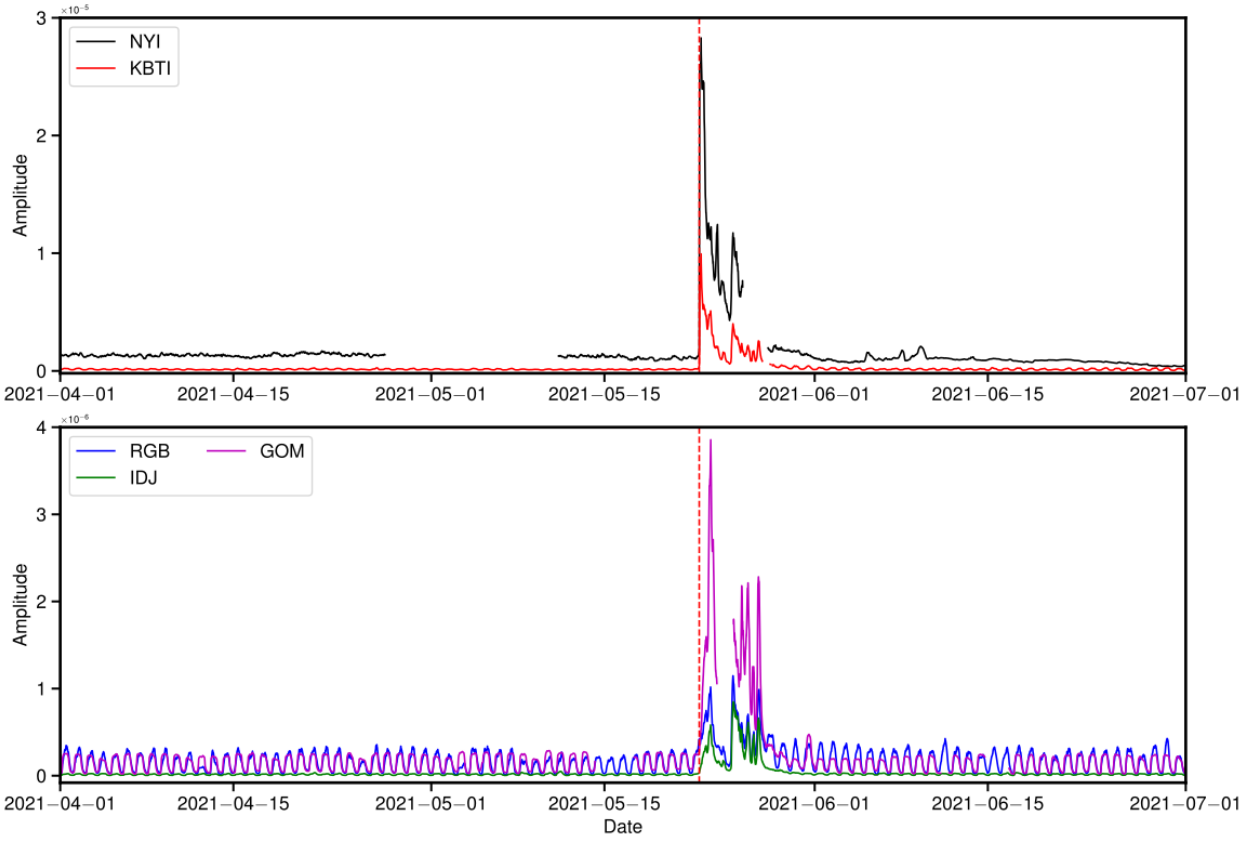

FIGURE 2.13: Amplitudes sismiques corrigées de la réponse instrumentale à haute fréquence du 1^{er} avril au 1^{er} juillet 2021. En haut, amplitudes aux stations de NYI et KBTI de l'ordre de $10^{-5}m/s$; en bas, amplitudes aux stations de RGB, IDJ et GOM de l'ordre $10^{-6}m/s$. La ligne rouge en pointillé marque le début de l'éruption.

Les rapports d'amplitudes sismiques LF sont représentés sur la Figure 2.14. Pour faciliter l'interprétation, la station choisie au numérateur de chaque rapport est la station la plus proche du sommet, soit KBTI ou NYI. Le premier signal de l'éruption est très fort pour les rapports impliquant une station proche du Nyiragongo et une station éloignée de celui-ci, comme par exemple le couple KBTI_IDJ. Le rapport d'amplitude entre stations plus éloignées du Nyiragongo ne montre par contre aucune variation significative, comme cela est illustré par le rapport GOM_IDJ. Il est donc logique d'estimer une région source proche de l'édifice. Néanmoins, le rapport d'amplitude NYI_KBTI a un comportement inverse avec une baisse suite à l'éruption, ce qui pourrait traduire une migration de la sismicité plus au sud qui se justifie par l'amplitude sismique à KBTI devenue plus importante qu'au sommet). En effet, au fur et à mesure que la sismicité évolue dans le temps, tous les rapports diminuent, traduisant une décroissance d'activité enregistrée par les stations proches du Nyiragongo (NYI, KBTI) au détriment de stations plus au sud. Cependant, le rapport entre KBTI et RGB (au nord-est du Nyiragongo) diminue également rapidement sous le niveau pré-éruptive. Dans ce cas la migration de la sismicité vers le sud ne peut expliquer cette baisse. Ainsi, il est probable que la diminution de ces rapports d'amplitude traduisent également la perte d'un signal au somment du Nyiragongo. Dans cette bande de fréquence, cette perte devrait correspondre au lac de lave, la principale source de trémor; après l'éruption, cette source a donc disparu ou son

amplitude a largement diminuée .

L'effet de la migration de la sismicité plus au sud lié à la propagation du dyke est plus claire à haute fréquence (Figure 2.15), ce qui est logique car cette bande de fréquence reflète principalement l'activité volcano-tectonique liée à l'intrusion magmatique. Le niveau du rapport entre KBTI et RGB ne tombe pas sous le niveau pré-éruptif et est significativement plus haut jusqu'au 25 mai. Le rapport entre KBTI et IDJ montre par contre une baisse progressive inférieure au niveau pré-éruptif, ce qui témoigne donc d'une migration de la source dominante de la sismicité vers le sud, et donc vers IDJ. Les variations des rapports NYI_KBTI et NYI_IDJ confirment cette interprétation. L'analyse de la paire GOM_IDJ se révèle plus délicate car le rapport baisse immédiatement après l'éruption et ne semble donc pas capturer la migration du dyke depuis l'édifice jusqu'à Goma (il est à noter que la station GOM a été hors service pendant une partie de la crise sismique). Le niveau pré-éruptif plus élévé est fortement modulé par le bruit anthropogénique, ce qui complique l'interprétation car l'activité humaine joue un rôle important dans les fluctuations des rapports d'amplitudes. En observant les amplitudes seules (Figure 2.13), il est clair que la région source est vraisemblablement plus proche de GOM que d'IDJ. Dans ce cas-ci, à cause de la forte activité humaine à GOM en temps normal, le ratio du bruit sismique ambiant HF à GOM et IDJ est plus élevé que lors de l'intrusion magmatique de mai 2021.

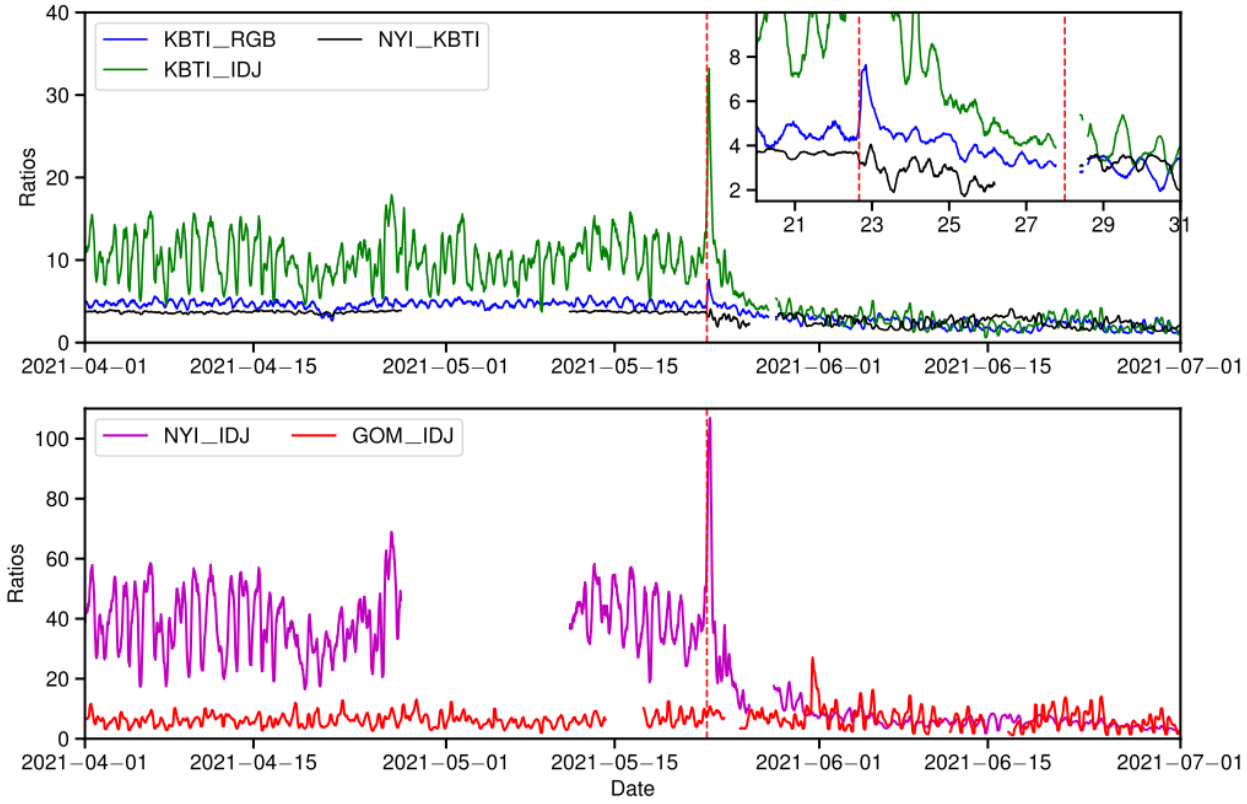

FIGURE 2.14: Rapports d'amplitude à basse fréquence du 1er avril au 1er juillet 2021. En haut, les rapports KBTI_RGB, NYI_KBTI, KBTI_IDJ avec sur le zoom, en haut à droite, les même rapports sur onze jours; en bas, les rapports NYI_IDJ, GOM_IDJ. La ligne rouge en pointillé marque le début de l'éruption.

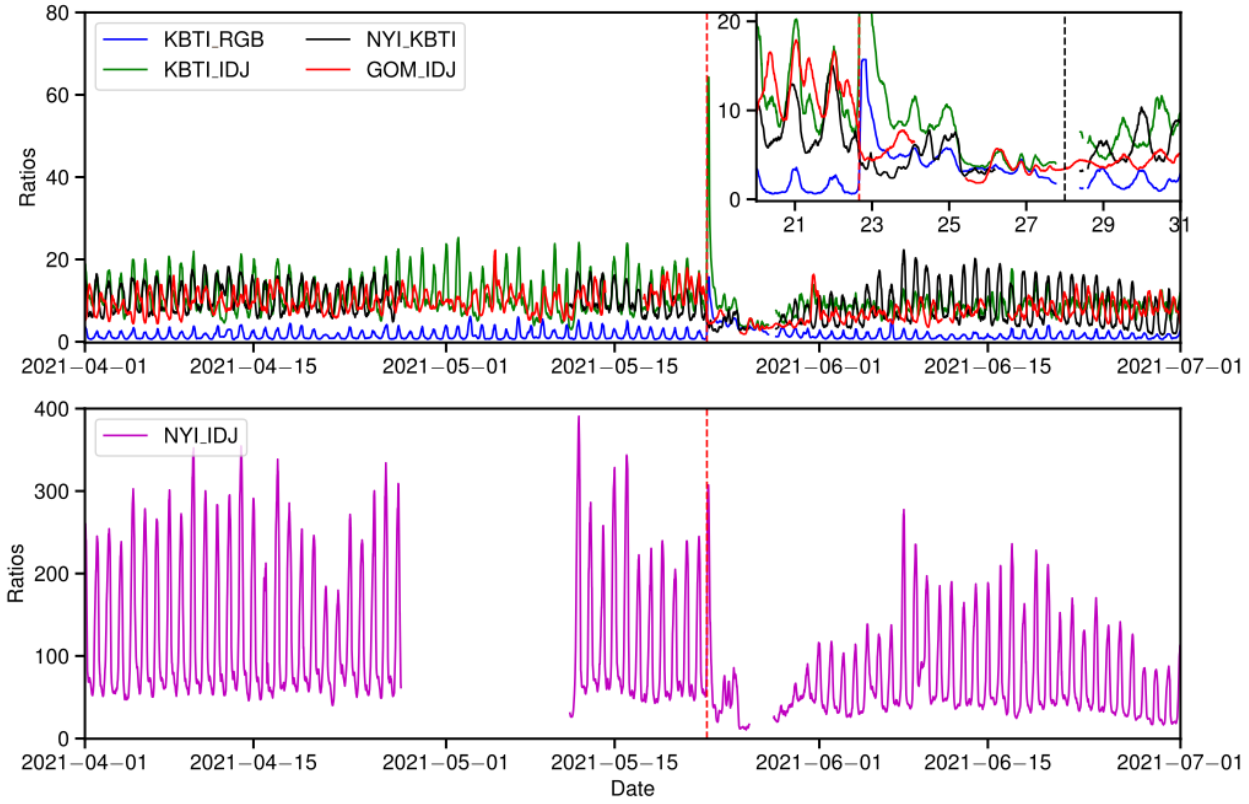

FIGURE 2.15: Rapports d'amplitude à haute fréquence du 1er avril au 1er juillet 2021. En haut, les rapports d'amplitude KBTI_RGB, NYI_KBTI, KBTI_IDJ, GOM_IDJ avec sur le zoom, en haut à droite, les mêmes rapports sur seulement 11 jours; en bas, le rapport NYI_IDJ. La ligne rouge en pointillé marque le début de l'éruption.

2.5.3 Mesures après l'éruption de mai 2021

L'analyse des spectrogrammes (Figure 2.11) indique la perte du trémor continu du volcan Nyiragongo (signature dans la bande LF) juste après la séquence éruptive de mai 2021, liée à la vidange du lac de lave lors de l'éruption. Le 28 septembre, soit environ 4 mois après l'éruption, un signal sismique particulier s'observe principalement sur la courbe d'amplitude sismique à la station de NYI. Ce signal se manifeste par une nette augmentation du niveau de l'intensité sismique par rapport au niveau de base avant cette date (Figure 2.16). Sa portée dépasse la station KBTI localisée sur le flanc sud du volcan à 5.6 km du sommet et s'observe aussi à la station comme RGB par exemple. Dans le bassin du Lac Kivu, les stations n'enregistrent pas cette augmention d'amplitude sismique et sont dominées par l'activité des microséismes du lac.

Nous remarquons également que la reprise de la sismicité associée au lac de lave se déroule en deux phases. Si la première phase commence le 28 septembre et s'achève avec un pic le 14 octobre 2021, une deuxième phase commence le 17 décembre 2021. Cette séquence est caractérisée par des fluctuations inhabituelles des amplitudes sismiques témoignant de sa forte intensité (Figure 2.16).

A haute fréquence (Figure 2.17), le premier signal du retour de l'activité le 28 septembre 2021 est plus marquée qu'à basse fréquence. Les deux phases de cette activité sis-

mique précédemment identifiées dans les amplitudes LF sont clairement identifiables, avec la détection plus claire d'autres fluctuations intermédiaires, comme en novembre 2021. Cependant, dans cette bande HF, seules les stations NYI et KBTI permettent la détection de ces signaux.

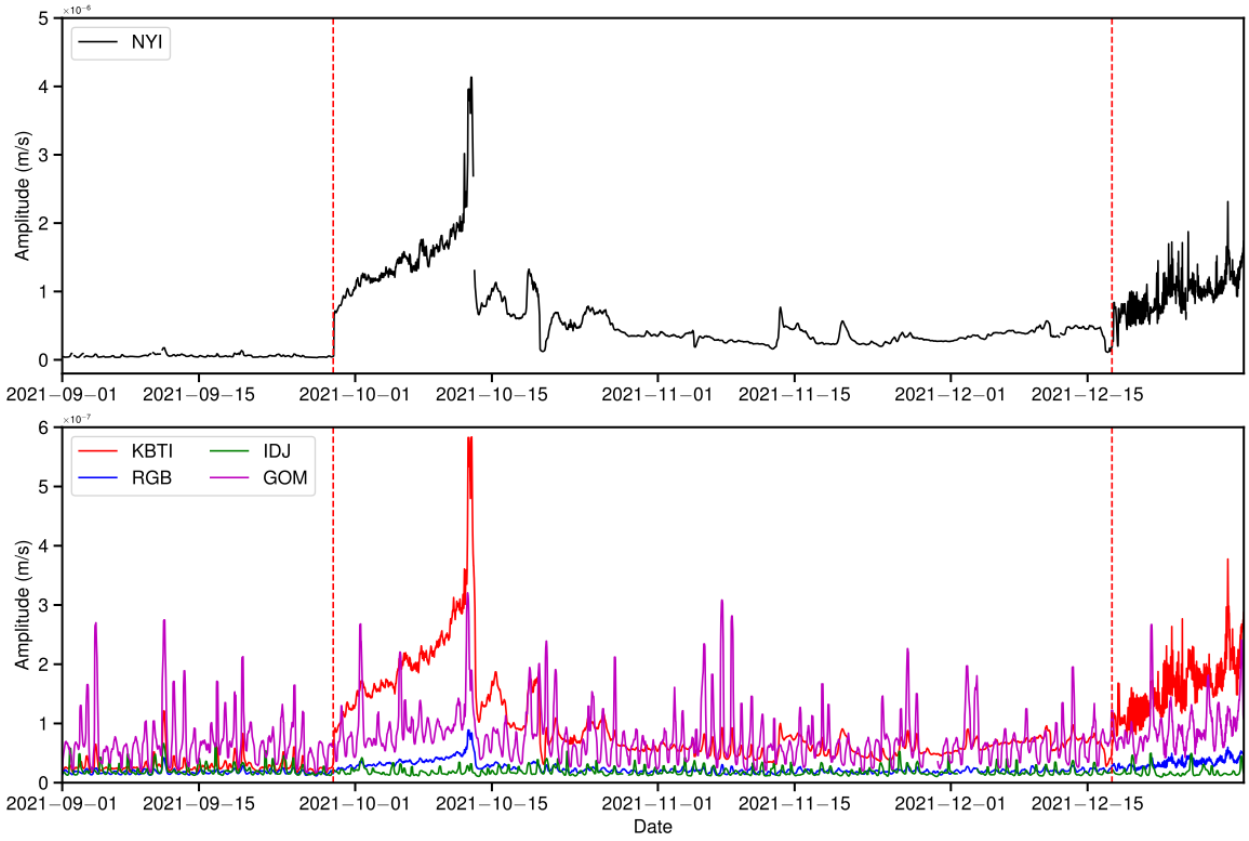

FIGURE 2.16: Amplitudes sismiques corrigées de la réponse instrumentale à basse fréquence du 1^{er} septembre au 31 décembre 2021. En haut, amplitude de la station NYI de l'ordre de $10^{-6}m/s$; en bas, amplitudes des stations de KBTI, RGB, IDJ et GOM de l'ordre $10^{-7}m/s$. Les amplitudes sismiques sont lissées avec une moyenne glissante centrée de six heures. La ligne rouge en pointillé marque le début de l'éruption.

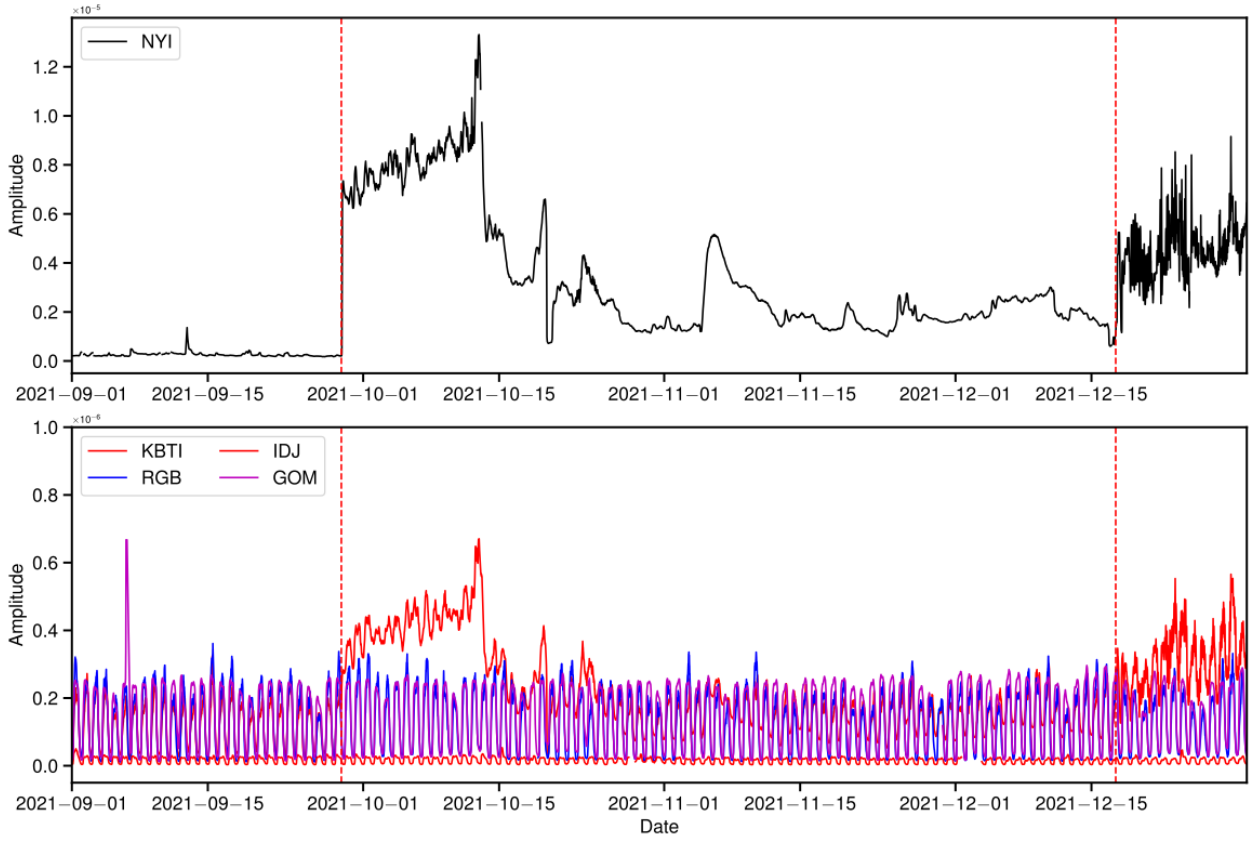

FIGURE 2.17: Amplitudes sismiques corrigées de la réponse instrumentale à haute fréquence du 1^{er} septembre au 31 décembre 2021. En haut, amplitude de la stations de NYI de l'orde de $10^{-5}m/s$; en bas, amplitudes des stations KBTI, RGB, IDJ et GOM de l'ordre de $10^{-6}m/s$. Les amplitudes sismiques sont lissées avec une moyenne glissante centrée de six heures. La ligne rouge en pointillé marque le début de l'éruption.

La Figure 2.18 présente les rapports d'amplitude LF sur quelques paires de stations. Comme précédemment, la station au numérateur est la plus proche du Nyiragongo. Le signal correspondant au retour d'activité demeure nettement identifiable entre les paires incluant une station proche du volcan, comme NYI et KBTI, et une station éloignée, comme IDJ, RGB et GOM. L'analyse de ces paires démontre clairement que l'activité provient du cratère du volcan. Si le couple implique la station du sommet, le rapport est grand. Par contre les paires impliquant des stations éloignées du volcan restent insensibles à la reprise d'activité. Les deux phases sismiques du 28 septembre 2021-14 octobre 2021 et celle démarrant du 17 décembre 2021 jusqu'à la fin de la fenêtre d'observation (1 janvier 2022) sont nettement visibles, comme illustré par le couple KBTI_IDJ ou NYI_KBTI.

Pour ce qui est de l'analyse HF (Figure 2.19), toutes les paires impliquées dans cette analyse sont affectées par les bruits diurnes. Néanmoins, le premier signal associé au retour d'activité au sommet reste nettement détectable sur toutes les paires sauf celles impliquant uniquement les stations éloignées de plus de 20 km, comme GOM_IDJ par exemple. Contrairement à l'analyse à basse fréquence, il y a lieu de noter que les deux principales phases mises en évidence précédemment sont fortement masquées par les variations diurnes dominés par l'activité humaine.

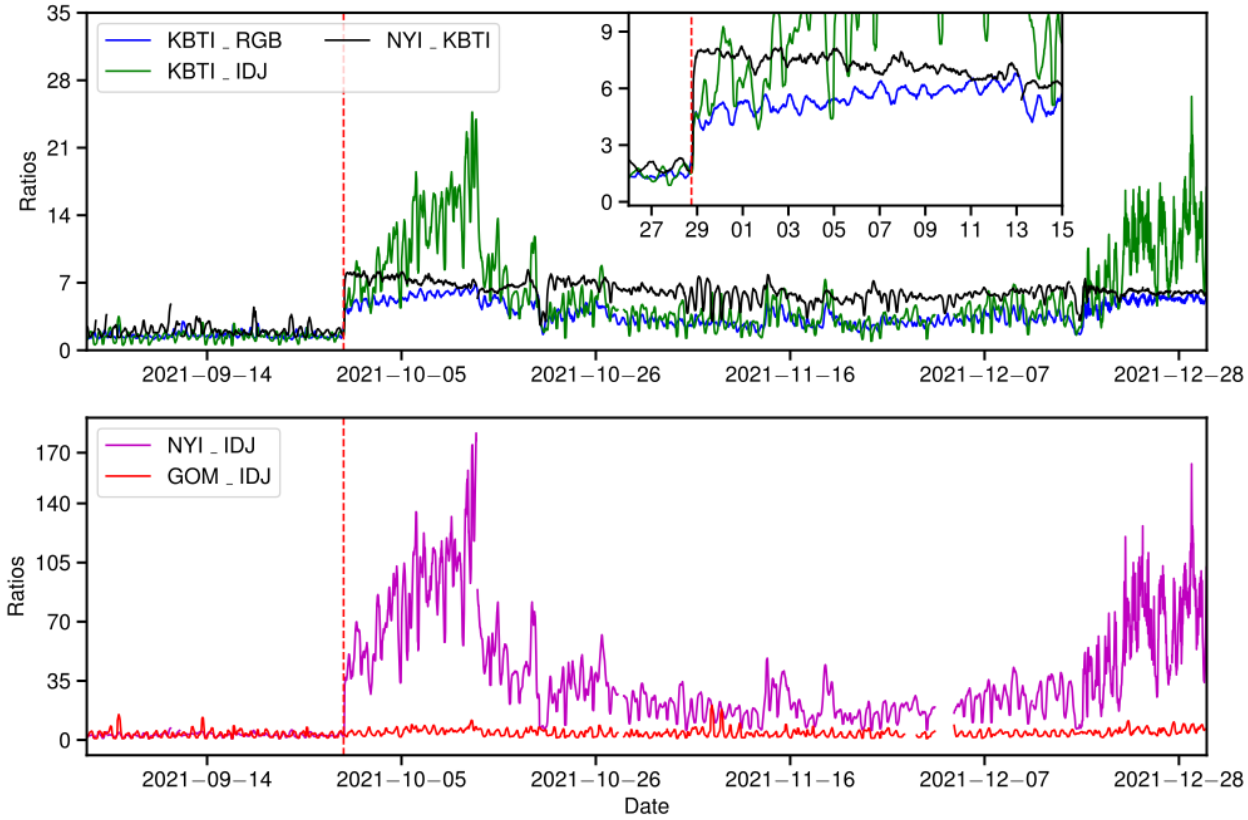

FIGURE 2.18: Rapports d'amplitude LF du 1er septembre au 31 décembre 2021. En haut, les rapports des stations KBTI_RGB, NYI_KBTI, KBTI_IDJ et zoom sur 20 jours pour faire ressortir les variations; en bas, les rapports des stations NYI_IDJ, GOM_IDJ. Les rapports sont lissés avec une moyenne glissante centrée de six heures. La ligne rouge en pointillé marque le début de l'éruption.

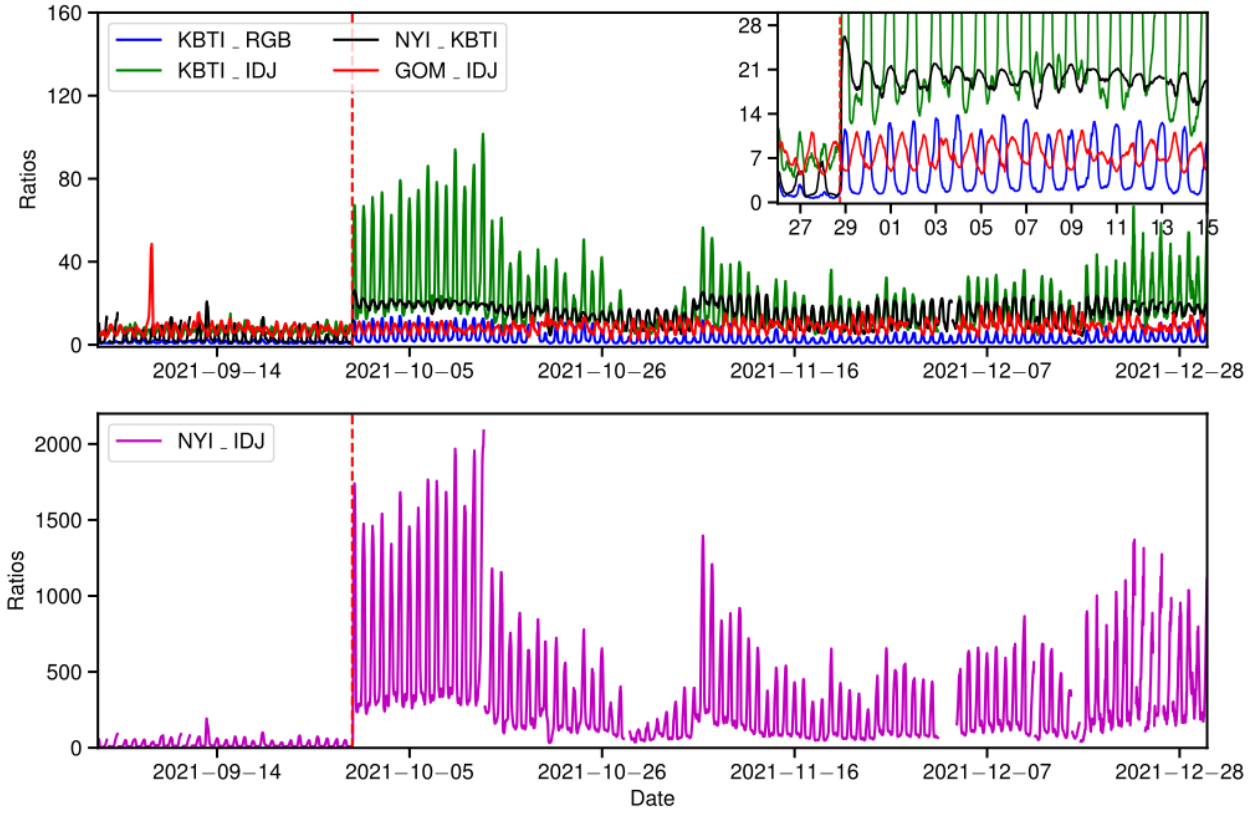

FIGURE 2.19: Rapports d'amplitude HF du 1^{er} septembre au 31 décembre 2021. En haut, les rapports des stations KBTI_RGB, NYI_KBTI, KBTI_IDJ, et zoom en haut à droite, sur 20 jours pour faire ressortir les variations; en bas, le rapport de la stations NYI_IDJ. Les rapports sont lissés avec une moyenne glissante centrée de six heures. La ligne rouge en pointillé marque le début de l'éruption.

2.6 Interprétation des variations d'amplitudes sismiques

2.6.1 4 années d'activité sismique du Nyiragongo (2018-2022)

L'activité éruptive dans le cratère du Nyiragongo a changé de façon notable à partir de fin 2015, avec l'apparition d'un cône éruptif à l'intérieur du cratère du Nyiragongo début 2016 et une montée constante de son niveau (et du fond du cratère par débordement) ponctuée par des fortes chutes récurrentes de plusieurs dizaines de mètres (Barrière et al., 2022; Walwer et al., 2023). Barrière et al. (2022) décomptent 10 chutes majeures du niveau de lac de lave depuis 2016. Elles sont interprétées comme étant associées à des chutes de pression dans le système magmatique puisqu'elles sont synchrones avec des essaims de séismes profonds à courtes et longues périodes se propageant vers le nord-est depuis l'édifice, signe d'intrusions magmatiques latérales profondes.

A partir du 22 mai 2021 intervient l'éruption de flanc, le drainage du lac de lave et l'effondrement du cratère sur une durée allant de quelques heures (coulées de lave, drainage du lac) à quelques jours (effondrements et approfondissements multiples du cratère, propagation d'un dyke superficiel et crise sismique associée) Barrière et al. (2023b) and Smittarello et al. (2022). S'ensuit une période de 4 mois sans activité effusive dans le cratère jusqu'à un retour de la lave le 28 septembre 2021. Un remplissage intermittent du cratère se produit depuis cette date et la présence de lave en continue est confirmée depuis la fin 2021 (cf. communications de l'OVG rapportées par le Smithsonian Institution, volcano.si.edu/volcano.cfm?vn=223030). Dans ce chapitre, nos séries temporelles se basant sur le réseau KivusNet s'arrêtent toutes au début de l'année 2022.

- **Amplitudes sismo-acoustiques à KBTI et niveaux du lac de lave**

  Afin de mieux décrire et comprendre l'activité sismique sur le Nyiragongo durant les quatre années d'analyse à partir de 2018, nous regardons spécifiquement les amplitudes sismiques LF et HF à la station de KBTI , qui est à la fois stratégiquement située au pieds de Nyiragongo et possède des données sismo-acoustique d'une continuité remarquable. À ces amplitudes sismiques à KBTI, nous ajoutons l'évolution du niveau de lac de lave dans le cratère de Nyiragongo et les amplitudes acoustiques (infrason) à la même station. La compilation de ces données est visible dans la Figure 2.20. Le calcul d'amplitude infrason suit le traitement de Barrière et al. (2023b). Il consiste en une valeur RMS toutes les 10 min (courbe grise) à partir d'enregistrement filtré entre $[0.4 - 2]$Hz. Cette bande de fréquence est également la plus adaptée pour détecter la composante acoustique du trémor volcanique provenant du Nyiragongo (Barrière et al., 2023b). Nous appliquons ensuite un filtre médian centré de 7 jours (courbe colorée). Afin de garder la cohérence entre les différents paramètres, les calculs d'amplitudes sismiques sont obtenus cette fois-ci sur base du même traitement (calcul RMS), qui reste toutefois totalement assimilable au traitement SARA effectué auparavant (Figures 2.9 et 2.10).

  Sur la Figure 2.20, on observe des pics sur les courbes d'amplitudes LF et HF (rouge et verte, respectivement) qui corrèlent avec chaque chute majeure du niveau du

lac De 2018 jusqu'à l'éruption de mai 2021. Chaque début de chute est marqué sur la Figure par des lignes pointillées. Ces pics dans l'amplitude continue correspondent aux chutes du lac de lave du 14-19 février 2018, 14-16 octobre 2018, 19-21 avril 2019, 17-19 mai 2019, 17-12 juillet 2019 et 17-19 avril 2020. La courbe HF étant mis à l'échelle par rapport au signal de l'éruption de mai 2021, un zoom permet de mieux visualiser ces différents pics. On remarque toutefois que la mesure RMS de 10 min (courbe grise) est bruitée par les variations diurnes dans cette bande de fréquence. Ces épisodes d'augmentation de l'activité sismique associées aux chutes du niveau de lac de lave sont similaires aux deux évènements documentés dans le chapitre 1 de février 2018 (visible aussi sur cette Figure) et de novembre 2016 (voir section "Monitoring the background lava-lake tremor at Nyiragongo"). Les plus fortes amplitudes sismiques et acoustiques sont obtenues entre décembre 2019 et avril 2020, se terminant par la dernière chute brutale du lac de lave plus d'un an avant l'éruption. Comme analysés par Barrière et al. (2023b) en y joignant des mesures de dégazage SO_2 et d'anomalies thermiques depuis l'espace, cette augmentation multi-paramètres témoignent d'un processus superficiel très actif et jamais observé à ce niveau avant l'éruption. Cela témoigne une fois de plus du potentiel d'une simple analyse des amplitudes sismiques à une station (dans des bandes de fréquence bien choisies) couplée à des informations complémentaires, comme ici le niveau du lac de lave.

- **Localisation du trémor basse-fréquence au Nyiragongo**

En complément, nous avons calculé la localisation journalière du trémor continu dans la bande LF ($[0.4 - 2]Hz$) pour la même période. La Figure 2.21 illustre la localisation persistante du trémor centré sur le Nyiragongo avant l'éruption de mai 2021. Barrière et al. (2018) ont caractérisé ce trémor sismique comme composé principalement d'ondes de surface et dont l'écart de temps entre arrivée acoustique et sismique sur le flanc correspondrait à une source superficielle dans le cratère. Au moment de l'éruption et pendant quelques mois, cette source disparaît et donne lieu à une localisation sans aucune source cohérente, reflétant la disparition du lac de lave. Une source de nouveau centrée sur le cratère du Nyiragongo réapparaît à partir de fin septembre 2021 et correspond à l'augmentation des amplitudes sismo-acoustiques dans la Figure 2.20.

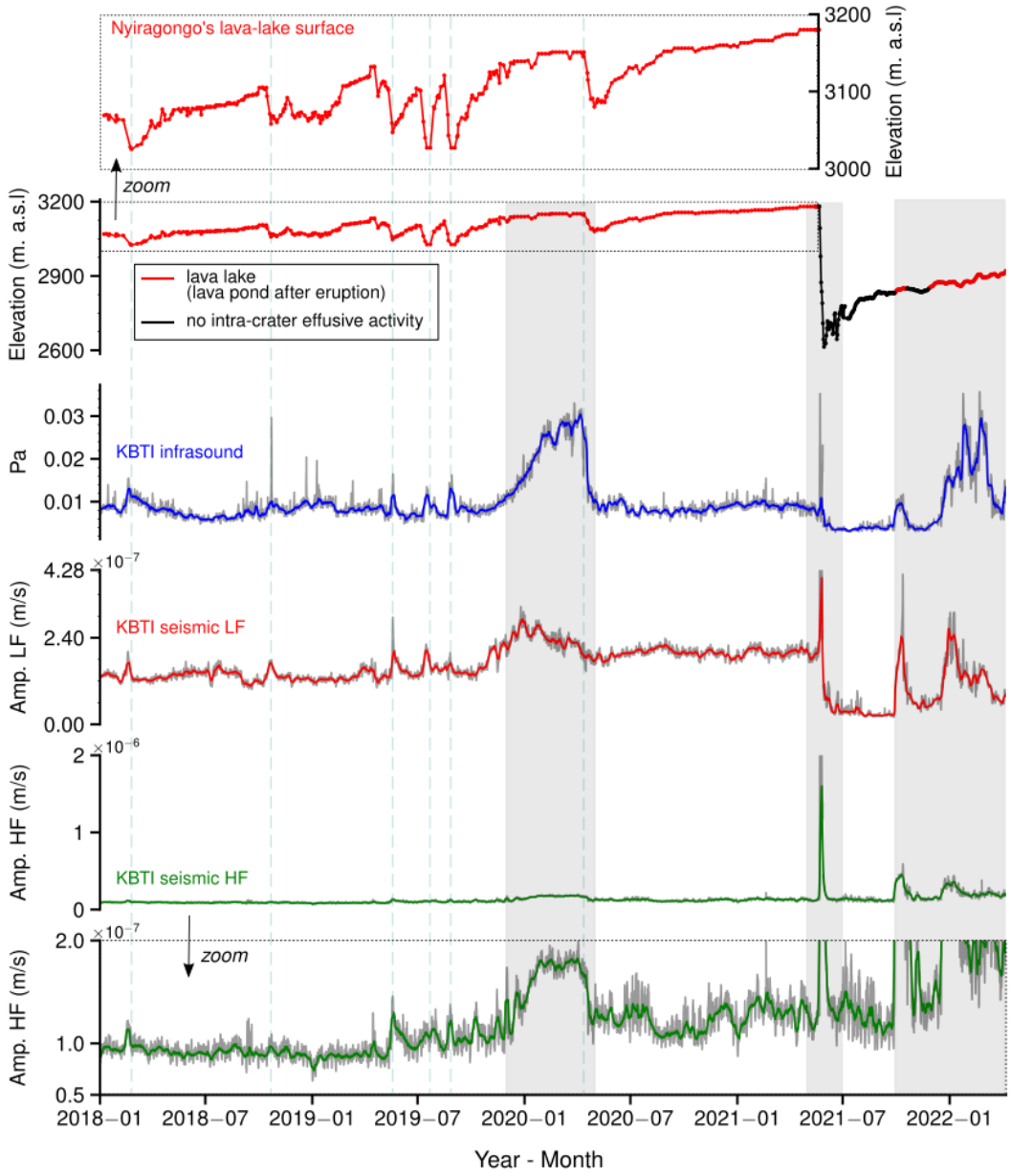

FIGURE 2.20: De haut en bas, variations du niveau du lac de lave ou du fond du cratère, de l'amplitude acoustique (infrason filtré entre 0.4 et 2 Hz) et sismique de la station KBTI, du 1^{er} janvier 2018 au 22 mai 2022. Pour le niveau du lac, une courbe rouge indique la présence d'une éruption dans le cratère (lac de lave avant l'éruption de 2021, bassin de lave de faible profondeur depuis fin 2021), une courbe noire dénote l'absence de lave et donc le fond du cratère (d'après Barrière et al. (2023b)). L'amplitude acoustique (bleu) est exprimée en Pascal. L'amplitude sismique LF de l'ordre de $10^{-7} m/s$ est représentée en rouge et l'amplitude HF est représentée en vert avec un pic autour de $2.10^{-6} m/s$ pendant l'éruption de flanc de mai 2021 (un zoom sur la période pré-éruptive est aussi montré dessous). Pour chaque courbe d'amplitude (acoustique et sismique), les courbes grises représentent les valeurs RMS obtenues sur une fenêtre glissante de 10 min. Les lignes pointillées verticales représentent les différentes chutes du lac de lave. Les bandes grises représentent, successivement, l'intense activité de décembre 2019 à avril 2020, la période autour de l'éruption du 22 mai 2021 et le retour de l'activité à partir du 28 septembre 2021

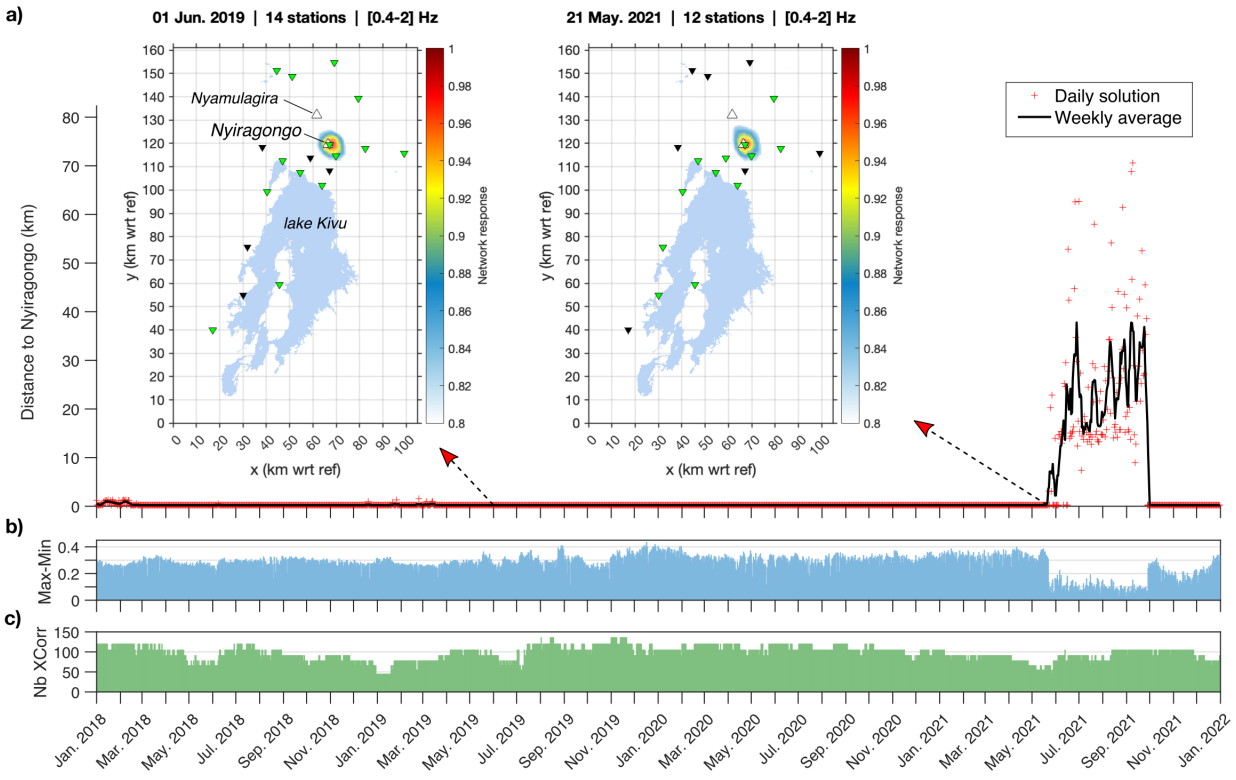

FIGURE 2.21: Localisation journalière 2D (longitude-latitude) du trémor volcanique continu obtenue par la méthode de corrélation croisée de signaux décrite dans Barrière et al. (2017) dans la bande de fréquence $[0.4 - 2]$Hz (voir aussi Chapitre 1 et Figure A.1). **(a)** Distance minimale entre la région source la plus probable et le cratère du Nyiragongo. La région source est visible sur chaque carte journalière (représentée en exemple pour les jours du 1er juin 2019 et du 21 mai 2021) et définie comme la zone où la valeur normalisée dite de "réponse du réseau" ("network response", représentée par l'échelle de couleur) est supérieur à 0.9. Sur les deux cartes, les triangles inversés en vert représentent les stations disponibles/utilisées pour la localisation, ceux en noir sont les stations indisponibles. **(b)** Max-Min : Évaluation de la qualité de la localisation en calculant l'écart entre le maximum et le minimum de la "réponse du réseau" pour chaque carte de localisation normalisée. Une plus faible valeur indique une localisation incertaine ou l'absence de trémor (voir Figure A.1). **(c)** Nb XCorr : Nombre de paires de stations utilisées (c-à-d. nombre de corrélations croisées) pour localiser la source de trémor. Cela permet de juger si une variation significative du nombre de stations utilisées peut jouer sur la localisation obtenue, ce qui n'est pas le cas ici pour l'entièreté de la période analysée.

2.6.2 Les possibles processus sources dominants à basses et hautes fréquences

Une question qui reste en suspend est l'interprétation des processus sources derrière l'augmentation des amplitudes sismiques dans les deux bandes de fréquences LF et HF. A l'échelle de temps des 4 années 2018-2022, les variations multi-journalières pendant les chutes majeures du lac de lave peuvent être affectées par les essaims sismiques lors des intrusions profondes (Barrière et al., 2022). Ceci est particulièrement vrai pendant l'éruption de 2021 et la propagation du dyke. Comme vu au chapitre 1, la bande LF en dessous de 2 Hz caractérise plutôt le trémor continu qui, même si le processus source

n'est pas clairement identifié, traduit un mécanisme superficiel lié à l'activité du lac de lave. L'absence de localisation du trémor au Nyiragongo s'accompagne de l'absence du lac de lave après l'éruption (voir Figure A).

Une observation clef venant confirmer cela en se basant sur les amplitudes sismiques seules est le niveau d'amplitude LF les mois après l'éruption qui est nettement plus faible que le niveau moyen avant l'éruption (Figure 2.20). Ainsi le lien entre activité du lac de lave et amplitude sismique LF à KBTI est évident. Cette baisse du niveau moyen d'amplitude est aussi visible dans l'acoustique. Enfin, on observe aussi une augmentation drastique des amplitudes sismo-acoustique lors du retour de la lave dans le cratère du Nyriagongo quelques mois après l'éruption. Ces observations confirment donc un mécanisme source superficiel sismo-acoustique à l'origine du trémor volcanique enregistré dans cette bande de fréquence LF. Cependant, il est frappant d'observer que l'augmentation d'amplitude sismique LF est en décalage avec l'amplitude acoustique de novembre 2019 à avril 2020 alors que l'amplitude HF colle parfaitement aux infrasons. Pour cette période-ci, l'amplitude HF reflète donc aussi le trémor continu surperficiel du Nyiragongo.

Un élément non considéré jusqu'à maintenant est la participation du cône éruptif (à environ 200 m du lac de lave au fond du cratère) à l'augmentation générale de tous ces signaux. Ce cône, très probablement connecté au lac de lave à faible profondeur (Barrière et al., 2022), produit du "spattering" (projections de lave), des coulées de lave et du dégazage lorsque le niveau du lac de lave est au plus haut, c'est à dire lorsque la pression dans le système magmatique est maintenue forte et/ou en augmentation. Sur base d'une expédition de quelques jours en 2016, Valade et al. (2018) a mis en évidence la participation très importante du cône à l'augmentation des amplitudes infrasons dans le cratère lorsque ce dernier est actif. Barrière et al. (2022) a noté que le cône pendant cette période 2019-2020 était particulièrement actif avec un remplissage du fond du cratère par coulées issues du cône. Bien qu'un trémor continu ait été enregistré avant l'apparition de ce cône et soit associé à la présence du lac de lave (Barrière et al., 2019), la similitude entre courbe sismique HF et courbe acoustique pourrait impliquer que le rôle du cône sur la signature sismo-acoustique est ici notable. L'augmentation plus précoce de la courbe LF est synchrone avec l'augmentation du niveau du lac de lave et commence à décroître lorsque le niveau du lac se maintient haut. C'est à ce moment que l'amplitude HF et acoustique augmente ensemble. La dernière chute du lac de lave en avril 2020 s'accompagne de l'arrêt de l'activité effusive du cône. Ainsi, les baisses d'amplitude HF et acoustique concomitantes à cette chute sont soit liées aux changements de comportement du lac, du cône ou les deux.

Le niveau plus bas de l'amplitude sismique LF après l'éruption (même pendant le retour d'un bassin de lave fin 2021) indique que cette composante pourrait être liée au couplage fluide-solide le long des parois de l'ancien lac de lave (environ 300 m de profondeur et 200 m de largeur avant l'éruption). Un modèle conceptuel liant convection de magma riche en gaz et dégazé dans le lac de lave et variations périodiques d'amplitude du trémor dans la bande LF a notamment été proposé par Barrière et al. (2019). Cette interprétation rejoindrait celle de Richardson and Waite (2013) concernant lac de lave du Villarica au Chili; cette étude suggère la génération de signaux LP (évènement seul ou trémor) comme ré-

sultant de forces de traction du magma sur les parois et le fond du lac ("drag forces") suite aux explosions de gaz en surface. Au Nyiragongo, le phénomène de gas pistonning (Smets et al., 2017), pendant lequel le niveau du lac de lave monte et l'agitation du lac en surface est moindre, module aussi clairement l'amplitude de ce trémor LF (Barrière et al., 2019), justifiant encore un mécanisme source très superficiel.

Ces résultats au Nyiragongo rejoignent les nombreuses observations au Kīlauea (Hawaii) (Patrick et al., 2016) montrant le lien évident entre activité du lac de lave (gas pistoning et spattering) et l'amplitude du trémor sismo-acoustique au sommet. Comme l'indique Thelen et al. (2022) pendant la période particulière de l'éruption de 2018 à ce même volcan, le spattering et le dégazage au niveau du lac de lave doivent contribuer au trémor sismique et acoustique enregistré. Cependant, un contenu fréquentiel qui évolue avec une augmentation d'amplitude traduit aussi certainement un mécanisme plus complexe avec de multiples sources.
Concernant un autre volcan ouvert possédant un lac de lave, les études de Jones et al. (2006) et Jones et al. (2012) à l'Erta 'Ale en Ethiopie suggèrent également que le trémor continu enregistré, bien que fortement lié à l'activité lac de lave, est un signal composite provenant de plusieurs sources, telles que le dégazage en surface, la résonance de fissures ("cracks") ou la coalescence de bulles de gaz dans le conduit alimentant le lac de lave. Tous ces mécanismes potentiels sont superficiels car la corrélation entre signaux sismiques et acoustiques est forte.

On peut également citer l'étude de Métaxian et al. (1997b) au volcan Masaya analysant un trémor continue dont le champ d'ondes est dominé par des ondes de surfaces et dont l'origine est associé au dégazage du lac de lave ou de volumes de magma superficiels ("magma bodies"). Ils observent notamment que l'amplitude du trémor décroit lorsque le lac de lave n'est plus apparent, suggérant ainsi un lien étroit entre amplitude du trémor et présence du lac de lave et de magma proche de la surface. Ainsi, les observations sismiques et acoustiques disponibles au Nyiragongo et l'étude de la littérature à d'autres volcans ouverts suggèrent que le trémor large bande enregistré pourrait très vraisemblablement inclure des sources multiples à différentes profondeurs comme les processus de dégazage du lac du lave, du cône éruptif et des mouvements de fluides dans le système magmatique superficiel alimentant le lac et le cône.
La composante HF du trémor pourrait retranscrire uniquement un phénomène plus superficiel lié au "spattering"/dégazage du lac de lave et du cône éruptif. Du fait d'une atténuation plus importante, cette composante HF, fortement corrélée avec l'amplitude infrason pendant la période d'intense dégazage en 2019-2020, n'est observable en continue qu'à la station du sommet (NYI) et également, bien que plus bruitée, à la station KBTI sur le flanc. Enfin, il est à noter que les niveaux moyens sismiques LF et HF se sont maintenus à des niveaux plus élevés après cette épisode 2019-2020, en lien avec un niveau du lac de lave en augmentation constante depuis la chute d'avril 2020 jusqu'à l'éruption de mai 2021. La tendance long-terme sur la dernière année avant l'éruption était donc à une pression continue dans le système magmatique (Barrière et al., 2022; Walwer et al., 2023), qui a conduit à une rupture de l'édifice soudaine le 22 mai 2021 (Smittarello et al., 2022). Dans la prochaine section, nous allons analyser plus en détail cette période critique pendant et quelques jours après l'éruption de flanc.

2.6.3 Éruption de flanc et intrusion magmatique vues par un couple de station (22 - 28 mai 2021)

Nous examinons sur une échelle de temps de quinze jours les variations des amplitudes sismiques LF et HF et leurs rapports aux stations KBTI et IDJ comme illustré sur la Figure 2.22. Sur base des analyses SARA précédentes, le choix de ces deux stations apparaît stratégiques car situés au nord et au sud de l'axe du dyke. KBTI est situé à environ 6 km du centre du cratère du Nyiragongo sur son flanc sud-est, IDJ est à une distance 10 fois plus grande en direction du sud. Nous ajoutons les données de sismicité issues de l'étude de Smittarello et al. (2022) (comptage de séismes et distance épicentrale par rapport au Nyiragongo).

Comme déjà mentionné dans ce chapitre, la sismicité précédant l'éruption ne révèle aucun signe pouvant être assimilé à un signal précurseur d'une éruption imminente. Le comptage d'évènements sismiques au Nyiragongo indique une "sismicité de fond" (background seismicity) sans augmentation anormale du nombre de séismes (Figure 2.22a,b). De la même manière, les courbes d'amplitudes sismiques LF et HF à KBTI ne reflètent aucune tendance à l'augmentation. Les fluctuations LF à IDJ sont dues aux variations des microséismes du lac Kivu. Enfin, l'analyse des rapports dans les deux bandes de fréquences ne révèle aussi aucun signe significatif d'augmentation de la sismicité, mais met en lumière les variations diurnes d'origine humaine ou naturelle (Figure 2.22e). Pendant cette période pré-éruptive, l'activité effusive et le dégazage continu provenant du lac de lave et du cône éruptif capturés par photo la veille de l'éruption n'indiquait pas de changement notable pouvant laisser présager l'éruption du lendemain (Photo dans la Figure 2.22a, avec l'autorisation de T. Nyandwi, chef cuisinier congolais, membre régulier lors de visites touritiques ou scientifiques au sommet).

A cette échelle de temps, deux changements majeurs dans les variations des amplitudes et leurs rapports sont clairement identifiables. La première variation (22 mai, ligne verticale colorée) est liée à l'éruption et au drainage du lac de lave, la seconde (25 mai, ligne noire pointillée) correspond à une nouvelle phase sismique lors de la progression du dyke vers le sud. Il est intéressant d'observer un comportement similaire dans les deux bandes de fréquences à KBTI. Les amplitudes diminuent plus la sismicité du dyke s'éloigne de la station, ce qui indique que nous mettons en évidence ici principalement des mécanismes sources large bandes liés à l'intrusion magmatique. Le ressaut à partir du 25 mai correspond à une progression soudaine du dyke de Goma vers le lake Kivu associée avec une augmentation de la magnitude et du nombre de séismes (Smittarello et al. (2022).

Le pic dominant à IDJ est celui du 25 mai, ce qui traduit une nouvelle fois que la sismicité a migré du nord vers le sud. Etant moins sensible à l'éruption proche du cratère avant le 25 mai, on note plus clairement sur l'enregistrement à IDJ la succession de quatres pics correspondant aux variations du niveau de sismicité lorsque le dyke bute sur la faille de Nyabihu (au niveau du lac Kivu) et ne progresse plus vers le sud. Lors de l'éruption, la courbe LF à IDJ capture néanmoins le démarrage de l'éruption mais l'augmentation des amplitudes HF est plus progressive. Ce n'est qu'au moment où le dyke progresse clairement de plusieurs kilomètres le 23 mai (Figure 2.22a) que les courbes LF et HF deviennent semblables.

Ainsi l'analyse du rapport d'amplitude KBTI/IDJ apparaît assez évident. L'unique pic majeur à l'éruption indique la localisation de la sismicité à l'édifice. La baisse qui suit ce premier pic dans le rapport KBTI/IDJ témoigne assez clairement de la migration de la sismicité avec une baisse notable après le 25 mai sous le niveau pré-éruptif. Il est ici important de rappeler une observation de la section 2.5.2 concernant un rapport entre IDJ et GOM, une station plus au nord et donc plus proche de l'éruption. Le rapport GOM/IDJ ne contient pas le pic initial de l'éruption dans les deux bandes fréquentielles (Figures 2.18 et 2.19) car le ratio du bruit ambiant entre ces deux stations est plus grand avant plutôt qu'après l'éruption. Cela implique que certaines paires de stations ne sont pas nécessairement appropriées pour une analyse directe des rapports d'amplitude en terme de distance à la source. La station GOM, tout particulièrement, est très bruitée par les microséismes du lac Kivu (bande LF) et l'activité anthropogénique (bande HF).

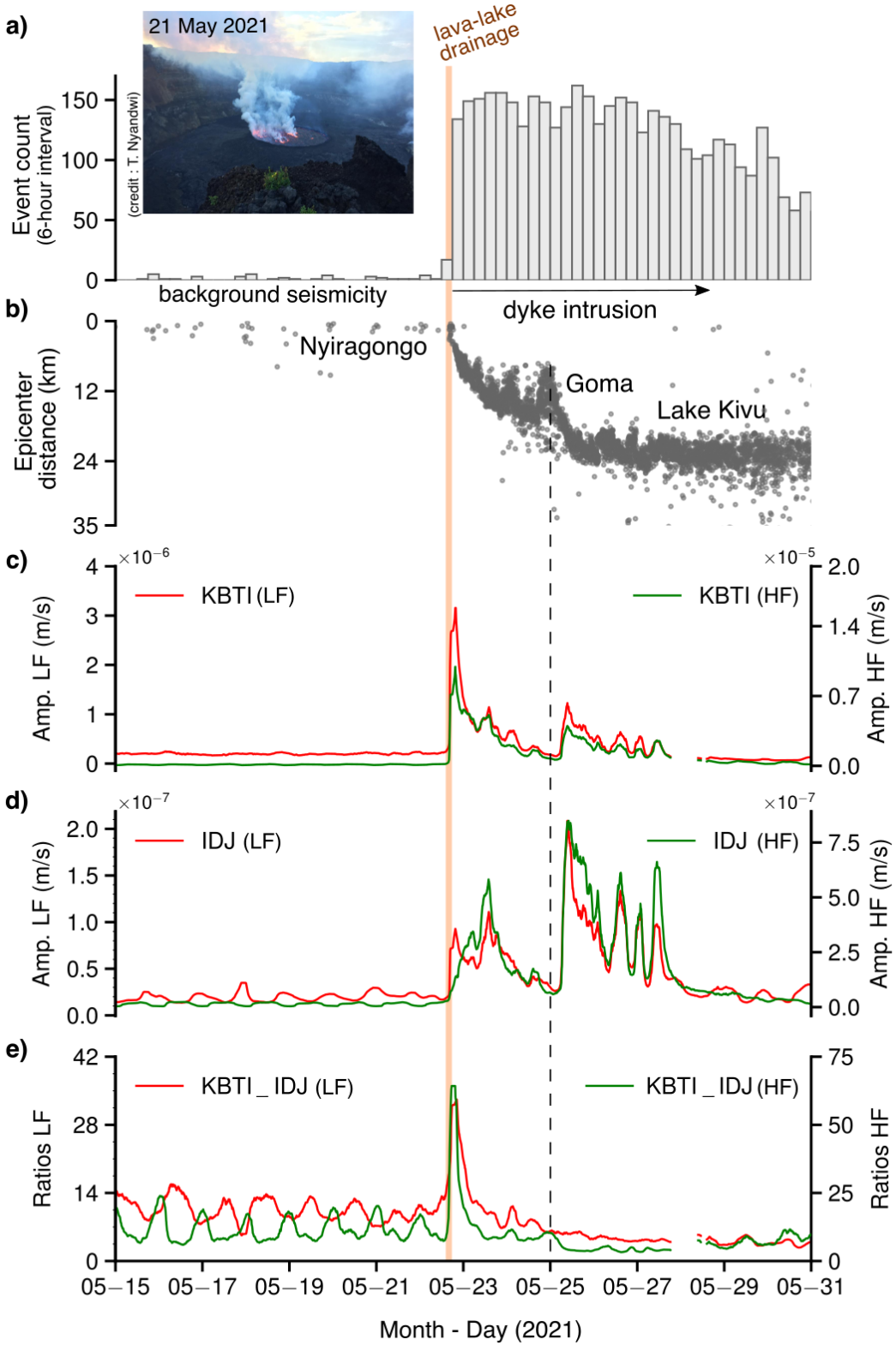

FIGURE 2.22: Éruption de flanc et intrusion magmatique vues par le couple de station KBTI-IDJ. **(a)** Comptage de séismes par interval de 6 heures. **(b)** Évolution dans le temps de la distance épicentrale des séismes par rapport au sommet de Nyiragongo. **(c)** Amplitudes sismiques LF à KBTI de l'ordre de 10^{-6} (couleur rouge) et HF de l'ordre de 10^{-5}(couleur verte). **(d)** Amplitudes sismiques LF à IDJ de l'ordre de 10^{-7} (couleur rouge) et HF de l'ordre de 10^{-7}(couleur verte). **(e)** Rapport d'amplitude entre KBTI et IDJ à basse (courbe rouge) et haute fréquence (courbe verte).

2.6.4 Comportement post-éruptif: Vers un retour à un état éruptif persistant au sommet du Nyiragongo

La reprise de l'activité effusive au sommet de Nyiragongo conduisant au retour d'un lac de lave (plus précisément un petit bassin de lave dans un premier temps, "lava pond" en anglais) est un événement majeur en cette fin d'année 2021. Il marque le commencement d'une nouvelle dynamique magmatique sur ce volcan avec une activité sismique associée à la recharge du lac de lave qui a été drainé lors de l'éruption. L'analyse en continue de cette nouvelle dynamique est cruciale pour la surveillance de ce volcan, car elle constitue un repère pour une nouvelle ligne de base pour différentes mesures géophysiques. Le retour de la lave dans le cratère s'est révélé relativement rapide après les éruptions de 2002 et de 2021, prenant respectivement dix mois (Komorowski et al., 2002) et quatre mois (Barrière et al., 2023b). En revanche, pour l'éruption de 1977, le retour du lac de lave n'a été observé que cinq années plus tard (Hamaguchi et al., 1992).

De mai à décembre 2021, nous retraçons ici l'évolution de l'activité sismique dans le cratère du Nyiragongo au travers de la localisation de trémors LF et des variations d'ampli tudes LF et HF. La Figure 2.23 illustre l'évolution de la source du trémor continu superficiel au Nyiragongo. Sa disparition s'amorce juste après le drainage du lac de lave le jour de l'éruption, comme le montre l'analyse de la distance entre la source du trémor la plus probable et le cratère (Figure 2.23a). La différence Max-Min de la réponse du réseau (Figure 2.23b) indique aussi clairement la perte d'un signal clair et localisable à partir de cette date, qui ne peut pas s'expliquer par un changement du nombre d'instruments utilisés (figure 2.23c). On peut voir effectivement que la carte journalière de localisation du 23 mai diffère de celles des jours précédant et que la source dominante du bruit ambiant ne pointe plus vers le Nyiragongo (Figure 2.23d). Cette localisation est plus diffuse et semble couvrir l'axe entre le Nyiragongo et le nord du lac Kivu mais la faible valeur Max-Min impose de ne pas considérer ce résultat comme réellement interprétatble car nous mettons ici en évidence aucune source dominante et des signaux peu ou non corrélés entre eux. Cependant, même si plus faibles que pendant la période pré-éruptive, des augmentations de valeurs Max-Min sont notables jusqu'en juin et correspondent à des dates où la région source identifiée est à faible distance du Nyiragongo. Ainsi, des exemples de cartes de localisation du 14 au 17 juin 2021 révèlent une source de trémor encore présente au Nyiragongo et, bien d'intermittente depuis l'éruption, suffisamment continue et détectable à l'échelle du réseau pour être identifiée par une localisation journalière. Les 15 et 16 juin représentent les dernières journées pendant lesquelles ce trémor résiduel est localisé, en l'absence d'un lac de lave depuis le soir du 22 mai 2021. De part sa nature semi-continue jusqu'au 16 juin dans la même bande de fréquence que le trémor pré-éruptif, il est fort probable que le mécanisme source soit toujours liée à des mouvements de fluides dans le système magmatique superficiel du volcan et donc témoigne d'un magma proche de la surface encore plusieurs semaines après l'éruption de flanc. Comme nous l'avons déjà fait remarqué plus haut au travers d'autres exemples de volcans à conduit ouvert (section 2.6.2), l'absence de lave en surface n'implique pas forcément la disparation du trémor mais un changement de ses propriétés, notamment l'amplitude à la source comme mis en évidence par Métaxian et al. (1997b) au volcan Masaya.

Ainsi, sur cette période charnière de 4 mois entre l'éruption (22 mai 2021) et le retour

de la lave au sommet (28 septembre 2021), nous analysons dans la Figure 2.24 les variations d'amplitudes sismiques LF et HF aux stations NYI et KBTI. Pour faire le lien avec les localisations de trémor présentées juste avant, nous calculons aussi les fonctions de cross-corrélation (CCFs, "cross-correlation functions" en anglais) entre ces deux stations dans la bande LF (0.4-2 Hz, celle utilisée pour la localisation) et dans la bande HF (2-15 Hz). Le traitement du signal est similaire au calcul employé pour localiser le trémor volcanique sur base d'enregistrements journaliers de différentes paires de station (Figures 2.21 et 2.23). Nous augmentons ici la résolution temporelle du calcul des CCFs entre NYI et KBTI en prenant des fenêtres d'enregistrement de 6 heures (durée aussi utilisée pour les calculs d'amplitudes) et chevauchées de 50 % (une CCF toutes les 3 heures, plutôt qu'une par jour). Dans la Figure 2.24a les CCFs sont représentées sous forme de matrice. Chaque colonne correspond à l'évolution du coefficient de corrélation normalisé (échelle de couleur) en fonction du décalage temporelle ("time lag", en secondes). La juxtaposition de chaque CCF pour chaque tranche de 3 heures sur toute la période étudiée donne le résultat final affiché. D'après Barrière et al. (2017), un temps de trajet théorique d'un signal basse-fréquence ($[0.4-2]$Hz) généré proche de la surface dans la cratère mettrait environ 4.3 s pour rejoindre KBTI après avoir été enregistré au sommet à NYI (voir aussi le chapitre 1 où ce modèle de vitesse est appliqué). Une ligne pointillée est ainsi tracé pour le délai ("time lag") égale à 4.3 s (Figure 2.24). On obtient effectivement un maximum de corrélation pour un délai autour de 4.3 s, lorsque le lac de lave était encore présent (avant l'éruption) et lorsque la lave est réapparu dans le cratère quelques mois plus tard (après "renewal"). Le signal généré dans le cratère ayant une très large bande spectrale comme vu dans ce chapitre, cette corrélation est aussi visible sur l'analyse à plus haute fréquence (2-15 Hz) bien que moins évidente qu'à plus basse fréquence. Les valeurs absolues de coefficient de corrélation sont de l'ordre de 5 fois inférieures aux coefficients à basses fréquences avec un maximum de corrélation qui ressort moins bien du bruit (Figure 2.24b). Après environ 2 mois (juillet-août) où aucun trémor n'est notable, il est intéressant d'observer un léger sursaut des coefficients LF autour de mi-septembre environ quinze jours avant le retour de la lave au sommet le 28 septembre marqué par une augmentation brutale de la corrélation du bruit ambiant entre les 2 stations, de nouveau dominé par un source persistante au cratère. Le bruit ambiant d'origine humaine à KBTI dans la bande HF est un facteur important pouvant affecter la corrélation croisée de signaux provenant du cratère avec la station NYI. Les effets de propagation plus complexe des ondes à ces plus hautes fréquences ("scattering") jouent aussi probablement un rôle significatif. L'hypothèse d'une propagation 2D d'ondes de surface reliant le temps de trajet et la distance par une simple "loi puissance" comme assumée dans Barrière et al. (2017) n'est certainement plus valable dans ce régime haute fréquence.

L'analyse des amplitudes sismiques et de rapports d'amplitudes sismiques LF et HF (Figure 2.24c) coïncide avec les observations relevées par les CCFs entre ces deux stations. On y voit clairement une activité résiduelle dans le cratère de Nyiragongo avec deux pics début et mi-juin dans la bande LF (courbes rouges). A plus haute fréquence (courbes vertes), seules les variations d'amplitudes à la station du sommet sont réellement notables. Comme déja analysé dans ce chapitre (section 2.5), le niveau d'amplitude moyen après l'éruption est significativement inférieur à celui pré-éruptif, dominé par le trémor superficiel continu du Nyiragongo. Ainsi, le niveau de bruit de fond étant réduit, cela permet de mettre en évidence des processus autrefois masqués. Les multiples pics ob-

servés aux deux stations pendant la période "calme" (juillet-septembre) peuvent être des signaux originaires de l'édifice mais l'absence de corrélation laisse à penser que l'origine est autre. Les microséismes provenant du lac Kivu dans la bande LF sorte ainsi plus clairement du bruit de fond (voir aussi les spectrogrammes de la section 2.5). L'intrusion magmatique majeure après l'éruption a également conduit à une réactivation de l'activité tectonique dans le bassin du lac Kivu que ces stations enregistrent clairement pendant ces 4 mois. Nous renvoyons ici le lecteur à la fin du prochain chapitre de cette thèse (chapitre 3, "Perspectives : Seismicity patterns in the Kivu rift, 2015-2022") pour plus d'informations. S'il y a des signaux provenant de l'édifice pendant cette période, ils ne sont alors pas clairement capturés par le processing choisi se basant sur des filtres médian de 6 heures. Les pics à la station du sommet dans la bande HF pourraient provenir de sources très locales à l'édifice mais une analyse plus détaillée, que nous ne fournirons pas ici, serait nécessaire. Smittarello et al. (2023) ont notamment montré que la majeur partie des effondrements dans le cratère (environ -600 m) se sont produit dans la dizaine de jours suivant l'éruption. Cependant, comme le montre Barrière et al. (2023b), le fond du cratère conique s'est ensuite rempli d'environ 200 m entre juin et septembre 2021, sans présence de lave et certainement à la faveur de multiples éboulements et agrandissement des parois du cratère. Ces multiples processus de surface peuvent naturellement conduire à une sismicté uniquement détectable au sommet. Des émissions de gaz volcaniques (et une sismicité associée) pendant cette période sont aussi possibles bien que les relevés SO_2 depuis l'espace ne peuvent le confirmer (Barrière et al., 2023b). Il semble toutefois clair qu'il n'y a pas eu d'augmentation drastique du niveau de sismicité avant le retour de la lave dans le cratère. Cela tend à indiquer que le système magmatique du volcan est resté ouvert pendant ces 4 mois de calme relatif à l'édifice, permettant une remontée rapide et soudaine du magma en surface fin septembre.

La dernière fenêtre d'observation analysée (Figure 2.25) concerne le retour progressive et persistant de la lave au sommet à partir de fin septembre 2021 (reprenant l'analyse SARA de la section 2.5.3). Nous illustrons une nouvelle fois cette période critique avec les stations NYI et KBTI, qui sont assez naturellement les plus adaptées pour étudier l'activité volcanique au Nyiragongo. Nous y ajoutons une série temporelle de l'amplitude acoustique infrason (une moyenne RMS par heure en Pa obtenue sur une fenêtre centrée de 6 heures) (Figure 2.25a). Les périodes d'activité effusives dans le cratère sont annotées suivant les observations multiparamètres (infrason, thermique, dégazage) de Barrière et al. (2023b) qui s'appuient notamment sur les mêmes données infrasons. Trois photos prises à différents instants de cette nouvelle activité permettent de mieux jauger les changements au sommet. La reprise de l'éruption au sommet le 28 septembre 2021 est nettement visible dans les enregistrement sismiques dans les deux bandes de fréquences LF et HF. Il est notable que la composante HF à KBTI est cette fois-ci de plus forte amplitude que la composante BF, en comparaison de la situation pré-éruptive avant le 22 mai 2021.L'analyse des spectrogrammes multi-annuels de la Figure 2.6 permettent de le visualiser également.

Les spectrogrammes à NYI (Figure 2.6) montre encore plus clairement ce changement de contenu fréquentiel entre le trémor pré-éruptif (avant le 22 mai 2021) et post-éruptif (après le 28 septembre 2021). Ce changement est très certainement attribuable à un changement de la source dominante et à l'absence du lac de lave. En comparaison du trémor continu pré-éruptif, cette nouvelle signature est plus énergétique mais également plus insta-

ble. Entre septembre et décembre 2021, les plus fortes amplitudes sont obtenues pendant les périodes d'éruption dans le cratère. Pendant environ un mois de fin octobre à fin novembre, aucune activité de surface n'était visible (pas de dégazage, pas d'infrason, pas d'anomalie thermique). Cependant, on peut observer que les enregistrements sismiques contiennent les signes d'une activité magmatique qui se maintient. Cette activité est cependant moins notable à KBTI (voir aussi la Figure 2.20). L'analyse des rapports d'amplitude entre NYI et KBTI (Figure 2.25d) est ainsi particulièrement instructif et témoigne d'une source sismique très locale et proche de NYI, constamment active tandis que les signes en surface indiquent une pause d'environ un mois. L'apparition d'un bassin de lave de manière plus persistante commence autour de mi-décembre 2021 (voir photo, Figure 2.25e). A l'augmentation des amplitudes sismiques aux deux stations s'ajoute une composante cyclique (une composante plus haute fréquence que les cycles diurnes d'origine humaine à KBTI). Ce signal sismique est en effet associé à des explosions acoustiques ("bursts") dont le nombre d'apparitions successives augmentent avec le temps comme Barrière et al. (2023b) l'ont mis en évidence (cf. Figure S9 de leur article).

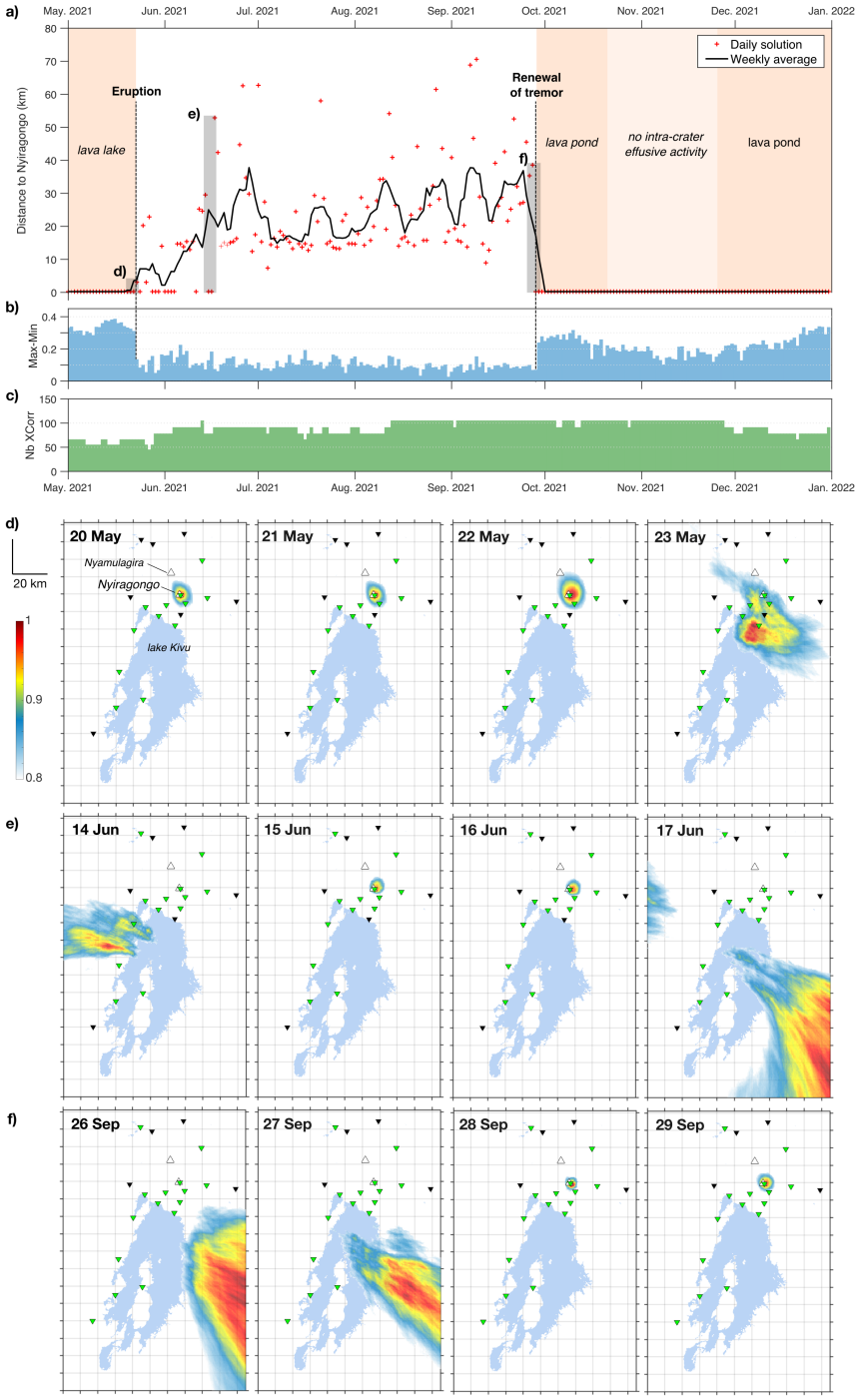

FIGURE 2.23: Zoom extrait de la Figure 2.21. **(a)** Distance minimale entre la région source du trémor la plus probable et le cratère du Nyiragongo obtenue à partir de cartes journalières de localisations. Les cartes correspondant aux périodes grisées sont représentées dans les sous-figures d, e et f dessous. **(b)** Max-Min : Évaluation de la qualité de la localisation en calculant l'écart entre le maximum et le minimum de la "réponse du réseau" pour chaque carte de localisation normalisée. **(c)** Nb XCorr : Nombre de paires de stations utilisées (c-à-d. nombre de corrélations croisées) pour localiser la source de trémor. **(d, e, f)** "Réponse du réseau" ("network response", représentée par l'échelle de couleur) indiquant la région source la plus probable pour 4 jours successifs autour de l'éruption de mai 2021 (**d**), 4 jours en juin 2021 lorsque le trémor a été la dernière fois localisé au Nyiragaongo (**e**) avant le retour d'une activité effusive au sein du cratère fin septembre 2021 (**f**). Sur chaque carte, les triangles inversés en vert représentent les stations disponibles/utilisées pour la localisation, ceux en noir sont les stations indisponibles.

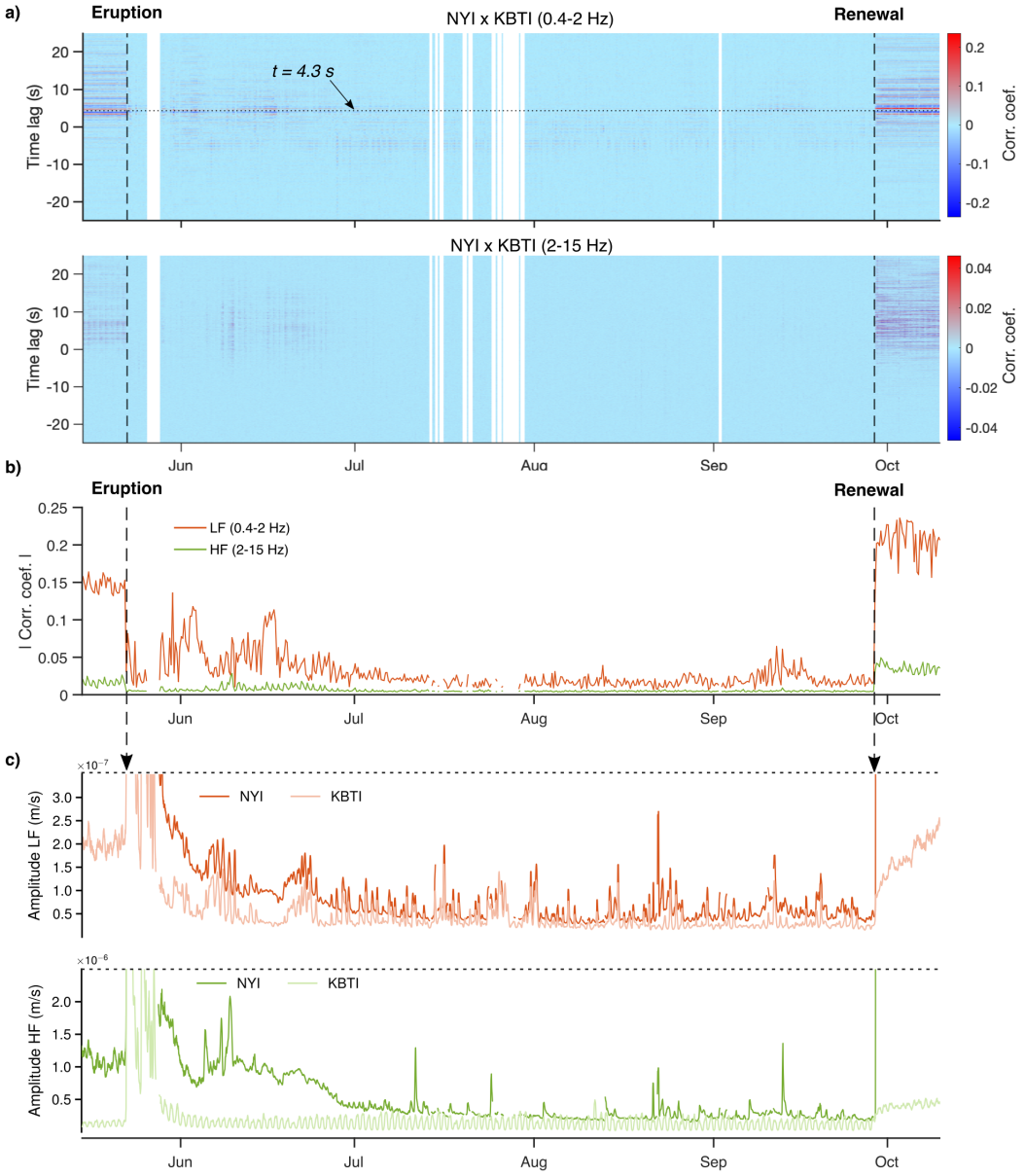

FIGURE 2.24: **(a)** Matrice de corrélation croisée entre les signaux aux stations NYI et KBTI. Représentation temps (month) vs. retard (time lag) à basses ($[0.4-2]$Hz) et hautes ($[2-15]$Hz) fréquences. Chaque colonne de la matrice représente une fonction de corrélation croisée pour deux signaux aux stations NYI et KBTI sur un intervalle de temps donné. **(b)** Valeurs absolues du coefficient de corrélation à basse (courbe rouge) et haute fréquence (courbe verte) extraites de **(a)** dans un intervalle de +/- 1 sec autour d'un retard de 4.3 sec. **(c)** Courbes d'amplitude sismique correspondantes à basses fréquences (NYI en rouge foncé, KBTI en rouge clair) et à hautes fréquences (NYI en vert foncé, KBTI en vert clair). Notez que les valeurs maximales (obtenues pendant la séquence éruptive et au retour de l'activité dans le cratère) sont coupées pour laisser apparaître les plus faibles variations pendant la période inter-éruptive.

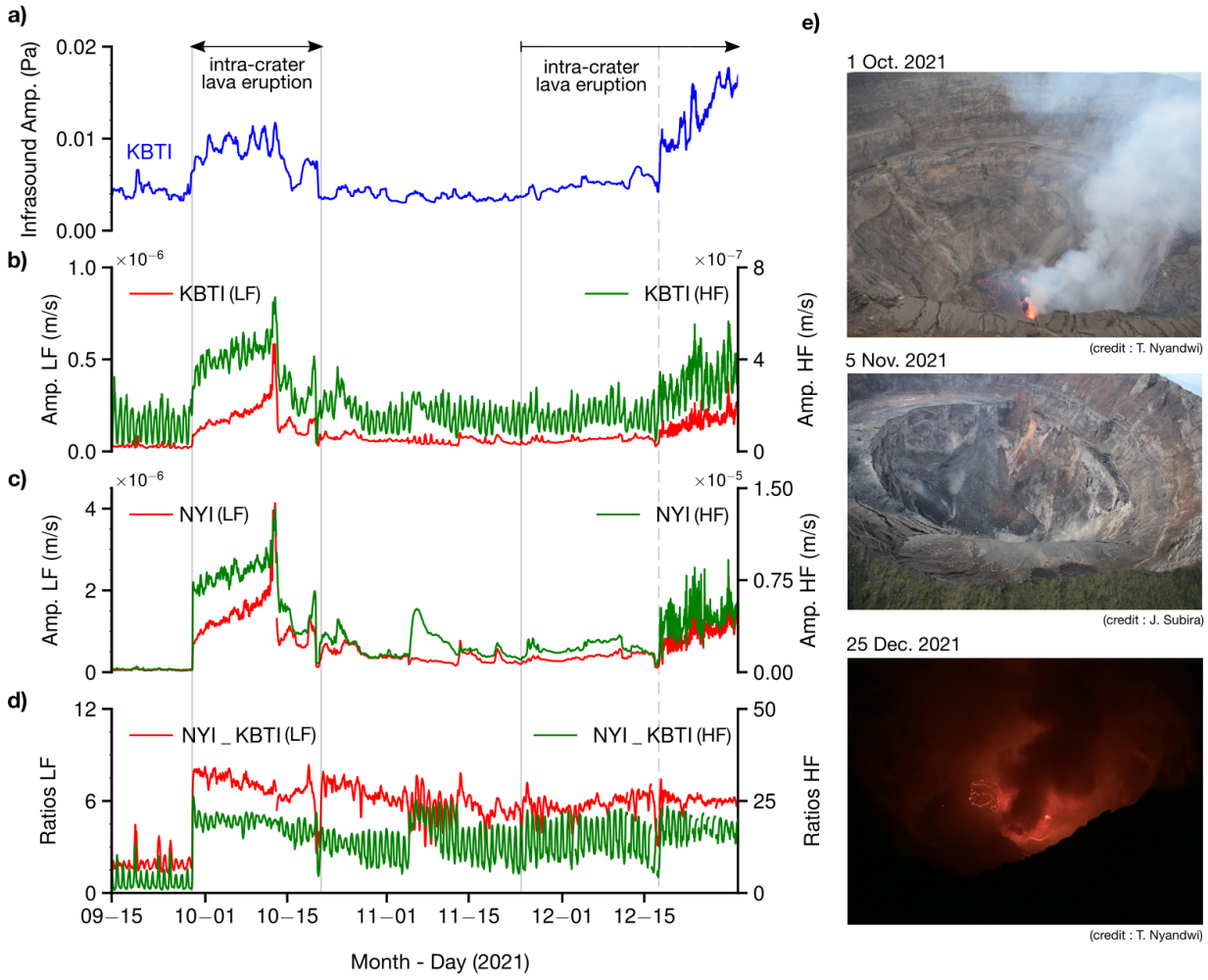

FIGURE 2.25: **(a)** Amplitude acoustique à la station de KBTI (bleu). **(b)** amplitudes sismique à basse (rouge) et à haute (vert) fréquence à la station de KBTI **(c)** amplitudes sismique à basse (rouge) et à haute fréquence (vert) à la station de NYI **(d)(e)** rapports d'amplitudes entre la station de NYI et KBTI à basse et à haute fréquence

2.7 Conclusion : Utilité et limites du calcul d'amplitudes sismiques dans les Virunga

Nous arrêtons notre interprétation de l'activité volcanique du Nyiragongo à cette dernière Figure 2.25 en ayant conscience encore du vaste potentiel des données analysées. A la lumière des éléments apportés ici, la richesse des signaux sismiques pendant cette période 2018-2022, et plus particulièrement l'année 2021, doit motiver de nouvelles explorations de ces enregistrements pour mieux comprendre la dynamique du volcan Nyiragongo. Les données du réseau KivuSNet s'arrêtent au 1er juillet 2022, et quelques mois avant pour des stations stratégiques comme NYI et KBTI. Au début de l'année 2022, il y a eu une diminution notable de l'amplitude du nouveau trémor du Nyiragongo (par ex., voir spectrogramme de la Figure 2.5). Jusqu'à la date d'écriture de ce manuscrit (2024), les rapports hebdomadaires produits par l'OVG [1] à destination des autorités et de la population locale laissent toutefois à penser que la baisse d'activité du début 2022 ne représentait qu'un état intermédiaire dans le processus de création d'un nouveau lac de lave au sommet du Nyiragongo. Nous avons, en effet, montré que les signaux sismiques sont primordiaux pour mieux comprendre la dynamique du système magmatique lors de cette reprise d'activité éruptive fin 2021, que les indicateurs de surface ne peuvent complètement capturer.

Au début de l'année 2022, une activité éruptive persistante est confirmée par des mesures satellitaires ou des observations visuelles au sommet. Les expéditions au sommet sont malheureusement devenues impossibles en raison de la détérioration du conflit armé dans la région du Kivu depuis 2022 [2]. Bien qu'un nouveau réseau maintenu par l'OVG ait pris le relai du réseau KivuSNet avec les mêmes caractéristiques (mêmes sites, transmission par réseau cellulaire, etc.), la maintenance des stations au nord de Goma est devenue rapidement problématique et l'efficacité de la surveillance du Nyiragongo s'en retrouve logiquement affaiblie. Dans ce contexte, le travail de ce chapitre a de multiples répercussions, à la fois sur une meilleure compréhension du volcan Nyiragongo dans des phases d'activité très différentes (lac de lave au sommet, éruption de flanc, intrusion magmatique majeure, absence d'éruption au sommet, reprise d'activité effusive) et sur des pistes de surveillance adaptées aux besoins/restrictions de l'OVG. Sur base d'analyses simples des amplitudes sismiques sur quelques stations appropriées, nous avons identifié plusieurs pistes de réflexions :

- Contrairement au travail pionnier de Taisne et al. (2011) dédié à la localisation de la source sismique, nous avons ici cherché à mettre en évidence l'importance de l'utilisation des amplitudes sismiques comme outils d'aide à la surveillance sismique pour un observatoire volcanologique. Cette approche qualitative d'analyse des amplitudes et de leurs rapports n'est pas nouvelle car Tan et al. (2019) l'abordent en utilisant la technique dite "red-flag SARA". Dans un contexte de surveillance par un observatoire, les auteurs l'utilisent pour suivre la migration de la sismicité au Piton de la Fournaise (Ile de la Réunion) et au mont Gede (Indonesie). Dans notre cas, nous devons, par contre, faire avec un nombre restreint d'instruments à proximité des volcans actifs et des stations aux caractéristiques de sites variées et parfois

[1] https://ovg-rdc.cd/bulletins-hebdomadaires-2/
[2] https://dtm.iom.int/reports/rdc-nord-kivu-evaluation-rapide-de-crise-m23-fevrier-2023-0

inadaptées (activité humaine, microséismes de lacs, effets de sites comme à BULE ou RSY, cf. chapitre 1). Précédemment dans le chapitre 1, nous avons pu démontrer le potentiel de la méthode avec l'utilisation de quelques paires de stations au sud et au nord des Virunga en détectant la fin d'éruptions dans le pit cratère de Nyamulagira. Il est à noter que pendant l'éruption de 2021, toutes les stations au nord du Virunga étaient inopérationnelles (problème d'accès, démantèlement du camp militaire de TGO), à l'exception de RGB.

- L'analyse des amplitudes sismiques et son interprétation en lien avec une analyse multi-paramètres déjà disponible dans la littérature sur la période 2018-2022 au Nyiragongo sont le résultat principal de ce chapitre 2. Ce travail met en lumière l'importance de confronter différents jeux de données pour mieux comprendre les processus en jeu. Pour chaque période où des signaux géophysiques montrent une évolution notable, confronter les amplitudes sismiques avec le niveau du lac de lave ou le niveau acoustique (infrason) a permis de mieux interpréter l'origine des variations observées. Une analyse conjointe avec une sismologie plus "classique" (détection d'évènements, localisation) est bien évidemment une plus-value non négligeable. Cependant l'attrait de la méthode SARA employée ici serait aussi de décoder l'activité magmatique du Nyiragongo si le nombre de stations est insuffisant pour d'autres analyses dites de réseau. L'intrusion magmatique ayant suivi l'éruption de flanc est un excellent exemple du potentiel d'une telle approche. En particulier la paire de stations KBTI-IDJ est tout à fait adapté à un tel scénario et permet une compréhension assez claire de la propagation du dyke.

- Il est très vite apparu évident dans ce chapitre 2 que les stations NYI et KBTI étaient quasiment primordiales à une surveillance appropriée du volcan Nyiragongo. Comme expliqué par Smittarello et al. (2022), lors de l'éruption du 22 mai 2021, seule la station du sommet a permis de détecter précisément le départ d'un signal anormal lié à l'intrusion de flanc vers 15:57 UTC couvrant le trémor de fond du lac de lave. Les séismes superficiels localisés par le réseau sont apparus à partir de 16:15 UTC. Moins de 40 min plus tard se produisaient les coulées de lave et la vidange du lac de lave. Dans ce travail, nous avons choisi d'utiliser des courbes d'amplitudes avec des filtres médians de plusieurs heures (pour la plus petite fenêtre) ne permettant pas de saisir ce genre de variations. Ce choix était dicté par le souhait de pouvoir comparer toutes les stations du réseau avec le même traitement, et en tenant compte des conditions de bruit ambiant importants non désirés à la plupart des stations. Il est clair que si un enregistrement au sommet est disponible en temps-réel, une analyse en continue de son amplitude et son contenu fréquentiel avec une fenêtre plus courte (de l'ordre de la minute) est hautement recommandée. Bien que plus bruitée et fortement affectée par l'activité humaine en journée, la station de KBTI est également une station clef. La possibilité d'y coupler des mesures infrasons est aussi un atout (Barrière et al., 2018, 2023b). Les derniers résultats fin 2021 pour la reprise de l'éruption au sommet confirment également l'importance de ces deux stations.

- Actuellement, la région est confrontée à une perte de la quasi-totalité des stations sismiques autour des volcans en raison d'un conflit armé en cours au moment de la rédaction de cette thèse (2024). Les stations stratégiques évoquées précédemment (NYI et KBTI), ont été démontées, ce qui pose un sérieux problème pour la surveillance des volcans par l'OVG. Les stations actuellement disponibles pour surveiller les volcans sont RSY, BULE et GOM. Comme analysé dans les deux premiers chapitres de cette thèse ou dans la littérature (e.g., Barrière et al., 2017, 2019), ces trois stations peuvent présenter des limites pour un suivi continu de l'activité volcanique: L'axe RSY-BULE est caractérisé par une forte amplification locale liée à la géologie complexe de cette zone; les enregistrements à GOM et BULE sont fortement influencés par les microséismes du lac Kivu; la station de GOM est la plus touchée par le bruit anthropogénique au dessus de 2 Hz associé à sa localisation en pleine ville.

Part II

Seismological models and seismicity patterns

Chapter 3

Earth's seismic velocity structure of the Kivu Rift

THe location of an earthquake is fundamental in seismological studies, serving as the cornerstone of seismic monitoring operations in volcanic areas alongside the analysis of the continuous seismic amplitude as performed in Chapters 1 and 2. However, the accuracy of such determinations is heavily reliant on various factors, including station coverage and observation quality, and the inferred ground velocity structure. Particularly in regions like the Kivu Rift and Virunga Volcanic Province (VVP), the ground velocity structure is poorly known and significantly influences earthquake location reliability. The recent instrumental improvement between 2013 and 2022 (i.e., the KivuSNet network; Oth et al., 2017, see also Chapter 2), offers promise for enhanced seismic analysis and this Chapter presents one of the later, a new 1D (i.e., layered) local velocity model developed for improving hypocenter locations in the region.

3.1 Brief bibliographic overview and motivation

Previous seismological studies over the past decades have consistently highlighted the challenges stemming from inadequate station coverage and poorly constrained seismic velocity structures in the Kivu rift region, impeding the accurate determination of earthquake locations. For moderate to large earthquakes, global solutions provided by international agencies are typically derived from teleseismic phase arrivals utilizing the iasp91 reference velocity model (Kennett & Engdahl, 1991), e.g.:

- USGS, https://www.usgs.gov/programs/earthquake-hazards;
- GEOFON, https://geofon.gfz-potsdam.de.

During the 2002 eruption crisis, for instance, the USGS supplied earthquake locations for major events, as no local solutions were available due to the operation of only two analog seismic stations in the region (Allard et al., 2002; Kavotha et al., 2002; Komorowski et al., 2002). Until 2004, seismic monitoring infrastructure, in collaboration with international partners, remained limited to a few temporary or permanent analog stations (Hamaguchi et al., 1992; Hamaguchi et al., 1982). Between 2004 and 2012, the installation of 7 digital stations (Pagliuca et al., 2009) marked the establishment of the first digital network of the GVO. However, technical issues such as telemetry dropouts, digitizer failures, loss of data on local storage lead to numerous data gaps that hindered extensive utilization of these data for seismicity or volcanic activity studies in the Virunga Volcanic Province (e.g. studies about Nyamulagira's 2006 and 2010 eruptions by T. Mavonga et al., 2010; Smets, D'Oreye, Kervyn, et al., 2014). Additionally, a temporary network comprising 8 broadband seismometers was deployed on the Rwandese side east of the lake Kivu, for eight months between March and November 2012, offering valuable but incomplete insights into local seismicity due to spatial and temporal coverage limitations (Wood et al., 2017).

During that period, some studies (D'Oreye et al., 2011; Kavotha et al., 2002; T. Mavonga, 2007; T. Mavonga et al., 2006) used a 1D model for P- and S-waves based on earlier velocity structure investigations by Bonjer et al. (1970) and Bram (1975) relying on the analysis of long-period body waves from distant earthquakes. T. Mavonga et al. (2010) further refined a P-wave velocity model using the receiver-function method (Ammon et al., 1990) based on 46 teleseismic recordings between May 2004 and December 2007 with two broadband stations deployed in the VVP. They inferred the crust-mantle transition zone at about 30 to 40 km depth, indicating potential low velocity zones but providing a simplified model for the Virunga area with velocity increasing with depth. Their final model described a simplistic structure between 0 and 30 km depth, comprising a superficial layer down to 4 km depth (with velocity 5.4 km/s) overlying a thick layer (with velocity 6.4 km/s). Since 2010, this velocity model has been routinely employed by GVO for seismicity monitoring in the region (i.e. epicentral locations).

The development of the KivuSNet network started with the deployment of the first station at GVO's facilities in 2013, progressing towards a permanent and telemetered network between October 2015 and June 2022, see Figures 2.3, 2.4, Chapter 2). This new ground instrumentation opened the door to an unprecedented understanding of the seismicity patterns in the region, particularly focusing on the volcanic activity in the VVP

(Barrière et al., 2017, 2018, 2019, 2022; Oth et al., 2017; Smittarello et al., 2022; Subira et al., 2023). The Figure 3.1 displays both the U.S. Geological Survey (USGS) catalog events for the period 1977–2012 and seismicity maps during the first two years of Kivus-Net operation (August 2014 and June 2016) as provided by Oth et al. (2017). Hypocenter were determined using the Mavonga et al. velocity model, and details about the location procedure (i.e., automatic algorithm for picking the seismic phases, computer method for calculating hypocenter solutions) can be found in the referenced article. Although preliminary, these maps shed light about tectonic and volcanic seismicity patterns in the region and evidenced the benefits of the new local network in significantly enhancing the detection of small to moderate earthquakes and delineating key seismically active zones.

Once a sufficient number of stations have recorded data over a significant period, the development of a new, more accurate seismic velocity model becomes essential for various applications such as seismic event location and focal mechanism determination. At local scale, a 3D velocity model would be ideally suited for complex geological zone with variable topography and strong lateral variation of velocities (Husen et al., 2003; Lomax et al., 2001). However, as emphasized by Kissling (1988), "3D Earth models may still oversimplify the complex, in most parts unknown, velocity structure of the Earth" and the use of 3D velocity models may not necessarily lead to improve earthquake location solutions compared to 1D models. Moreover, for the studied region (i.e., Lake Kivu region and VVP), deriving a robust 3D model would notably require a denser spatial distribution of stations (see Figure 2.3, Chapter 2). Therefore, as a first step before potential further developments in the region, enhancing the existing 1D velocity models appears to be the most crucial task.

In this regard, an interesting approach is the "1D minimum model" introduced by Kissling (1988) and applied as new reference 1D velocity model in numerous volcanic and tectonic settings worldwide to improve earthquakes locations (e.g, Costa Rica: Quintero and Kissling, 2001; Mayotte : Lavayssière, Crawford, Saurel, et al., 2022; Guatemala : Brill et al., 2018; Campania-Lucania region (Italia): Matrullo et al., 2013).
The concept of 1D minimum model was originally developed to be used as starting model for local earthquake tomography, the final 3D model obtained after inversion being a perturbed version of the initial (layered) minimum model, which is a 1D tomographic solution (Kissling et al., 1994). The 1D minimum model minimizes data misfit and provides a suitable velocity model for absolute routine earthquake location (Husen et al., 2011) (where "absolute location" means each hypocenter determination is performed independently, as in routine operations). Furthermore, station correction terms (i.e., delays to add/subtract to the observed arrival times) can be estimated in the inversion process to compensate for near-surface and large-scale heterogeneity in the crust not considered in the 1D solution (Husen et al., 2011). Seismic velocities of the 1D minimum model can thus be interpreted as average velocities within a depth range (i.e., layers) sampled by the selected seismic ray paths (Kissling, 1988). Seismic rays are conceptually similar to optical rays based on ray theory deduced from Fermat's principle (Aki & Richards, 2002), providing a simplified high-frequency approximation of seismic wave propagation suitable for most seismological applications relying on travel time observations (Rawlinson et al., 2010). It is important to note that advanced travel time tomography studies consider more realistic structural sensitivities of the data, including finite-frequency effects

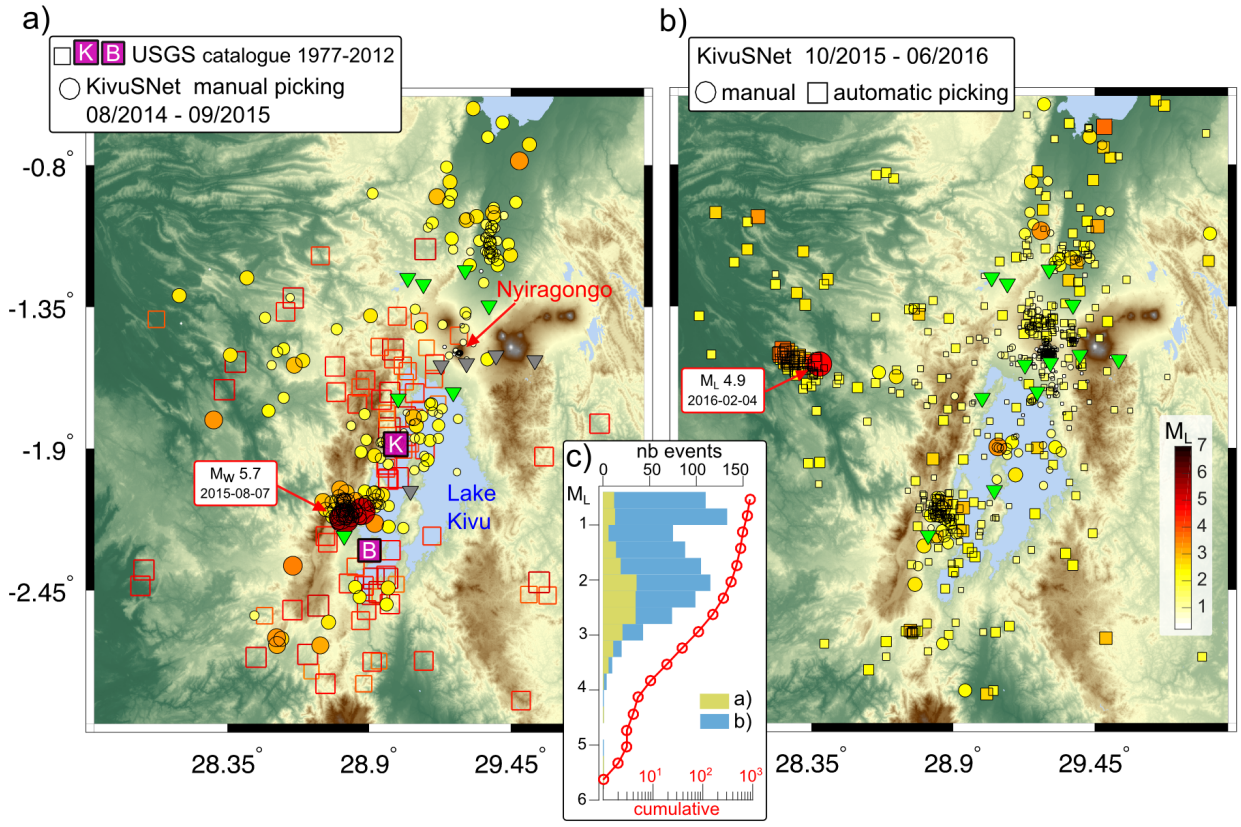

FIGURE 3.1: Seismicity maps for the first two years of KivuSNet operation from Oth et al. (2017). **(a)** U.S. Geological Survey (USGS) catalog events for the 1977–2012 time period and the seismicity detected and located using KivuSNet between August 2014 and September 2015 (212 events have been manually picked and located during this 13-month time period). Active seismic stations during this time period are indicated as green inverted triangles, whereas not-yet-installed stations are shown as gray inverted triangles. The two most significant events prior to KivuSNet deployment are the 2002 Mw 6.2 Kalehe (K) and 2008 Mw 5.9 Bukavu-Cyangugu (B) events. The location of the 2015 Mw 5.7 Katana earthquake and its detected aftershocks is indicated by a red arrow. **(b)** Seismicity detected and located using KivuSNet from October 2015 to June 2016, which corresponds to the time period since the full development of the current network. Six hundred and seventy events have been automatically detected and located during this 9-month time period, of which 198 were manually repicked and relocated. The location of the 2016 ML 4.9 Walikale event is indicated by a red arrow. **(c)** Event count histograms relative to ML for the two indicated time periods (only KivuSNet results, no USGS catalog data). The red circles and dotted lines represent the cumulative number of events with magnitudes larger or equal to the given ML value on log scale.

e.g. Dahlen et al., 2000), which are ignored in standard ray theory and not discussed in this thesis.

Preliminary results obtained before 2019 (Oth et al., 2018), although highly promising, suffered from several limitations at that time, primarily:

- Insufficient well-locatable earthquakes into the VVP (typical volcanic seismicity, i.e., low SNR, long-period events). A longer observational period was required.

- Inadequate station coverage around Lake Kivu, which does not allow for sufficient high-quality observations of the numerous earthquakes in this area. More seismic stations were necessary.

The period 2019-2021 has been a game-changer (see also Chapter 2) and served as the motivation of this Chapter for several reasons:

- Three additional years of high-quality data were collected during which many stations were fully operational.
- Two additional permanent stations, KALEH, NYAB, were installed in 2019 on the shore of Lake Kivu by the GVO and integrated to the KivuSNet framework (with identical instrumentation and acquisition system).
- The intense seismicity recorded during the 2021 flank eruption associated with a shallow dyke intrusion was well recorded by the KivuSNet and accurately located within the network (Smittarello et al., 2022).

The calculation of a 1D minimum model requires at least several hundred of events with high-quality travel-time observations (i.e., P and S-wave phases) located within the network of stations (Kissling et al., 1994). Over a time period lasting for 6 years (October 1, 2015 - October 1, 2021), hundreds of "good candidates" meeting these essential criteria were detected and selected. The following sections outline the successive steps we followed to estimate a new 1D local velocity model for the Kivu rift region and Virunga volcanic province by solving the coupled hypocenter-velocity inverse problem.

3.2 The coupled hypocenter-velocity inverse problem

Before delving into the methodology and results presented in the subsequent sections 3.3, 3.4, 3.4.2 and 3.5, we address important preliminary considerations about the coupled hypocenter-velocity inverse problem. For a given seismic event in the simplest medium (i.e., homogeneous with constant seismic wave velocity V), the arrival time t at a seismic station located in space at a point (x, y, z) can be expressed as :

$$t = t_0 + u\sqrt{[(x - x_0)^2 + (y - y_0)^2 + (z - z_0)^2]}, \tag{3.1}$$

where t_0 is the origin time, (x_0, y_0, z_0) are the spatial coordinates of the hypocenter and u is the slowness defined $u = 1/V$. From equation 3.1 it becomes evident that even in the simplest possible medium, a variation in the spatial position of the source leads to a non-linear change in t. In a more realistic heterogeneous medium, the arrival time can be generalized as (e.g.Lomax et al., 2009):

$$t = t_0 + \int_{r_0(s)} u(r_0)\, ds, \tag{3.2}$$

where $r_0(s)$ is a point at distance s along ray path r_0 between the source and the station. Using an *a priori* velocity model, seismic rays can be traced between a trial source location and the stations to obtain theoretical (or calculated) arrival times. This forward problem (i.e., finding t) can be formulated using the general function F, which depends on the vector of hypocenter parameters $\boldsymbol{h}$ (spatial coordinates and origin time):

$$t_i = F_i(\boldsymbol{h}), \tag{3.3}$$

where t_i is the observed arrival time for the i-th phase. The earthquake location, which is an inverse problem, involves finding $\mathbf{h}$ as the solution that minimizes the difference between the observed and calculated arrival times. This is a non-linear problem that cannot be solved by simple analytical methods. In routine operations, seismic analysts at GVO use the SEISAN software, a suite of computer programs designed for various seismological applications (Havskov et al., 2020). After manually detecting events and picking seismic phases (i.e., the observed arrival times t_i), they use the main location program implemented in SEISAN, called HYPOCENTER (Lienert & Havskov, 1995). HYPOCENTER is part of the family of linearized and iterative methods that were primarily developed in the past decades when computational resources were limited. These methods remain widely used for routine locations at observatories because they are not computationally demanding (Havskov & Ottemoller, 2010). HYPOCENTER is linearized in the sense that it solves a non-linear problem using linear algebraic methods and is iterative because the inversion process is iterated until a convergence criterion is reached. The linearization is possible if the true hypocenter $\boldsymbol{h}$ is assumed to be close to a first guess estimate $\boldsymbol{h_0}$ so that the corrections (or adjustments) in travel times needed to reach the best solution can be considered small, such that (e.g. Abril, 2018):

$$\boldsymbol{h} = \boldsymbol{h_0} + \delta\mathbf{h} \tag{3.4}$$

Then, the general function F can be expanded as a Taylor Series, after neglecting the second and higher terms:

$$F_i(\boldsymbol{h}) \approx F_i(\boldsymbol{h_0}) + \frac{\delta F_i}{\delta h_j}\delta h_j \tag{3.5}$$

The residual between the observed arrival time and the estimated arrival time can be written as :

$$\delta t_i = F_i(\boldsymbol{h}) - F_i(\boldsymbol{h_0}) \approx \frac{\delta F_i}{\delta h_j}\delta h_j \tag{3.6}$$

Assuming a local linear approximation to F, the inverse problem is given by :

$$\delta t_i = F_{ij}\delta h_j, \tag{3.7}$$

where $F_{ij} = \delta F_i/\delta h_j$ is the adjustment of the calculated i-th arrival time (t) related to the j-th hypocenter parameter (origin time and spatial coordinates). Thus, the observed and the calculated (predicted) arrival-times are linearly related to the change of the model. This problem can be written as the explicit linear equation in matrix form:

$$\boldsymbol{d} = \boldsymbol{G}\boldsymbol{m}, \tag{3.8}$$

where $\boldsymbol{d}$ is the set of data (vector of residual arrival times), $\boldsymbol{m}$ is the set of model parameters (correction vector in location and origin time) and $\boldsymbol{G}$ is the forward modeling operator (matrix form) relating changes in travel times to changes in location (Havskov & Ottemoller, 2010). The earthquake location poses an over-determined problem since the number of data exceeds the number of unknowns. We must consider errors that cannot be explained by adjustments of the unknown parameters (e.g., incorrect timing of observed arrival times, use of wrong velocity model, linear approximation). The error vector is defined as $\boldsymbol{e} = \boldsymbol{d} - \hat{\boldsymbol{d}}$ between observed data $\boldsymbol{d}$ and predicted data $\hat{\boldsymbol{d}} = \boldsymbol{G}\hat{\boldsymbol{m}}$ from the estimated model $\hat{\boldsymbol{m}}$:

$$\boldsymbol{d} = \boldsymbol{G}\boldsymbol{m} + \boldsymbol{e} \tag{3.9}$$

Solving this linear inverse problem can be done with the frequently used least-squares method consisting in minimizing the total misfit error E defined as the squared Euclidean norm of vector $\boldsymbol{e}$:

$$\begin{aligned} E &= \boldsymbol{e}^T\boldsymbol{e} \\ E &= (\boldsymbol{d} - \boldsymbol{G}\hat{\boldsymbol{m}})^T(\boldsymbol{d} - \boldsymbol{G}\hat{\boldsymbol{m}}), \end{aligned} \tag{3.10}$$

where the superscript T means transposed. Minimizing the error misfit with respect to the model parameters leads to the generalized inverse solution written as:

$$\boldsymbol{G}^T\boldsymbol{d} - \boldsymbol{G}^T\boldsymbol{G}\hat{\boldsymbol{m}} = 0 \tag{3.11}$$

The estimated model found after inversion of the square matrix $\boldsymbol{G}^T\boldsymbol{G}$ is the least squares solution:

$$\hat{\boldsymbol{m}} = [\boldsymbol{G}^T\boldsymbol{G}]^{-1}\boldsymbol{G}^T\boldsymbol{d} \tag{3.12}$$

Given a first-guess hypocenter, iterative application of Equation 3.12 to minimize the total misfit error allows us to obtain a solution to the earthquake location problem, which forms the basis of all linearized least-squares solutions to this problem (Lienert et al., 1986).

Kissling et al. (1994) and Kissling (1988) developed the VELEST software (Kissling et al., 1995a) for solving the location problem (similar to HYPOCENTER) combined with the estimation of the velocity model. Unlike earthquake location, determining the velocity model poses an under-determined problem because the continuous (true) medium

must be discretized with a finite number of velocity parameters. Consequently seismic travel-time tomography, which involves determining the earthquake locations and the velocity model, is referred to as a mixed-determined, non-linear problem. Similar to the single earthquake location problem, a linear relationship can be approximated between the travel time residuals and the corrections to the hypocenter/velocity parameters after applying 1st-order Taylor series expansion (Kissling et al., 1994). The final linear system of equations can be expressed in matrix notation as (Kissling et al., 1994):

$$\boldsymbol{t} = \boldsymbol{A}\,\boldsymbol{d} + \boldsymbol{e} = \boldsymbol{H}\,\boldsymbol{h} + \boldsymbol{M}\,\boldsymbol{m} + \boldsymbol{e}, \tag{3.13}$$

where $\boldsymbol{t}$ is the vector of travel time residuals;
$\boldsymbol{A}$ is the matrix of all partial derivatives;
$\boldsymbol{e}$ is the vector of errors;
$\boldsymbol{d}$ is the vector of hypocenter and model parameter corrections;
$\boldsymbol{H}$ is the matrix of partial derivatives of travel time with respect to hypocenter parameters
$\boldsymbol{h}$ is the vector of hypocenter parameter corrections;
$\boldsymbol{M}$ is the matrix of partial derivatives of travel time with respect to velocity model parameters
$\boldsymbol{m}$ is the vector of velocity model parameter corrections;

Neglecting the velocity term ($\boldsymbol{M}\,\boldsymbol{m}$) reduces to the earthquake location problem as solved by HYPOCENTER. Neglecting the hypocenter part ($\boldsymbol{H}\,\boldsymbol{h}$) leads to the determination of the velocity model. However, unless we already have the true hypocenter parameters, the unbiased determination of the velocity model requires the simultaneous inversion of both hypocenter and velocity parameters (Thurber, 1992). An exact solution to the coupled hypocenter-velocity problem (eq. 3.13) being not available, this linearized inverse problem is solved in VELEST using the damped least squares solution defined as (e.g. Menke, 2018):

$$\hat{\boldsymbol{m}} = [\boldsymbol{G}^T\boldsymbol{G} + \lambda\boldsymbol{I}]^{-1}\boldsymbol{G}^T\boldsymbol{d}, \tag{3.14}$$

where $\boldsymbol{I}$ is the identity matrix and λ is the damping parameter, which tunes the trade-off between the adjustments to the model and the minimization of the misfit. At this point, it is important to emphasize the non-uniqueness of solutions to such geophysical inverse problems, and identifying potential trade-off between hypocenter parameters and velocity models remains challenging (Kissling et al., 1994). The 1D minimum velocity model (and hypocenter locations) derived from the selected dataset (section 3.3) will be regarded as the best solutions that satisfy minimal misfit between observed and calculated seismic wave arrival times (section 3.4). Achieving a successful result leading to a robust (global) minimum 1D model rather than local minima in the solution space necessitates appropriate dataset selection and an extensive trial-and-error process involving multiple inversions. Validation tests will be conducted to ensure the stability of this solution (section 3.4.2) and to assess the improvement of hypocenter locations in the region (section 3.5).

3.3 Dataset selection and characteristics

We utilized SEISAN as the software framework for detecting seismic events, picking seismic phases (P and S) and computing the 1D minimum model. Seismic event detection was performed using the traditional short-term average / long-term average (STA/LTA) detection algorithm implemented in the program CONDET. Manual picking of seismic phases followed the principles outlined by Bormann (2002) and Havskov and Ottemöller (1999) for local seismic events. Preliminary locations were obtained with the HYPOCENTER routine using the Mavonga et al. routine velocity model ((T. Mavonga et al., 2010)) after classifying candidate events in a database and reading them with the EEV command. In the final stage, after selecting the best events suitable for the inversion process, the VELEST software was called in SEISAN through the command VELMENU (refer to the user manual of SEISAN for more details about the different commands mentioned).

Following other research studies using VELEST (Brill et al., 2018; Lavayssière, Crawford, Saurel, et al., 2022; Matrullo et al., 2013; Quintero and Kissling, 2001), we established standard criteria for selecting a robust dataset. Each selected event must have a minimum of seven clear (i.e., impulsive onset) P-arrival time measurements, an azimuthal gap of less than 180°, and a maximum RMS (root-mean-square) error of 1 sec (i.e., the misfit between observed and calculated travel times). The first criterion ensures enough high-quality observations, the second criterion ensures the event is located within the network, and the third criterion indicates that the preliminary solution using HYPOCENTER and Mavonga et al. model will be considered as the first correct guess of the true solution. The final dataset, comprising 410 events between October 2015 and September 2021, is plotted in Figure 3.2. In this figure, seismic rays are traced for an homogeneous medium as straight lines from the source to the station. We can visualize the region covered by the data and anticipate an average 1D minimum model encompassing the northern and western parts of Lake Kivu and the VVP around Nyiragongo and Nyamulagira volcanoes. The depths investigated range mostly from 0 to 15 km below sea level. A total of 4156 P-phase and 1254 S-phase arrival times were manually picked.

Based on the spatial distribution of the events, the dataset can be divided into three main spatial clusters:

- VVP's events: They are located beneath both active volcanoes and are related to magmatic activity. They are less numerous due to their low magnitude and most of them have a low signal-to-noise ratio (SNR), making it challenging to pick arrival times. We selected events with clear onsets only. Observing emerging onset of seismic phases in volcanic regions is common and can be either due to source mechanisms, path effects or both (Bormann, 2012).

- Lake Kivu's events: These events occur in the western part of the Lake Kivu basin over the full period 2015-2021. They are typical of "traditional tectonic events", in contrast with the volcanic events previously mentioned. They reflect active faulting deformation in the region, driven by rift dynamics (Oth et al., 2017; Smets et al., 2016).

- 2021 eruption's events: These events are located between Nyiragongo and the north of the Lake Kivu basin, near the city of Goma. They are the result of tectonic and

magmatic activity during the shallow dyke intrusion (a few km deep) extending from Nyiragongo to Lake Kivu over several days after the onset of the short 6-hours flank eruption (Smittarello et al., 2022).

Figure 3.3 displays each event's number with respect to its origin time, highlighting the numerous seismic events selected during and after the 2021 Nyiragongo's eruption. Three temporal subdatasets can be defined :

- Subdataset 1 "pre-eruptive": 150 events selected within a 5-year period between October 2015 and February 2021, encompassing VVP's and Lake Kivu's events.
- Subdataset 2 "syn-eruptive/dyke": 161 events between 22 May 2021, 22:42 UTC and 31 May 2021, 21:43 UTC. These events are 2021 eruption's events and Lake Kivu's events related to changing crustal stress field conditions. (Smittarello et al., 2022).
- Subdataset 3 "post-eruptive": 89 events between 1 June 2021 and 21 September 2021. These are tectonic, Lake Kivu's events occurring mostly in the northern part of Lake Kivu and still related to the past intrusive event.

The histograms depicted in Figure 3.4 offer an overview of the database statistics including the number of P and S waves per event and per station, azimuthal gap, RMS error, distribution of hypocenters with depth. There are significantly fewer observations of S-phase due to the difficulty of picking clear onsets in the coda of the P-phase for local events with small $S-P$ arrival times (i.e., the delay between P and S-phase arrivals). Similar to other studies where the database for S-phase is insufficient for deriving a robust model (e.g. Brill et al., 2018; Matrullo et al., 2013), this study primarily focuses on the determination of a V_P model only. However, we can determine a V_S model *a posteriori* using a constant V_P/V_S ratio derived from available P and S picks.
Following the methodology of Matrullo et al. (2013) and Romano et al. (2013), we compute a modified Wadati diagram (Figure 3.5) to determine the average ratio between P-wave velocity (V_P) and S-wave velocity (V_S). This approach also allows to identify potential outliers in observed arrival times. In the standard Wadati diagram for a single event, the relationship between $S-P$ arrival times versus P arrival times is plotted, where the origin time t_0 is given at the intercept with the P-arrival axis, and the slope is equal to (V_P/V_S-1) (Havskov & Ottemoller, 2010). The modified Wadati diagram enables the consideration of all events simultaneously such as :

$$\frac{t_{Pi}-t_{Pj}}{t_{Si}-t_{Sj}}=\frac{(x_i-x_j)/V_P}{(x_i-x_j)/V_S}=\frac{V_P}{V_S} \tag{3.15}$$

where t_P and t_S are the arrival times for P and S waves at station pair i and j, x_i and x_j are the hypocentral distances at stations i and j. Thus, the modified Wadati diagram is independent of the origin time and the slope of this linear relationship obtained for all events gives the average V_P/V_S ratio. For the region sampled with the selected dataset we obtain $V_P/V_S=1.71$, which is close to the global average ratio of 1.73 within the upper crust as defined in the reference (global) iasp91 model (Kennett & Engdahl, 1991). Higher V_P/V_S ratio can be observed in volcanic regions (e.g., $1.85-1.95$, Hua et al., 2019; H. Zhu, 2018), where partial melt may be an important contributions to slow V_S. However, the average V_P/V_S ratio of 1.71 in the Kivu rift at crustal depth is not surprising, considering that

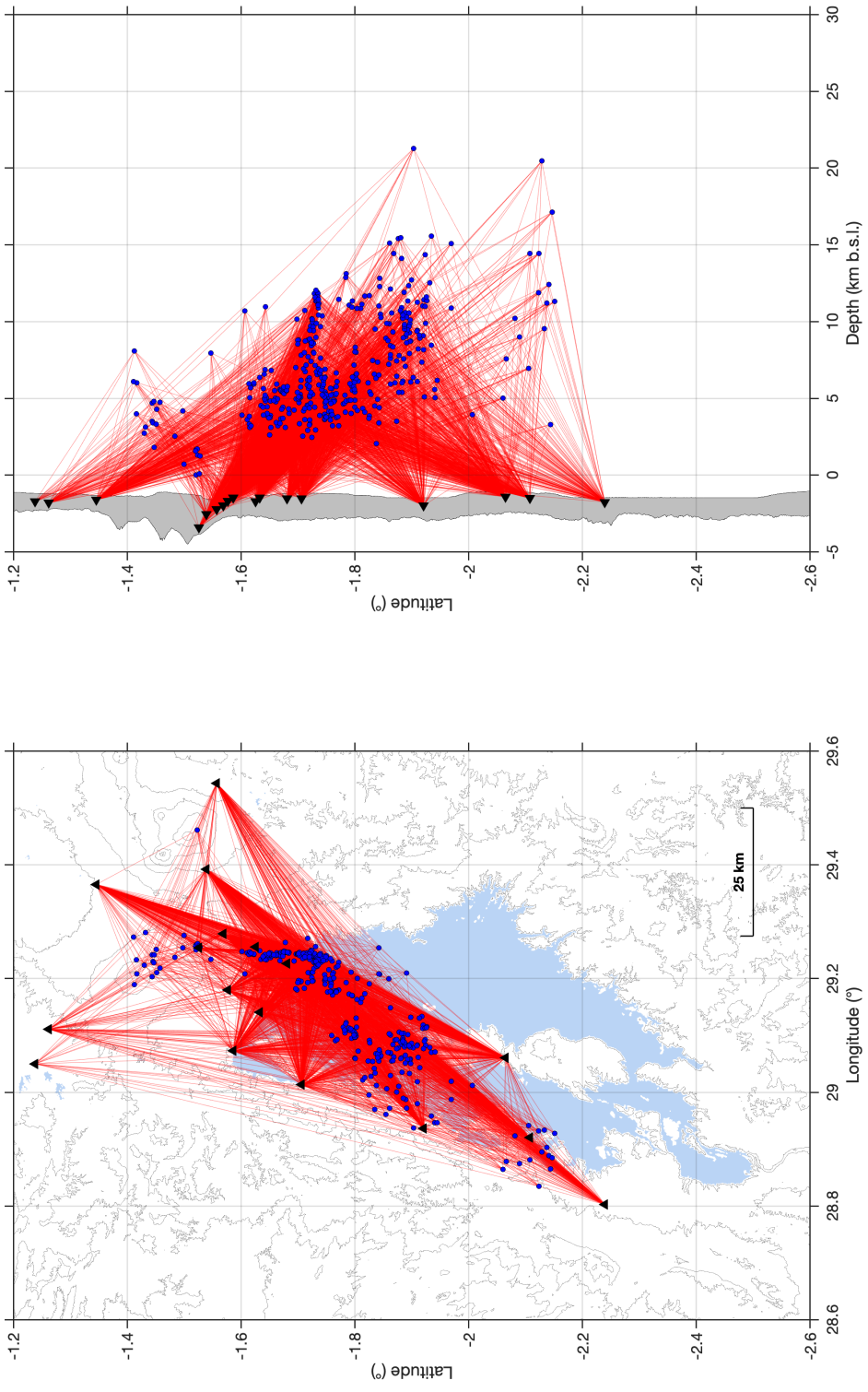

FIGURE 3.2: Map and depth view of the spatial distribution of 410 events (blue circles) selected for the inversion of travel-time seismic observations. Direct ray paths from events to stations are plotted as red lines.

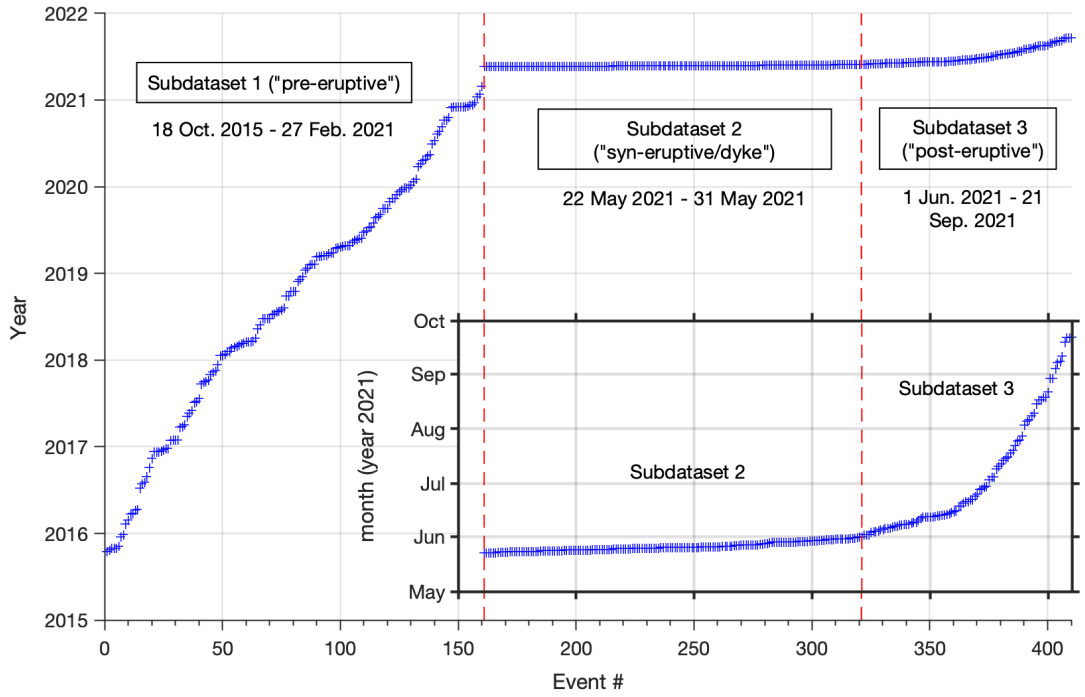

FIGURE 3.3: Temporal distribution of 410 events selected (blue crosses) for the inversion of seismic travel-time observations. The two subdatasets ("2021 eruption" and "post-eruptive") gathering events located in 2021 after the May 22th eruption represent about 60 % of the full dataset.

relatively few selected earthquakes are located beneath the active volcanoes Nyiragongo and Nyamulagira (see Figure 3.2).

The fit of data is excellent with a coefficient of determination $R^2 = 0.99$ and a root-mean-square of residuals $RMSE = 0.25s$. No clear outliers were detected. Additional evaluation of the quality of the P-phase readings could be conducted. For instance, we tested the algorithm developed by Antunes et al. (2020), adapted from the work by Diehl et al. (2009) for estimating the uncertainty interval around the manual picks based on signal-to-noise ratio criterion (SNR). Weight can then be assigned to each picks, classified from 0 (best) to 5 (worst), and integrated into the inversion process of VELEST to mitigate the effects of bad picks. We found that most of the picks belongs to the best class, and inversion tests performed with or without including weights yielded similar result. Therefore, the analysis presented in this thesis was conducted with all available manual P-phase readings (without weight) from up to 17 KivuSNet stations (Figure 3.2). Unfortunately, despite their strategic locations, we do not have good quality observations for stations TGO and MUSK operational prior to 2020, which are excluded from the inversion process (see figures 2.3 and 2.4 in Chapter 2 for the location of these two stations). Nonetheless, they will be integrated at the end to derive dedicated station correction terms (see section 3.6). Finally, we need to choose a reference station for the calculation of station correction terms, which means the delay for this station will be zero. Following recommendations by Kissling et al. (1994), the station KBTI (on the southern flank of Nyiragongo) is chosen because it is located in the central part of the network, has good data availability for the period 2015-2021, and provides good quality picks for events located either in Lake Kivu

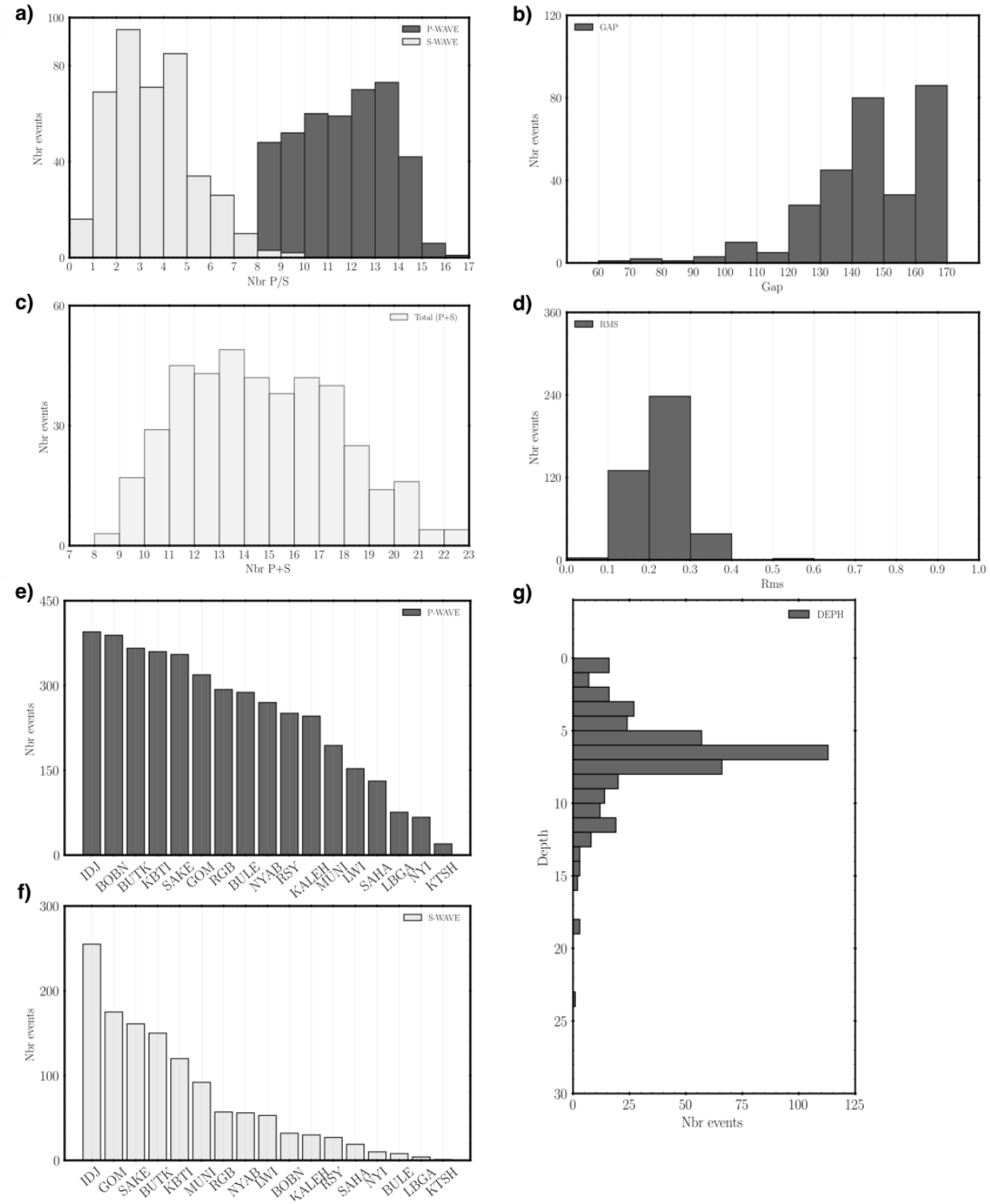

FIGURE 3.4: Database statistics. **(a)** Number of P- and S-wave phase observations per event. **(b)** Azimuthal gap (in °). **(c)** Total number of P- and S-wave phases per event. **(d)** Event's RMS error (in s). **(e)** Number of P-phase observations per station. **(f)** Number of S-phase observations per station **(g)** Depth distribution per events (in km).

or in the volcanic area.

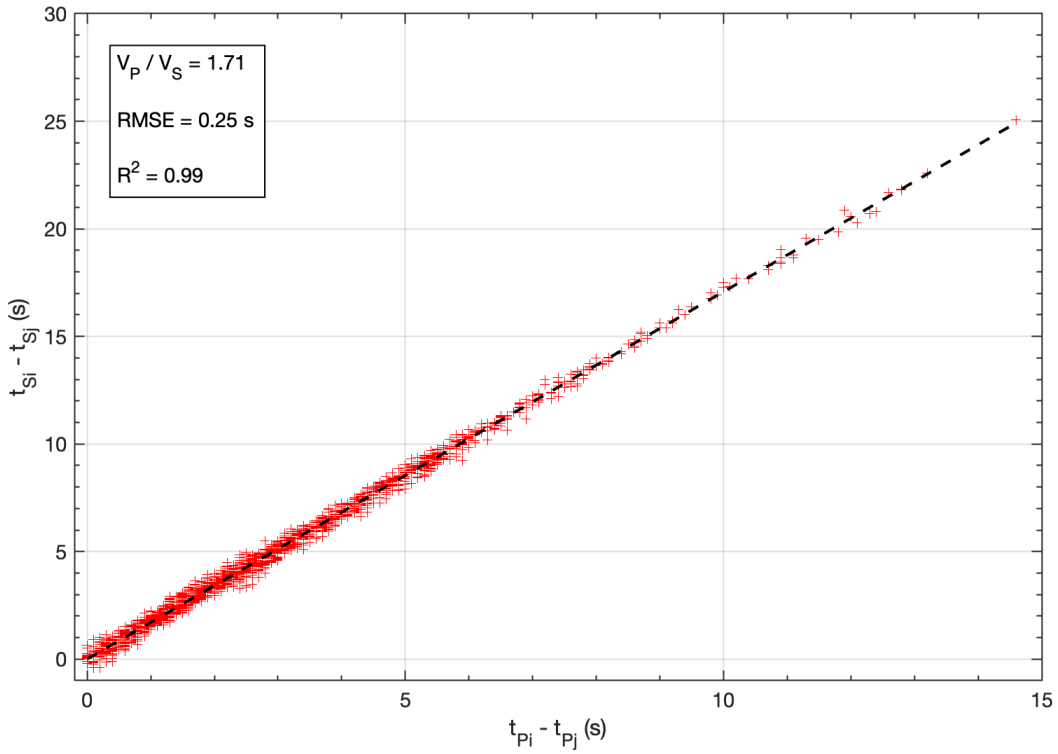

FIGURE 3.5: Modified Wadati diagram with corresponding statistics : V_P/V_S ratio (slope), $RMSE$ (Root-Mean-Square Error) and R^2 (see text).

3.4 Kivu 1D: A new local minimum model

4156 P-wave picks from 410 seismic events were used as input for the inversion. The P-wave minimum velocity model with corresponding station delays was built constructed following the procedure described in the VELEST user manual (Kissling et al., 1995b). Because the linearized inversion approach relies on an iterative process for finding the best solution, the starting velocity structure and the initial hypocenters play crucial roles in driving the final inversion result. It is imperative to ensure, as much as possible, that we explore the entire solution space to determine a global minimum of the coupled velocity-hypocenter problem. One iteration of inversion involves iteratively inverting P-wave arrival times until a convergence criterion is met (see Section 3.2). This criterion is linked to the error between observed and calculated arrival times. The L2-norm is often used to measure this error via the root-mean-squared (RMS) error (Havskov & Ottemoller, 2010). In VELEST, a single iteration of inversion is terminated when the RMS error between calculated and observed times does not significantly improve. However, this solution does not necessarily correspond to the best model (hypocenters and velocity structure) as other solutions could exhibit similar or lower data misfit. This aspect is illustrated in Figure 3.6 extracted from the VELEST user manual.

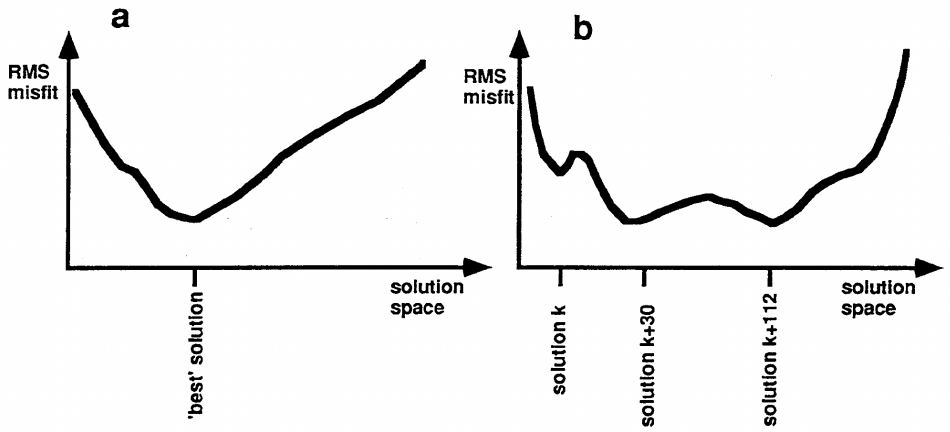

FIGURE 3.6: Quality evaluation of solutions to the coupled hypocenter-velocity problem from Kissling et al. (1995b) . **(a)** Simple case with an unique "best fit" solution. **(b)** Normal case with several local minima in RMS misfit. This function being unknown, the search for the best fit solution can only be achieved with a trial-and-error process.

Thus, the methodological approach in VELEST involves repeated rounds of iterative inversions where the input model parameters are slightly modified versions of the previous results. This extensive, manual, and repetitive procedure termed "trial-and-error" aims to explore numerous potential final solutions by refining certain model parameters and identifying/avoiding trade-off between hypocenter and velocity parameters (subsection 3.4.1). This manual operation mainly relies on modifying the initial velocity structure, including the number of layers, layer thicknesses, and average layer velocities.

3.4.1 Trial-and-error inversion approach

As first step, any relevant *a priori* information (e.g., geological structure, results from geophysical surveys) must be considered to constrain the input model parameters. We assume that the initial hypocenters obtained with the routine 2-layers model are sufficiently accurate as first guess estimates, requiring only small corrections to the hypocentral parameters to reach the best solution. Tests with other 1D models (such as iasp91, Bonjer/Bram, see section 3.1) yielded close epicenter estimates, but significant discrepancies at depth were also noted due to different sharp velocity contrasts (see later section 3.5). Therefore, we started almost from scratch concerning the velocity structure. In a similar situation, Matrullo et al. (2013) proposed to explore different set of preliminary solutions using several simplistic input velocity models. These models are either homogeneous (constant velocity) or depict an increasing velocity gradient from shallow to bottom layers. We followed this approach and considered, as initial velocity models, in addition to Mavonga et al.'s routine model, three constant and four gradient initial velocity models, with velocity ranging from 3.5 to 7.1km/s (Figure 3.7). VELEST accounts for station elevations and zero elevation refers to the mean sea level. The first layer of any inverted models is defined above the sea level (a.s.l.) and includes all stations, thus having a thickness of 4 km in our case (NYI at the the summit of Nyiragongo is the highest station). Depths are indicated as positive values below sea level (b.s.l.).

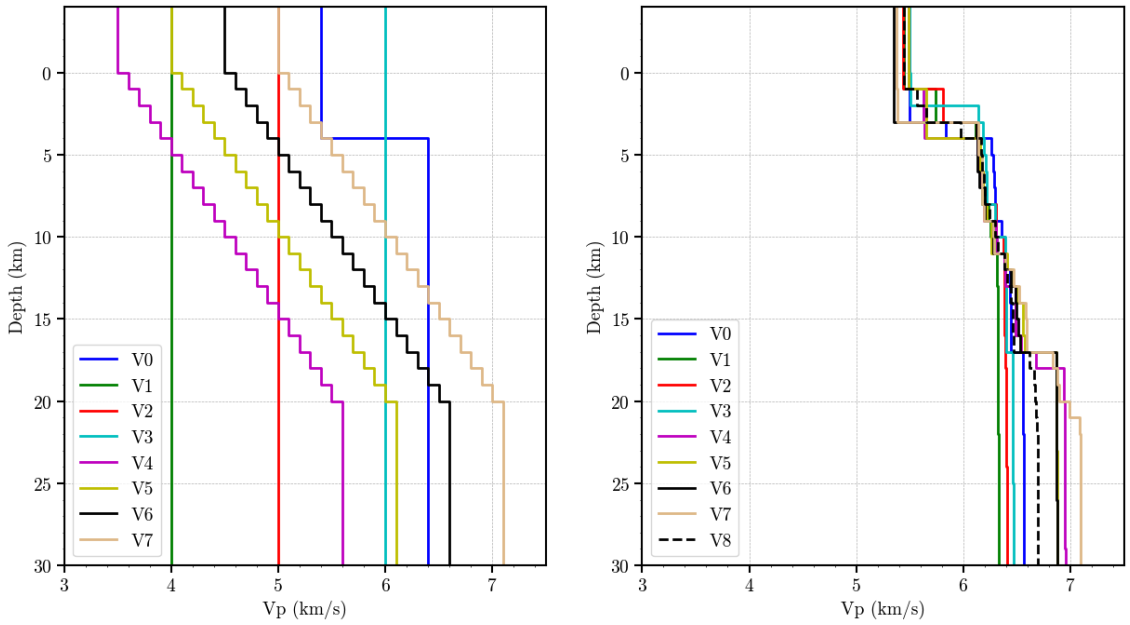

FIGURE 3.7: **Left**, Mavonga et al.'s velocity model from 0 to 30 km depth (V0) and 7 initial velocity models built without *a priori* information (V1 to V3 : homogeneous velocity; V4 to V7: constant velocity gradient from 0 to 20 km). **Right**, inversion results using initial hypocenters obtained with the Mavonga et al. model after one round of iterative inversions (i.e., no trial-and-error, no station correction terms). V8 indicates the average of all models V0 to V7.

The default damping parameters as defined in VELEST were used: the hypocentral damping parameter was set to 0.01, the velocity damping parameter was set to 1, and the station delay damping parameter was set to 0.1. A higher damping value restricts the parameter

from changing significantly between iterations, thereby ensuring the stability of the iterative process. Only one round of inversion was performed, which means that we analyze the first solution without trial-and-error nor station correction terms to refine the result. All output models converged after at least 9 iterations (Figure 3.8).
A notable observation is the common convergence around 6-6.5 km/s at depths between 4 and 17 km b.s.l., indicating a robust structural feature for the region sampled by the data (Figure 3.7). As expected, "extreme" input models (i.e., V1, V4) led to final models that did not converge as quickly as models with velocity variations within the range of 5-6.5 km/s. The larger variability observed at shallow depth and below 20 km can be attributed to the depth distribution of the hypocenters, where the coverage of seismic ray paths is insufficient (Figures 3.2 and 3.4). To assess the influence of the chosen initial hypocenters, we conducted the same inversion test using hypocenters obtained with the Bonjer/Bram velocity model (D'Oreye et al., 2011) (Figure 3.9). The Bonjer/Bram model also comprises a 2-layers structure at the depth of interest (0-20 km) but exhibits a sharper velocity contrast at 3 km b.s.l. (from 4 km/s to 6 km/s). Upon inversion, similar final velocities were observed for layers between 4 and 17 km b.s.l., along with a shift towards lower velocities for the shallowest layers. This first test suggests that resolving shallow layers (<4 km) will be difficult, but a well-constrained velocity structure down to approximately 20 km is anticipated.

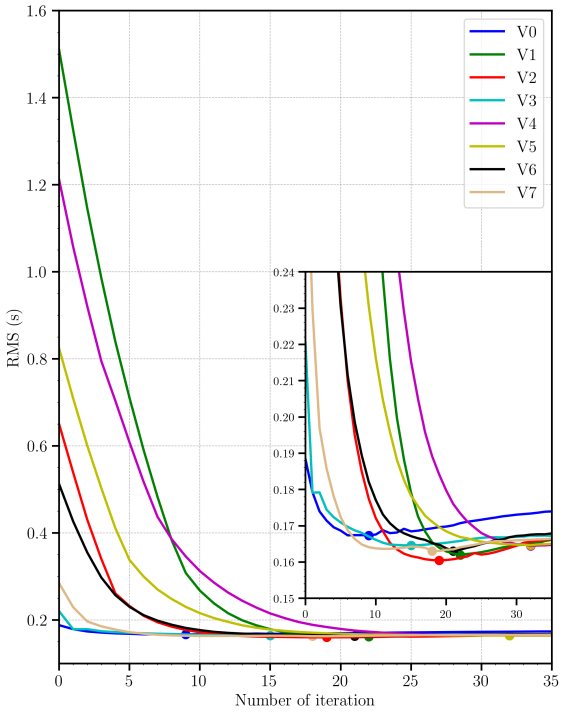

FIGURE 3.8: RMS error (s) as a function of number of iterations for each starting velocity model V0 to V7. The zoom allows to better identify when the minimum misfit (round marker) is reached for each iteration procedure.

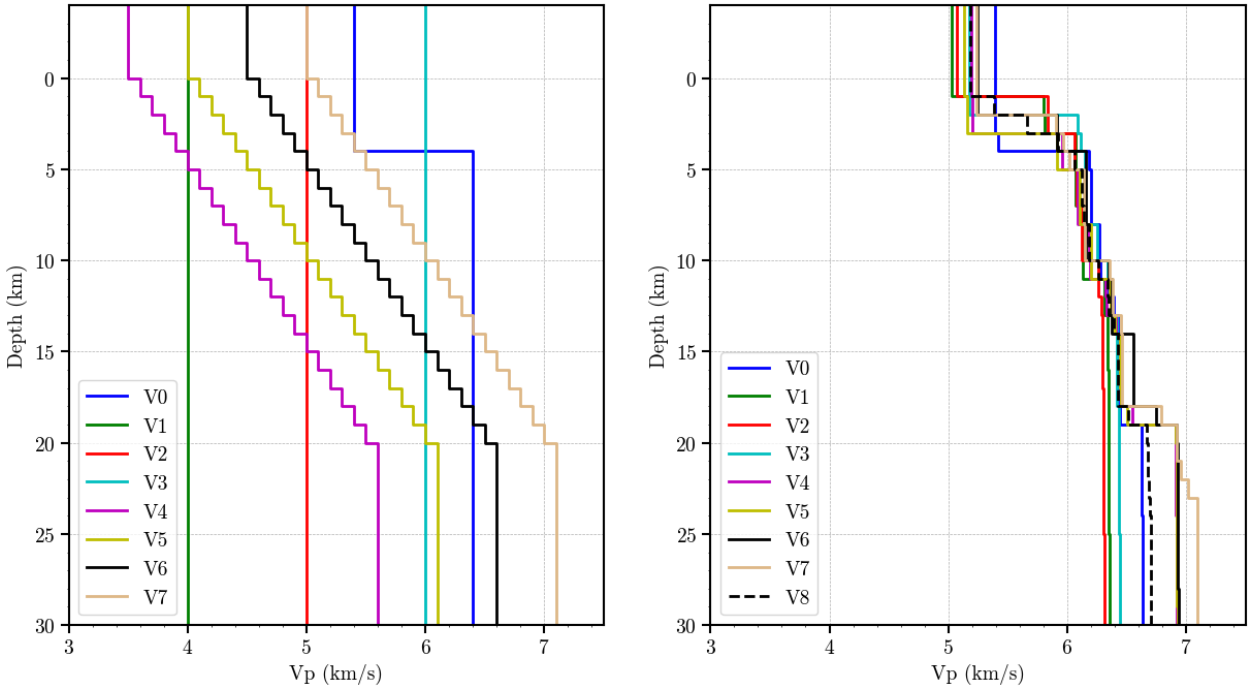

FIGURE 3.9: **Left**, initial velocity models from 0 to 30 km depth: V0, Mavonga et al. model and v1-v7, models built without *a priori* information (V1 to V3 : homogeneous velocity; V4 to V7: constant velocity gradient from 0 to 20 km). **Right**, velocity inversion results using initial hypocenters obtained with the Bonjer/Bram model after one round of iterative inversions (i.e., no trial-and-error, no station correction terms). V8 indicates the average of all models V0 to V7.

The arithmetic mean of output models V0 to V7 formed the new input velocity model for the trial-and-error process (V8, black dashed line in Figure 3.7). Additionally, we imposed the conditions that the final 1D layered model would feature increasing velocities with depth. We avoided incorporating low-velocity layers because while they could potentially reduce data misfit, they might also increase inversion instability (Kissling et al., 1995b; Matrullo et al., 2013). As VELEST does not directly invert for layer thicknesses, we needed to determine an appropriate model layering. Initially, we began with 1 km thick layer and the computation of station delays, but we found that our dataset couldn't resolve such fine layering between 0 and 30 km depth. Consequently, in subsequent iterations, we had to merge adjacent layers with similar velocities to reduce the total number of layers. Following the VELEST user manual, damping parameters remains constant during this step. Each trial-and-error test was considered complete when hypocenters, station delays and the velocity model showed no significant changes. We tested numerous layer configurations and values of damping parameters that we do not described all of them here. Through this procedure, the dataset was reduced from 410 to 404 events, with 6 events excluded due to azimuthal gap exceeding 180° after relocation. Local minima were reached multiple times and clear trade-off between all model parameters were observed when attempting to minimize the RMS misfit alone. We considered our final solution sufficiently constrained to a robust minimum when a low RMS value was acheived, but more importantly, when similar model parameters were consistently obtained across various trial-and-error processes. The final RMS error is equal to 0.06 s, more than three times smaller than the one obtained with the former routine Mavonga et al.'s model (0.19

s).

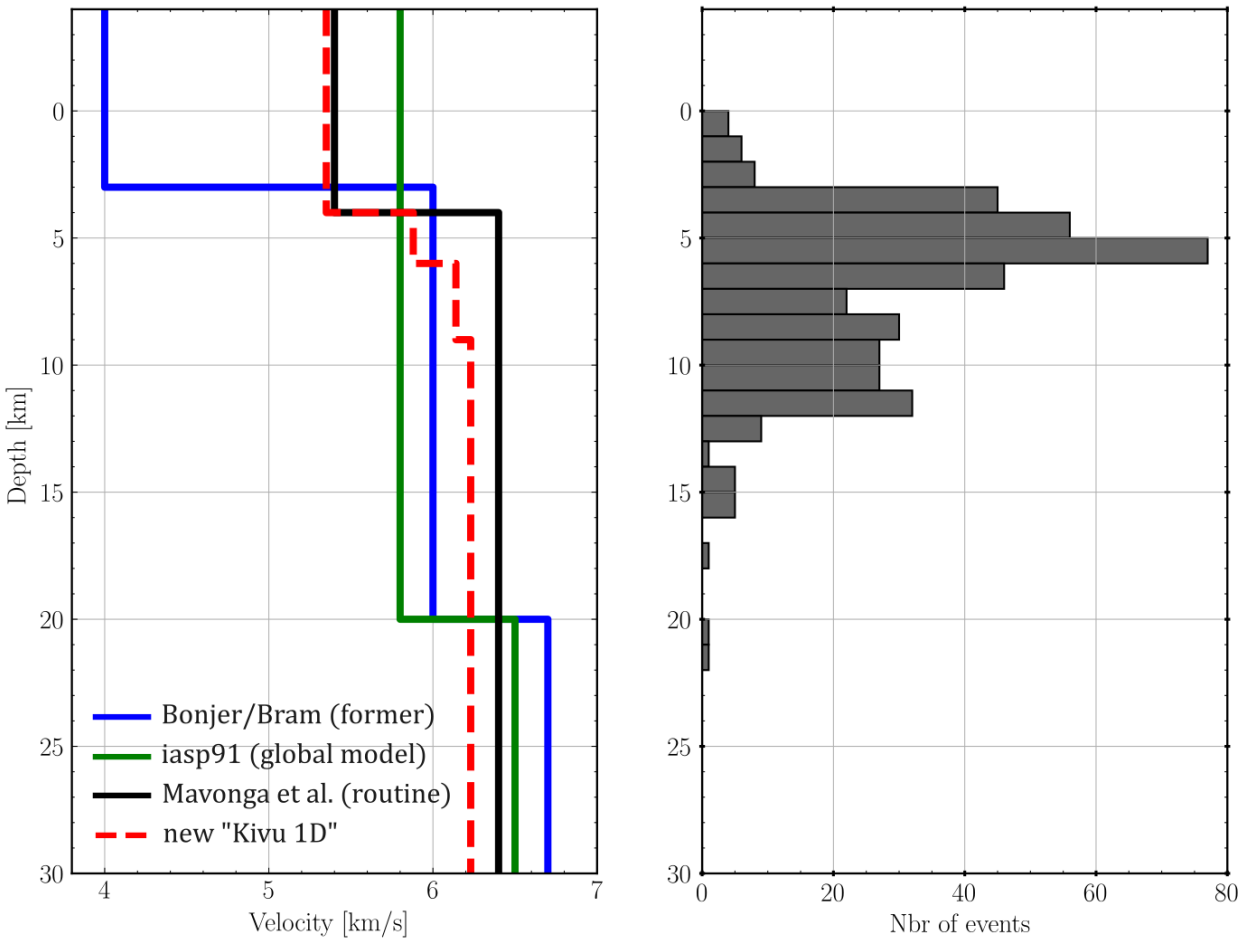

FIGURE 3.10: (**Left**) Final 1-D minimum P-wave velocity model "Kivu 1D" (red dashed line) plotted against other velocity models for the region: The former Bonjer/Bram model (solid blue line), the iasp91 global reference model (green) and the Mavonga et al. routine model (black). (**Right**) Depth distribution of events used for deriving the new "Kivu 1D" model.

Figure 3.10 shows the new velocity model, referred to as "Kivu 1D" and the final depth distribution of hypocenter (Figure 3.10b). The Kivu 1D velocity model consists of 4 layers, with velocities ranging from 5.3 km/s for the shallowest layer to 6.23 km/s at the top of the deepest layer (9 km b.s.l.) , with velocities ranging from 5.3 km/s for the shallowest layer to 6.23 km/s at the top of the deepest layer (9 km b.s.l.) (Table 3.1). The former Bonjer/Bram model appears to be unsuitable for this region due to its large velocity contrast (4-6 km/s) at 3 km depth, which is not observed in our results. In contrast, the global iasp91 model, while overly simplistic for the depth range of interest (0-20 km), shares a similar P-wave velocity (5.8 km/s) to that of the Kivu 1D model. Essentially, the Kivu 1D model is a refinement of the 2-layers model proposed by T. Mavonga et al. (2010), featuring a comparable shallow layer, a more gradual increase in velocity with depth between 4 and 9 km, and a slightly lower velocity bottom layer (6.23 km/s compared to 6.4 km/s). Seismic ray paths for the Kivu 1D model, to be compared with those from an homogeneous velocity structure (Figure 3.2), are plotted in Figure 3.11. The near vertical-incidence ray paths at shallowest depths do not uniformly sample the whole region, with

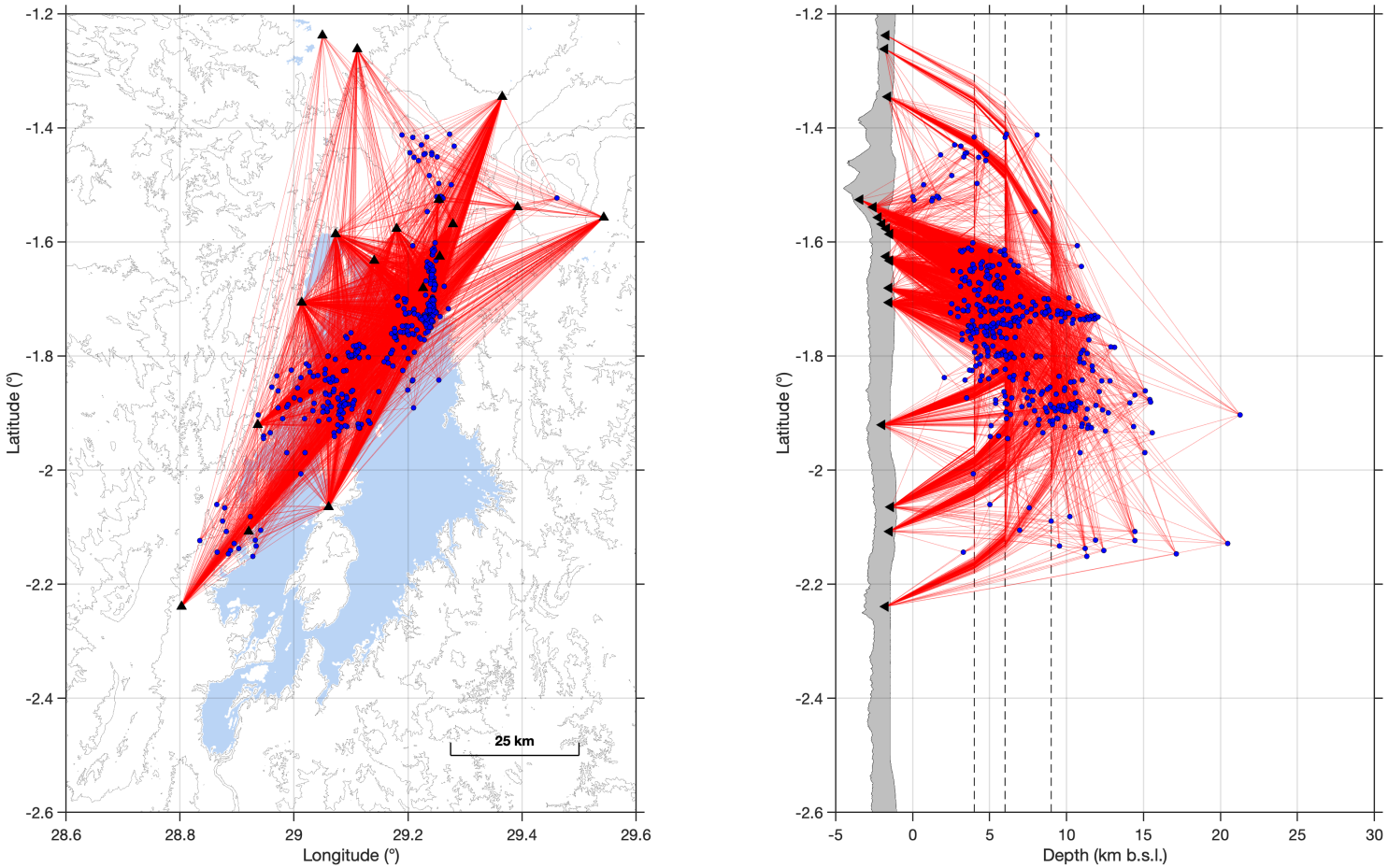

FIGURE 3.11: Seismic ray paths from the final set of selected events using the 1D minimum velocity model "Kivu 1D" derived from the VELEST procedure.

Top of layers (km b.s.l.)	P-wave velocity (km/s)	S-wave velocity (km/s)
0	5.35	3.13
4	5.88	3.44
6	6.14	3.59
9	6.23	3.64

TABLE 3.1: Final 1-D minimum P-wave velocity model "Kivu 1D". S-wave velocities are obtained from a constant V_P/V_S ratio of 1.71 (see section 3.3).

Stations	Latitude (°N)	Longitude (°E)	Elevation (m a.s.l.)	P delay (s)
RSY	-1.5768	29.1798	1700	0.42
BULE	-1.6330	29.1405	1482	0.35
NYI	-1.5258	29.2540	3411	0.24
SAKE	-1.5863	29.0732	1477	0.10
BUTK	-1.5388	29.3923	2557	0.04
KBTI	-1.5690	29.2785	1992	0.00
LWI	-2.2392	28.8025	1760	-0.01
MUNI	-1.6258	29.2553	1722	-0.03
GOM	-1.6812	29.2267	1524	-0.05
RGB	-1.3458	29.3655	1610	-0.09
KALEH	-2.1072	28.9208	1508	-0.12
KTSH	-1.2383	29.0500	1714	-0.12
IDJ	-2.0645	29.0607	1415	-0.24
LBGA	-1.2620	29.1110	1809	-0.24
BOBN	-1.7063	29.0132	1531	-0.27
SAHA	-1.5573	29.5435	2217	-0.31
NYAB	-1.9210	28.9367	1976	-0.34

TABLE 3.2: Spatial coordinates and P-wave station correction terms (delays in s) for the 17 KivuS-Net stations used in this work. Delays must be subtracted from observed P arrival times.

the most densely sampled area lying between Nyiragongo and the northern part of Lake Kivu (between Goma and the Idjwi Island). Local site effects may also be significant; therefore, another important improvement brought by the new model is the determination of station correction terms (Table 3.2). Compensating for near-surface heterogeneity that cannot be accounted for by the 1D layered velocity model, inverted station delays may provide additional information about the geological formations and, , conversely, can be considered meaningful if they agree with known geological characteristics. As mentioned earlier (see section 3.3), station delays are calculated relative to the reference station, which is KBTI (i.e., the delay equals 0 for this station).

The geological map of the Kivu Rift can be simplified into three main geological formations and several geological structures (escarpments, fault lineaments, volcanic cones, Maars, and Tuff rings): the South Kivu volcanic province (south of Lake Kivu), the Virunga volcanic province and the Precambrian basement (Figure 3.12) (Smets et al., 2016). The

delays associated to the known geological features make sense. The positive and near zero anomalies (i.e., lower velocity zones) are associated with stations located in the volcanic fields. All stations installed "off-rift" on the Precambrian rocks or at the border of the volcanic provinces are associated with negative anomalies (i.e., higher velocity zones). These observations are also represented in Figure 3.13. Lower velocity in the edifice may explain the positive anomaly (+0.24 s) for the station at Nyiragongo's summit (NYI). We do note also the particular case of nearby stations BULE and RSY with strong localized positive anomalies (markers colored in red in Figure 3.12). From a preliminary ambient noise tomography, Oth et al. (2018) identified this area (and its extension to the lake Kivu where Maars and Tuff rings are localized) as a low-velocity zone for surface Rayleigh waves. Subira et al. (2023) observed strong site amplification at these two stations (see Chapter 1). These anomalies are likely caused by the local geology, which consists of subsiding volcanic deposits and lake sediments including high density of diffuse magmatic degassing areas (called "mazuku") (Wauthier et al., 2018).

3.4.2 Evaluation of model's stability

Husen et al. (2011) and VELEST user manual (Kissling et al., 1995a) provide guidelines for evaluating the validity (or robustness) of the selected final solution. We tested the stability of the Kivu 1D velocity model by randomly shifting the final hypocenter locations by 3 to 6 km in longitude, latitude and depth before performing another inversion run. The total shifting of hypocenters thus ranges between approximately 5.2 and 10.4 km. In Figure 3.14, the black crosses represent the initial hypocenters, which are linked with black lines to the corresponding shifted hypocenters represented as colored circles (the color scale is proportional to the distance between both locations). We kept all damping parameters the same as in the trial-and-error inversion process, except for the damping velocity parameter, which is underdamped as suggested by Kissling et al. (1995a). After inversion, these perturbed hypocenters should ideally converge to the hypocenter locations before pertubation. The inverted velocity model and station correction terms should also be similar to the 1D minimum model if the final model parameters are robust solutions to the coupled hypocenter-velocity problem (i.e., stable and consistent solutions across different iterations or variations in the input data).

The results of this validity test were satisfying (Figures 3.15 and 3.16). Velocities and station delays only changed marginally after introducing this pertubated hypocenters as initial parameters. As shown in Figure 3.15, a high proportion of new hypocenter solutions returned to their "best" locations. In Figure 3.16 the green dots represent the difference between the unperturbed (best solutions) and perturbed (before inversion) hypocenters in the three directions of space. The grey circles represent the difference between the unperturbed (best solutions) and new hypocenters (after inversion using perturbed inputs). As also observed by Matrullo et al. (2013), initial longitude and latitude are better retrieved than depth in such validation procedure, pointing out once again the inherent uncertainty in solutions of the coupled hypocenter-velocity problem. Nonetheless, the error in depth is less than 2 km for about 95% of the events. It is also noteworthy that events associated with the 2021 Nyiragongo eruption are best retrieved (between the two vertical dashed black lines in Figure 3.16). These are events located well within the network with numerous good quality observations for each of them. Kissling et al. (1995a) recom-

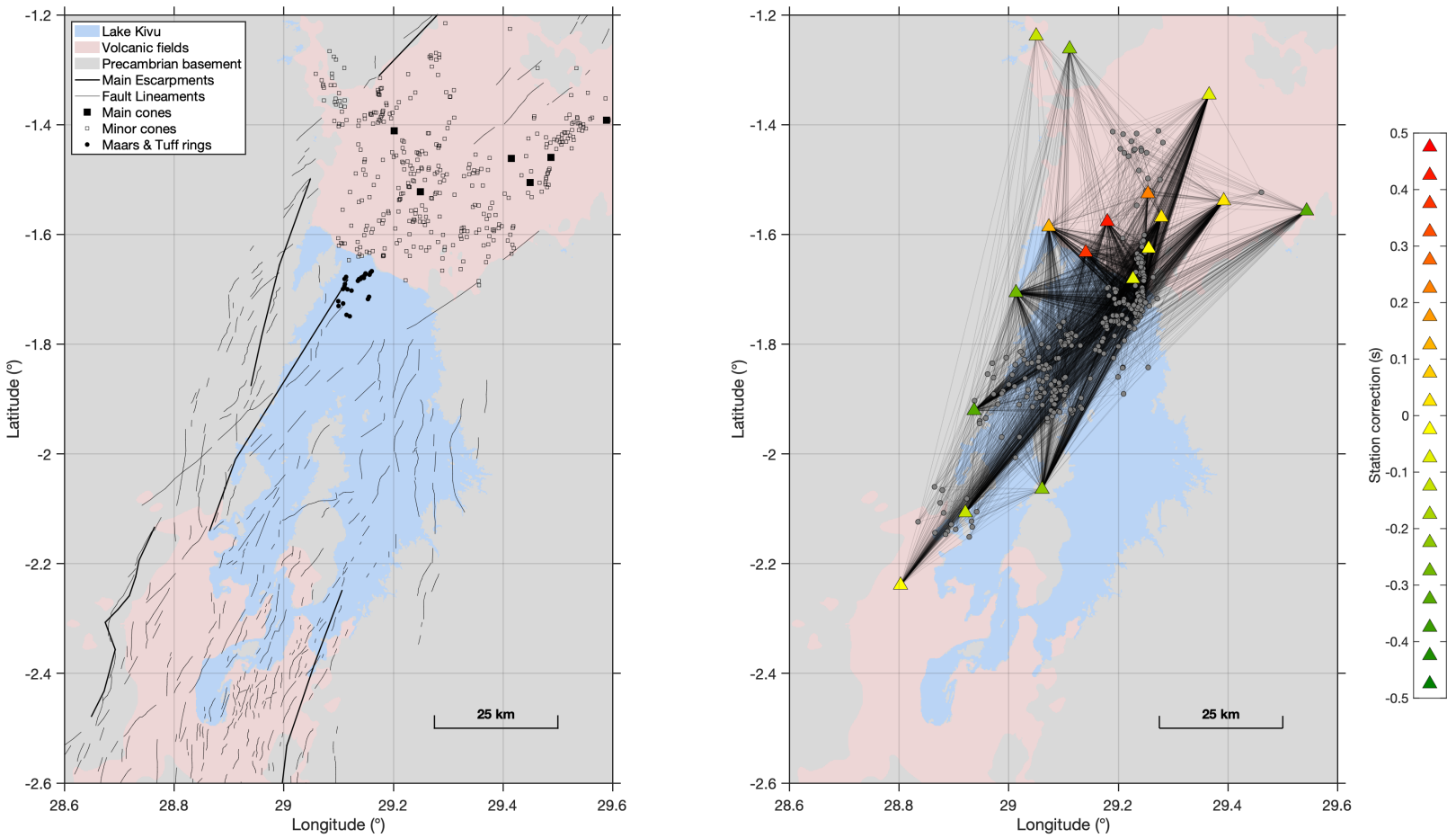

FIGURE 3.12: **(Left)** Simplified geological map of the Kivu rift adapted from Smets et al. (2016) showing different main geological formations: volcanic fields (light red), Precambrian basement (gray), main escarpments (Bold black line), fault lineaments (black line), main volcanic cones (filled black square), minor volcanic cones (small black square), Maars and Tuff rings (black circle). **(Right)** P-wave station delays plotted (green to red for negative to positive values) on the same simplified geological map displayed on left.

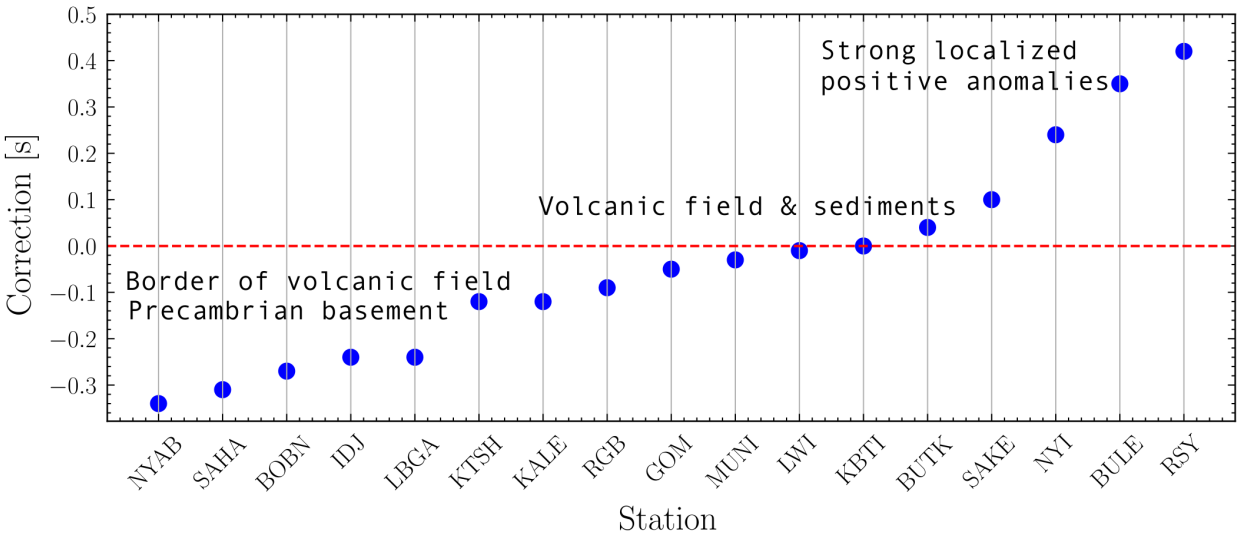

FIGURE 3.13: P-wave correction terms for KivuSNet stations used in the inversion process. Three groups of stations may be linked to different site properties with regards to the reference station (KBTI) located in the volcanic field (See text). Negative delays are observed at NYAB, SAHA, BOBN, IDJ, LBGA, KTSH, KALEH, which are located at the border of the volcanic field with Precambrian outcrop; Minor to positive delays correspond to stations located in the volcanic fields (RGB, GOM, KBTI, BUTK, SAKE, LWI). Significant positive anomalies (lower velocity zones) are detected at NYI (Nyiragongo's summit) and for stations BULE and RSY (subsiding area with degassing, see text).

mend verification for events that fail the stability test. In the next section 3.5, we provide a comprehensive analysis of location errors for the full dataset relocated with the new 1D minimum velocity model. This helped us to identify events with poorly constrained uncertainty and to validate the final model parameters.

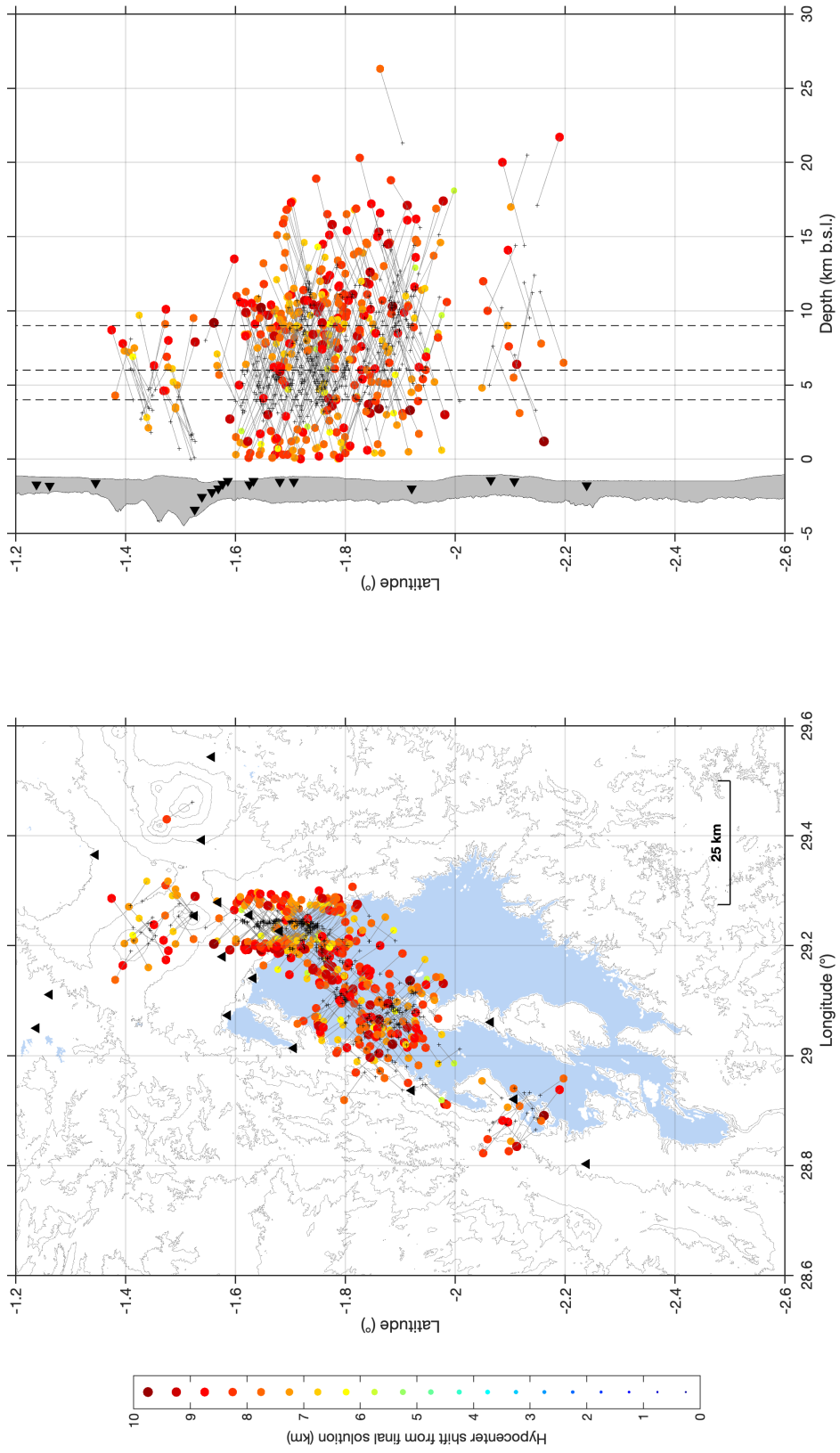

FIGURE 3.14: Stability test - Inputs : Random perturbation of hypocenters by 3 to 6 km in longitude, latitude and depth (see text). Final solutions of the hypocenters obtained with the 1D minimum model are represented by black crosses and perturbed hypocenters (before inversion) are colored circles (with color marker size proportional to the 3D spatial shift in km.

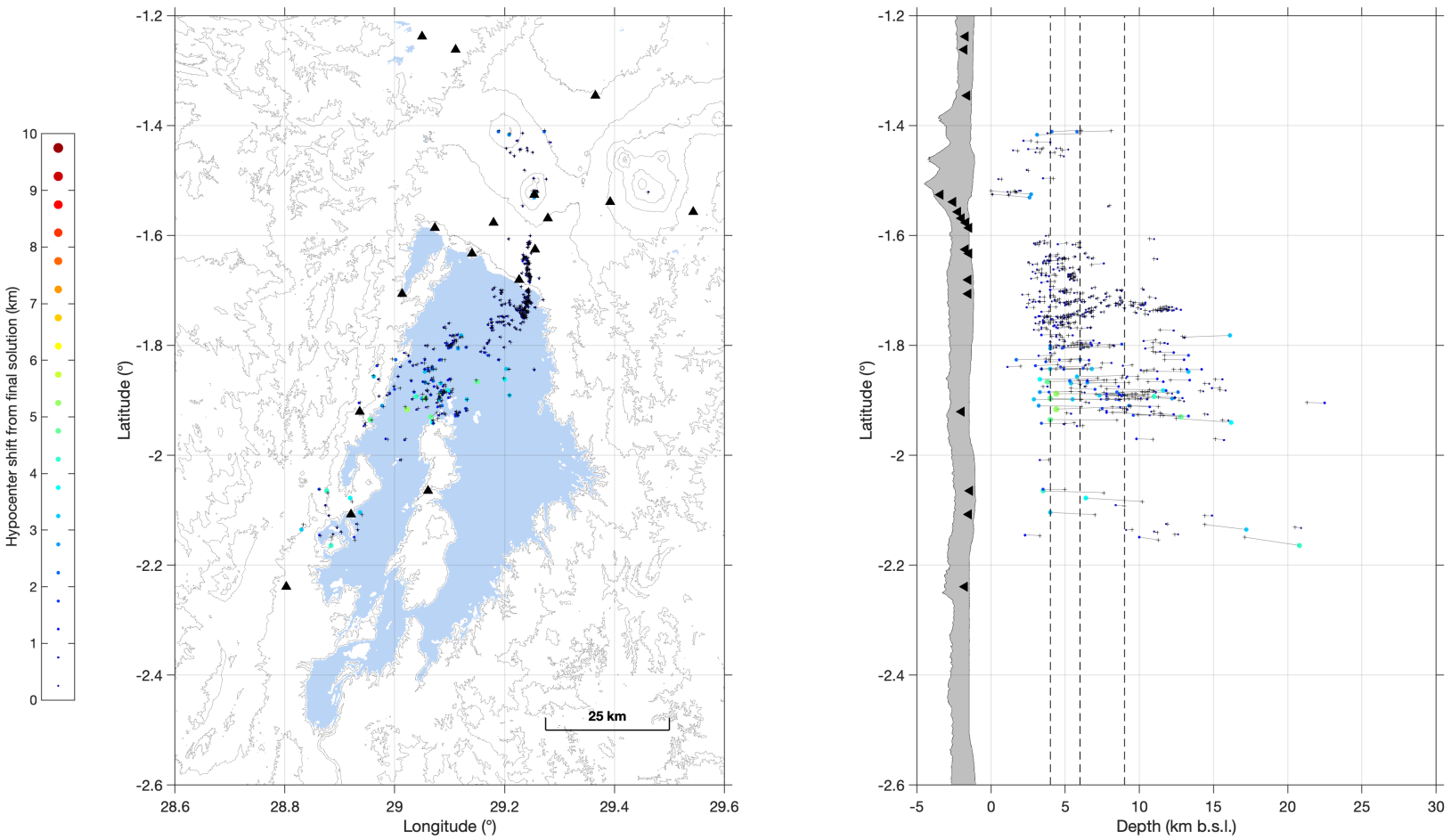

FIGURE 3.15: Stability test - Results : New hypocenters after VELEST inversion using perturbed hypocenters as input (Figure 3.14). Final solutions of the hypocenters obtained with the 1D minimum model are represented by black crosses and new hypocenters (after inversion) are colored circles (with color marker size proportional to the 3D spatial shift in km.

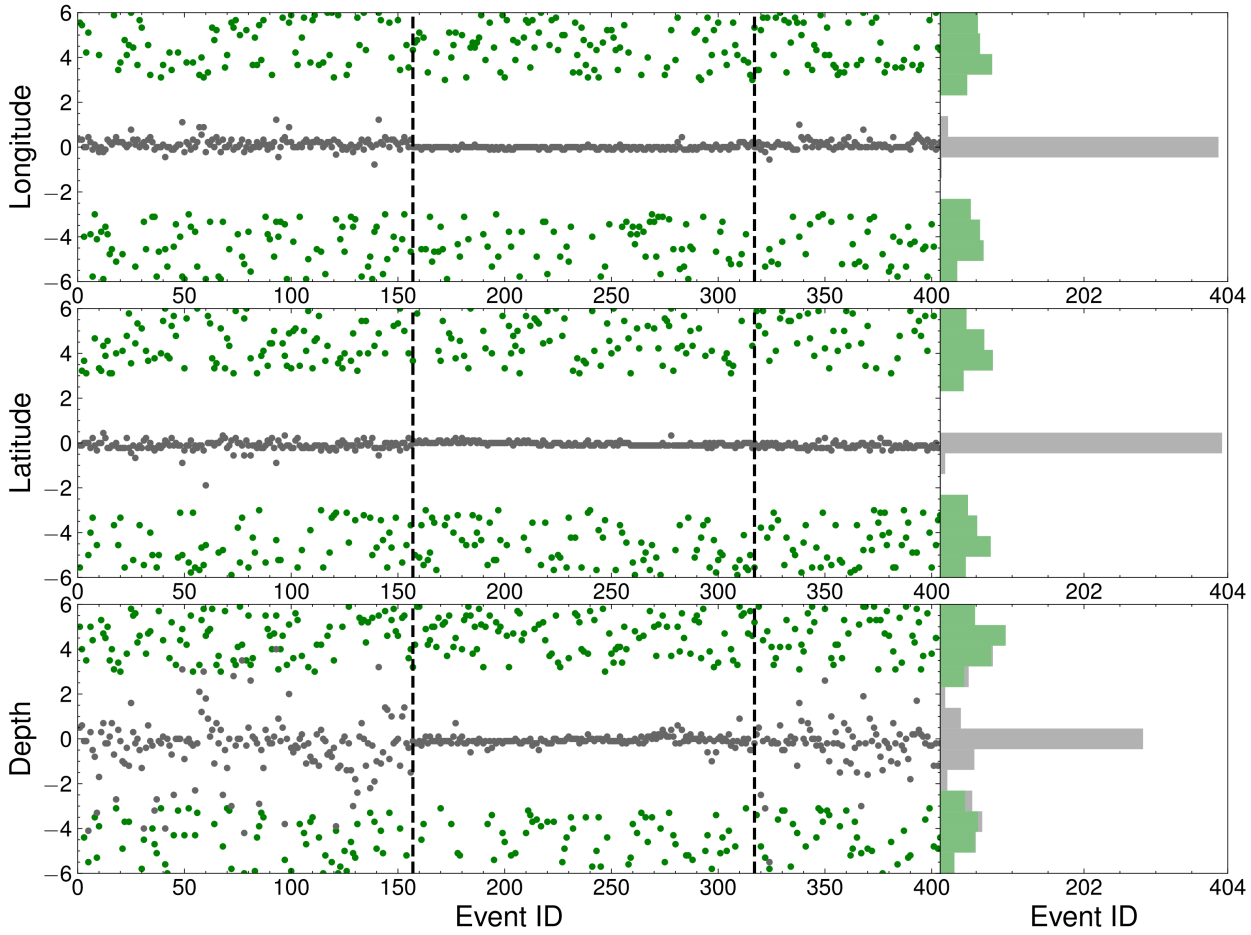

FIGURE 3.16: Stability test - Results : Longitude, latitude and depth difference (in km) between best and perturbed coordinates before inversion (green dots), best and new coordinates after inversion (gray dots). Corresponding histograms on the right side show that the initial best hypocenters are well retrieved after a round of inversion using perturbed hypocenters as inputs. The two dashed lines demarcate the three temporal subdatasets defined previously : "pre-eruptive", "syn-eruptive/dyke" and "post-eruptive"

3.5 Location errors analysis

In this section, we address a crucial aspect about the earthquake location problem: the estimation of location errors encompassing arrival-time picking errors and travel-time calculation errors due to incorrect velocity model. It is indeed of primary importance to get a reliable quantification of these errors in order to definitively validate our final result (new 1D velocity model and hypocenter locations).

3.5.1 Limits of linearized methods for quantifying location errors

As mentionned earlier in this Chapter, the earthquake location problem is highly non-linear. The linearized method implemented in VELEST overcomes this complexity by assuming a first guess location close to the true hypocenter to iteratively reach a satisfying global solution (see section 3.2). For least-square solution, hypocenter errors are assumed to follow Gaussian distribution, and errors in data are independent. This allows understanding error statistics in term of a covariance matrix of model parameters $\boldsymbol{C_m}$, defining the errors in the hypocenter spatial coordinates and origin time defined as described by (Havskov & Ottemoller, 2010):

$$\boldsymbol{C_m} = \begin{bmatrix} \sigma_{xx}^2 & \sigma_{xy}^2 & \sigma_{xz}^2 & \sigma_{xt}^2 \\ \sigma_{yx}^2 & \sigma_{yy}^2 & \sigma_{yz}^2 & \sigma_{yt}^2 \\ \sigma_{zx}^2 & \sigma_{zy}^2 & \sigma_{zz}^2 & \sigma_{zt}^2 \\ \sigma_{tx}^2 & \sigma_{ty}^2 & \sigma_{tz}^2 & \sigma_{tt}^2 \end{bmatrix} \tag{3.16}$$

The diagonal element are variances of the location parameters x_0, y_0, z_0 and t_0, while the off-diagonal elements give the coupling between the errors for the different hypocenter parameters. Assuming equal uncertainty for all data leads to simple calculation of the covariance matrix:

$$\boldsymbol{C_m} = \boldsymbol{C_d}[\boldsymbol{G}^T\boldsymbol{G}]^{-1}, \tag{3.17}$$

where $\boldsymbol{C_d}$ is the covariance matrix of the data (variance of the arrival times σ_d^2 multiplied with the identity matrix $\boldsymbol{I}$). $\boldsymbol{G}$ is the known matrix of eq. 3.9. The square root of the diagonal elements gives the standard deviation of the hypocenter parameters (i.e., 68% probability of finding the solution within one standard deviation). We can thus define error ellipsoid having semi axes σ_{xx}, σ_{yy} and σ_{zz}. Such statistics are often reported in location error statistics, using for instance a threshold of 90% probability given by a bit less than 2 standard deviations, (Havskov & Ottemoller, 2010). The off diagonal elements define the orientation and shape of error ellipsoid, which depends on the geometry of the network and the velocity model.

Nonetheless, despite such available error statistics, linearized methods produce a single best-fit hypocenter (and origin time) that is a poor representation of the location uncertainty (Lomax et al., 2014). Intuitively, for better considering the non-linearity of the earthquake location problem (and thus its associated uncertainty), a method that could "scan" all potential solutions will provide a better estimate of location errors than the above-mentioned error ellipse. This kind of approach can be identified as grid-search type because all possible locations are scanned over a pre-defined grid of potential locations (Havskov & Ottemoller, 2010). Then, the most probable location defined as the

maximum likelihood (or lower misfit) can be retrieved and the associated error can be inferred from the misfit obtained for all other locations. One common approach to calculate this misfit is again the least-squares solution where the root-mean-squared (RMS) residual is calculated at each grid points and defined as :

$$RMS = \sqrt{\frac{\sum_{i=1}^{n}(t_i^{obs} - t_i^{calc})^2}{n}}, \tag{3.18}$$

where n is the total number of observations, t_i^{obs} and t_i^{calc} are the observed and calculated arrival times, respectively, and $t_i^{calc} = t_i^{tra} + t_0$ with t_i^{tra} the calculated travel time as a function of the known station location (x_i, y_i, z_i) and an assumed hypocenter (x_0, y_0, z_0). This RMS parameter (expressed in secondes) is given in almost all location programs for the best hypocenter solution provided by linearized location methods. However, a low RMS does not necessarily mean an accurate hypocenter determination but always a good fit to the data (Havskov & Ottemoller, 2010). Hence, the purpose of grid-search based technique is to better infer the location uncertainty by observing the full (3D) spatial distribution of this misfit parameter. For instance, a sharp increase of RMS values around a single (global) minimum would convey a well-resolved hypocenter while multiples local minima or slightly varying RMS values spreading over a large area would indicate inaccurate hypocenter determinations. Obviously, because of this exhaustive search over the solutions space, such calculation is computationally demanding and explains why linearized methods remain widely used, especially at observatories providing near-real time solutions (Bormann, 2002). However, both the improvement in computer power and the use of adequate algorithms overcome the inefficiency of nonlinearized procedures for computing the locations of a large number of events and/or over a large volume (e.g., Lomax et al., 2014; Poiata et al., 2016). For quantifying errors of the selected dataset located with the new 1D minimum model, we exploit the well-known computer program called NonLinLoc (Lomax et al., 2000) described in the following part.

3.5.2 On the use of NonLinLoc, a "nonlinear" location method

In the family of grid-seach methods, NonLinLoc performs a probabilistic, global-search event location. In contrast with the final solution provided by linearized methods as a unique 3D point (x_0, y_0, z_0), the solution in NonLinLoc can be expressed as a posterior probability density function (PDF) following the probabilistic formulation of inversion presented in Tarantola (1987) and Tarantola, Valette, et al. (1982). The PDF represents the complete probabilistic solution to the earthquake location problem, including information on uncertainty and resolution. We refer the reader to Lomax et al. (2014) for more details about the method and we explain below the main characteristics of this approach.

The building of the PDF relies on the so-called *likelihood* function, which gives the measure of how good a model is in explaining the data. The formulation of Tarantola, Valette, et al. (1982) provided the least-square (L2-norm) likelihood function L after assuming Gaussian errors for uncorrelated observed arrival-times (t^{obs}) and calculated travel-times (t^{tra}):

$$L(\boldsymbol{x}) = exp\left[-\frac{1}{2}\sum_{i=1}\frac{(t_i^{obs} - t_i^{tra})^2}{\sigma_i^2}\right], \tag{3.19}$$

where $\boldsymbol{x}$ is the spatial part of the model parameters $\boldsymbol{m}$ (i.e., the vector of spatial coordinates and origin time), and σ_i is the associated standard deviation of uncertainty in ${t_i}^{\text{obs}}$ and ${t_i}^{\text{tra}}$. A more robust function to be minimized in presence of potential outliers is the Equal Differential Time (EDT) formulation, also implemented in NonLinLoc, where the location *likelihood* is expressed as a function of pairs of observations (see Lomax et al., 2014 for the full mathematical formulation). The EDT's PDF has its largest values for grid points where the most pairs of observations are satisfied, which means where the differences between the observed arrival times and the differences between the calculated travel times for most pairs of observations tends to be equal (hence giving the name to this approach). In contrast, the L2-norm aims to satisfy all observations simultaneously, being thus more sensitive to outlier data. The errors in the observed arrival times and in the forward problem (travel-time calculation) are still assumed to be Gaussian in the EDT formulation. However, in contrast to the L2 function, the EDT does not require calculation of the origin time t_0 and the 4D problem of hypocenter location reduces to a 3D search over the spatial coordinates (x_0, y_0, z_0) (an origin time can be assigned *a posteriori* once the spatial coordinates have been determined). For each station, the travel times are first calculated once at all grid nodes using a 3D version of the Eikonal finite-difference scheme of Podvin and Lecomte (1991). The earthquake location is then performed efficiently with the oct-tree importance sampling method where the sampling density of the grid, after recursive subdivisions, tends towards to the PDF. This oct-tree structure will have a larger number of cells in the regions of higher PDF (lower misfit) and thus gives approximate importance sampling of the PDF (Lomax et al., 2014). The grid-search approach could give a more detailed sampling of the PDF, but at the cost of higher computational time. With correct tuning, the oct-tree search produces much more quickly a solution (i.e., a mapped PDF in 3D space) that is nearly identical to that of the grid-search.

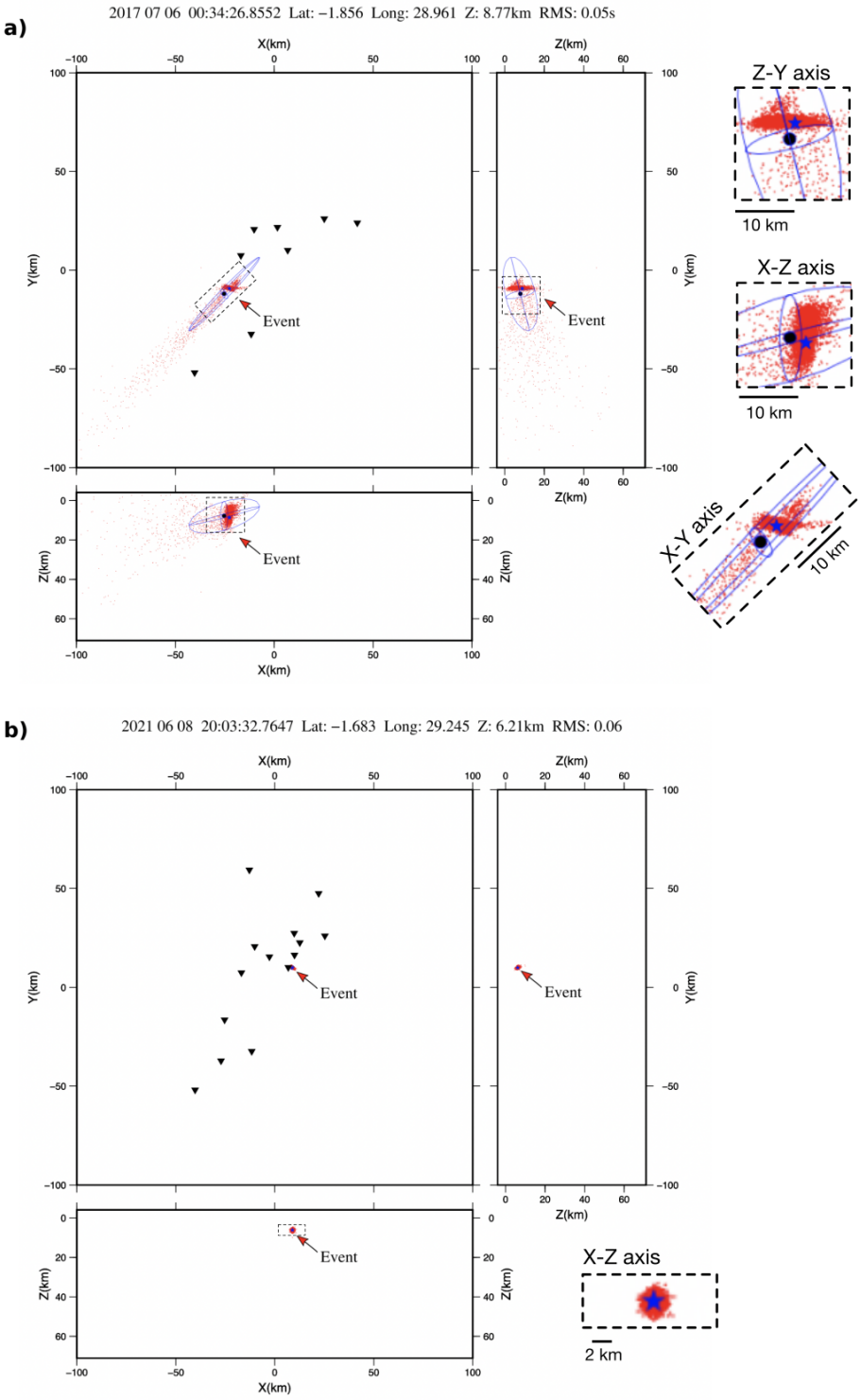

FIGURE 3.17: Two seismic events located with NonLinLoc **(a)** on 6 July 2017 and **(b)** on 8 June 2021, plotted in 2D planes X-Y (Longitude-Latitude), X-Z (Longitude-Depth) and Z-Y (Depth-Latitude). Zooms are provided on the right. Red dots correspond to the PDF scatter sample, the black circle is the center of the Gaussian ellipsoid and the blue star is the maxL hypocenter. In panel **(b)** the PDF scatter sample masks the small fitted ellipsoid obtained for the well-resolved hypocenter associated with low uncertainty.

The Figure 3.17 illustrates the NonLinLoc location procedure that we applied in this thesis (i.e., EDT likelihood function + oct-tree search) for two different seismic events using the new 1D minimum model. These examples allow us to present the main features of NonLinLoc solutions and the associated statistics we used to distinguish a "good" solution from a "bad" one, despite both satisfying very low RMS misfit (0.05 and 0.06 s). The panel **a)** shows the location of a seismic event occurring in the western part of lake Kivu (close to KALEH station) on 6 July 2017 using observations from 9 stations. The final *RMS* between observed and theoretical times is very low (0.05 sec), but the importance sampling PDF (red scatter points) depicts large uncertainty. The PDF scatter sample is directly proportional to the PDF value. The area with denser scatter points corresponds to the maximum likelihood source region (further refereed as "MaxL"), the higher probability region of the PDF. The shape of the PDF spreading over the Southwest is due to the network geometry. Additional observations to the West/Southwest of this event would probably reduces this spatial error drastically. For a single event, such graphical representation allows easy assessment of the uncertainty related to the final solution. However, deriving simple statistics from the PDF scatter sample for comparing all events together would be convenient.

One solution proposed in NonLinLoc is to approximate the 3D spatial error of location using the notion of a confidence ellipsoid, as used in linearized methods. The covariance matrix of the PDF scatter sample is first calculated, then singular value decomposition (SVD) of the covariance matrix gives the error ellipsoid (plotted here in blue as 2D ellipses in x-y, y-z and x-z planes). This ellipsoid will fit perfectly the PDF if the errors follow a Gaussian distribution. In this case, the center of the ellipsoid will correspond to the maximum likelihood ("MaxL") hypocenter and the normal statistic approximation of the final PDF is an accurate, compact representation of the 3D spatial error. On contrary, ellipsoid poorly represents large non-Gaussian errors distribution, which is the case here. However, because NonLinLoc can always fit an ellipsoid to the PDF scatter sample, the shape of the resulting ellipsoid can convey the overall location error. Indeed, the large ellipsoid as plotted for this event, despite being a poor representation of location uncertainty, remains a good indicator of this large error. In addition, in such case, the center of the ellipsoid (black circle) can significantly deviate from the MaxL location (blue star). The second panel **(b)** from Figure 3.17 represents a much better constrained location for an event occurring on 8 June 2021 close to Goma (station GOM) and recorded by 14 stations. This earthquake is related to the sustained post-eruptive/dyke intrusion seismicity recorded in the northern part of Lake Kivu. Compared to the previous example (panel **(a)**), the PDF scatter sample is significantly reduced and can be well fitted by a small Gaussian ellipsoid. The center of the ellipsoid and the MaxL hypocenters are obtained at similar coordinates. Therefore, it seems relevant to define *ad hoc* criteria for distinguishing a well constrained event from a poorly constrained one based on the size of the Gaussian ellipsoid and the distance between the MaxL and the center of the ellipsoid. We follow this approach in the next analysis.

3.5.3 Comparative analysis between the former routine model and the new 1D minimum model

Based on the NonLinLoc framework described in the previous section, we compare the quality of solutions provided with the former routine velocity model (Mavonga et al.'s model) and the new 1D minimum model (Kivu 1D model). We used the initial dataset of 410 seismic events, including S-phase observations ignored in the VELEST procedure (see Figure 3.3).

Figure 3.18 shows hypocenters obtained with the Kivu 1D model. Maximum likelihood ("MaxL") solutions are depicted as black crosses and Gaussian estimates as colored circles for the centers of 2D ellipses, which are plotted in gray. The marker size and color of the Gaussian solution is proportional to the shift from the corresponding MaxL position. Overall, the agreement between both hypocenter solutions is very good, and the size of Gaussian ellipses is small (i.e., within 0-3 km range). In accordance with the quality criteria previously defined, this results indicates well-resolved hypocenters with corresponding small uncertainties. However, we do also note some badly resolved solutions characterized by large shifts (> 3 km) between MaxL and Gaussian estimates and large error ellipses that can exceed 25 km in total extent, especially at depth. These events are localized at the edge of the seismic network and may be due to the network geometry. To better understand the factors influencing these significant location errors, we define two error criteria MaxERH and MaxERZ expressed in km :

- MaxERH : Maximum horizontal error, which is the total extent of the Gaussian ellipsoid in longitude and latitude.
- MaxERZ : Maximum vertical error, which is the total extent of the Gaussian ellipsoid in depth.

MaxERH and MaxERZ are plotted against the number of S-wave picks, the number of P-wave picks, the RMS error, the azimuthal gap, the center of ellipsoid (longitude, latitude, depth), and the distance to the closest seismic station (minimum distance) in Figures 3.19 and 3.20, respectively. As also observed in stability test's results, events related to the 2021 eruption (subdataset "syn-eruptive/dyke") are better constrained (events 161 to 321, see also Figure 3.3). These events are characterized by high SNR with numerous good quality observations (often more than 10 P-phases picks) and distance to the closest seismic station often less than 10 km. They are also localized at the center of the seismic network despite having large azimuthal gap ranging approximately between 140 and 180° due to the absence of permanent stations on the Rwandese side of lake Kivu. Note also that the RMS error is low for most of events of the full dataset (< 0.1 s), pointing out again that this criterion itself cannot be a reliable indicator of location uncertainty. Shallow or deep events are similarly affected by large locations errors in both horizontal or vertical planes. Overall, events with highest uncertainties are the ones from the subdataset "pre-eruptive" (event numbers below 161). The "post-eruptive" subdataset (event numbers above 321) is also affected by larger errors than the "syn-eruptive/dyke". Complex combinations of factors may lead to poor location constraints but, in addition to picking errors and the inherent uncertainty associated to the use of a 1D velocity model, we can emphasize :

- The number of observations : Largest errors are obtained for the lowest number of P- and S-phases picks;

- The influence of the network geometry : Largest errors are obtained for events located at the edge of the network (both in longitude and latitude);
- The minimum distance to seismic stations : Largest errors are obtained for events farther away than 10 km from the closest station.

Figures 3.21, 3.22, 3.23 present the same analysis applied to Mavonga et al.'s routine model. It is clear that every hypocenter solutions are much more often affected by large uncertainty exceeding 10 km in horizontal and vertical planes. Comparing corresponding figures between both models allow to gauge the importance of the velocity model on final solutions and associated uncertainties. The influence of the number of observations, the network geometry and the distance to the seismic stations remain obvious. The overall RMS error is higher using the routine model but the maximum misfit is below 0.3 s, which is generally considered as a good data fit. Using the routine model, some events from the "syn-eruptive/dyke" subdataset can also depict significant horizontal and vertical errors. We provide further comparisons between both models in Figures 3.24 and 3.25.

Figure 3.24 shows in the form of histograms, that the overall hypocenter shift (in km) between the MaxL and Gaussian solutions using the Kivu 1D model is much lower that the shift observed using the Mavonga et al. model (top histrogram). This figure also displays the hypocenter shift between both models (bottom histrogram). Considering the Kivu 1D solutions as the best ones, this histogram can be viewed as the error distribution introduced by the use of the Mavonga et al. model for the selected 410 events. This information can also be visualized on a map (Figure 3.25) depicting the distance between the MaxL solutions obtained with both velocity models. We clearly observe that using the Mavonga et al. model may move hypocenters by more than 5 km to deeper focus (> 10 km b.s.l.) or to the Earth surface (in this case, the top of the NonLinLoc grid, which is 4 km a.s.l.). Errors in longitude-latitude can also be significant within the three main spatial clusters (active volcanoes, dyke intrusion, lake Kivu). We thus expect that the use of the new Kivu 1D model will help to refine some previously located datasets, such as the one for the Nyiragongo 2021 eruption published in Smittarello et al. (2022), who used the routine model.

We also provide in appendices B similar analyses of location errors using the former Bonjer/Bram model, the reference iasp91 model, the Kivu 1D model without P-wave station delays and the Kivu 1D model without S-phase observations. Bonjer/Bram and iasp91 models provide both poorer location constraints than the Kivu 1D and Mavonga et al. models. The sharp contrast at 3 km depth in the Bonjer/Bram model is well identified because many events are "stuck" at this interface, which is an obvious artefact of location. The global iasp91 model gives the worst result. The single layer between 0 and 20 km in the iasp91 model leads to much deeper hypocenters in order to satisfy low RMS misfit. Analyzing solutions with the Kivu 1D without station delays allow highlighting the importance of considering these correction terms for overcoming the limits of the layered model. Indeed, without stations delays, the range of location errors with the Kivu 1D model is significantly larger, and location results tend to the ones obtained with the Mavonga et al. model. Despite a better resolution between 0 and 10 km, the new Kivu 1D model is not drastically different from the former routine model (see Figure 3.10). Using only P-phase observations with the Kivu 1D model, the MaxL solutions are very close to

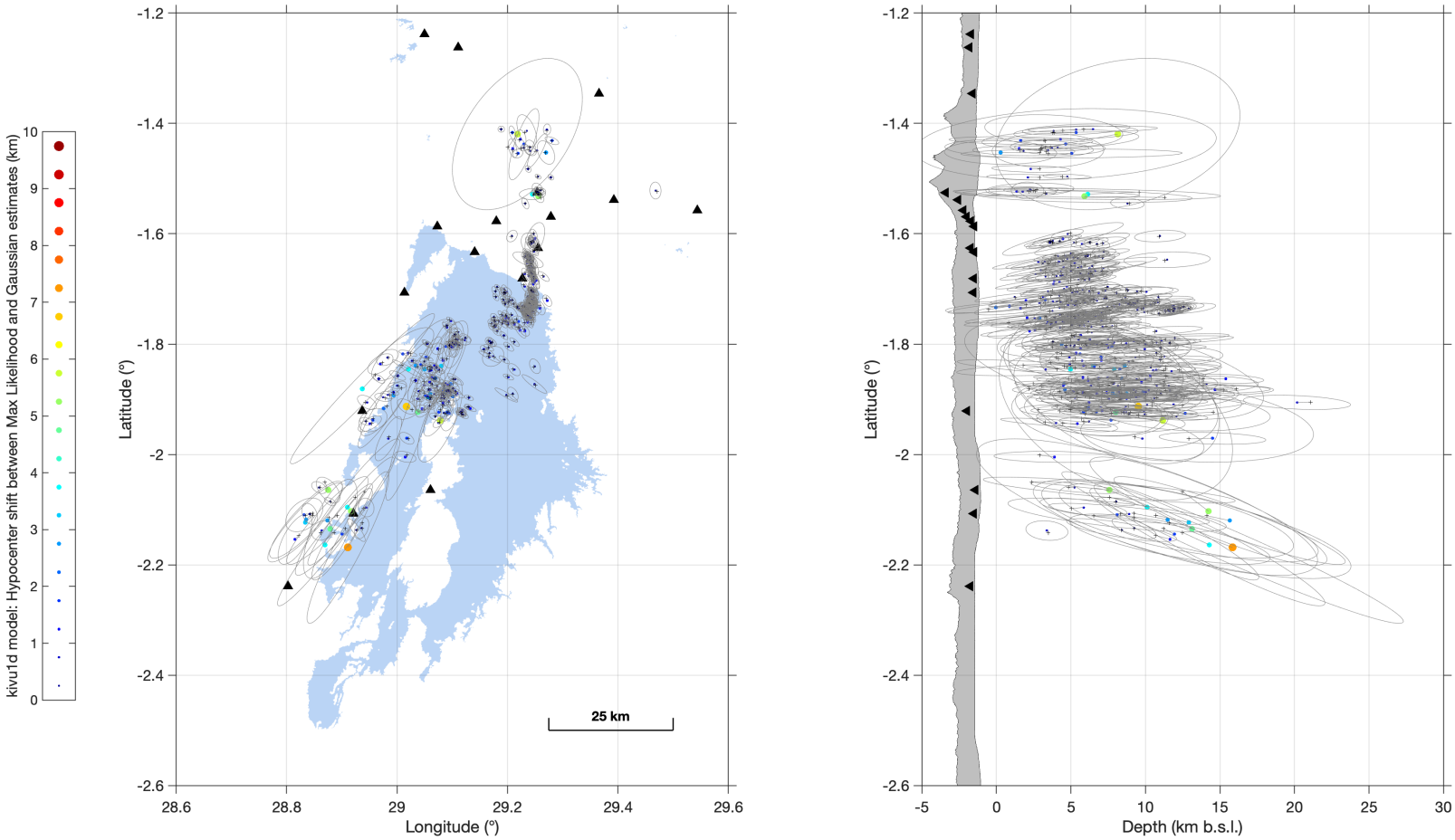

FIGURE 3.18: Using the Kivu 1D model, comparison between computed MaxL (black crosses) and Gaussian solutions (colored circles) obtained with NonLinLoc for 410 events. The color scale corresponds to the distance (in km) between both solutions (clipped at 10 km).

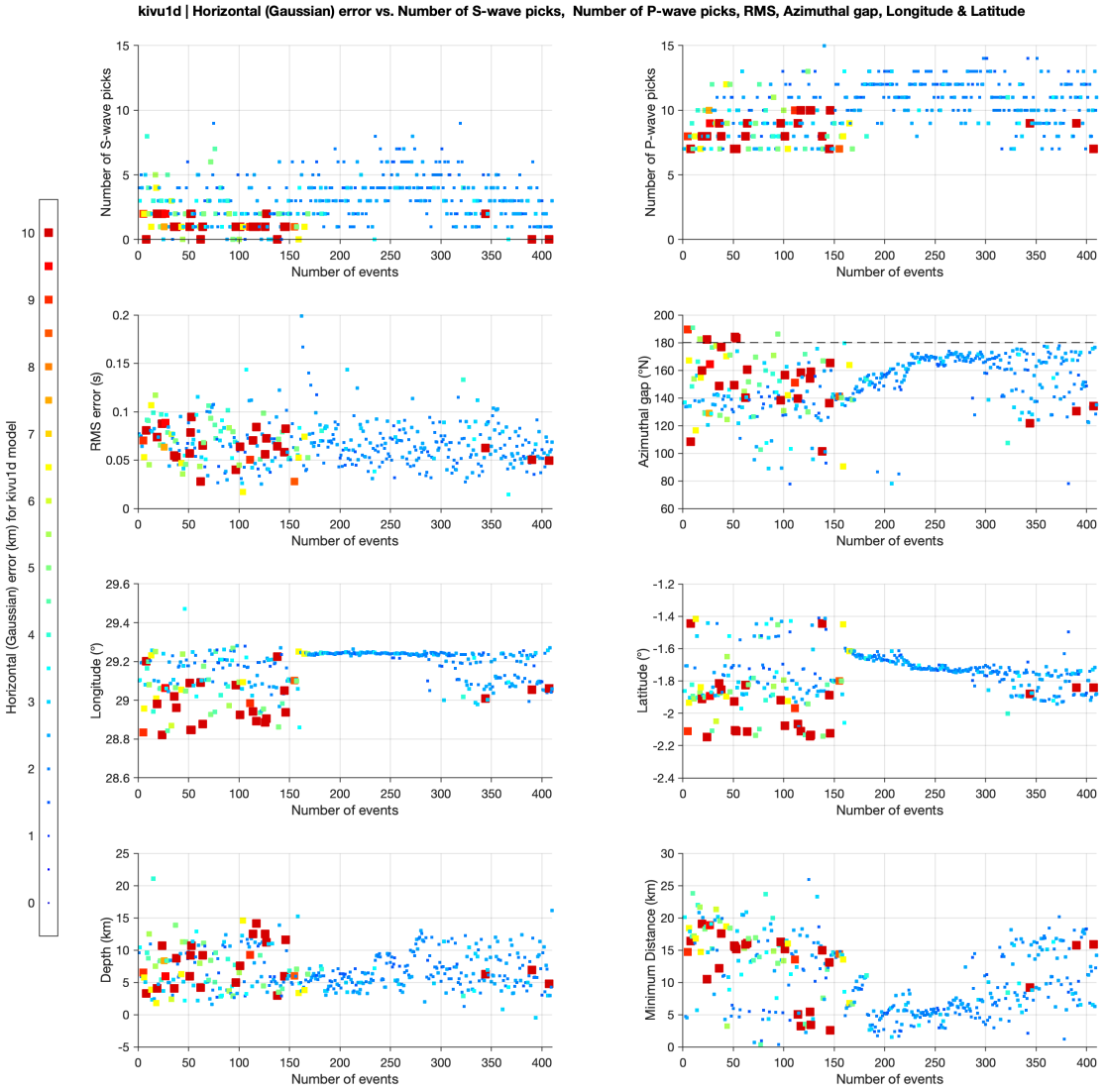

FIGURE 3.19: Using the Kivu 1D model, computed maximum horizontal (Gaussian) error MaxERH (in km) for 410 events as a function of number of S-wave picks, number of P-wave picks, RMS error, azimuthal gap, longitude, latitude, depth and minimum distance to the seismic stations. Marker size and colors are proportional to MaxERH. The color scale ranges between 0 and 10 km (i.e., values exceeding 10 km are set to 10 km).

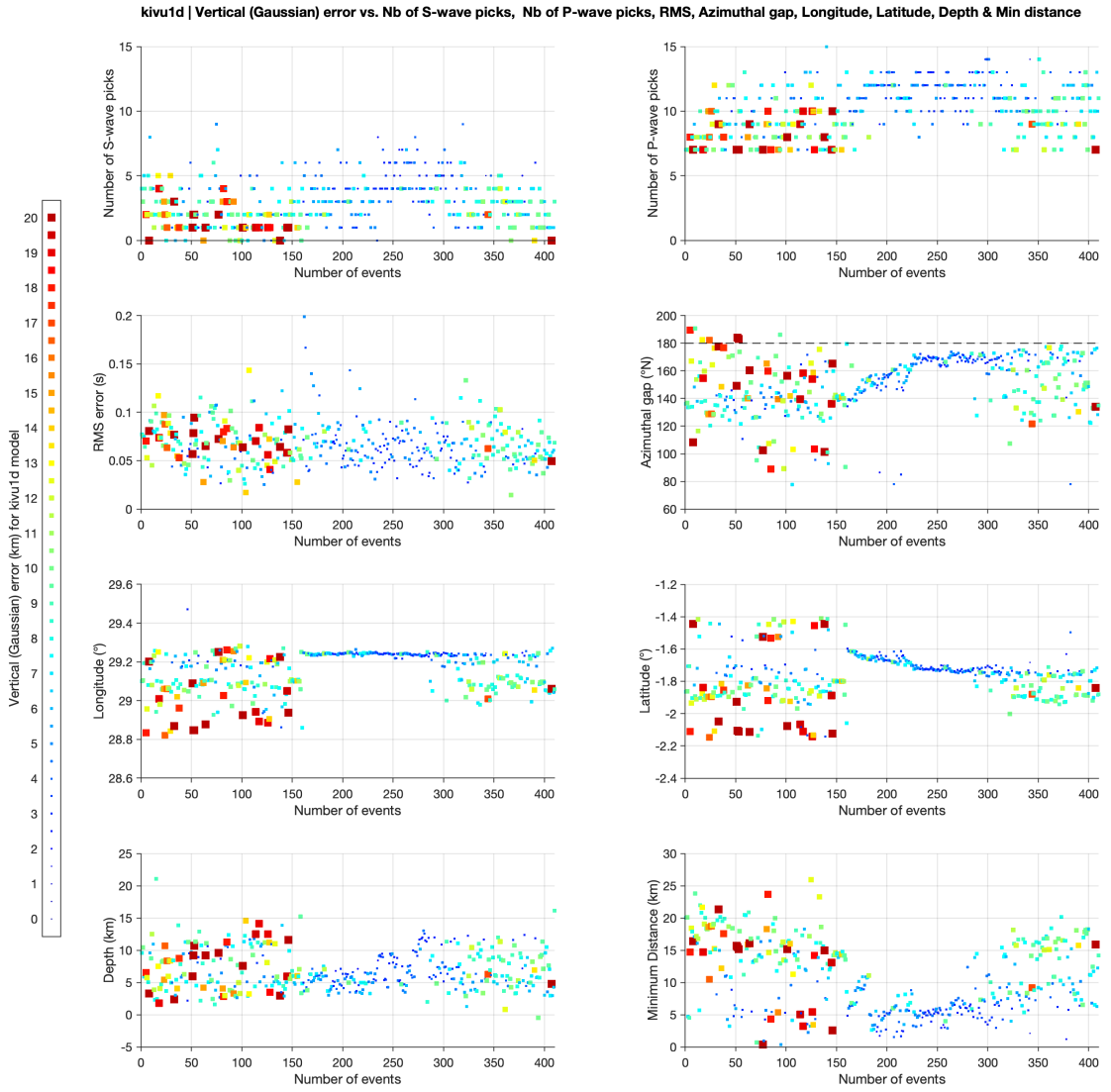

FIGURE 3.20: Using the Kivu 1D model, computed maximum vertical (Gaussian) error MaxERZ (in km) for 410 events as a function of number of S-wave picks, number of P-wave picks, RMS error, azimuthal gap, longitude, latitude, depth and minimum distance to the seismic stations. Marker size and colors are proportional to MaxERZ. Note that the range of the color scale is twice the one used for MaxERH (0 to 20 km).

the ones when using P- and S-phases. However, when plotting Gaussian estimates (ellipsoids and centers), we notice some very large errors with ellipsoids exceeding 100 km and centers of ellipsoid that largely deviate from the MaxL estimates. The importance of using different seismic phases for better constraining the location uncertainty is clearly highlighted with this example.

In conclusion, the Kivu 1D velocity model (including P-wave station correction terms) shows a minimal hypocenter shift between the MaxL and Gaussian estimates compared to the routine velocity model (Mavonga et al.) (Figure 3.24). Two significant biases are observed when using the former routine model: the VVP events are overall much deeper, and those in the Lake Kivu basin become shallower (Figure 3.25). Errors with the Kivu 1D model are significantly minimized by the correction of station delays (Figure 3.18), whose values are in accordance with the known geological features (Figure 3.12), confirming the suitability of the new model for the Kivu rift region.

Before launching the VELEST inversion process, we carefully selected a dataset of 410 events (see section 3.3). Once the final solutions were obtained (1D minimum model and hypocenters), our analysis based on NonLinLoc results highlighted several events with large location uncertainty. The main factors influencing the size of errors were the number of observations, the geometry of the network, and the distance to the seismic stations. These "bad" events (i.e., events with poorly constrained hypocenter solutions) should be disregarded for deriving a 1D minimum model. In Figure 3.26, we remove events with total horizontal error (MaxERH) exceeding 5 km and vertical error (MaxERZ) exceeding 10 km (see also Figures 3.27 and 3.28). The dataset is now restrain to 324 events with corresponding small location uncertainty. Most of events at the extreme north (Nyamulagira volcano) and at the extreme south (Lwiro) are consequently removed. Another round of VELEST inversion using this reduced dataset does not lead to different model parameters (velocity, station delays, hypocenters), so removing these events have negligible effects. However, this result could also imply that the final model is strongly driven by a particular cluster of events (the "syn-eruptive/dyke intrusion" subdataset for instance). In such a case, station correction terms may be also inappropriate for events located outside this spatial cluster, which would be a strong limitation of our final model. In the next section, we exclude this potential issue with a final validation procedure based again on NonLinLoc.

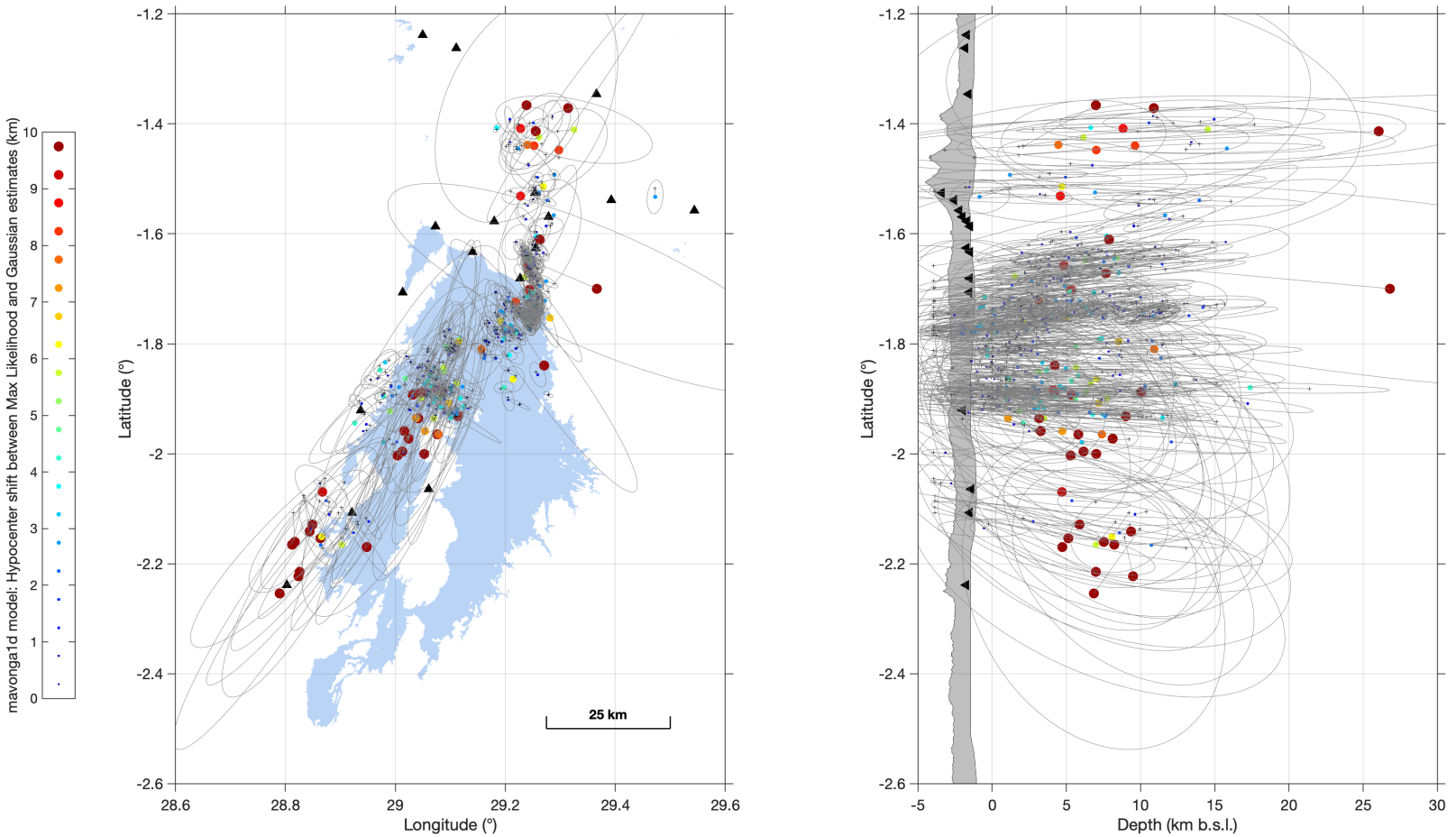

FIGURE 3.21: Using the routine velocity model of T. Mavonga et al. (2010), comparison between MaxL (black crosses) and Gaussian solutions (colored circles) obtained with NonLinLoc for 410 events. The color scale corresponds to the distance (in km) between both solutions (clipped at 10 km).

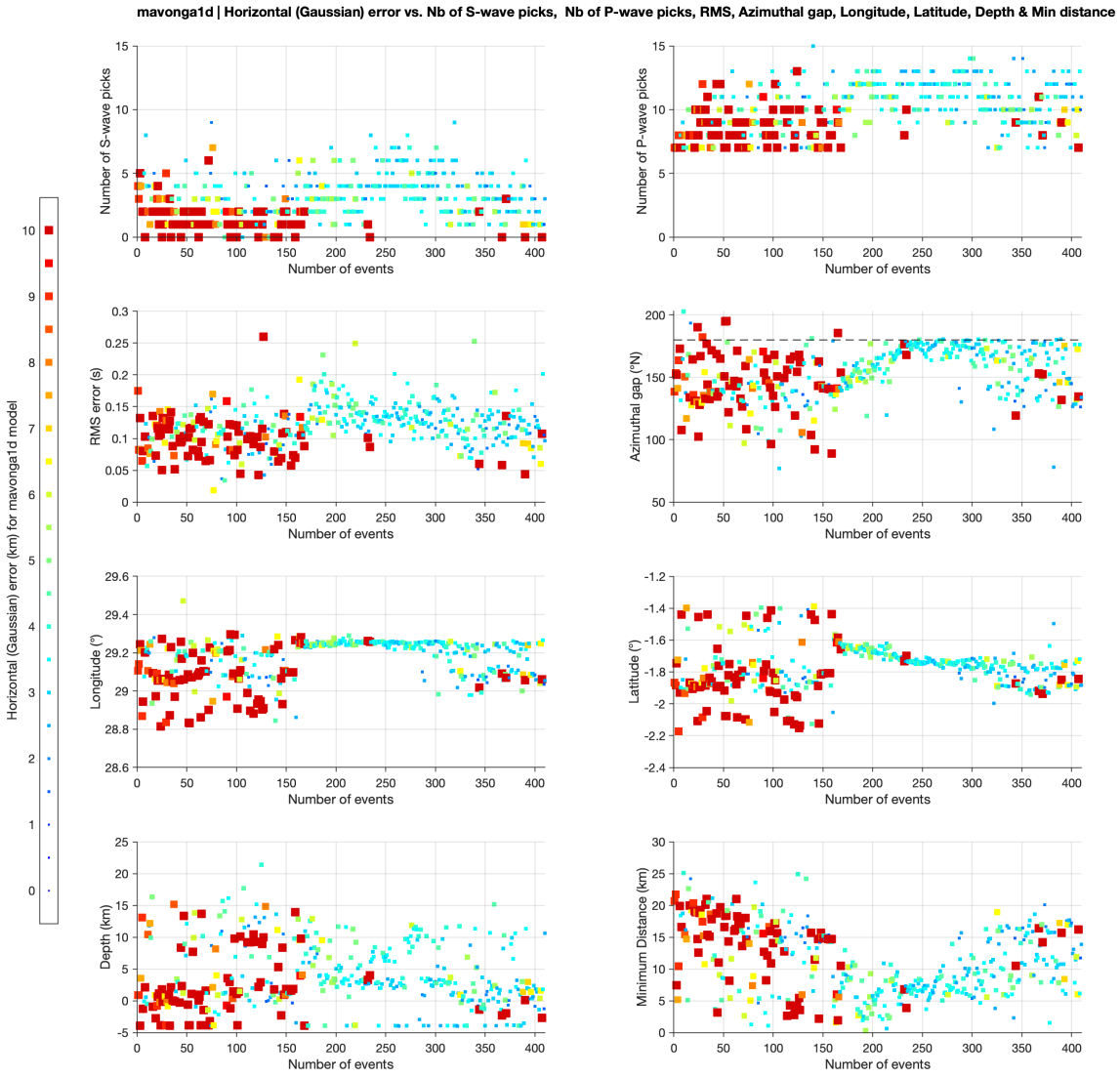

FIGURE 3.22: Using the routine velocity model of T. Mavonga et al. (2010), computed maximum horizontal (Gaussian) error MaxERH (in km) for 410 events as a function of number of S-wave picks, number of P-wave picks, RMS error, azimuthal gap, longitude, latitude, depth and minimum distance to the seismic stations. Marker size and colors are proportional to MaxERH. The color scale ranges between 0 and 10 km (i.e., values exceeding 10 km are set to 10 km).

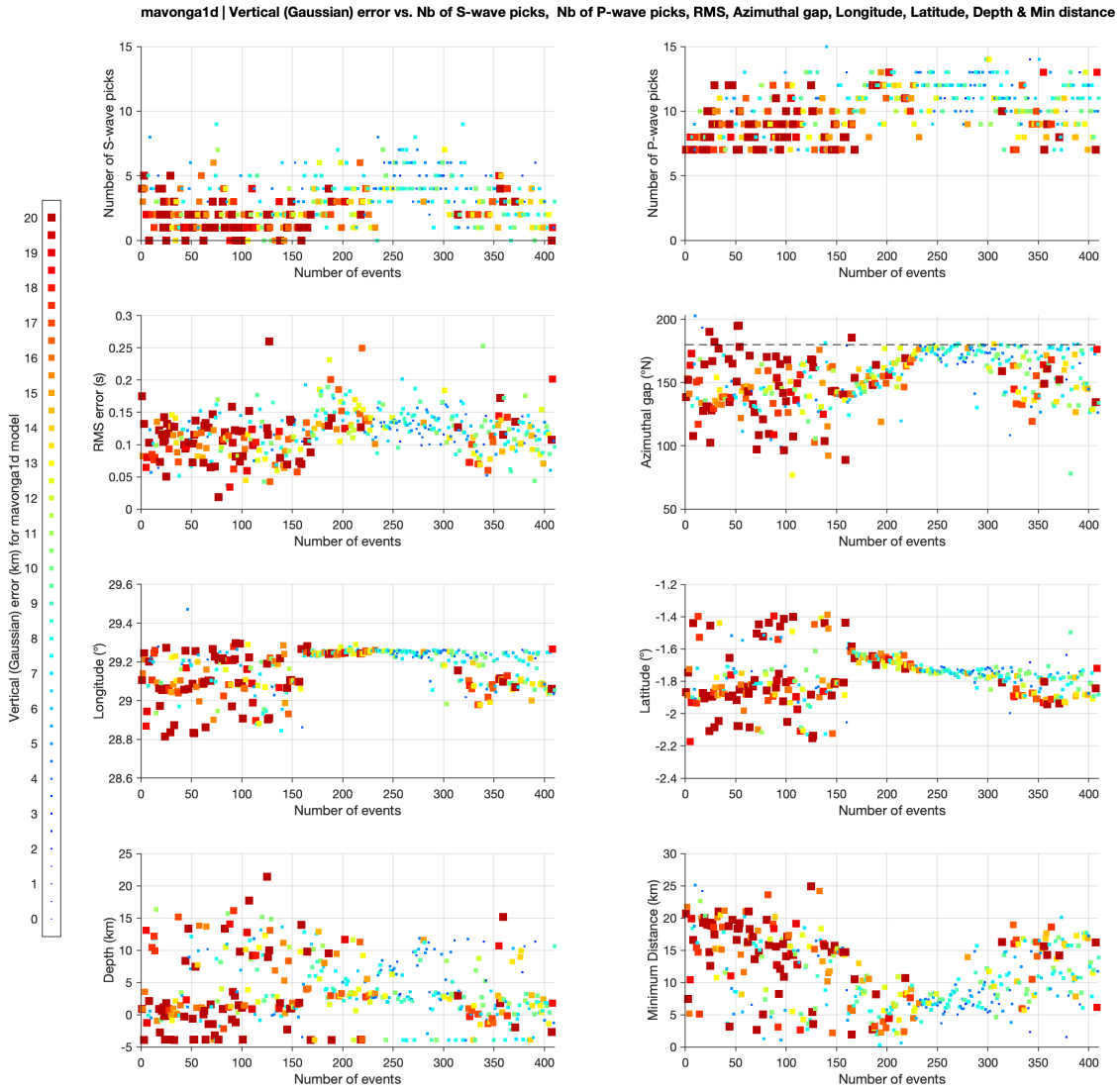

FIGURE 3.23: Using the routine velocity model of T. Mavonga et al. (2010), computed maximum vertical (Gaussian) error MaxERZ (in km) for 410 events as a function of number of S-wave picks, number of P-wave picks, RMS error, azimuthal gap, longitude, latitude, depth and minimum distance to the seismic stations. Marker size and colors are proportional to MaxERZ. Note that the range of the color scale is twice the one used for MaxERH (0 to 20 km).

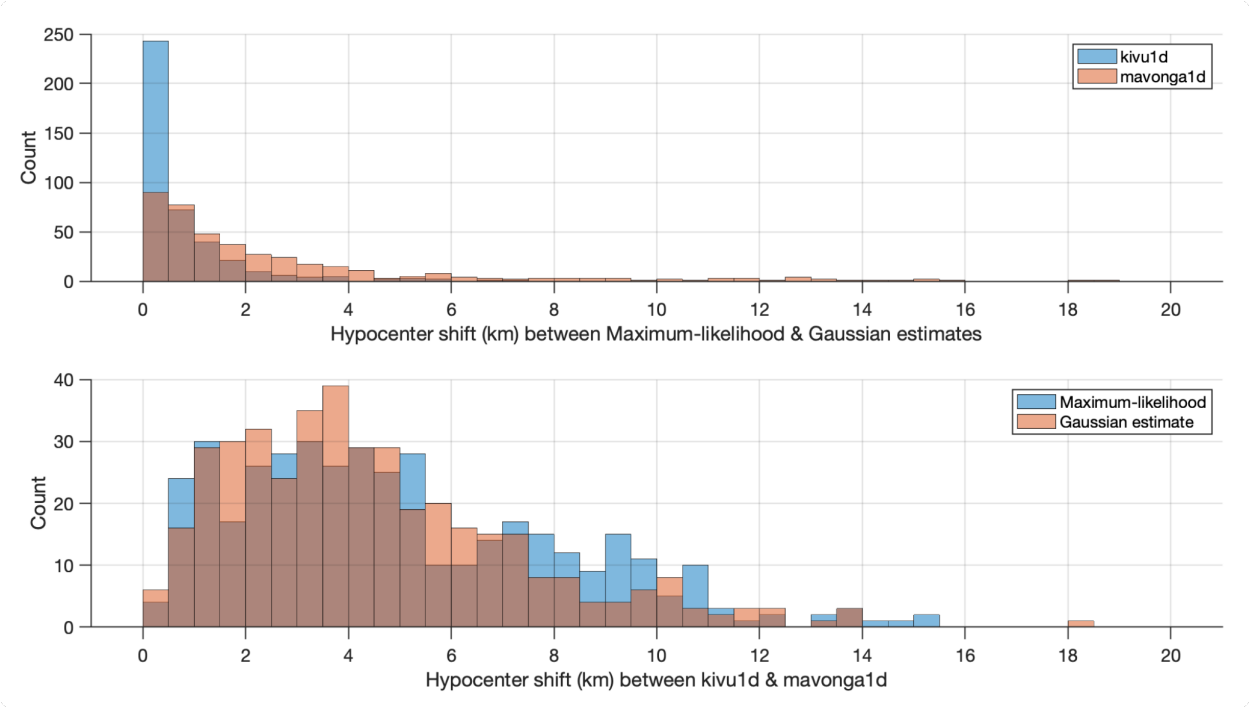

FIGURE 3.24: **(Top)** Histograms showing the hypocenter shift (in km) between the MaxL and Gaussian solutions using the Kivu 1D model (blue) and Mavonga et al. model (red). **(Bottom)** Hypocenter shift between both models for MaxL solutions (blue) and Gaussian estimates (red).

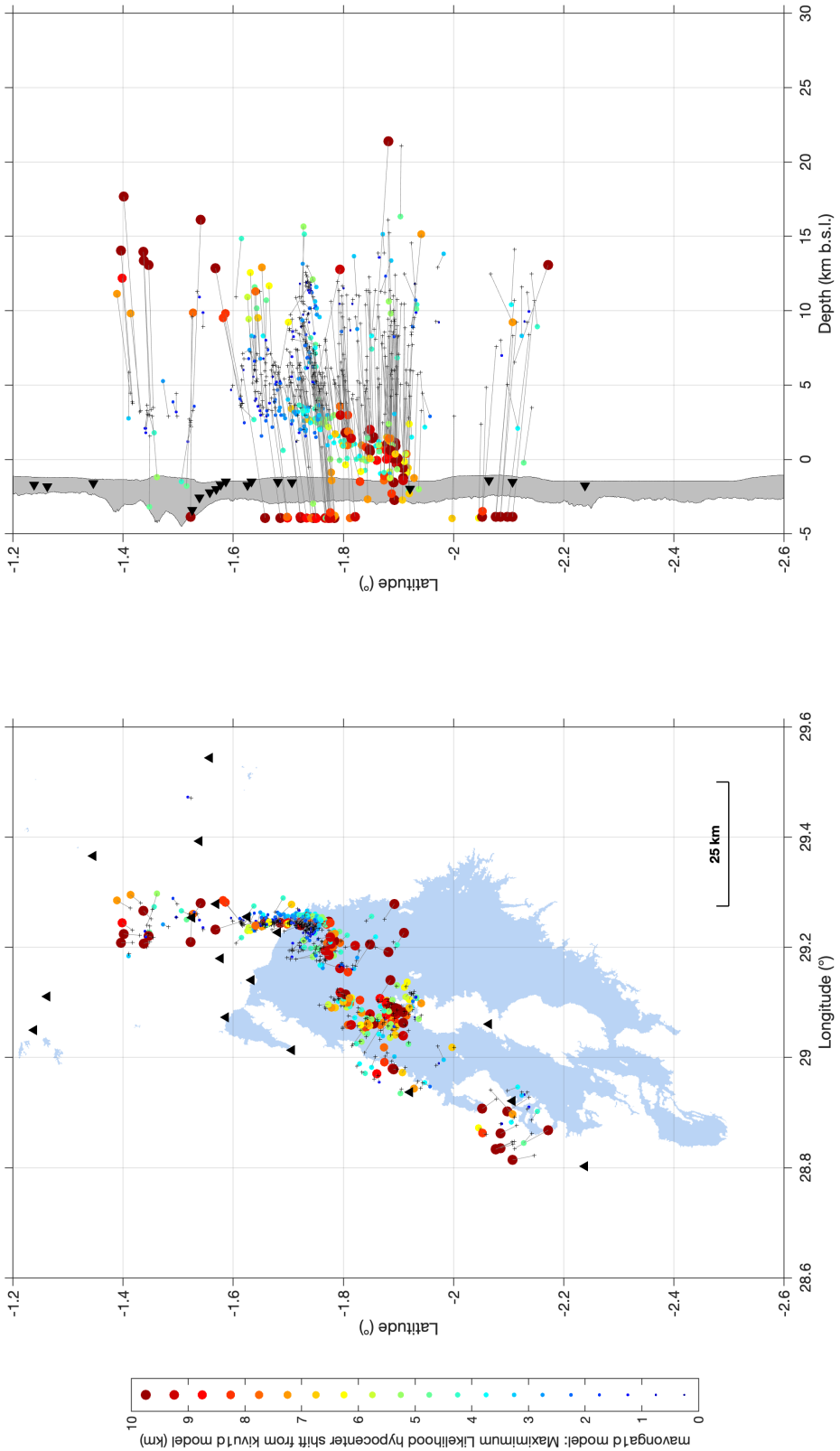

FIGURE 3.25: Distance (in km) between MaxL solutions obtained with the Kivu 1D model (black crosses) and the Mavonga et al. model (colored circles). The color scale corresponds to the distance (in km) between both solutions (clipped at 10 km).

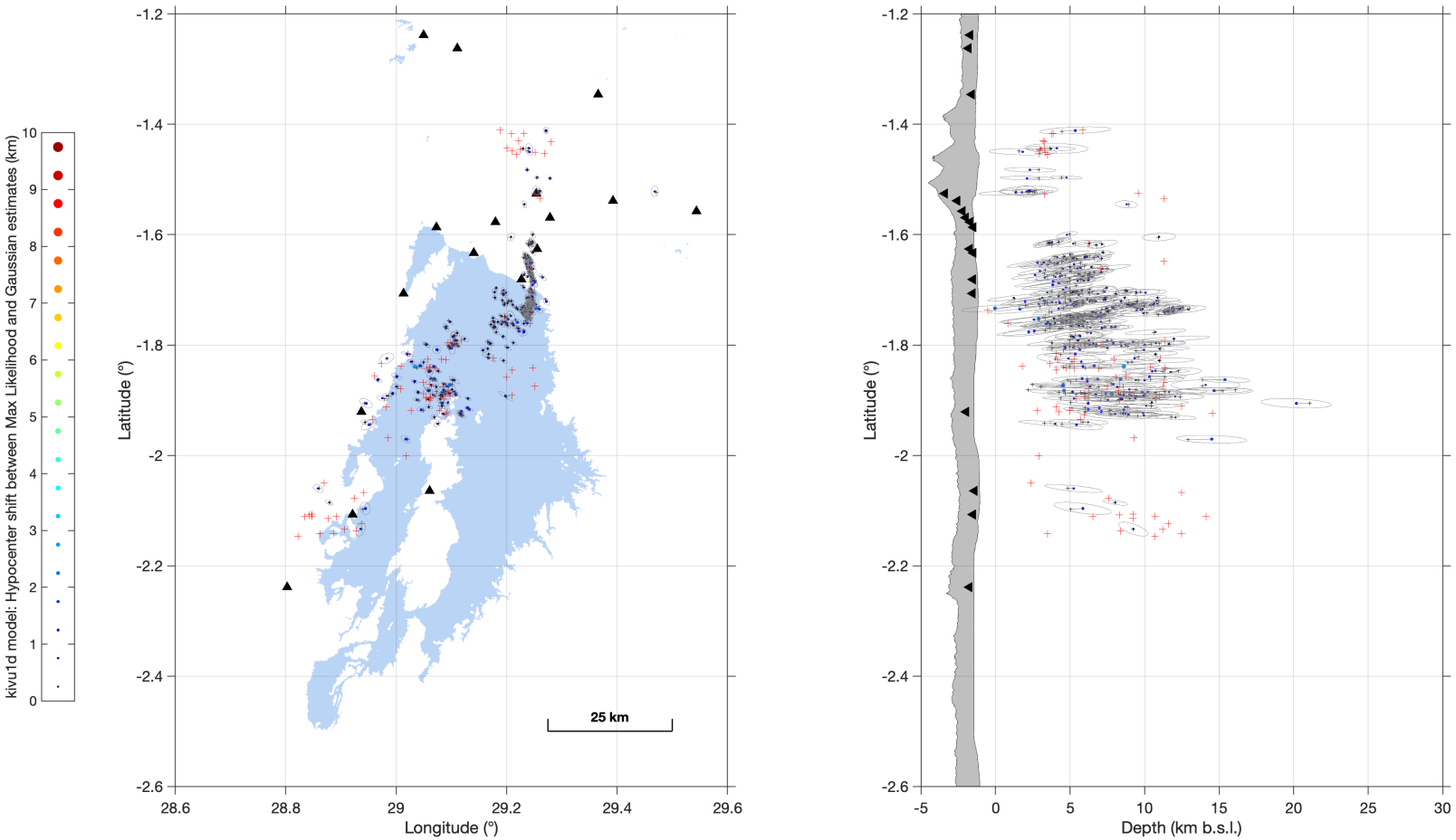

FIGURE 3.26: Final dataset (324 events) after excluding "bad events" from the initial dataset (410 events). Black crosses are MaxL solutions, colored circles (center of ellipsoid) and gray ellipses are Gaussian estimates. The red crosses are deleted events. Marker size and color of the Gaussian estimate is proportional to the distance (in km) from the MaxL solution (clipped at 10 km).

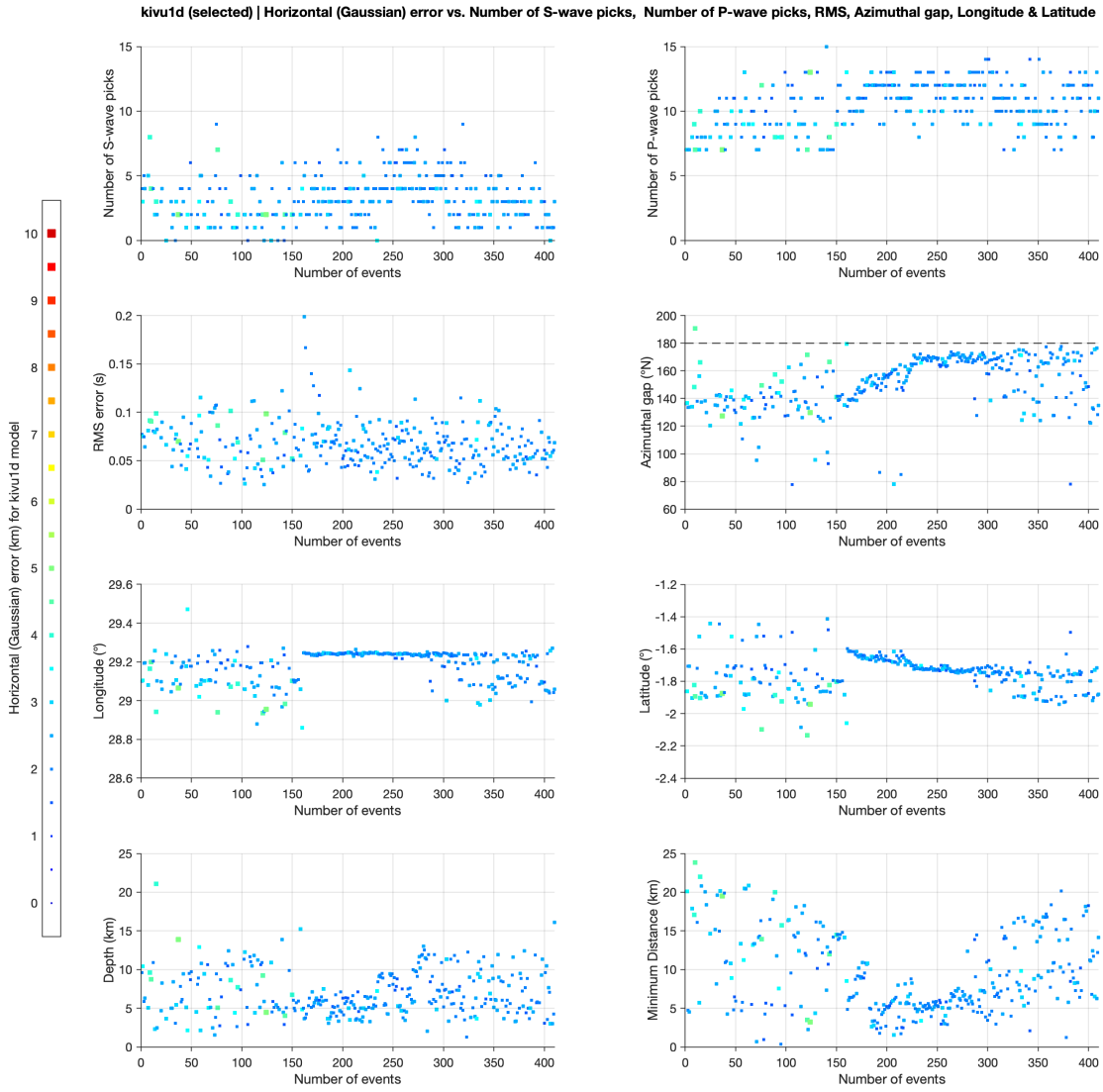

FIGURE 3.27: Same as Figure 3.19 after excluding "bad events" (see text). Kivu 1D model: Maximum horizontal (Gaussian) error MaxERH (in km) for 324 events as a function of number of S-wave picks, number of P-wave picks, RMS error, azimuthal gap, longitude, latitude, depth and minimum distance to the seismic stations. Marker size and colors are proportional to MaxERH. The color scale ranges between 0 and 10 km (i.e., values exceeding 10 km are set to 10 km).

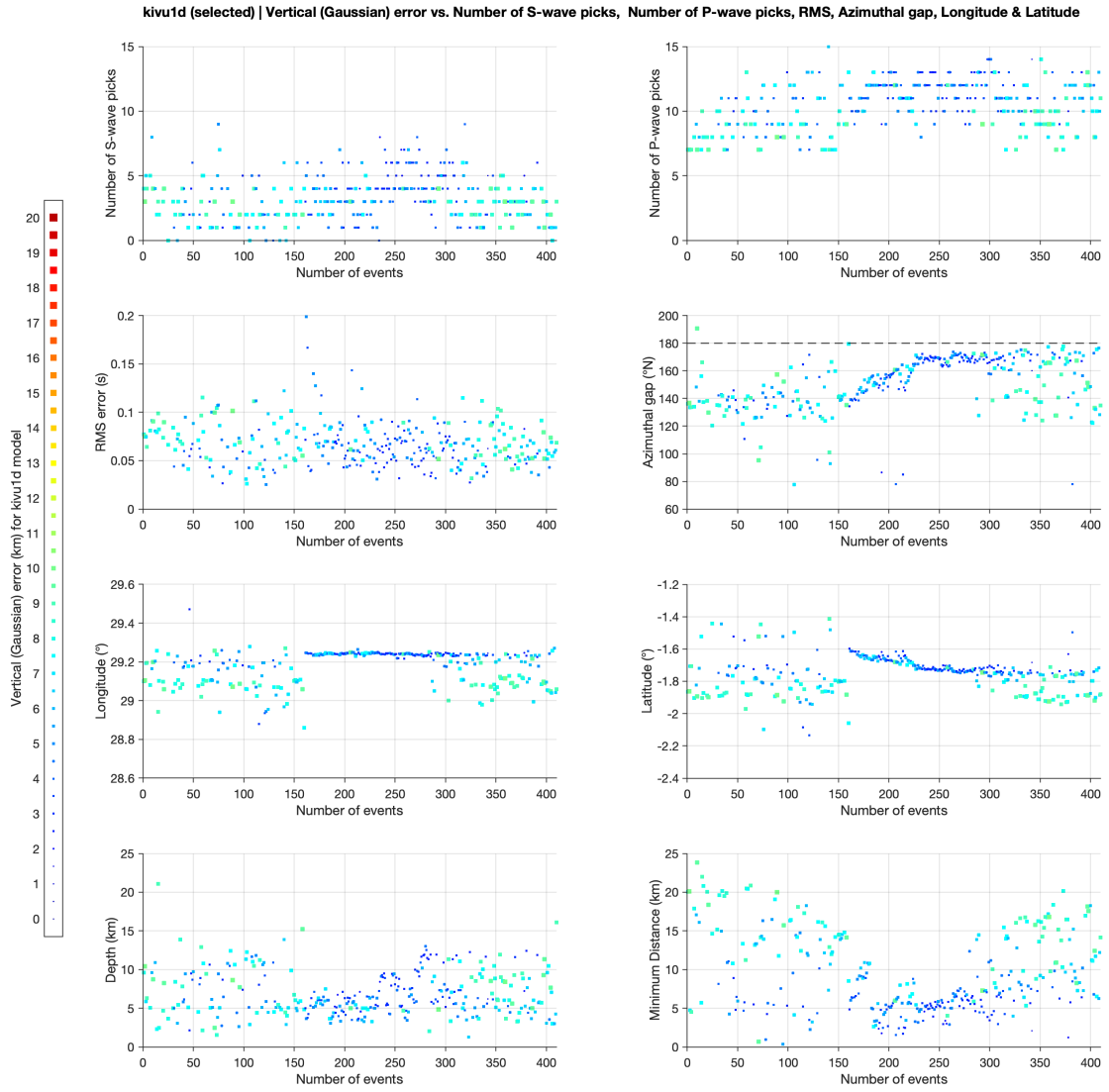

FIGURE 3.28: Same as Figure 3.20 after excluding "bad events" (see text). Maximum vertical (Gaussian) error MaxERZ (in km) for 324 events as a function of number of S-wave picks, number of P-wave picks, RMS error, azimuthal gap, longitude, latitude, depth and minimum distance to the seismic stations. Marker size and colors are proportional to MaxERZ. Note that the range of the color scale is twice the one used for MaxERH (0 to 20 km).

3.6 Final validation of the Kivu 1D minimum model and station correction terms

We divide the "best events" dataset (324 events, see previous section) into three spatial clusters (Figure 3.29):

- "North" dataset : events plotted in red, above latitude of -1.75°N;
- "South" dataset : events plotted in blue, below latitude of -1.75°N;
- "Eruption/Dyke" dataset : events plotted in green, within a box defined by longitude limits [29.225 : 29.255]°E and latitude [-1.765 : -1.61]°N.

For each subdataset, we launch NonLinLoc using the model parameters obtained from the final VELEST outputs (1D minimum model, hypocenters, P-wave delays). NonLinLoc is able to produce station correction terms from a specific dataset, equal to the sum of the mean residuals obtained at each station and the corresponding input correction terms. We can now compare if station delays derived from a subdataset are identical to the delays obtained for the full dataset. In other words, we want to know if each station correction term is not affected by the path from specific source regions (path effects) and rather reflects local conditions around the station site (site effects). Moreover, because we use S-phase picks, we can derive S-wave delays that could be further used as station correction terms for S-wave arrival times if consistent values are obtained for each subdataset. Contrary to P-wave correction terms, these S-wave correction terms are thus obtained with NonLinLoc only, outside the VELEST inversion process.

Results are depicted in Figure 3.30. Initial (input correction terms) and final (mean NonLinLoc's residuals + input correction terms) P-wave delays for all subdatasets are in very good agreement. This means that the residuals between observed and predicted arrival times at all stations tend to zero for all subdatasets. Hence, we confirm the applicability of these P-wave correction terms with the 1D minimum model for any events located in the Kivu region with the KivuSNet stations. Furthermore, we observe that newly derived S-wave delays remain consistent across the three spatial clusters, despite much less observations. As expected, the delays are larger than for P-wave but remain below 1 second. They also follow the same trend than P-wave delays, e.g., high positive anomalies for BULE/RSY and negative anomaly for SAHA. We can thus consider these S-wave delays as robust station correction terms.

As final step, we rescan all waveforms from the 324 events and picked P and S-wave arrival times that would not be kept at first glance due to unclear phase onsets (considering high-quality criteria initially set). This includes observations at permanent stations TGO and MUSK, operational prior to 2020 and excluded from the VELEST process (see section 3.3). The temporary stations MBL1, MBL2, MBLWI deployed during the post-eruptive seismic crisis in 2021 were also added. Another NonLinLoc run with these new observations gave final P- and S-wave corrections terms (Figure 3.31 and Table 3.3). As observed with the previous test (Figure 3.30), the station correction terms for P- and S-wave remain consistent, regardless of new observations/stations added or which subdataset of events is considered. We ignore delay estimates if less than 3 observations per station/phase;

hence, there is no S-wave delays for 3 permanent stations (TGO, KTSH, MUSK) and 2 temporary (MBL1 and MBL2). The Figure 3.32 depicts the final locations of these 324 events using the Kivu 1D minimum model (Figure 3.10) after correction for P- and S-wave delays (Table 3.3).

Station	**Lat. (°)**	**Long. (°)**	**Elev. (m)**	**P (s)**	**S (s)**	**Mag.** M_L
RSY	-1.5768	29.1798	1700	0.39	0.91	0.028473
BULE	-1.6330	29.1405	1482	0.35	0.94	-0.059926
NYI	-1.5258	29.2540	3411	0.19	0.61	-0.24542
SAKE	-1.5863	29.0732	1477	0.10	0.54	-0.095291
BUTK	-1.5388	29.3923	2557	0.04	0.09	-0.058801
KBTI	-1.5690	29.2785	1992	-0.02	0.13	-0.034849
LWI	-2.2392	28.8025	1760	0.00	0.28	0.033033
MUNI	-1.6258	29.2553	1722	-0.06	0.14	-0.059926
GOM	-1.6812	29.2267	1524	-0.07	0.04	0.36107
RGB	-1.3458	29.3655	1610	-0.15	-0.24	-0.067397
KALEH	-2.1072	28.9208	1508	-0.08	0.00	-0.17996
KTSH	-1.2383	29.0500	1714	-0.15	0	-0.26557
IDJ	-2.0645	29.0607	1415	-0.22	-0.07	0.031274
LBGA	-1.2620	29.1110	1809	-0.29	-0.42	0.52721
BOBN	-1.7063	29.0132	1531	-0.25	-0.15	0.077422
SAHA	-1.5573	29.5435	2217	-0.30	-0.58	0.29825
NYAB	-1.9210	28.9367	1976	-0.29	-0.23	-0.14908
TGO	-1.2081	29.2732	1415	-0.03	0	0
MUSK	-1.5364	28.9945	2075	-0.28	0	0
MBLWI	-1.8847	29.3508	2010	-0.03	-0.04	-0.25517
MBL1	-2.1137	29.2925	1669	-0.06	0	-0.10825
MBL2	-1.7485	29.2985	1832	0.02	0	-0.24673

TABLE 3.3: Final station correction terms. Stations list with, from left to right, the latitude (°N), the longitude (°E), the elevation (m a.s.l.), the P-wave delay (s) and S-wave delay (s) to use with the Kivu 1D minimum model (see Table 3.1). Delays must be subtracted from observed P and S arrival times. The last column gives the correction terms to be added to the first local magnitude scale M_L for the Kivu derived from the same dataset of 324 events (see section 3.7).

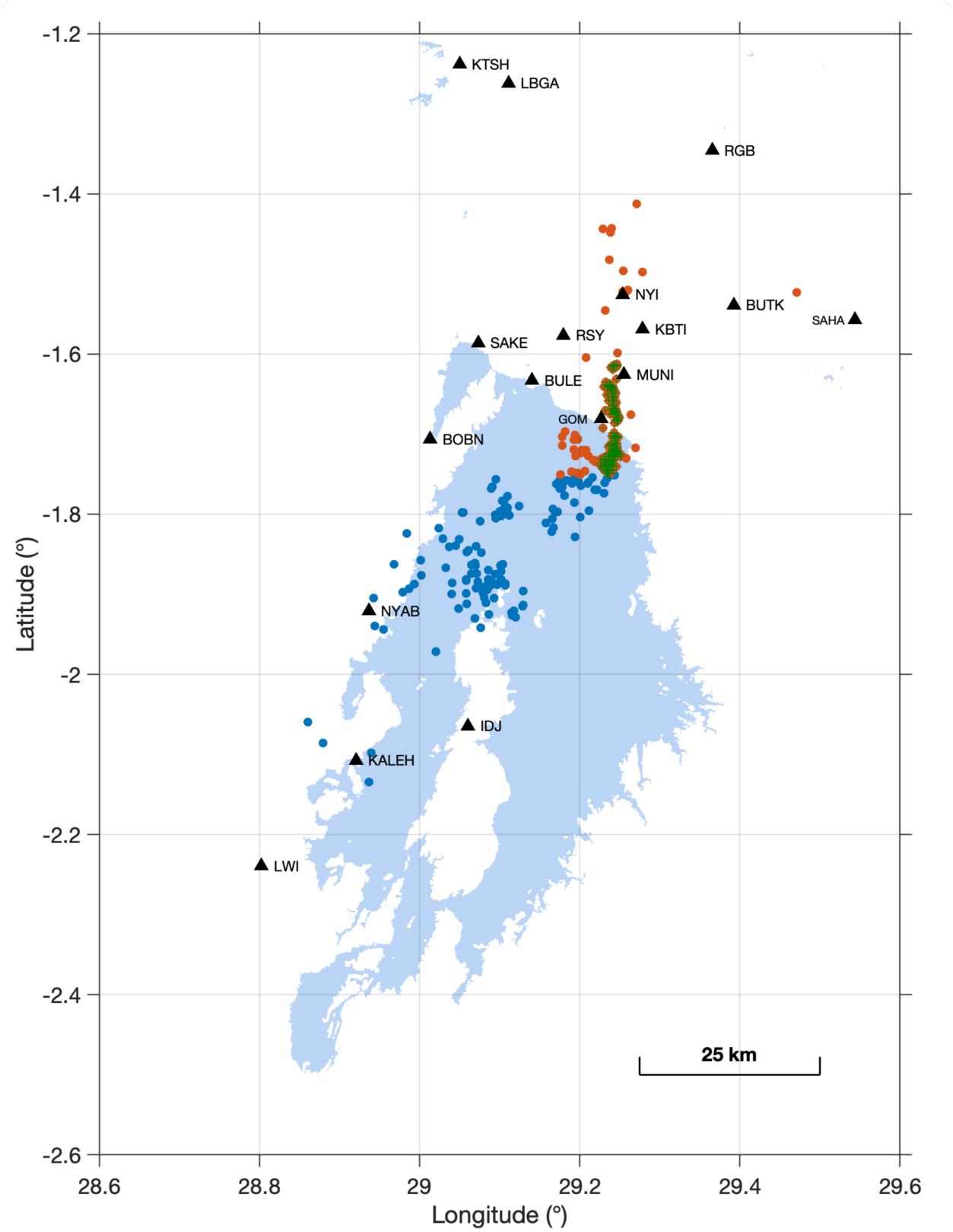

FIGURE 3.29: "Best events" dataset (324 events) divided into three clusters: "North" (red), "South" (blue) and "Eruption/Dyke" (green). Stations are plotted as black triangles.

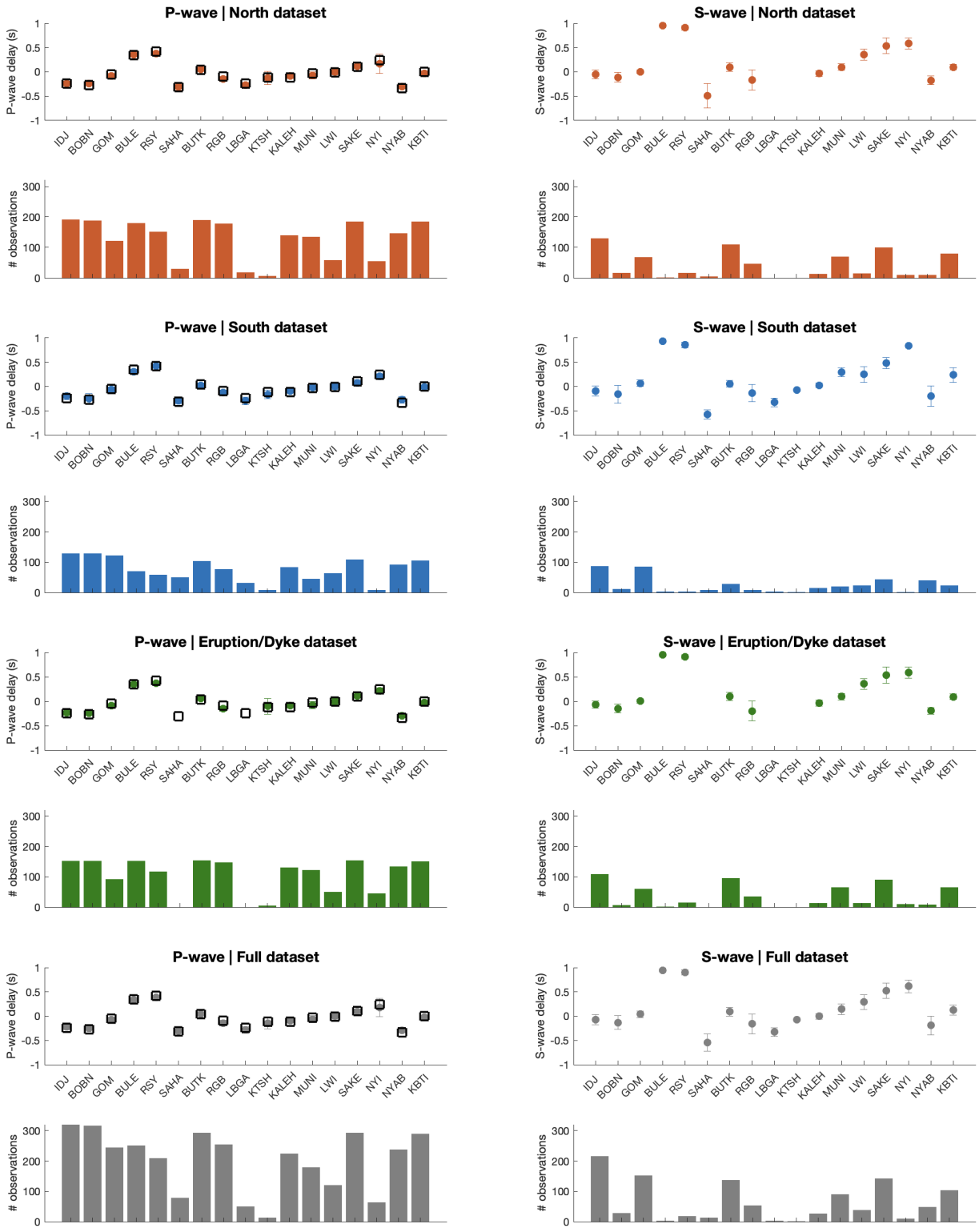

FIGURE 3.30: P-wave delays **(left)** and S-wave delays **(right)** obtained for the three clusters plotted in Figure 3.29. Black squares correspond to correction terms used as inputs (i.e., the ones obtained with VELEST, only applicable to P-wave). Colored circles are average station residuals (i.e., new correction terms) after relocating the three subdatasets with NonLinLoc (error bar correspond to one standard deviation). Histograms indicate the number of observations per station.

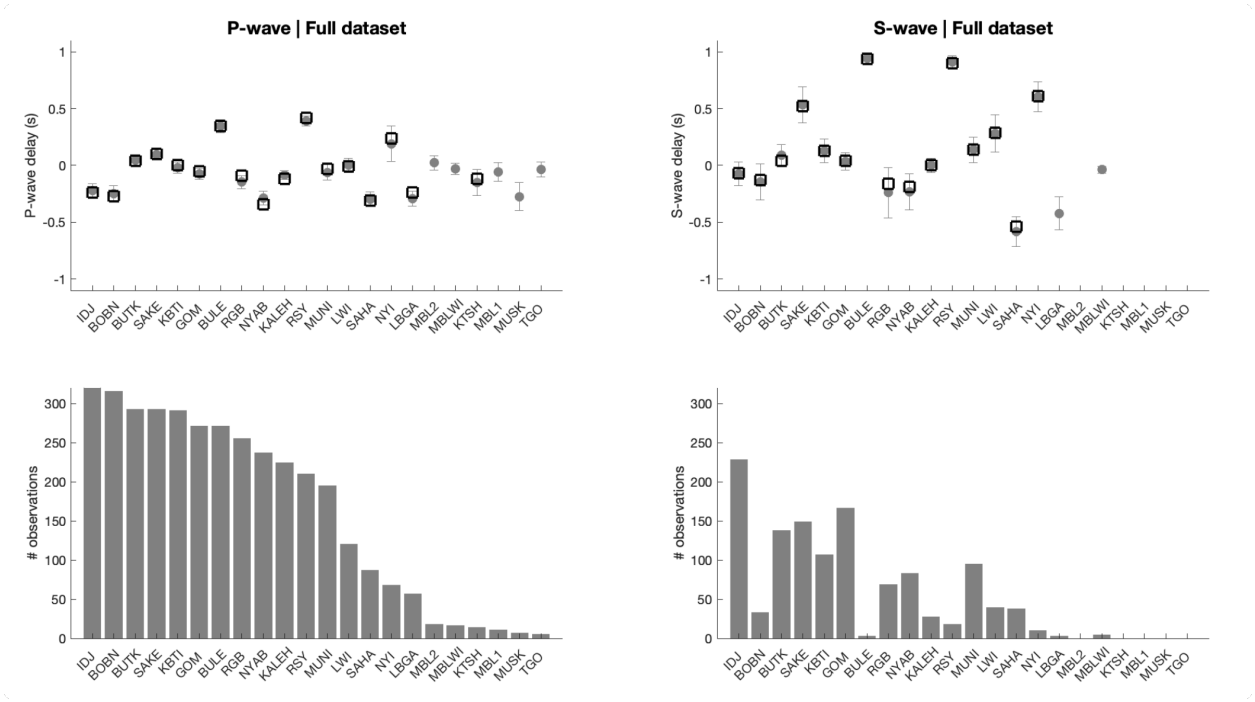

FIGURE 3.31: Final P-wave and S-wave delays after re-scanning waveforms and phase picks and relocating the "best events" dataset (324 events) with NonLinLoc. Black squares correspond to correction terms used as inputs (Figure 3.30 and gray circles correspond to final correction terms (error bar = one standard deviation). Histograms indicate the number of observations per station (sorted in descending order for P-wave delays).

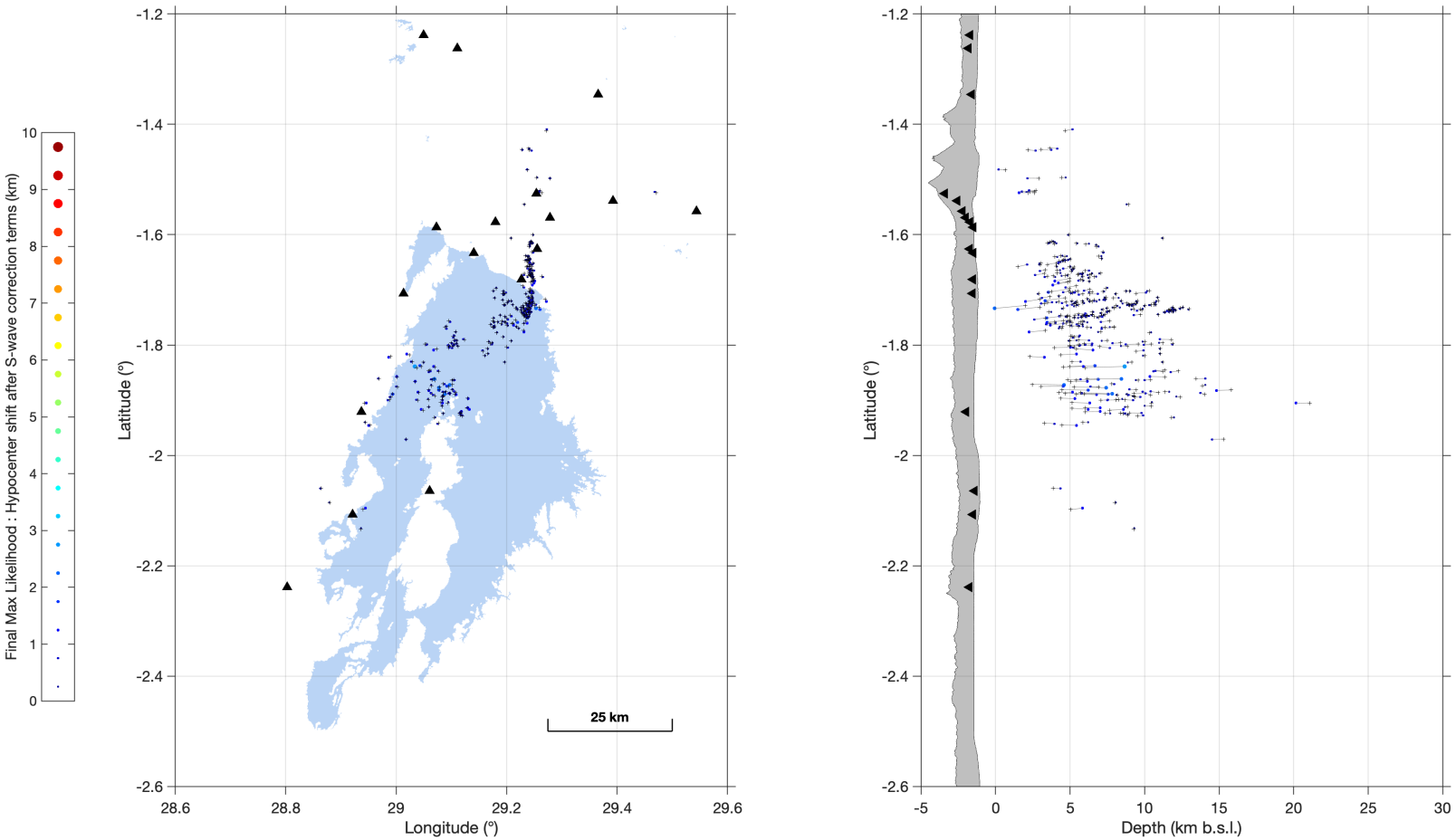

FIGURE 3.32: Final "best events" dataset (324 events) located without S-wave correction terms (black crosses, see Figure 3.26) and after considering new P- and S-wave delays (colored circles, see Figure 3.31). As for previous plots, the color scale corresponds to the distance (in km) between both solutions, set from 0 to 10 km.

3.7 A first local magnitude scale (M_L) for the Kivu region

A local magnitude scale M_L with the corresponding station correction terms was derived based on the final dataset of 324 well-constrained earthquakes (see previous section). This analysis, which was performed by A. Oth (ECGS), is not detailed in this thesis. A comparison between this new scale for the Kivu and the standard M_L scale for Southern California (Hutton & Boore, 1987) is provided in Figure 3.33 for the range 1-5. While both scales give close estimates, one can note that the new scale adjusts estimates for low magnitudes (below 3.5), which are underestimated if the relation for Southern California is applied. The first M_L scale for the Kivu is given by:

$$M_L = log10(A) + 1.898\, log10(R/R_{ref}) - 0.0045\,(R - R_{ref}) + M_{ref} + Sh, \tag{3.20}$$

where A is the maximum amplitude on horizontal components measured on a ground displacement trace (expressed in mm) which has been filtered with the Wood-Anderson response. The static magnification for the Wood-Anderson instrument is 2080, which means A (in mm) must be multiplied by 2080 (Wassermann, 2012). R is the distance (in km), R_{ref} is the reference distance equals to 17 km and M_{ref} is the reference magnitude equals to 2. Sh are the stations correction terms given in Table 3.3.

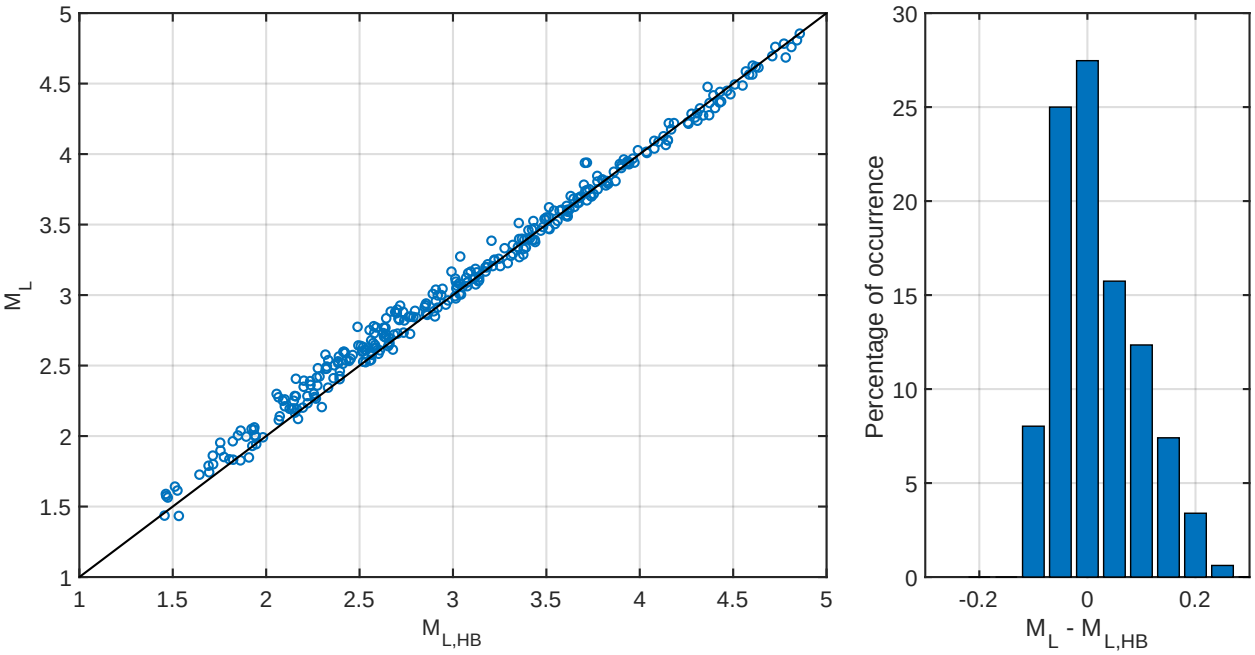

FIGURE 3.33: Comparison of local magnitude estimates for the selection of 324 earthquakes using the newly derived scale (y-axis) and the one applied for Southern California (M_L, HB) (x-axis). The histogram on the right show the distribution of difference between both estimates, mostly below 0.2 unit of magnitude.

3.8 Conclusion

This Chapter addresses a fundamental aspect in seismology for improving further studies in the Kivu Rift relying on the local seismic velocity structure. It provides a detailed methodological approach that led to the establishment of a new robust local velocity model referred to as "Kivu 1D".

This study was made possible thanks to a dense data set that can be divided into 3 temporal sub-datasets related to seismicity patterns in the area recorded by the KivuSNet before, during and after the May 2021 flank eruption at Nyiragongo. These include VVP's events (located beneath both active volcanoes and related to magmatic activity), Lake Kivu's events (mostly the western part of the Lake Kivu basin over the full period 2015-2021) and 2021 eruption's events (between Nyiragongo and the north of the Lake Kivu, near the city of Goma).

The data inversion framework was based on the VELEST software consisting in many trial-error operations. A total of 4156 P-wave picks from 410 seismic events were initially used (then refined to 324 events) to produce the 1D P-wave minimum velocity model with corresponding station delays. The final Kivu 1D velocity model is defined by 4 layers, with velocities ranging from 5.3 km/s for the shallowest layer to 6.23 km/s at the top of the deepest layer (9 km b.s.l.). The robustness of the new model was validated by stability tests and a comparison of the station delays with the local geology, as required by the method. We deepened this validation procedure by providing an error analysis by comparing the new model with the former ones using the NonLinLoc software. This additional step led us to refine a final dataset of 324 earthquakes. It is important to note that the S-wave velocity model was derived from a Vp/Vs ratio value fixed at 1.71 (using a modified Wadati-diagram approach), and the station correction terms for S-wave are derived from the error analysis stage (NonLinLoc). Lastly, calibrated with the same dataset, the first local magnitude for the region is briefly presented.

Chapter 4

An overview of seismicity patterns in the Kivu rift, 2015-2022

Once the new local velocity model has been obtained, the next stage is to compile a catalog of local earthquakes. A seismic catalog provides a comprehensive record of earthquakes, including their locations, magnitudes, and other relevant parameters. Such a catalog for the Kivu rift region would serve as a basis for studying the spatial and temporal patterns of seismic activity, with the objective of improving our understanding of local tectonic seismicity and to identify patterns in the volcanic events related to magmatic processes. The last hapter of this thesis can be seen as a first dive into this dense dataset, leading to an overview of the seismicity patterns during the period 2015-2022. This preliminary work should motivate further studies in the Kivu rift using the Kivus-Net data with newly derived seismological models. Part of this work was presented as poster presentations at the 2023 AGU (American Geophysical Union) fall meeting and at the 2024 SSA (Seismological Society of America) Annual Meeting under the title *"Seismological models and seismicity patterns in the Kivu rift and Virunga volcanic Province (D.R. Congo)"* by J. Subira, J. Barrière, C. Caudron, A. Oth, N. d'Oreye, A. Hubert-Ferrari and F. Kervyn.

4.1 Earthquake location method

Seismic events between July 2015 to end of June 2022 are detected and located using an in-house program called XCloc developed at ECGS by J. Barrière under the MATLAB environment (Barrière et al., 2022, 2023b). This method is part of a set of automatic techniques commonly referred to as "source-scanning" algorithms (Kao & Shan, 2004), which recently emerged as valuable location tool for events with low signal-to-noise ratio (SNR) and/or emergent onsets, both characteristics typical of volcanic environments. These methods, which mostly consist in the application of delay-and-sum processes (Grigoli et al., 2013; Langet et al., 2014) or cross correlation-based approaches (Gal et al., 2021; Poiata et al., 2016), rely on the computation of a characteristic signal-time function at each single station, such as short-term/long-term average ratio, kurtosis or envelope waveforms.

The XCloc method use a similar approach to the one employed by Poiata et al. (2016) or Gal et al. (2021) based on station pair time delay estimate (TDE) functions obtained by cross correlation. The principle of this interstation cross-correlation technique is similar to the 2D tremor location procedure presented in Chapters 1 and 2 where TDE functions are calculated from long-duration records to identify sources of continuous noise.

First, differential 3D travel-time grids need to be calculated once for each station pair using the 1D Kivu velocity model. To achieve this, the program uses NonLinLoc's Vel2Grid and Grid2Time routines implementing the Eikonal finite-difference scheme of Podvin and Lecomte (1991). Second, for each detected event using a network-based STA/LTA detector, single-station characteristic functions are obtained by transforming the signal into a moving kurtosis function for characterising P-wave and into an envelope function for S-wave. Third, XCloc computes TDE functions for each station pair (i.e., cross-correlation procedure) and the grid-search is performed to get the most probable source region.

Similarly to Poiata et al. (2016), the program does not perform an explicit grid-search over all possible locations (i.e., nested loops over all grid points). Instead, it maps directly the TDE functions onto the 3D grids by assigning time delays to grid positions (3D matrix indices), thereby significantly enhancing computational efficiency. Once all interstation cross-correlation functions are stacked/projected onto the 3D grid, we obtain 3D gridded location coefficients, which can be normalized from 0 to 1 (i.e., the most probable location).

As previously explained in Chapter 3, this grid-search approach allows for a better evaluation of the location error compared to traditional iterative inversion techniques. Similarly to NonLinLoc, XCloc provides two estimates of the final hypocenter solution, the maximum of the location coefficients (i.e., comparable to the maximum likelihood) and the center of the Gaussian ellipsoid (with 68.3% confidence). The confidence ellipsoid is constructed from the gridded location data following the approach of Lomax et al. (2009). In XCloc, this calculation considers the location coefficients as weights (specifically, those greater or equal to 0.8) for estimating the covariance matrix, similar to the method used by the python function "numpy.cov" (https://numpy.org).

As selection criteria for the events plotted in this final part of the thesis, we exclude events that have fewer than 6 good observations (over fewer than 5 stations) and those with a distance between the maximum likelihood and the center of the ellipsoid larger than 10 km. A good observation is defined as one where the difference between the theoretical and calculated arrival time for P- or S-phases is below 0.5 and 1 sec, respectively. Two examples of event locations obtained with XCloc at Nyiragongo and Nyamulagira are provided in Figures 4.1 and 4.2, respectively. A total of 49294 earthquakes were selected to build up a catalogue of the regional seismicity between July 1, 2015 and July 1, 2022. For each earthquake, The catalogue provides its location (latitude, longitude, depth), its origin time, the associated location errors, and the local magnitude M_L (using the new scale presented at the end of Chapter 3). Another calculated attribute is the Frequency Index, which is introduced in section 4.5.

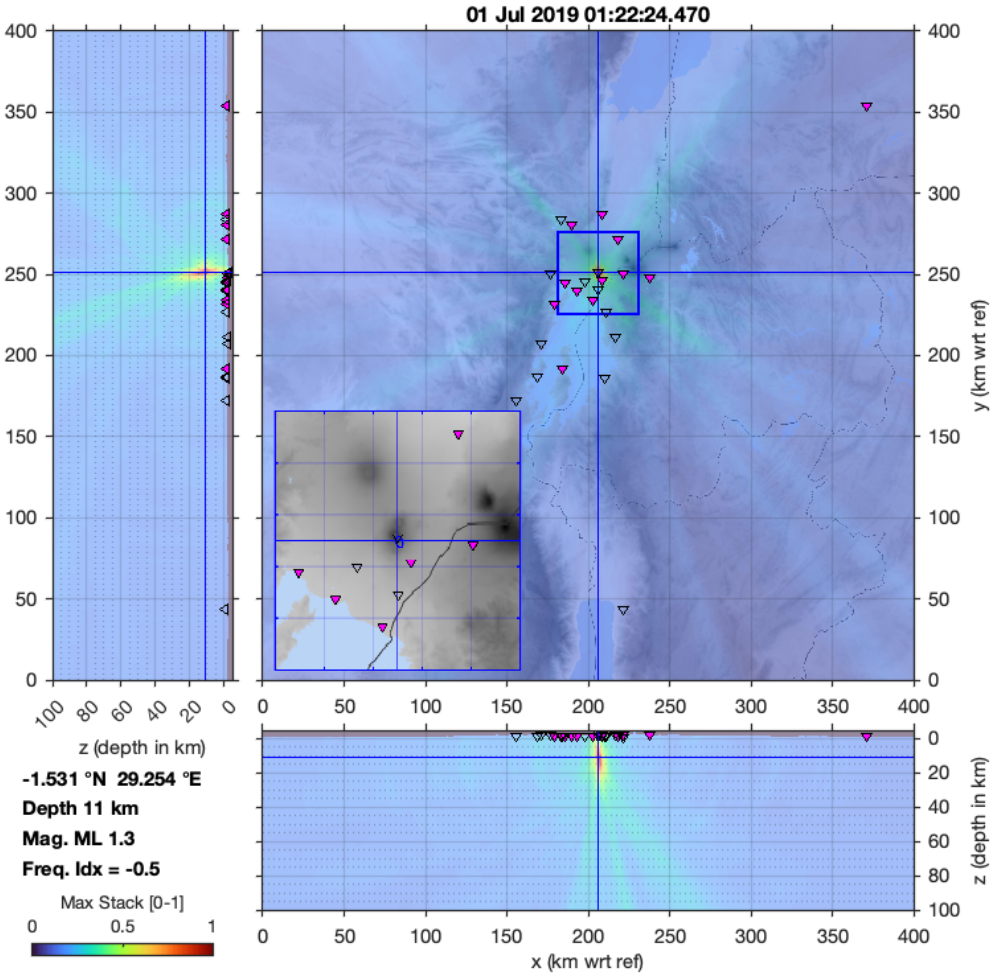

FIGURE 4.1: Example of a location result for a Nyiragongo event on 1 July 2019, using the program XCloc. The blue-to-red color scale correspond to the 3D gridded location coefficients (called Max Stack, normalized between 0 and 1). The most probable location is given at the intersection of the blue vertical and horizontal lines. Stations are represented with inverted triangles, with those used for the location filled in magenta.

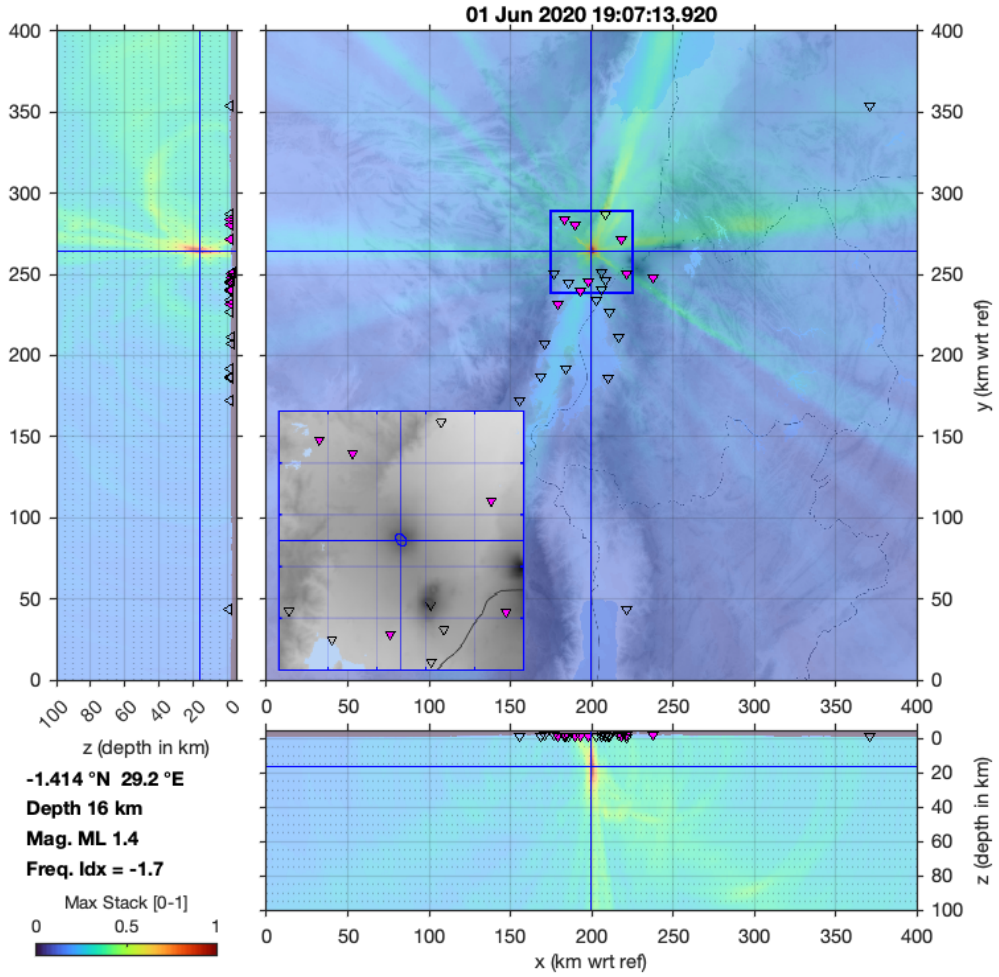

FIGURE 4.2: Example of a location result for a Nyamulagira event on 1 June 2020, using the program XCloc. The blue-to-red color scale correspond to the 3D gridded location coefficients (called Max Stack, normalized between 0 and 1). The most probable location is given at the intersection of the blue vertical and horizontal lines. Stations are represented with inverted triangles, with those used for the location filled in magenta.

4.2 Spatial clustering of seismic events

The Figure 4.3 depicts the density of seismic events per km^3, allowing us to visually identify six main spatial clusters of the seismicity in the Kivu rift. These clusters are discussed briefly below from North to south, considering their geological features (Delvaux et al., 2017; Smets et al., 2016; Wood et al., 2017). On the right, histograms of events density along the latitude are calculated before (green) and after (red) the May 2021 eruption in order to help discriminating the following different seismic patterns described in the following text from North to South.

- **Cluster 1: North Virunga**
  The northernmost cluster corresponds to an half-graben tectonically active marking the transition between the northern Kivu basin and the southern lake Edward Basin. This zone forms one of the 3 seismic zones delimited by Delvaux et al. (2017) for the Kivu rift valley, where a M_W 5.4 occurred in 1968.

- **Cluster 2: Nyamulagira** and **Cluster 3: Nyiragongo**
  To the south, the intense volcanic seismicity associated with Nyamulagira (cluster 2) and Nyiragongo (cluster 3) is well separated spatially, despite some overlap due to the small distance between both volcanoes and location errors. While former seismological investigations pointed out the difficulty to differentiate the seismicity from both volcanoes (Pagliuca et al., 2009; Wood et al., 2017), the present results allow to be confident about the discrimination between Nyiragongo and Nyamulagira. Nyamulagira's seismicity is dominated by low-frequency events with depths not well constrained ranging from 0 to 30 km b.s.l. (Barrière et al., 2017). Nyiragongo's seismicity primarily ranges between 5 to 15 km. It is mostly attributed to several deep magmatic intrusions and a repetitive non-destructive source within its plumbing system generating highly similar events on a daily basis (Barrière et al., 2019).

- **Cluster 4: Goma/Giseyni**
  Encompassing the two major cities Goma (DRC) and Gisenyi (Rwanda), this cluster is related to the the week-long intrusion of the dyke in 2021. It corresponds to a magmatic intrusion zone between the southern flank of Nyiragongo and the lake Kivu at the tip of the dyke close the the Nyabihu fault (see also Figure 2.2).

- **Cluster 5: North Lake Kivu**
  Located in the deepest part of the lake Kivu (maximum depth of nearly 500 m) between the northern part of the Idjwi island ("Idjwi horst" in geological term) and the northern shore of the lake Kivu, this area is an extension of the Virunga lava fields into the lake. It features numerous submarine volcanic cones and faults within the bedrock and sediments. This cluster highlights an important density of events on the Western side of the lake where the 2002 Kalehe M_W 6.2 took place (Wauthier et al., 2015).

- **Cluster 6: South Lake Kivu**
  This cluster represents the southern portion of the lake Kivu basin, also known as the South Kivu Volcanic Province (Smets et al., 2016). Although there is no evidence of major recent volcanism, the volcanic field is highly affected by N-S or NE-SW

faulting, the dominant fault orientation in the Kivu rift. Significant earthquake in this region include the 2008 M_W 5.9 Bukavu-Cyangugu earthquake (D'Oreye et al., 2011) and the 2015 M_W 5.7 Katana earthquake (Geirsson et al., 2017) (see Figure 3.1).

In summary, clusters 1, 5 and 6 are associated with the rifting process with earthquake's depth generally not exceeding 20 km for most of events. These clusters reflect the seismic activity along the numerous faults across the region. Clusters 5 and 6 are characteristic of the tectonic seismicity of the Lake Kivu Basin, which is an asymmetric graben bordered by major faults and escarpments. Little or no seismicity is detected in the northwestern part of the lake, which contains a high density of volcanic cones, maars and tuff rings (Smets et al., 2016). This area is thus excluded from the clusters 5 or 4. The part of the cluster 5 overlapping with the cluster 4 will not be taken into account in the final count. Clusters 2 and 3 delineate the volcanic activity of Nyamulagira and Nyiragongo, respectively. Cluster 4 is dominated by the 2021 dyke intrusion and the subsequent reactivation of faults.

Notable seismicity outside the rift is detected further west in the Masisi region. However, we will not discuss the remaining seismicity patterns outside the rift as they are largely located outside the network and cannot therefore be accurately characterised.

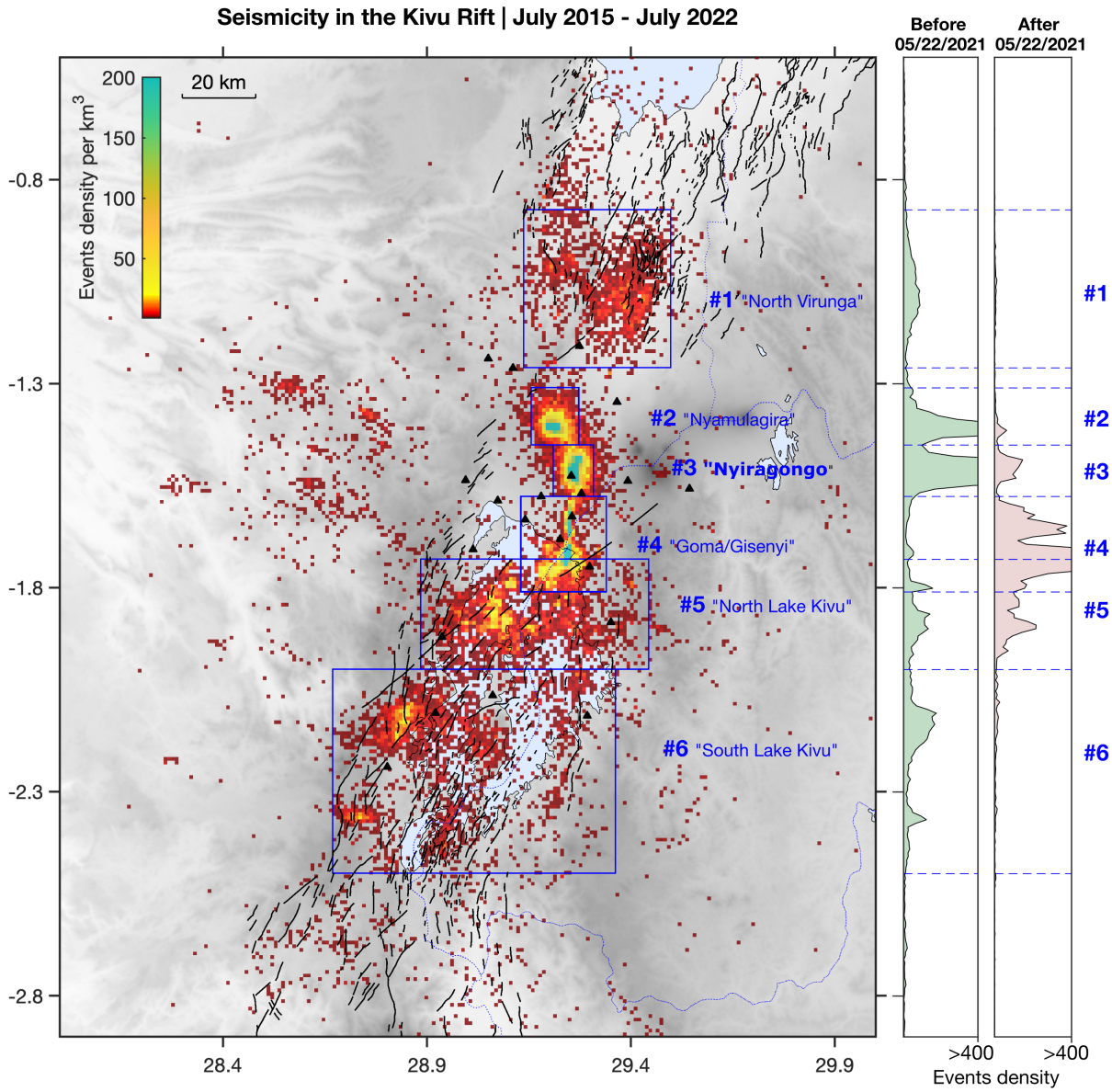

FIGURE 4.3: Seismic clusters identified based on events density per km^3 between July 2015 and July 2022 (color scale red to green). The blue triangles delineate the six clusters identified, from North to South: "North Virunga", "Nyamulagira", "Nyiragongo", "Goma/Gisenyi", "North Lake Kivu", "South Lake Kivu". The main fault lineaments are plotted as solid black lines (source : Smets et al. (2016))

4.3 Moderate magnitude seismic events

A map and time-depth distributions of moderate-magnitude earthquakes ($M_L \geq 3.5$) are provided in Figure 4.4a,b. Two significant events have marked the seismic activity in the Kivu Rift during this period.

- **Katana earthquake**
  The first event is the Katana earthquake sequence (M_L 6.1) in the cluster 6 "South Lake Kivu" area on 7 August 2015, followed by several major aftershocks (zoom in Figure 4.4c).

- **Dyke intrusion**
  The second major event is the 1-week dyke intrusion following the flank eruption on 22 May 2021, which was accompanied by sustained seismicity in Lake Kivu (zoom in Figure 4.4c). This recent crisis, discussed in detail in section 2.3 in Chapter 2 was marked by a number of felt earthquakes in Goma, Gisenyi and surrounding area.

Apart from these two major events, significant felt seismicity is noticeable within cluster 1 in the northern part of VVP and clusters 5/6 in Lake Kivu. These observations from the moderate seismicity between 2015-2022 are also consistent with the seismotectonic delimitation zones in the Kivu rift proposed by Delvaux et al. (2017). These delimitations are based on various instrumental and historical catalogs ranging from 1888 to 2015 (1031 events with $M_W = [1.4 - 6.3] + 37$ macroseismic events after assessing reports of felt seismicity). It is important to note that no moderate-size earthquake was detected in the VVP, thus confirming that the volcanic seismicity was dominated by low-magnitude events and tremors.

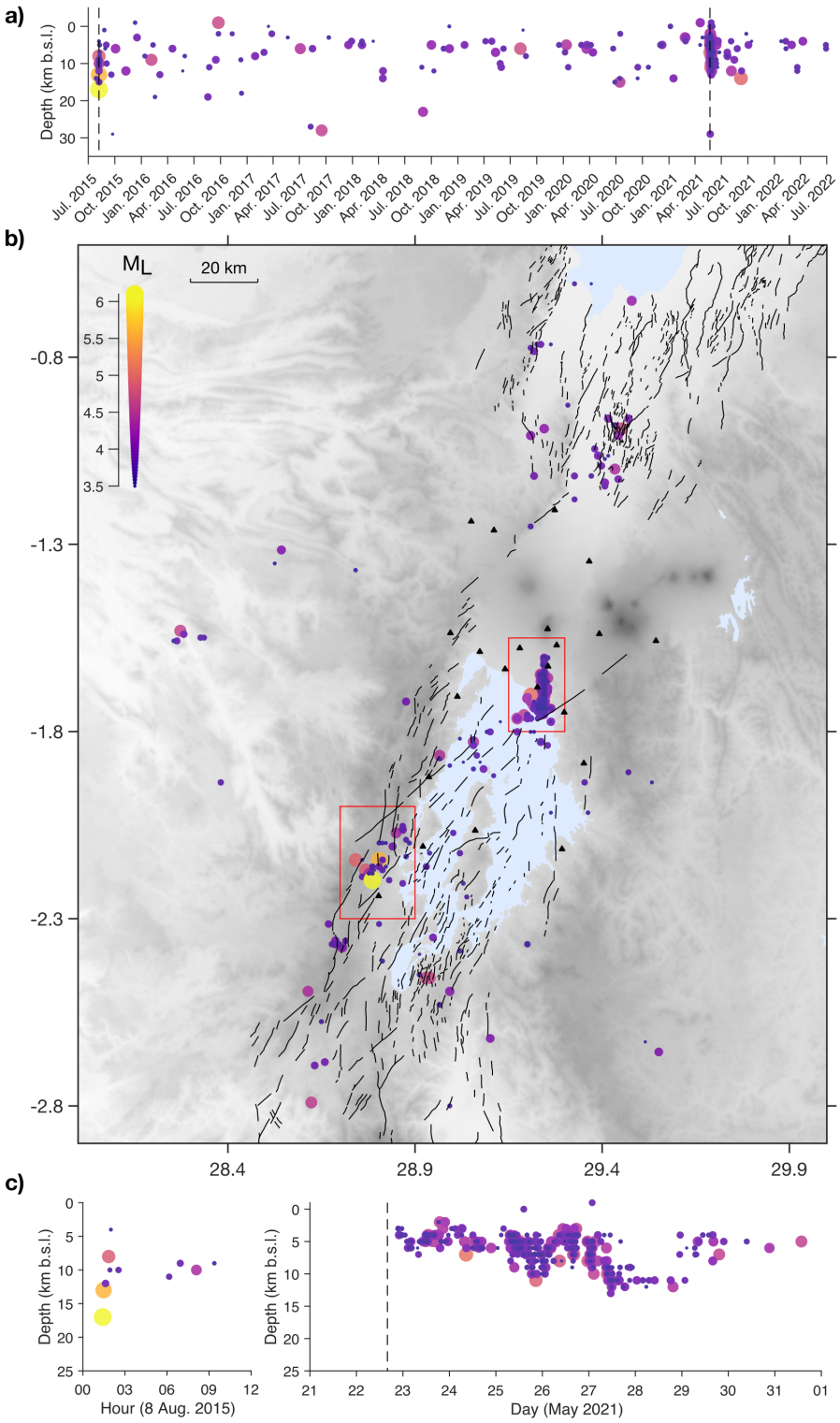

FIGURE 4.4: **(a)** Time-depth distribution of events from the catalogue of seismicity with magnitude larger than $M_L \geq 3.5$. The 2 dashed black lines represent the the 8/08/2015 Katana earthquake sequence and the 22 may 2021 dyke intrusion seismicity **(b)** Events with magnitude larger than $M_L \geq 3.5$ plotted on the regional topographic map with fault indicated by black lines (Smets et al., 2016). The two red rectangles delineate the area affected by the 22 may 2021 dyke intrusion seismicity and the 8/08/2015 Katana earthquake sequence. **(c)** Time-depth distribution of the 8/08/2015 Katana earthquake sequence and the May 2021 dyke intrusion

4.4 Seismicity at Nyiragongo and Nyamulagira: 2015 - 2022

It is rather logical to conclude this thesis by giving an overview and interpretation of the seismicity at Nyiragongo and Nyamulagira during the period from 2015 to 2022. To better evaluate the potential relationship between the magmatic activity at both volcanoes, we plot together in Figure 4.5 the time-series of the lava-lake level at Nyiragongo and the daily count of seismic events at Nyiragongo and Nyamulagira.

While the epicenters are relatively well constrained, the depth estimates must be treated with caution due to large uncertainties, often spanning several kilometers. These uncertainties stem from the use of a 1D velocity model that poorly represents both volcanoes structure, the sparse network and the occurrence of low signal-to-noise ratio (SNR) - low magnitude events. Therefore, we divide the catalog into three depth ranges: shallow (<7.5 km b.s.l.), intermediate (7.5 - 15 km b.s.l.) and deep (>15 km b.s.l.). In-depth analysis of the 2015-2022 earthquake catalog, such as the magnitude of completeness, has not been yet performed. However, events with M_L as low as 0.5 can generally be well recorded with KivuSNet (Oth et al., 2017).

The evolution of the event magnitudes for cluster 2 (Nyamulagira) and cluster 3 (Nyiragongo) for the three depth ranges are plotted in Figure 4.6. As expected, magnitude are overall low, between 1 and 3. We do not observe significant differences for the three depth ranges but it is noteworthy that Nyamulagira cluster overall exhibit events with higher M_L between 2 and 3, particularly during swarm episodes. Events with magnitude above 3 sporadically occur at Nyamulagira during swarms, often at large depths > 15 km b.s.l. At Nyiragongo, such events were only observed at shallow levels during the 2021 eruption/dyke intrusion (the strongest events with magnitude up to 5 belong to the Goma/Gisenyi cluster 4, see Figure 4.4). In short, one can summarize observations for both volcanoes as follows:

- **Nyiragongo**
  The seismic activity at Nyiragongo is associated with swarm sequences linked to magmatic intrusions (i.e., deeper than 10 km b.s.l.). Figure 4.5 show that these swarms are synchronous with large lava lake drops, In addition, the swarm sequences contain many events with characteristics similar to hybrid events (i.e., high-frequency onset up to 10 Hz and low-frequency wavetrains) (Barrière et al., 2022). These swarms are clearly visible in Figure 4.5b , indicated by peaks exceeding daily count of 30 (scale on the right). The background seismicity is largely dominated by events at intermediate depths (Figure 4.5b). Among this background seismicity, daily repetitive events suggest a non-destructive source beneath Nyiragongo at large depths (11-15 km) (Barrière et al., 2019), likely controlled by geological or conduit structure within Nyiragongo's plumbing system. Template matching procedure at a single station (e.g., KBTI) can be applied to filter out such repetitive events (e.g., Barrière et al., 2019), but this filtering is not applied here. The daily rate of occurrence of these events is quite stable and does not exceed a few tens locatable per day using the network. In appendix C, we provide an example of Nyiragongo's timeseries (Figure 4.5b) after removal of these repetitive events. Such procedure al-

lows to better highlight swarms but the overall trend of seismicity does not change.

- **Nyamulagira**
  The 2015-2022 seismic catalogue of the Nyamulagira shows alternating periods of day to month-long seismic swarms and quiescent seismicity (4.5b). The Nyamulagira volcano features a large, approximately 2-km wide caldera with a smaller, roughly 500-m wide pit crater inside. The lava lake in Nyamulagira's pit crater, which appeared in 2014 (Smets, D'Oreye, & Kervyn, 2014b), disappeared between late 2015 and early 2016 (Barrière et al., 2017). Since late 2016, the pit crater has intermittently been filled with the temporary small lava lake, multiple hornitos and lava flows. Burgi et al. (2021) showed that the lava filling between 2016 and 2020 was progressive with only one stop and a collapse of the pit crater floor by about 100 m in mid-2019. This collapse is associated with a clear signal in the seismic catalogue, characterized by the largest peak in daily count (4.5b) and a well defined increase in magnitude for the deep earthquakes (4.7). While no studies provide crater morphology changes at Nyamulagira after early 2020, unpublished SAR-based analyses performed at ECGS (using the PickCraterSAR python program developed in Smittarello et al., 2023) indicate that the pit crater floor has maintained approximately at the level of the caldera floor up to today (2024), despite another collapse of hundred of meters occurring in April 2021. This last collapse also corresponds to a change in the earthquake daily count (4.5b) and to an increase in magnitude for the deep earthquakes (4.7).

It is striking that both Nyiragongo and Nyamulagira volcanoes exhibit a sustained filling of their pit craters over the same period 2016-2021. Even more notable are the 2019 and 2020 pit-crater collapses at Nyamulagira, which occurred at about the same time as the large lava-lake drops in 2019 and the May 2021 flank eruption at Nyiragongo. Indeed, the occurrence of a significant LP swarm at Nyamulagira about a month before the May 2021 flank eruption at Nyiragongo raise questions, although no clear links can be established between both events (Smittarello et al., 2022). Linking activity at close volcanoes is controversial, but models exist for explaining potential coupling, such as the pore-pressure diffusion in the astenosphere proposed by Gonnermann et al. (2012) for Mauna Loa and Kīlauea in Hawaii. These adjacent volcanoes have distinct lithospheric magmatic plumbing systems but share a common asthenospheric magma supply system, which can explain simultatenous inflation. Futhermore, the model of Gonnermann et al. (2012) applied to Hawaii, indicates that eruptions at one volcano may inhibit eruptions at the adjacent under certain supply conditions. In the VVP, Nyamulagira and Nyiragongo produce very different lavas, which also suggest distinct plumbing systems (Morrison et al., 2020).

Geirsson et al. (2017, 2019) showed that small, cm-scale, surface deformations in the VVP between 2016 and 2019 could be associated with magma accumulation under the Nyamulagira-Nyiragongo volcanic system. The similar surface response to a sustained pressure build-up at both volcanoes may reflect a common deep magma supply like in Hawaii. However, a clear relationship between eruptive activity at both volcanoes does not exist according to Smets et al. (2015). Determining how or why a volcano reacts to

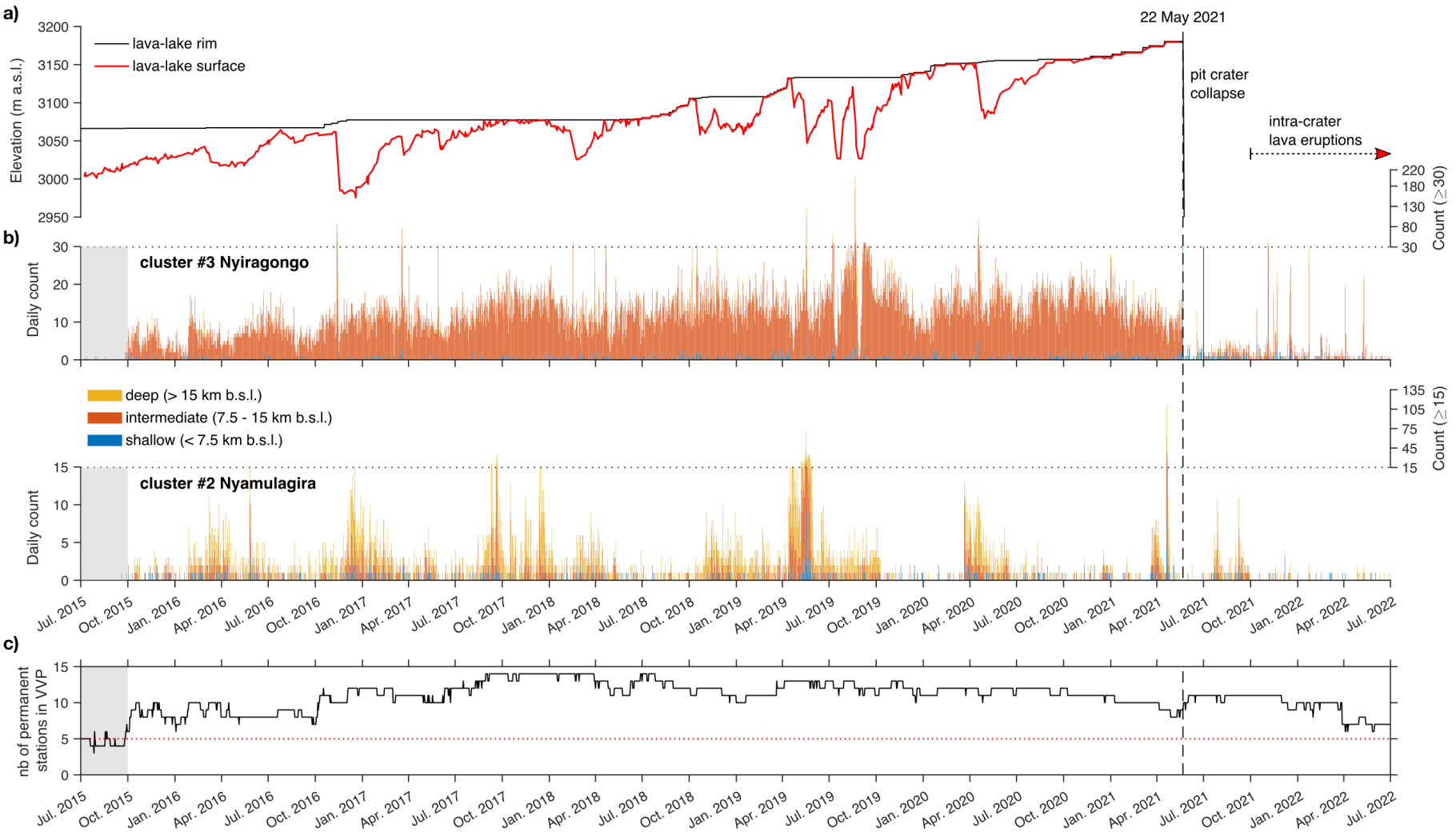

FIGURE 4.5: **(a)** Elevation change of lava-lake rim (in black) and lava-lake surface (in red) for the Nyiragongo volcano between 2015 to 2022. **(b)** Histogram of daily seismicity at Nyiragongo (cluster 3) and Nyamulagira (cluster 2) with a depth classification : deep ($> 15km$) in yellow, intermediate $7.5 - 15kmb.s.l.$ in red and shallow ($< 15km$) in blue. **(c)** Available number of stations

the flank and/or intra-crater eruptions at the other remains elusive, especially in absence of long-term geophysical records as in the VVP. We can still question whether magmatic fluid movements at Nyamulagira can affect the behavior of Nyiragongo, and vice-versa.

We merely touch this complex question in Figure 4.7 by comparing the seismic activity associated to magmatic processes at both volcanoes. This Figure provides a detailed view of the daily count of seismic events over three relevant periods lasting 6 months :

- October 2016 - March 2017
- April 2019 - September 2019
- January 2021 - June 2021

We recall that swarm events at Nyiragongo occurred at large depth (>10 km b.s.l.) due to repetitive magmatic intrusions toward the NE. Dominant LP seismicity at Nyamulagira takes place from 0 to to 30 km b.s.l. The first October 2016 - February 2017 window corresponds to the first deep swarm at Nyiragongo associated with a large lava-lake drop in November 2016. Seismicity increased about a month after at Nyamulagira. Another swarm occured at Nyiragongo in March 2017 without associated increase of seismicity at Nyamulagira (see also Figure 4.5b). The second April 2019 - September 2019 time period begins with a two-month increase of seismicity at Nyamulagira (April-May) followed by successive major day/week-long swarms (and lava-lake drops) at Nyiragongo on May, July, August and September 2019. The third January 2021 - June 2021 period corresponds to the first six months of the year 2021 encompassing the Nyiragongo flank eruption. Significant seismicity at Nyamulagira preceded the flank eruption by about a month.

This preliminary analysis does not allow to define a clear pattern between both volcanoes. These observations could suggest that Nyamulagira responds to Nyiragongo (November - December 2016), the reverse (April - May 2019, April - May 2021) or that there are no link at all (March 2017, August-September 2019). Both volcanoes are very active and the inferred relationships between major volcanic events are potentially misleading.

For the past flank eruptions at Nyiragongo in 1977 and 2002, Smets et al. (2015) indicated that these eruptions were preceded by voluminous and/or long-lived Nyamulagira eruptions (summit, flank and distal flank eruptions). The authors highlighted the occurrence of lava eruptions from Nyamulagira along the structural axes near Nyiragongo, suggesting a potential effect on the stress field of Nyiragongo. The dynamics of eruptions at Nyamulagira before the 2021 eruptions were different, as no more flank eruptions had occurred since 2012, which is unprecedented for this volcano characterized by an eruption every 4 years on average over the past century Smets et al. (2015).

It is yet unclear if magmatic processes behind the repeated summit eruptions into Nyamulagira's pit crater between 2016 and 2021, sometimes halted by large collapses associated with seismic swarms, could have promoted changes in the magmatic system of Nyiragongo. More research is needed to gain insight into this intriguing scientific question, including a better undertanding of the plumbing systems, a comparison of the long-term behaviors of both volcanoes using historical records, more extensive gas-deformation-seismic measurements over a larger observational window, and comparison with other

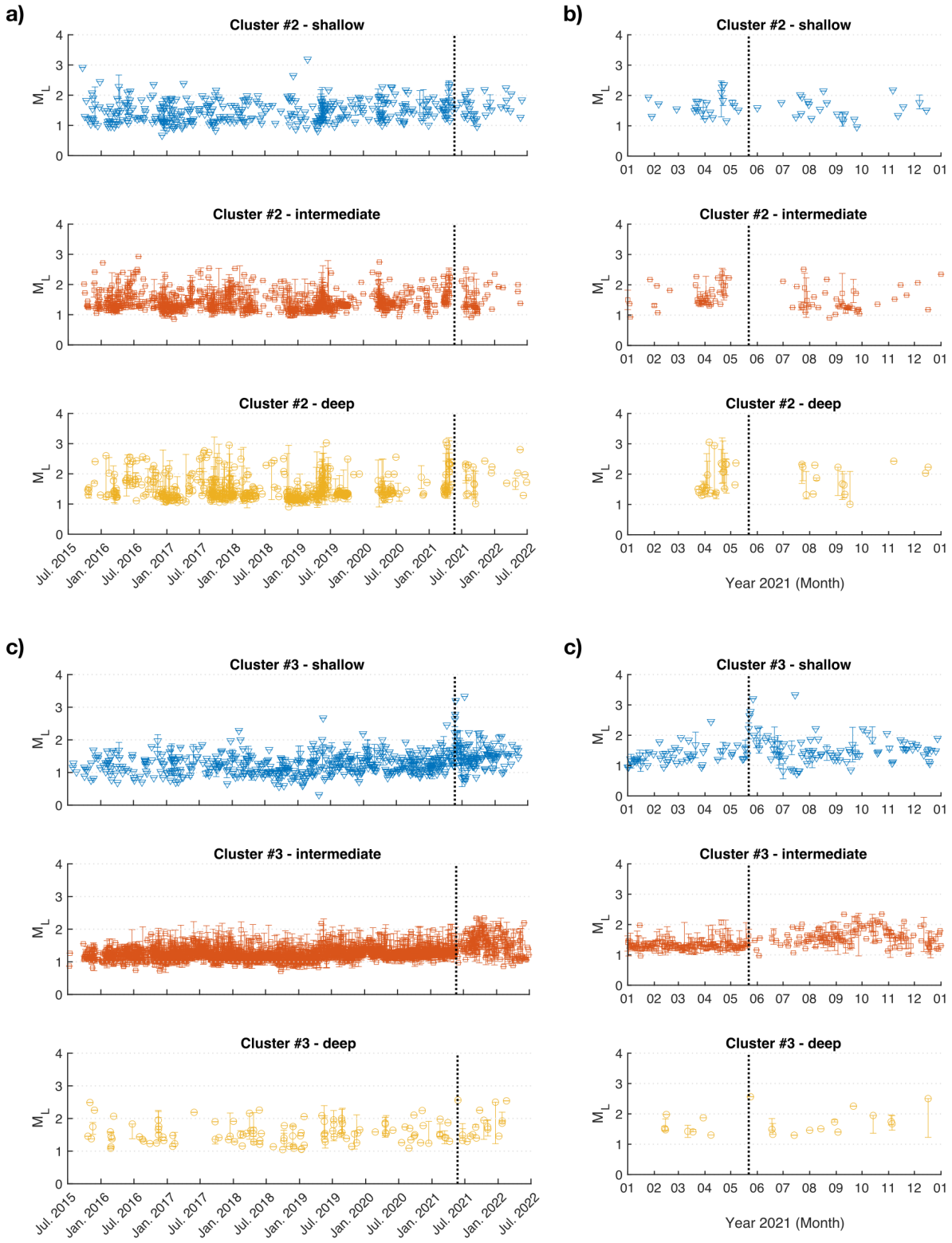

FIGURE 4.6: **(a)** Temporal evolution of event magnitudes from 2015 to 2022 for cluster 2 (Nyamulagira) with an event depth classification : shallow in blue, intermediate in red and deep in yellow. **(b)** Zoom for the 2021 year with dyke intrusion. **(c)** and **(d)** Same as a) and b) for cluster 3 (Nyiragongo). Daily estimates are given with error bar (minimum and maximum values) if more than an event per day is located. The May 2021 eruption is indicated by a dash line

systems of adjacent volcanoes.

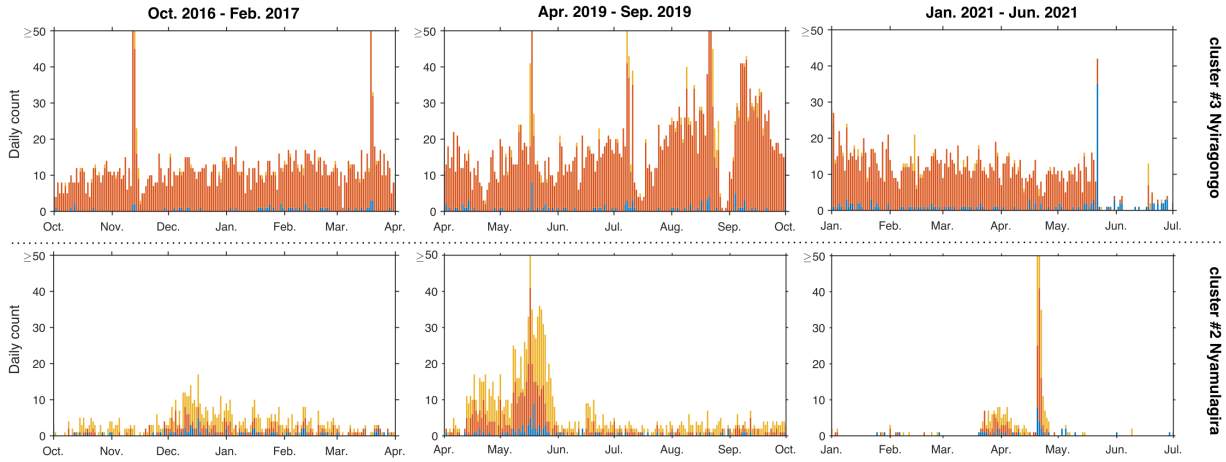

FIGURE 4.7: Daily count of shallow, intermediate and deep events for Nyiragongo and Nyamulagira clusters for three different periods of 6 months in 2016-2017, 2019 and 2021.

4.5 Characterization of seismic events based on their frequency content

In order to gain insight into the geodynamic processes within the Kivu Rift, and more specifically the magmatic processes within the VVP, it is essential to monitor the evolution of the different seismic sources. The frequency of the seismic signal is a fundamental attribute used to infer the source processes in a volcanic context (Chouet & Matoza, 2013). From fluid flow to brittle failure, the spectrum of source mechanisms is large and is generally reflected in the frequency content of the seismic record.

As an outlook to further studies using the new 2015-2022 seismic catalog, we tested the use of the Frequency Index (FI) introduced by Buurman et al. (2006), which is a metric that quantifies the frequency content for each seismic event. Using the FI, it becomes feasible to classify and differentiate between various types of seismic events, such as long-period, hybrid, and volcano-tectonic events, on the basis of their spectral properties. Furthermore, the FI facilitates the identification of patterns or shifts in the frequency content of seismic signals, which could indicate specific volcanic processes or stages of volcanic activity. However, it is important to keep in mind that path and site effects, which can be significant in volcanic environment, can substantially influence this frequency content and can potentially mask the source signature.

The FI is defined as:

$$FI = log_{10}\frac{\bar{A}_{upper}}{\bar{A}_{lower}}, \tag{4.1}$$

where $\bar{A}_{upper}$ and $\bar{A}_{lower}$ are the mean spectra in the high and low frequency bands. Regarding the available literature at Nyiragongo,including the present work, and at other volcanoes, we set the low-frequency band to $[0.5-4]Hz$ and the high-frequency band to $[4-15]Hz$.

Following Matoza et al. (2014) who applied this approach at Kīlauea, the FI was computed on the bandpass filtered vertical component in a 4-sec time window, 1 s before and 3 s after the P-wave arrival. In the catalogue, the observed P-wave arrival is represented by the maxima of the characteristic kurtosis function used in the location program XCloc (see section 4.1). The FI calculation is retained only if the gap between the calculated and the observed arrivals is less than 0.5 s and the SNR of the P-wave onset is above 3 (calculated from two 2-sec windows for the signal and the noise around the P-wave arrival).

FI were calculated from all available stations, but we only present results from BOBN. Calculating an average or median using estimates from all stations would be beneficial for mitigating site and path effects (Matoza et al., 2014). However, in our case, the availability of stations during the analysed period can vary significantly (e.g., no more stations in the northern part of the VVP in 2021). This change can be detrimental to obtain a consistent metric along the full period. Some stations also depict significant site effects, such as BULE and RSY, where high-frequency content is strongly filtered for any type of signals. Nonetheless, similar trends were observed at some stations, which means the estimates at BOBN being typical. Station BOBN is located in the middle of the network, outside the volcanic area, and is conveniently situated relative to all seismic clusters. Characterized

by a good site response, it is one of the KivuSNet stations with the largest number of P-wave observations with high SNR (see Chapter 3). Moreover, for characterizing long-period (LP) events at Nyamulagira, Barrière et al. (2017) found that the waveform onset and the frequency content at BOBN for such LP events are well preserved (see Figure S8 of their article).

Figure 4.8 shows the first results of the FI distributions for each seismic clusters. At Kīlauea, Matoza et al. (2014) found a bimodal distribution of FI, allowing the isolation of LP events from other volcanic and tectonic seismicity, though an overlap exists between both classes. Similarly, we can obtain a bimodal distribution for the Kivu by merging all clusters together with clusters 2 and 3 being volcanic clusters and the others tectonic clusters.

The volcanic clusters 2 and 3 highlight lower frequency content compared to all other clusters, but when analyzed individually, clusters 2 and 3 do not exhibit any clear multi-modal distribution. The observed FI distributions appear representative of the volcanic seismicity in the VVP, as open-vent volcanoes are known to generate high-frequency seismicity at much lower levels than closed-conduit volcanoes (Acocella et al., 2024). The absence of a clear delimitation in frequency content between the typical classes of volcanic seismicity, i.e., volcano-tectonic, hybrid and LP events, if generated at both volcanoes, can be also explained by the stronger attenuation in this volcanic region. Thus, at this stage, the obtained preliminary classification differentiate volcanic from tectonic seismicity, but does not give clear indications about the source processes behind the volcanic signals.

There are differences between clusters 2 and 3. The seismicity in the Nyamulagira cluster 2 shows the lowest FI values. It is dominated by low frequency events, in agreement with the detection of numerous LP events by Barrière et al. (2017) at this volcano over the period 2014-2017. The distribution of FI in the Nyiragongo cluster 3 is slightly shifted toward higher values, but still below 0, indicating a dominant frequency content below 4 Hz. This result aligns with observations by Barrière et al. (2019) or Barrière et al. (2022) showing that both repetitive or swarms events at this volcano also contain energy at high frequency.

The cluster 4 "Goma/Gisenyi" to the south of clusters 2 and 3 exhibits higher FI than clusters 2/3, consistent with the magmatic intrusive process in May 2021 characterized by brittle failure with fluid movements. This strengthens the relevance of the calculated FI. The tectonic clusters (1, 5 and 6) exhibit a wide range of FI values, reflecting the complex multi-effects of source, path and site. Yet the overall trend shows FI significantly larger than those obtained for the volcanic clusters 1 and 2.

To examine the temporal change in FI, the time series of FI at BOBN were computed between July 2015 and July 2022 and are depicted in Figure 4.9. A color code is given to each of the six main spatial clusters. The delimitation between the tectonic (blue, green) and the volcanic clusters (red, yellow) is clear. Events of the Goma/Gisenyi cluster 4 (in black) spreads over the full range of FI. A zoom into the one-year period November 2020 - November 2021 (Figure 4.9b) gives a clear picture of different seismic patterns occurring in the Kivu rift:

- A tectonic swarm-like sequence occurred in November 2020 on the northwestern edge of Lake Kivu, the same region as the 2002 Kalehe earthquake. This sequence was unprecedented since the start of the monitoring with the KivuSNet.
- A significant swarm of LP events was recorded at Nyamulagira in April 2021, about one month before the flank eruption at Nyiragongo. Other major swarms occurred at Nyamulagira in the past years (see previous section).
- The seismicity at Nyiragongo (in yellow) did not exhibit any marked trends such as a shift in frequency content up to the eruption.
- The 2021 dyke intrusion (black) and the subsequent tectonic seismicity in the Lake Kivu region (blue) are generally characterized by higher FI values than the volcanic clusters.
- FI varies from low ([-2:-1]) to high ([-1:1]) values between the Nyiragongo cluster 3, the Goma/Gisenyi cluster 4 and the North Lake Kivu cluster 5, respectively. This variation likely reflects different sources processes from volcanic mechanisms (involving fluid movements and/or brittle failure) to pure faulting during the 2021 event. Focal mechanisms have not yet been computed but dedicated analyses on this aspect should be further addressed.

Though it is not shown here, it is important to note that the distribution of FI obtained at KBTI follow the trends of FI obtained at BOBN except for the Nyiragongo cluster. Indeed, BOBN have much more high-quality P-wave observations for most of clusters allowing the calculation of FI, but the cluster 3 is better recorded at KBTI, where FI exhibits higher frequency content. All FI obtained at KBTI are shifted toward higher values around 0 (compared to -1 for BOBN). It implies that a significant attenuation occurs along the seismic path between Nyiragongo and the station BOBN. Future investigations should be dedicated to the volcanic clusters by studying in detail the variability of the frequency content and the shape of the signal (onset, full waveform, vertical and horizontal components) with respect to the stations used, the magnitude, the source region and the depth.

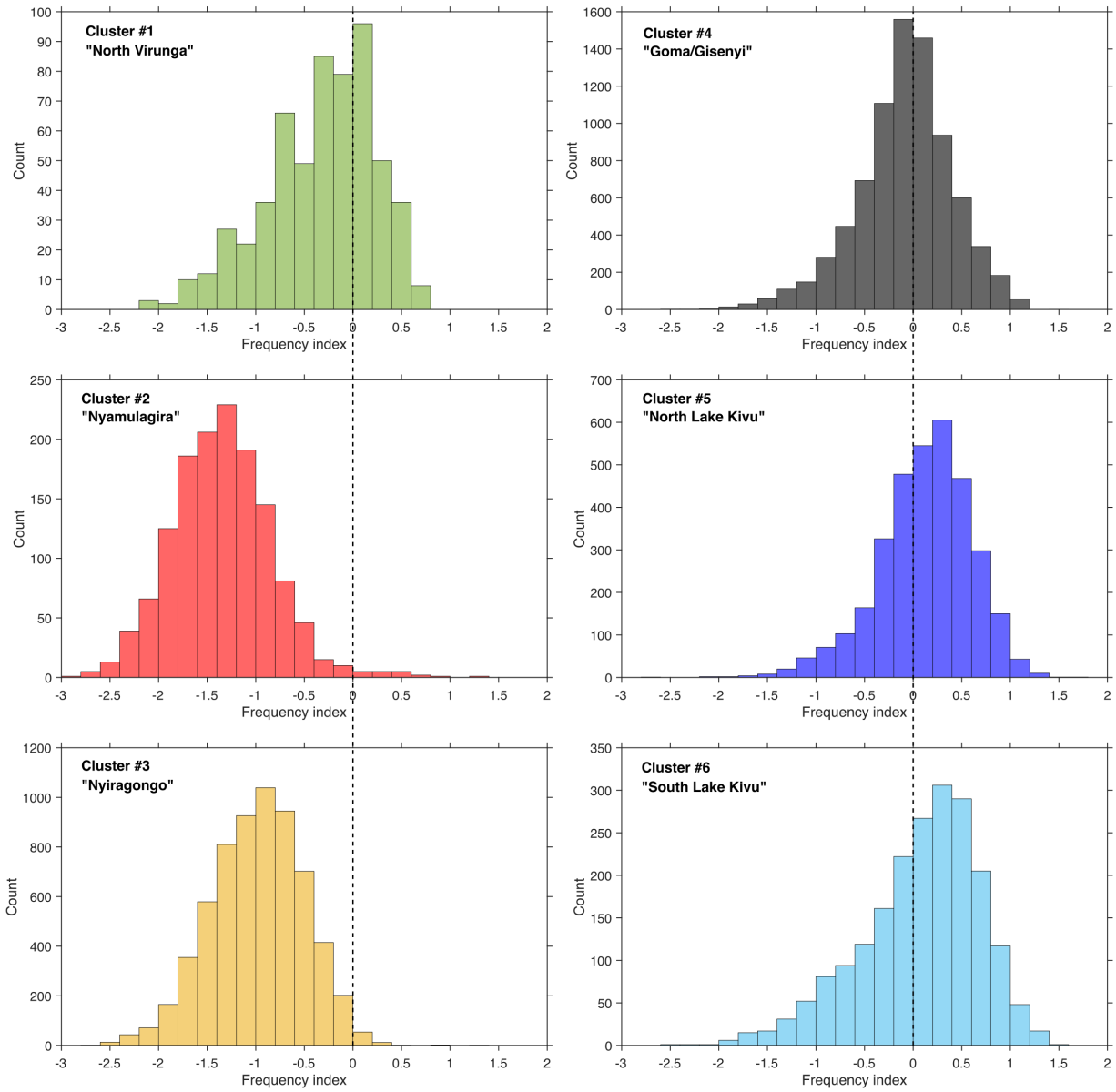

FIGURE 4.8: Histograms of FI values at BOBN station for each seismic clusters identified based in event density (satisfying the SNR criterion for FI calculation, see text). The dashed line represents the limit between dominant low frequency content below 4 Hz (FI<0) and higher frequency content (FI>0).

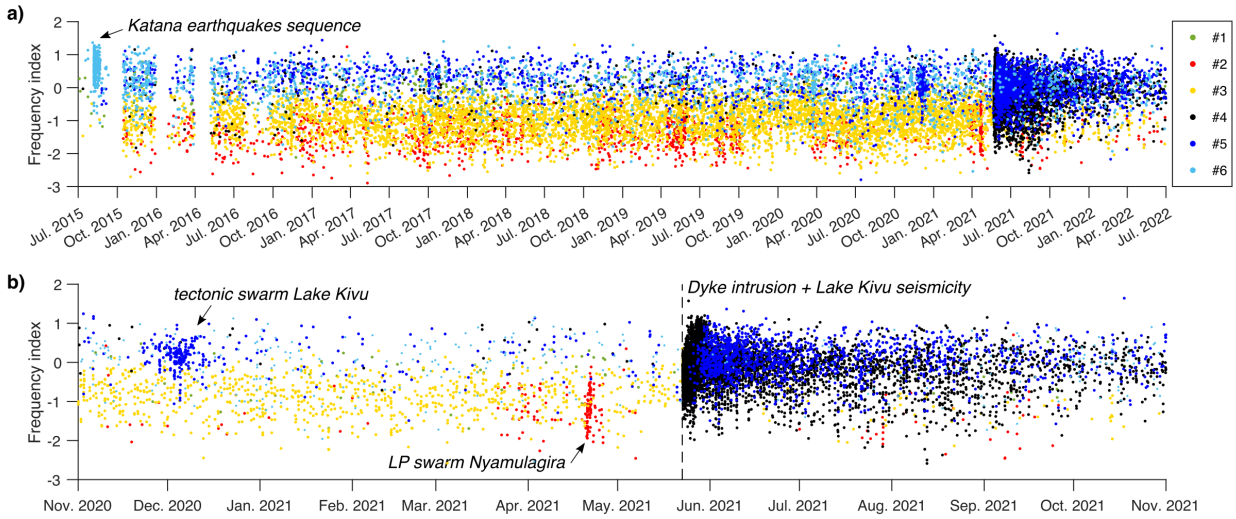

FIGURE 4.9: **(a)** FI Temporal evolution at single-station BOBN from 2015 to 2024 following Matoza et al. (2014) for each seismic clusters. A color code is used to differentiate the seismic clusters.**(b)** Zoom for the time window from November 2020 to November 2021. The vertical line represents the beginning of the 2021 flank eruption/dyke eruption on 22 May 2021. Note that data gaps are either due to the absence of data or to too noisy data without clear arrivals (i.e., hampering the calculation of FI) at the considered station BOBN.

General conclusions & perspectives

The results presented in this thesis highlight the critical importance of a local seismic monitoring network for understanding a complex, active tectonic and volcanic region such as the Kivu. Using seven years of seismic data from KivuSNet, the first dense local seismic network in the area, this work brings essential insights into the dynamics of the Kivu Rift, the magmatic behaviour of the Virunga Volcanic Province (VVP), and thus can provide guidance to the Goma Volcano Observatory (GVO) for its monitoring duties in an harsh field environment.

Based on the analysis of seismic amplitudes, the SARA (Seismic Amplitudes Ratios Analysis) technique or other similar popular approaches such as RSAM (Real-Time Seismic Amplitude Measurement) are commonly used to track volcano-tectonic activity worldwide. In this thesis, we investigated the possibility of using SARA to assess the seismic activity in the VVP in line with GVO's monitoring tasks. Initially, we leveraged the existence of background seismic tremors in the low-frequency range (< 2 Hz) recorded across the network to apply this technique for the first time in this context. In the VVP, the ambient seismic noise below 2 Hz is indeed dominated by persistent volcanic sources, reflecting summit eruption dynamics at Nyiragongo and Nyamulagira volcanoes. We thus qualitatively discussed the temporal and spatial variations of the seismic amplitude ratios in the VVP, assuming isotropic radiation pattern from these sources and neglecting station site effects (though this aspect was also investigated since stations BULE and RSY were spotted as problematic). The obtained results demonstrated that this simple approach is well-suited for deriving information related to the superficial magmatic activity in the VVP from this tremor-rich low frequency band.

Secondly, we deepened this SARA analysis over the period 2018-2022 in order to better understand the seismicity before, during and after the 2021 Nyiragongo eruption. The technique was applied in low $[0.3 - 2]$Hz and high $[2 - 15]$Hz frequency bands, coupled with other geophysical data (lava lake level, infrasound, seismic events and tremor location). This multi-disciplinary approach allowed to interpret the changing temporal properties (amplitude, frequency content) of the seismic signal. The observed fluctuations in the seismic-amplitude time series reflect the activity of the lava lake and the spatter cone at Nyiragongo before the May 2021 eruption, the magmatic intrusion during the eruptive crisis and the renewal of lava effusion within the crater by the end of the year 2021. A detailed look at the 2021 eruptive sequence demonstrated the usefulness of this amplitude-based seismic analysis to decipher the spatio-temporal extent of the severe week-long magmatic and tectonic crisis using only a few pairs of stations. Properly monitoring the ongoing magmatic processes in the VVP strongly relies on GVO's ability to maintain some key stations operational, such as KBTI (flank) and NYI (summit) for Nyiragongo.

Deriving new seismological models (seismic velocity, magnitude) from several years of continuous seismic monitoring in the Kivu basin has been the second major goal of this thesis. The absence of a permanent seismic network and the lack of adequate local models has been a long-standing obstacle for monitoring/studying the seismicity of the Kivu rift as the use of inappropriate models can introduce large errors. Before this thesis, a 1D (layered) model of the Earth structure was obtained from a receiver function analysis using a set of teleseismic events recorded in the Virunga by two digital stations now dismantled (T. Mavonga et al., 2010). To date, this model has been the routine model used at GVO for locating earthquakes. From a detailed, manual inspection of recorded events with KivuSNet, we selected hundred of local events as input to a seismic travel-time inversion scheme (VELEST) and a non-linear location program (NonLinLoc). This was the first time such an approach was tested in the Kivu and we successfully established new 1D velocity models of the Kivu Rift referred to as "Kivu 1D" (for P- and S-wave), outperforming previous models. These new models comes with station corrections terms to account for lateral variations not captured by the 1D simplification and with a first local magnitude scale derived from the same dataset. The obtained models should be strongly considered as new reference models for routine work at GVO and as basis for future research, including for instance 3D travel-time tomography.

The compilation of a new instrumental seismic catalogue of the region between July 2015 and July 2022 using a grid-search type location program (XCloc) was the final significant achievement of this thesis. The spatial distribution of around 50,000 events revealed six seismic patterns that characterizing the Kivu Rift: the northernmost cluster of tectonic seismicity between the Virunga and the lake Edward, the volcanic seismicity associated to Nyamulagira and Nyiragongo volcanoes, the Goma/Giseyni seismicity related to the week-long intrusion of the dyke in 2021 and two clusters of tectonic seismicity in the lake Kivu. We provided a preliminary investigation of this dataset highlighting interesting avenues of future research. We discussed the relationship between Nyiragongo and Nyamulagira by analysing the seismicity associated with both volcanoes during the study period. Although the data could suggest a certain degree of interaction due to the occurrence of seismic swarms and changing eruptive behaviors at both volcanoes, there is no conclusive evidence that changes at one volcano induce changes at the other yet. We then briefly discussed the first attempt of classifying seismic events in the VVP using the Frequency Index (FI) metric. In addition to the location and the magnitude, such simple calculation can be relevant for characterizing seismic events in the Kivu Rift, where FI values exhibits a clear distinction between volcanic and tectonic events.

Based on the results of this thesis, several areas of future research can be proposed to deepen our understanding of the seismic activity in the Kivu rift and Virunga Volcanic Province, e.g.:

- **SARA methodology**
  At the end of this work, the SARA method had not been used to its full potential, i.e., locating seismic sources based on seismic amplitude ratios to follow magmatic intrusions. However, this work has laid the foundations for the use of the technique in the area and has demonstrated its usefulness for monitoring purpose at GVO using only a few station pairs. Two further improvements can be envisaged: First, the most accessible is the use of KivuSNet data for locating the migration of the seis-

micity during the 2021 dyke intrusion, as it was done for instance by Caudron et al. (2018) for the analysis of the 2014–2015 Bárðarbunga-Holuhraun dike propagation in Iceland; second, only if a dense network of sensors is someday deployed around Nyiragongo and/or Nyamulagira, testing the continuous location of seismicity in the edifices using the SARA method is an interesting avenue, as done by Taisne et al. (2011) at Piton de la Fournaise during magma propagation before eruption.

- **Automatic classification of seismic events in the VVP**
  In volcano-seismology, it is well-known that seismic signals carry a marker of the ongoing tectonic/magmatic processes (source effect) as well as path and site effects. Classifying these events with regard to their probable source mechanisms is an important task as its brings crucial information for interpreting unrest periods (Maggi et al., 2017; Malfante et al., 2018). To date, the main obstacle to this classification work in the region has been the absence of a labelled catalogue, which is the basis for supervised automatic learning. Indeed, a trained catalog consists in a manually labelled catalog of events (e.g., Long-Period, Volcano-Tectonic, Hybrid, Explosions, etc.), from which several attributes are calculated in order to characterize these classes of events. As pointed out by Cortés et al. (2021), this procedure is not always affordable for observatories. This first entry is generally made by seismic analysts during the daily routine work, which has not been not the case at GVO. It would thus take a long time to label a large and representative set of seismic events from scratch, so it is imperative to envisage other strategies. Unsupervised techniques exist when working with unlabelled catalogs (e.g., Duque et al., 2020; Ríos et al., 2024) but *a priori* knownledge of different seismic classes is always an advantage. Template matching procedures consist in detecting similar events/sources in near-real-time stream using cross-correlation with event templates (so called master events). As discussed in this thesis, some templates are already identified seismic events in the VVP (e.g., LP events, seismo-acoustic events from lava-lake activity, deep repetitive source, etc.) and such cross-correlation procedure could be implemented within a monitoring strategy (e.g., Hotovec-Ellis and Jeffries, 2016). Moreover, these templates can serve as a starting point to a first labelled catalog. The calculation of the Frequency Index (FI) is also an interesting, simple and fast approach in this direction (Matoza et al., 2014) but our preliminary investigation points out the limits of this single metric for characterizing the volcanic seismicity, which needs further investigations. Finally, deep learning methods are recent powerful approaches (e.g., Mousavi et al., 2020; W. Zhu and Beroza, 2019) that are most likely the best approach to provide automatic detection and accurate picks for volcanic, low SNR events. These AI-based methods require to be trained on the KivuSNet data before working properly.

- **Monitoring seismic velocity changes based on ambient noise**
  In absence of monitoring networks, the mechanisms of the 1977 and 2002 Nyiragongo eruptions were poorly understood at that time but the presence of some precursors (e.g., felt earthquakes, rumbling, ash clouds) appearing months to days before the eruptions have been considered as well-established facts (e.g., Hamaguchi et al., 1982; Kavotha et al., 2002; Komorowski et al., 2002). In 2021, there was no clear short-term (weeks/days/hours) precursors (ground deformation, seismicity, infrasound, degassing) that could be associated with an impending eruption in

a prospective forecasting framework Barrière et al. (2022, 2023b) and Smittarello et al. (2022). The analysis carried out in this thesis (Chapter 2) brings new elements to the available literature in relation to Nyiragongo's 2021 eruption. Such scenario can also occur at other volcanoes (e.g., Lesage et al., 2018; Pesicek et al., 2018) and it is particularly worrying in the case of the Virunga where Nyamulagira and Nyiragongo threaten more than one million inhabitants. Since very-short term signs of unrest were detected at the summit within an hour before the 2021 flank eruption, strong efforts must concentrate in the instrumental monitoring of the edifice or at least in the maintenance of a telemetered, operational station at its summit. It is also of primary importance to continue the analysis of the seismic data using a full panel of methods for better understanding the pre-/syn-eruptive mechanisms and potentially retrieving subtle signals of changes in the edifice. This includes the detection and classification of micro-seismicity as previously mentioned or the monitoring of temporal velocity change based on NCFs (Noise Cross-Correlation Functions, a notion introduced in Chapters 1 and 2). The latter is a popular method in volcano-seismology (e.g., Brenguier et al., 2008; Lecocq et al., 2014; Lesage et al., 2018) which allow the continuous measurement of very small velocity changes (called dv/v) linked with changes of Earth's material properties. Preliminary investigations in the VVP by C. Caudron (ULB) are promising and highlight the potential of this approach by revealing short-term (days/weeks) and long-term (months/years) trends following the evolution of Nyiragongo's lava-lake level (see Figure D). Further work will focus on the reliability of these results depending on the time periods and the station used in order to understand the role of noise source effects and changes within the medium on the obtained dv/v. Though any clear signals that could be interpreted as pre-eruptive unrest are for now detected, a deeper investigation would allow to gauge if the pressure state in the magmatic plumbing system can be inferred from the analysis of station pairs close to Nyiragongo, such as done at Kīlauea (lava-lake) volcano (Donaldson et al., 2017).

Bibliography

Abril, C. (2018). *Seismicity and crustal structure in iceland* (Publication No. 1734) [Doctoral dissertation, Uppsala University, Department of Earth Sciences].

Acocella, V., Ripepe, M., Rivalta, E., Peltier, A., Galetto, F., & Joseph, E. (2024). Towards scientific forecasting of magmatic eruptions. *Nature Reviews Earth & Environment*, *5*(1), 5–22.

Aki, K., & Ferrazzini, V. (2000). Seismic monitoring and modeling of an active volcano for prediction. *Journal of Geophysical Research: Solid Earth*, *105*, 16617–16640. https://doi.org/10.1029/2000JB900033

Aki, K., & Richards, P. G. (2002). *Quantitative seismology*.

Allard, P., Baxter, P., Halbwachs, M., & Komorowski, J.-C. (2002). The january 2002 eruption of nyiragongo volcano (dem. repub. congo) and related hazards: Observations and recommendations. *Final Report of the French–British Team, Paris*.

Ammon, C. J., Randall, G. E., & Zandt, G. (1990). On the nonuniqueness of receiver function inversions. *Journal of Geophysical Research*, *95*. https://doi.org/10.1029/jb095ib10p15303

Anthony, R. E., Ringler, A. T., & Wilson, D. C. (2018). The widespread influence of great lakes microseisms across the midwestern united states revealed by the 2014 polar vortex. *Geophysical Research Letters*, *45*, 3436–3444.

Antunes, V., Planès, T., Zahradník, J., Obermann, A., Alvizuri, C., Carrier, A., & Lupi, M. (2020). Seismotectonics and 1-d velocity model of the greater geneva basin, france–switzerland. *Geophysical Journal International*, *221*(3), 2026–2047.

Ballmer, S., Wolfe, C. J., Okubo, P. G., Haney, M. M., & Thurber, C. H. (2013). Ambient seismic noise interferometry in hawai'i reveals long-range observability of volcanic tremor. *Geophysical Journal International*, *194*(1), 512–523.

Barrière, J., D'Oreye, N., Oth, A., Geirsson, H., Mashagiro, N., Johnson, J. B., Smets, B., Samsonov, S., & Kervyn, F. (2018). Single-station seismo-acoustic monitoring of nyiragongo's lava lake activity (d.r. congo). *Frontiers in Earth Science*, *6*, 1–17. https://doi.org/10.3389/feart.2018.00082

Barrière, J., D'Oreye, N., Oth, A., Theys, N., Mashagiro, N., Subira, J., Kervyn, F., & Smets, B. (2019). Seismicity and outgassing dynamics of Nyiragongo volcano. *Earth and Planetary Science Letters*, *528*, 115821. https://doi.org/10.1016/j.epsl.2019.115821

Barrière, J., D'Oreye, N., Smets, B., Oth, A., Delhaye, L., Subira, J., Mashagiro, N., Derauw, D., Smittarello, D., Syavulisembo, A. M., & Kervyn, F. (2022). Intra-Crater Eruption Dynamics at Nyiragongo (D.R. Congo), 2002–2021. *Journal of Geophysical Research: Solid Earth*, *127*(4), e2021JB023858. https://doi.org/10.1029/2021JB023858 e2021JB023858 2021JB023858.

Barrière, J., Oth, A., d'Oreye, N., Subira, J., Smittarello, D., Brenot, H., Theys, N., & Smets, B. (2023a). Local infrasound monitoring of lava eruptions at nyiragongo volcano (d.r. congo) using urban and near-source stations. *AGU General Assembly Conference Abstracts*.

Barrière, J., Oth, A., d'Oreye, N., Subira, J., Smittarello, D., Brenot, H., Theys, N., & Smets, B. (2023b). Local infrasound monitoring of lava eruptions at nyiragongo volcano (dr congo) using urban and near-source stations. *Geophysical Research Letters*, *50*(18), e2023GL104664.

Barrière, J., Oth, A., Theys, N., D'Oreye, N., & Kervyn, F. (2017). Long-term monitoring of long-period seismicity and space-based SO 2 observations at African lava lake volcanoes Nyiragongo and Nyamulagira (DR Congo). *Geophysical Research Letters*, *44*(12), 6020–6029. https://doi.org/10.1002/2017GL073348

Battaglia, J., & Aki, K. (2003). Location of seismic events and eruptive fissures on the piton de la fournaise volcano using seismic amplitudes. *Journal of Geophysical Research*, *108*, 2364. https://doi.org/10.1029/2002JB002193

Bensen, G., Ritzwoller, M., Barmin, M., Levshin, A. L., Lin, F., Moschetti, M., Shapiro, N., & Yang, Y. (2007). Processing seismic ambient noise data to obtain reliable broad-band surface wave dispersion measurements. *Geophysical journal international*, *169*(3), 1239–1260.

Bonjer, K. P., Fuchs, K., & Wohlenberg, J. (1970). *Crustal structure of the East African Rift System from spectral response ratios of long-period body-waves* (Vol. 36). Geophysical Inst.

Bormann, P. (2012). New manual of seismological observatory practice (nmsop-2). iaspei, gfz ger. *Research Centre for Geosciences*. https://doi.org/10.2312/GFZ.NMSOP-2

Bormann, P. (2002). New manual of seismological observatory practice.

Bram, K. (1975). *Zum Aufbau der Kruste und des oberen Mantels im Bereich des westlichen Grabens des ostafrikanischen Grabensystems und im östlichen Zaire-Becken: Ergebnisse e. Unters. d. Raumwellen von Nah-Erdbeben* [Doctoral dissertation]. Verlag nicht ermittelbar.

Brenguier, F., Shapiro, N. M., Campillo, M., Ferrazzini, V., Duputel, Z., Coutant, O., & Nercessian, A. (2008). Towards forecasting volcanic eruptions using seismic noise. *Nature Geoscience*, *1*(2), 126–130.

Brill, K. A., Waite, G. P., & Chigna, G. (2018). Foundations for forecasting: Defining baseline seismicity at fuego volcano, Guatemala. *Frontiers in Earth Science*, *6*(July), 1–18. https://doi.org/10.3389/feart.2018.00087

Burgi, P.-Y., Valade, S., Coppola, D., Boudoire, G., Mavonga, G., Rufino, F., & Tedesco, D. (2021). Unconventional filling dynamics of a pit crater. *Earth and Planetary Science Letters*, *576*, 117230. https://doi.org/https://doi.org/10.1016/j.epsl.2021.117230

Buurman, H., West, M. E., Power, J., & Coombs, M. (2006). Seismic precursors to volcanic explosions during the 2006 eruption of augustine volcano. *The*, 41–57.

Caplan-Auerbach, J., & Petersen, T. (2005). Repeating coupled earthquakes at shishaldin volcano, alaska. *Journal of Volcanology and Geothermal Research*, *145*, 151–172. https://doi.org/10.1016/j.jvolgeores.2005.01.011

Carchedi, C. J. W., Gaherty, J. B., Webb, S. C., & Shillington, D. J. (2022). Investigating short-period lake-generated microseisms using a broadband array of onshore and lake-bottom seismometers. *Seismological Society of America*, *93*(3), 1585–1600.

Caudron, C., Taisne, B., Kugaenko, Y., & Saltykov, V. (2015). Magma migration at the onset of the 2012–13 tolbachik eruption revealed by seismic amplitude ratio analysis [SI: 2012-13 Tolbachik eruption]. *Journal of Volcanology and Geothermal Research*, *307*, 60–67. https://doi.org/https://doi.org/10.1016/j.jvolgeores.2015.09.010

Caudron, C., White, R. S., Green, R. G., Woods, J., Ágústsdóttir, T., Donaldson, C., Greenfield, T., Rivalta, E., & Brandsdóttir, B. (2018). Seismic amplitude ratio analysis of the 2014-15 bárðarbunga-holuhraun dike propagation and eruption. *Journal of Geophysical Research: Solid Earth*, *123*, 264–276. https://doi.org/10.1002/2017JB014660

Chouet, B. A., & Matoza, R. S. (2013, February). A multi-decadal view of seismic methods for detecting precursors of magma movement and eruption. https://doi.org/10.1016/j.jvolgeores.2012.11.013

Cortés, G., Carniel, R., Lesage, P., Mendoza, M. Á., & Della Lucia, I. (2021). Practical volcano-independent recognition of seismic events: Vulcan. ears project. *Frontiers in Earth Science*, *8*, 616676.

Dahlen, F. A., Hung, S. H., & Nolet, G. (2000). Fréchet kernels for finite-frequency traveltimes-i. theory. *Geophysical Journal International*, *141*. https://doi.org/10.1046/j.1365-246X.2000.00070.x

Dawson, J. B., Pinkerton, H., Norton, G. E., & Pyle, D. M. (1990). Physicochemical properties of alkali carbonatite lavas:Data from the 1988 eruption of Oldoinyo Lengai, Tanzania. *Geology*, *18*(3), 260–263. https://doi.org/10.1130/0091-7613(1990)018<0260:PPOACL>2.3.CO;2

Delvaux, D., Mulumba, J.-L. L., Sebagenzi, M. N. S., Bondo, S. F., Kervyn, F., & Havenith, H.-B. B. (2017). Seismic hazard assessment of the Kivu rift segment based on a new seismotectonic zonation model (western branch, East African Rift system). *Journal of African Earth Sciences*, *134*, 831–855. https://doi.org/10.1016/j.jafrearsci.2016.10.004

Diehl, T., Kissling, E., Husen, S., & Aldersons, F. (2009). Consistent phase picking for regional tomography models: Application to the greater Alpine region. *Geophysical Journal International*, *176*(2), 542–554. https://doi.org/10.1111/j.1365-246X.2008.03985.x

Docquier, D., Thiery, W., Lhermitte, S., & Lipzig, N. V. (2016). Multi-year wind dynamics around lake tanganyika. *Climate Dynamics*, *47*, 3191–3202.

Donaldson, C., Caudron, C., Green, R. G., Thelen, W. A., & White, R. S. (2017). Relative seismic velocity variations correlate with deformation at kılauea volcano. *Science advances*, *3*(6), e1700219.

D'Oreye, N., González, P. J., Shuler, A., Oth, A., Bagalwa, L., Ekström, G., Kavotha, D., Kervyn, F., Lucas, C., Lukaya, F., Osodundu, E., Wauthier, C., & Fernández, J. (2011). Source parameters of the 2008 Bukavu-Cyangugu earthquake estimated from InSAR and teleseismic data. *Geophysical Journal International*, *184*(2), 934–948. https://doi.org/10.1111/j.1365-246X.2010.04899.x

Droznin, D., Shapiro, N., Droznina, S. Y., Senyukov, S., Chebrov, V., & Gordeev, E. (2015). Detecting and locating volcanic tremors on the klyuchevskoy group of volcanoes (kamchatka) based on correlations of continuous seismic records. *Geophysical Journal International*, *203*(2), 1001–1010.

Duque, A., González, K., Pérez, N., Benítez, D., Grijalva, F., Lara-Cueva, R., & Ruiz, M. (2020). Exploring the unsupervised classification of seismic events of cotopaxi volcano. *Journal of Volcanology and Geothermal Research*, *403*, 107009. https://doi.org/https://doi.org/10.1016/j.jvolgeores.2020.107009

Ebinger, C. J. (1989). Tectonic development of the western branch of the east african rift system. *Geological Society of America Bulletin*, *101*(7), 885–903.

Ebmeier, S. K., Biggs, J., Mather, T. A., & Amelung, F. (2013). Applicability of insar to tropical volcanoes: Insights from central america. *Geological Society, London, Special Publications*, *380*(1), 15–37.

Endo, E. T., & Murray, T. (1991). Real-time seismic amplitude measurement (RSAM): a volcano monitoring and prediction tool. *Bulletin of Volcanology*, *53*(7), 533–545.

Farrell, J., Koper, K. D., & Sohn, R. A. (2023). The relationship between wind, waves, bathymetry, and microseisms in yellowstone lake, yellowstone national park. *Journal of Geophysical Research: Solid Earth*, *128*(7), e2022JB025943.

Gal, M., Lotter, E., Olivier, G., Green, M., Meyer, S., Dales, P., & Reading, A. M. (2021). Ccloc—an improved interferometric seismic event location algorithm applied to induced seismicity. *Seismological Society of America*, *92*(6), 3492–3503.

Geirsson, H., D'Oreye, N., Mashagiro, N., Syauswa, M., Celli, G., Kadufu, B., Smets, B., & Kervyn, F. (2017). Volcano-tectonic deformation in the Kivu Region, Central Africa: Results from six years of continuous GNSS observations of the Kivu Geodetic Network (KivuGNet). *Journal of African Earth Sciences*, *134*, 809–823. https://doi.org/10.1016/j.jafrearsci.2016.12.013

Geirsson, H., d'Oreye, N., Nobile, A., Smets, B., d'Oreye, N., & Kervyn, F. (2019). Deformation of tectonic and volcanic origin in the greater Kivu region. *Journées Luxembourgeoises de Géodynamique Conference Abstracts*, 25.

Gonnermann, H. M., Foster, J. H., Poland, M., Wolfe, C. J., Brooks, B. A., & Miklius, A. (2012). Coupling at mauna loa and kılauea by stress transfer in an asthenospheric melt layer. *Nature Geoscience*, *5*(11), 826–829.

Grigoli, F., Cesca, S., Vassallo, M., & Dahm, T. (2013). Automated seismic event location by travel-time stacking: An application to mining induced seismicity. *Seismological Research Letters*, *84*(4), 666–677.

Grigoli, F., Scarabello, L., Böse, M., Weber, B., Wiemer, S., & Clinton, J. F. (2018). Pick-and waveform-based techniques for real-time detection of induced seismicity. *Geophysical Journal International*, *213*(2), 868–884.

Hamaguchi, H., Nishimura, T., & Zana, N. (1992). Process of the 1977 nyiragongo eruption inferred from the analysis of long-period earthquakes and volcanic tremors. *Tectonophysics*, *209*, 241–254. https://doi.org/10.1016/0040-1951(92)90028-5

Hamaguchi, H., Zana, N., Tanaka, K., Kasahara, M., Mishina, M., Ueki, S., Sawa-Sawa, K., & Tachibana, K. (1982). Observations of Volcanic Earthquakes and Tremors at Volcanoes Nyiragongo and Nyamuragira in the Western Rift Valley of Africa. *Tohoku Geophysics Journal*, *29*(1), 41–56.

Havskov, J., & Ottemoller, L. (2010). *Routine data processing in earthquake seismology: With sample data, exercises and software*. https://doi.org/10.1007/978-90-481-8697-6

Havskov, J., & Ottemöller, L. (1999). SeisAn earthquake analysis software. *Seismological Research Letters*, *70*(5), 532–534. https://doi.org/10.1785/gssrl.70.5.532

Havskov, J., Voss, P. H., & Ottemöller, L. (2020). Seismological observatory software: 30 yr of seisan. *Seismological Research Letters*, *91*(3), 1846–1852.

Hotovec-Ellis, A., & Jeffries, C. (2016). Near real-time detection, clustering, and analysis of repeating earthquakes: Application to mount st. helens and redoubt volcanoes. *Seismological society of america annual meeting*.

Hua, Y., Zhang, S., Li, M., Wu, T., Zou, C., & Liu, L. (2019). Magma system beneath tengchong volcanic zone inferred from local earthquake seismic tomography. *Journal of*

Volcanology and Geothermal Research, *377*. https://doi.org/10.1016/j.jvolgeores.2019.04.002

Husen, S., Kissling, E., Deichmann, N., Wiemer, S., Giardini, D., & Baer, M. (2003). Probabilistic earthquake location in complex three-dimensional velocity models: Application to switzerland. *Journal of Geophysical Research: Solid Earth*, *108*. https://doi.org/10.1029/2002jb001778

Husen, S., Kissling, E., & Clinton, J. F. (2011). Local and regional minimum 1D models for earthquake location and data quality assessment in complex tectonic regions: Application to Switzerland. *Swiss Journal of Geosciences*, *104*(3), 455–469. https://doi.org/10.1007/s00015-011-0071-3

Hutton, L., & Boore, D. M. (1987). The ml scale in southern california. *Bulletin of the Seismological Society of America*, *77*(6), 2074–2094.

Ji, K. H., Stamps, D. S., Geirsson, H., Mashagiro, N., Syauswa, M., Kafudu, B., Subira, J., D'Oreye, N., D'Oreye, N., D'Oreye, N., D'Oreye, N., D'Oreye, N., & D'Oreye, N. (2017). Deep magma accumulation at Nyamulagira volcano in 2011 detected by GNSS observations. *Journal of African Earth Sciences*, *134*, 824–830. https://doi.org/10.1016/j.jafrearsci.2016.06.006

Johnson, J. B., & Aster, R. C. (2005). Relative partitioning of acoustic and seismic energy during strombolian eruptions. *Journal of Volcanology and Geothermal Research*, *148*, 334–354.

Jones, J., Carniel, R., Harris, A. J., & Malone, S. (2006). Seismic characteristics of variable convection at erta ale lava lake, ethiopia. *Journal of Volcanology and Geothermal Research*, *153*(1-2), 64–79.

Jones, J., Carniel, R., & Malone, S. (2012). Decomposition, location, and persistence of seismic signals recovered from continuous tremor at erta'ale, ethiopia. *Journal of Volcanology and Geothermal Research*, *213*, 116–129.

Kao, H., & Shan, S.-J. (2004). The source-scanning algorithm: Mapping the distribution of seismic sources in time and space. *Geophysical Journal International*, *157*(2), 589–594.

Kavotha, S. K., Mukambilwa, K., Durieux, J., & Mavonga, T. (2002). The january 2002 eruption-towards a more detailed seismic picture of the january 17th, 2002 nyiragongo eruption. *The January 2002 eruption-Towards a more detailed seismic picture of the January 17th, 2002 Nyiragongo eruption*, 1000–1014.

Kennett, B. L., & Engdahl, E. R. (1991). Traveltimes for global earthquake location and phase identification. *Geophysical Journal International*, *105*. https://doi.org/10.1111/j.1365-246X.1991.tb06724.x

Kerman, B. R., & Mereu, R. F. (1993). Wind-induced microseisms from lake ontario. *Atmosphere-Ocean*, *31*, 501–516.

Kervyn, F. (2022). Leçons tirée par le groupe belux du déroulement et du suivi de l'éruption volcanique du nyiragongo de mai 2021. *International Conference on Mitigating Volcanic Risks in the Virunga Region*.

Kervyn, M., Kervyn, F., Goossens, R., Rowland, S. K., & Ernst, G. (2007). Mapping volcanic terrain using high-resolution and 3d satellite remote sensing. *Geological Society, London, Special Publications*, *283*(1), 5–30.

Kilburn, C. (2018). Forecasting volcanic eruptions: Beyond the failure forecast method. front earth sci 6: 133.

Kissling, E., Ellsworth, W. L., Eberhart-Phillips, D., & Kradolfer, U. (1994). Initial reference models in local earthquake tomography. *Journal of Geophysical Research*, *99*(B10), 635–654. https://doi.org/10.1029/93jb03138

Kissling, E., Kradolfer, U., & Maurer, H. (1995a). Program VELEST user's guide-Short Introduction. *Institute of Geophysics, ETH Zurich*.

Kissling, E., Kradolfer, U., & Maurer, H. (1995b). Program velest user's guide-short introduction. *Institute of Geophysics, ETH Zurich*.

Kissling, E. (1988). Geotomography with local earthquake data. https://doi.org/10.1029/RG026i004p00659

Komorowski, J.-C. C., Tedesco, D., Kasereka, M., Allard, P., Papale, P., Vaselli, O., Durieux, J., Baxter, P., Halbwachs, M., Akumbe, M., Baluku, B., Briole, P., Ciraba, M., Dupin, J.-C., Etoy, O., Garcin, D., Hamaguchi, H., Houlié, N., J Kavotha, A. L., K.S Lemarchand, … Wafula, M. (2002). The january 2002 flank eruption of nyiragongo volcano (democratic republic of congo): Chronology, evidence for a tectonic rift trigger, and impact of lava flows on the city of goma. *Acta Vulcanologica*, *14*, 27–62.

Kranenburg, W., Tiessen, M., Veenstra, J., de Graaff, R., Uittenbogaard, R., Bouffard, D., Sakindi, G., Umutoni, A., Van de Walle, J., Thiery, W., & van Lipzig, N. (2020). 3d-modelling of lake kivu: Horizontal and vertical flow and temperature structure under spatially variable atmospheric forcing. *Journal of Great Lakes Research*, *46*(4), 947–960. https://doi.org/https://doi.org/10.1016/j.jglr.2020.05.012

Langet, N., Maggi, A., Michelini, A., & Brenguier, F. (2014). Continuous kurtosis-based migration for seismic event detection and location, with application to piton de la fournaise volcano, la reunion. *Bulletin of the Seismological Society of America*, *104*(1), 229–246.

Lavayssière, A., Crawford, W. C., Saurel, J. M., Satriano, C., Feuillet, N., Jacques, E., & Komorowski, J. C. (2022). A new 1D velocity model and absolute locations image the Mayotte seismo-volcanic region. *Journal of Volcanology and Geothermal Research*, *421*. https://doi.org/10.1016/j.jvolgeores.2021.107440

Lavayssière, A., Crawford, W. C., Saurel, J.-M., Satriano, C., Feuillet, N., Jacques, E., & Komorowski, J.-C. (2022). A new 1d velocity model and absolute locations image the mayotte seismo-volcanic region. *Journal of Volcanology and Geothermal Research*, *421*, 107440.

Lecocq, T., Caudron, C., & Brenguier, F. (2014). Msnoise, a python package for monitoring seismic velocity changes using ambient seismic noise. *Seismological Research Letters*, *85*, 715–726. https://doi.org/10.1785/0220130073

Lesage, P., Carrara, A., Pinel, V., & Arámbula-Mendoza, R. (2018). Absence of detectable precursory deformation and velocity variation before the large dome collapse of july 2015 at volcán de colima, mexico. *Frontiers in Earth Science*, *6*, 93.

Lienert, B. R., & Havskov, J. (1995). A computer program for locating earthquakes both locally and globally. *Seismological Research Letters*, *66*. https://doi.org/10.1785/gssrl.66.5.26

Lienert, B. R., Berg, E., & Frazer, L. N. (1986). Hypocenter: An earthquake location method using centered, scaled, and adaptively damped least squares. *Bulletin of the Seismological Society of America*, *76*. https://doi.org/10.1785/bssa0760030771

Lomax, A., Michelini, A., & Curtis, A. (2014). Earthquake location, direct, global-search methods. In R. A. Meyers (Ed.), *Encyclopedia of complexity and systems science* (pp. 1–33). Springer New York. https://doi.org/10.1007/978-3-642-27737-5_150-2

Lomax, A., Michelini, A., Curtis, A., & Meyers, R. (2009). Earthquake location, direct, global-search methods. *Encyclopedia of complexity and systems science*, *5*, 2449–2473.

Lomax, A., Virieux, J., Volant, P., & Berge-Thierry, C. (2000). Probabilistic Earthquake Location in 3D and Layered Models, 101–134. https://doi.org/10.1007/978-94-015-9536-0_5

Lomax, A., Zollo, A., Capuano, P., & Virieux, J. (2001). Precise, absolute earthquake location under Somma-Vesuvius volcano using a new three-dimensional velocity model. *Geophysical Journal International*, *146*(2), 313–331. https://doi.org/10.1046/j.0956-540X.2001.01444.x

Lukaya, N., Ciraba, M., Mavonga, T., & Wafula, M. (1992). Main pattern of waveforms observed in the virunga volcai zone, western rift valley of africa. *Tectonophysics*, *209*, 261–265. https://doi.org/10.1016/0040-1951(92)90031-Z

Maggi, A., Ferrazzini, V., Hibert, C., Beauducel, F., Boissier, P., & Amemoutou, A. (2017). Implementation of a multistation approach for automated event classification at piton de la fournaise volcano. *Seismological Research Letters*, *88*(3), 878–891.

Malfante, M., Dalla Mura, M., Metaxian, J.-P., Mars, J. I., Macedo, O., & Inza, A. (2018). Machine learning for volcano-seismic signals: Challenges and perspectives. *IEEE Signal Processing Magazine*, *35*(2), 20–30. https://doi.org/10.1109/MSP.2017.2779166

Matoza, R. S., Shearer, P. M., & Okubo, P. G. (2014). High-precision relocation of long-period events beneath the summit region of kılauea volcano, hawai 'i, from 1986 to 2009. *Geophysical Research Letters*, *41*(10), 3413–3421.

Matrullo, E., De Matteis, R., Satriano, C., Amoroso, O., & Zollo, A. (2013). An improved 1-D seismic velocity model for seismological studies in the Campania-Lucania region (Southern Italy). *Geophysical Journal International*, *195*(1), 460–473. https://doi.org/10.1093/gji/ggt224

Mavonga, G. T. (2010). Seismic Hazard Assessment and Volcanogenic Seismicity for the Democratic Republic of Congo and Surrounding Areas, Western Rift Valley of Africa, 142.

Mavonga, T., Zana, N., & Durrheim, R. J. (2010). Studies of crustal structure, seismic precursors to volcanic eruptions and earthquake hazard in the eastern provinces of the Democratic Republic of Congo. *Journal of African Earth Sciences*, *58*(4), 623–633. https://doi.org/10.1016/j.jafrearsci.2010.08.008

Mavonga, T. (2007). Some characteristics of aftershock sequences of major earthquakes from 1994 to 2002 in the kivu province, western rift valley of africa. *Tectonophysics*, *439*, 1–12. https://doi.org/10.1016/j.tecto.2007.01.006

Mavonga, T., Kavotha, S. K., Lukaya, N., Etoy, O., & Durieux, J. (2006). Seismic activity prior to the may 8, 2004 eruption of volcano nyamuragira, western rift valley of africa. *Journal of Volcanology and Geothermal Research*, *158*, 355–360. https://doi.org/10.1016/j.jvolgeores.2006.06.021

McNamara, D. E., & Buland, R. P. (2004). Ambiente noise levels in the continental united states. *Bulletin of the Seismological Society of America*, *94*, 1517–1527. https://doi.org/10.1785/012003001

Menke, W. (2018). *Geophysical data analysis: Discrete inverse theory*. Academic press.

Métaxian, J.-P., Lesage, P., & Dorel, J. (1997a). Permanent tremor of masaya volcano, nicaragua: Wave field analysis and source location. *Journal of Geophysical Research: Solid Earth*, *102*, 22529–22545.

Métaxian, J.-P., Lesage, P., & Dorel, J. (1997b). Permanent tremor of masaya volcano, nicaragua: Wave field analysis and source location. *Journal of Geophysical Research: Solid Earth*, *102*(B10), 22529–22545.

Moran, S. C., Freymueller, J. T., LaHusen, R. G., McGee, K. A., Poland, M. P., Power, J. A., Schmidt, D. A., Schneider, D. J., Stephens, G., Werner, C. A., et al. (2008). *Instrumentation recommendations for volcano monitoring at us volcanoes under the national volcano early warning system* (tech. rep.). US Geological Survey.

Morrison, A. A., Whittington, A. G., Smets, B., Kervyn, M., & Sehlke, A. (2020). The rheology of crystallizing basaltic lavas from Nyiragongo and Nyamuragira volcanoes, D.R.C. *Volcanica*, *3*(1), 1–28. https://doi.org/10.30909/vol.03.01.0128

Mousavi, S. M., Ellsworth, W. L., Zhu, W., Chuang, L. Y., & Beroza, G. C. (2020). Earthquake transformer—an attentive deep-learning model for simultaneous earthquake detection and phase picking. *Nature Communications*, *11*(1), 1–12.

Nyandwi, B. M., Kervyn, M., Habiyaremye, F. M., Kervyn, F., & Michellier, C. (2023). To go or not to go when the lava flow is coming? understanding evacuation decisions of goma inhabitants during the 2021 nyiragongo eruption crisis. *Journal of Volcanology and Geothermal Research*, 107947.

Oth, A., Barrière, J., d'Oreye, N., Mavonga, G., & Kervyn, F. (2018). The broadband seismic network KivuSNet in the Virunga Volcanic Province (Democratic Republic of the Congo): seismicity catalogues and fundamental seismological models after more than 2 years of continuous operation. *EGU General Assembly Conference Abstracts*, 16556.

Oth, A., Barrière, J., d'Oreye, N., Mavonga, G., Subira, J., Mashagiro, N., Kadufu, B., Fiama, S., Celli, G., de Dieu Bigirande, J., et al. (2017). Kivusnet: The first dense broadband seismic network for the kivu rift region (western branch of east african rift). *Seismological Research Letters*, *88*(1), 49–60.

Pagliuca, N. M., Badiali, L., Cattaneo, M., Ciraba, H., Delladio, A., Demartin, M., Garcia, A., Lisi, A., Lukaya, F., Marchetti, A., Monachesi, G., Mavonga, A., Sgroi, T., & Tedesco, D. (2009). Preliminary results from seismic monitoring at Nyiragongo Volcano (Democratic Republic of Congo) through telemetered seismic network, Goma volcanological observatory. *Bollettino di Geofisica Teorica ed Applicata*, *50*(2), 117–127.

Patrick, M. R., Anderson, K. R., Poland, M. P., Orr, T. R., & Swanson, D. A. (2015). Lava lake level as a gauge of magma reservoir pressure and eruptive hazard. *Geology*, *43*(9), 831–834.

Patrick, M. R., Orr, T., Swanson, D., & Lev, E. (2016). Shallow and deep controls on lava lake surface motion at kılauea volcano. *Journal of Volcanology and Geothermal Research*, *328*, 247–261.

Pesicek, J. D., Wellik, J. J., Prejean, S. G., & Ogburn, S. E. (2018). Prevalence of seismic rate anomalies preceding volcanic eruptions in alaska. *Frontiers in Earth Science*, *6*, 100.

Podvin, P., & Lecomte, I. (1991). Finite difference computation of traveltimes in very contrasted velocity models: A massively parallel approach and its associated tools. *Geophysical Journal International*, *105*. https://doi.org/10.1111/j.1365-246X.1991.tb03461.x

Poiata, N., Satriano, C., Vilotte, J.-P., Bernard, P., & Obara, K. (2016). Multiband array detection and location of seismic sources recorded by dense seismic networks. *Geo-*

physical Journal International, *205*(3), 1548–1573. https://doi.org/10.1093/gji/ggw071

Quintero, R., & Kissling, E. (2001). An improved p-wave velocity reference model for costa rica. *Geofisica Internacional*, *40*. https://doi.org/10.22201/igeof.00167169p.2001.40.1.416

Rawlinson, N., Pozgay, S., & Fishwick, S. (2010). Seismic tomography: A window into deep earth. https://doi.org/10.1016/j.pepi.2009.10.002

Richardson, J. P., & Waite, G. P. (2013). Waveform inversion of shallow repetitive long period events at villarrica volcano, chile. *Journal of Geophysical Research: Solid Earth*, *118*(9), 4922–4936.

Ríos, D., Parra, C., Grijalva, F., Benítez, D., Pérez, N., Rosero, K., & Orozco, N. (2024). Learning feature representations from unlabeled data for volcano-seismic event classification. *Journal of Volcanology and Geothermal Research*, *445*, 107970. https://doi.org/https://doi.org/10.1016/j.jvolgeores.2023.107970

Romano, M., De Nardis, R., Garbin, M., Peruzza, L., Priolo, E., Lavecchia, G., & Romanelli, M. (2013). Temporary seismic monitoring of the sulmona area (abruzzo, italy): A quality study of microearthquake locations. *Natural Hazards and Earth System Sciences*, *13*(11), 2727–2744.

Saria, E., Calais, E., Altamimi, Z., Willis, P., & Farah, H. (2013). A new velocity field for Africa from combined GPS and DORIS space geodetic Solutions: Contribution to the definition of the African reference frame (AFREF). *Journal of Geophysical Research: Solid Earth*, *118*(4), 1677–1697. https://doi.org/10.1002/jgrb.50137

Smets, B., Kervyn, M., 'oreye, N. D., & Kervyn, F. (2015). Spatio-temporal dynamics of eruptions in a youthful extensional setting: Insights from nyamulagira volcano (d.r. congo), in the western branch of the east african rift. *Earth Science Reviews*, *150*, 305–328. https://doi.org/10.1016/j.earscirev.2015.08.008

Smets, B. (2015). *Dynamics of volcanic activity in youthful extensional setting studied by means of remote sensing and ground-based monitoring techniques* [Doctoral dissertation, Vrije Universiteit].

Smets, B., Delvaux, D., Ross, K. A., Poppe, S., Kervyn, M., D'Oreye, N., & Kervyn, F. (2016). The role of inherited crustal structures and magmatism in the development of rift segments: Insights from the Kivu basin, western branch of the East African Rift. *Tectonophysics*, *683*, 62–76. https://doi.org/10.1016/j.tecto.2016.06.022

Smets, B., D'Oreye, N., & Kervyn, F. (2014a). Toward another lava lake in the virunga volcanic field? *Eos, Transactions American Geophysical Union*, *95*, 377–378.

Smets, B., D'Oreye, N., Kervyn, F., Kervyn, M., Albino, F., Arellano, S. R., Bagalwa, M., Balagizi, C., Carn, S. A., Darrah, T. H., Fernández, J., Galle, B., González, P. J., Head, E., Karume, K., Kavotha, D., Lukaya, F., Mashagiro, N., Mavonga, G., … Yalire, M. M. (2014). Detailed multidisciplinary monitoring reveals pre- and co-eruptive signals at nyamulagira volcano (north kivu, democratic republic of congo). *Bulletin of Volcanology*, *76*, 1–35. https://doi.org/10.1007/s00445-013-0787-1

Smets, B., D'Oreye, N., Kervyn, M., & Kervyn, F. (2017). Gas piston activity of the Nyiragongo lava lake: first insights from a stereographic time-lapse camera system. *Journal of African Earth Sciences*, *134*, 874–887.

Smets, B., Wauthier, C., & D'Oreye, N. (2010). A new map of the lava flow field of Nyamulagira (D.R. Congo) from satellite imagery. *Journal of African Earth Sciences*, *58*(5), 778–786. https://doi.org/10.1016/j.jafrearsci.2010.07.005

Smets, B., D'Oreye, N., & Kervyn, F. (2014b). Toward another lava lake in the virunga volcanic field? *Eos, Transactions American Geophysical Union*, *95*(42), 377–378.

Smith, K., & Tape, C. (2019). Seismic noise in central alaska and influences from rivers, wind, and sedimentary basins. *Journal of Geophysical Research: Solid Earth*, *124*, 11678–11704.

Smittarello, D., Smets, B., Barrière, J., Michellier, C., Oth, A., Shreve, T., Grandin, R., Theys, N., Brenot, H., Cayol, V., Allard, P., Caudron, C., Chevrel, O., Darchambeau, F., de Buyl, P., Delhaye, L., Derauw, D., Ganci, G., Geirsson, H., … Syavulisembo Muhindo, A. (2022). Precursor-free eruption triggered by edifice rupture at Nyiragongo volcano. *Nature*, *609*(7925), 83–88. https://doi.org/10.1038/s41586-022-05047-8

Smittarello, D., Grandin, R., Jaspard, M., Derauw, D., d'Oreye, N., Shreve, T., Debret, M., Theys, N., & Brenot, H. (2023). Nyiragongo crater collapses measured by multi-sensor sar amplitude time series. *Journal of Geophysical Research: Solid Earth*, *128*(10), e2023JB026683.

Stutzmann, E., Ardhuin, F., Schimmel, M., Mangeney, A., & Patau, G. (2012). Modelling long-term seismic noise in various environments. *Geophysical Journal International*, *191*(2), 707–722.

Subira, J., Barrière, J., Caudron, C., Hubert-Ferrari, A., Oth, A., Smets, B., D'Oreye, N., & Kervyn, F. (2023). Detecting sources of shallow tremor at neighboring volcanoes in the virunga volcanic province using seismic amplitude ratio analysis (sara). *Bulletin of Volcanology*, *85*, 27. https://doi.org/10.1007/s00445-023-01640-5

Syavulisembo Muhindo, A., Kervyn, F., Lennert, M., Wolff, E., & Caroline, M. (2021). Spatio-temporal location of population: Strengthening the capacities of sudden hazards risk management in goma, drc. *International Journal of Disaster Risk Reduction*, *66*, 102565.

Taisne, B., Brenguier, F., Shapiro, N. M., & Ferrazzini, V. (2011). Imaging the dynamics of magma propagation using radiated seismic intensity. *Geophysical Research Letters*, *38*, 2–6. https://doi.org/10.1029/2010GL046068

Takemura, S., Furumura, T., & Saito, T. (2009). Distortion of the apparent s-wave radiation pattern in the high-frequency wavefield: Tottori-ken seibu, japan earthquake of 2000. *Geophys J Int*, *178*, 950–961. https://doi.org/10.1111/j.1365-246X.2009.04210.x

Tan, C. T., Taisne, B., Neuberg, J., & Basuki, A. (2019). Real-time assessment of potential seismic migration within a monitoring network using Red-flag SARA. *Journal of Volcanology and Geothermal Research*, *384*, 31–47. https://doi.org/10.1016/j.jvolgeores.2019.07.004

Tanaka, K. (1983). Seismicity and focal mechanism of the volcanic earthquakes in the virunga volcanic region. *Volcanoes Nyiragongo and Nyamuragira: Geophysical Aspects*, 19–28.

Tarantola, A. (1987). Inverse problem theory: Methods for data fitting and model parameter estimation. *Inverse problem theory: methods for data fitting and model parameter estimation*. https://doi.org/10.1016/0031-9201(89)90124-6

Tarantola, A., Valette, B., et al. (1982). Inverse problems= quest for information. *Journal of geophysics*, *50*(1), 159–170.

Tazieff, H. (1977). An exceptional eruption: Mt. Niragongo, Jan. 10 th, 1977. *Bulletin Volcanologique*, *40*(3), 189–200. https://doi.org/10.1007/BF02596999

Thelen, W., Waite, G., Lyons, J., & Fee, D. (2022). Infrasound observations and constraints on the 2018 eruption of kılauea volcano, hawaii. *Bulletin of Volcanology*, *84*(8), 76.

Thompson, G., Beer, M., Kougioumtzoglou, I., Patelli, E., & Au, S. (2015). Seismic monitoring of volcanoes. *Encyclopedia of earthquake engineering*, *10*, 1–25.

Thurber, C. H. (1992). Hypocenter-velocity structure coupling in local earthquake tomography. *Physics of the Earth and Planetary Interiors*, *75*(1-3), 55–62.

Tilling, R. I. (2008). The critical role of volcano monitoring in risk reduction. *Advances in Geosciences*, *14*, 3–11. https://doi.org/10.5194/adgeo-14-3-2008

Valade, S., Ripepe, M., Giuffrida, G., Karume, K., & Tedesco, D. (2018). Dynamics of mount nyiragongo lava lake inferred from thermal imaging and infrasound array. *Earth and Planetary Science Letters*, *500*, 192–204.

Vergniolle, S., & Métrich, ·. N. (2022). An interpretative view of open-vent volcanoes. *Bulletin of Volcanology*, *84*, 83. https://doi.org/10.1007/s00445-022-01581-5

Walwer, D., Wauthier, C., Barrière, J., Smittarello, D., Smets, B., & d'Oreye, N. (2023). Modeling the intermittent lava lake drops occurring between 2015 and 2021 at nyiragongo volcano. *Geophysical Research Letters*, *50*(8), e2022GL102365.

Wassermann, J. (2012). Volcano seismology. In *New manual of seismological observatory practice 2 (nmsop-2)* (pp. 1–77). Deutsches GeoForschungsZentrum GFZ.

Wauthier, C. (2011). Insar applied to the study of active volcanic and seismic areas in africa, 245.

Wauthier, C., Cayol, V., Smets, B., d'Oreye, N., Kervyn, F., D'Oreye, N., & Kervyn, F. (2015). Magma pathways and their interactions inferred from insar and stress modeling at nyamulagira volcano, d.r. congo. *Remote Sensing*, *7*, 15179–15202. https://doi.org/10.3390/rs71115179

Wauthier, C., Smets, B., Hooper, A., Kervyn, F., & D'Oreye, N. (2018). Identification of subsiding areas undergoing significant magmatic carbon dioxide degassing, along the northern shore of Lake Kivu, East African Rift. *Journal of Volcanology and Geothermal Research*, *363*, 40–49. https://doi.org/10.1016/j.jvolgeores.2018.08.018

Wood, D. A., Zal, H. J., Scholz, C. A., Ebinger, C. J., & Nizere, I. (2017). Evolution of the Kivu Rift, East Africa: interplay among tectonics, sedimentation and magmatism. *Basin Research*, *29*, 175–188. https://doi.org/10.1111/bre.12143

Wright, R., Blackett, M., & Hill-Butler, C. (2015). Some observations regarding the thermal flux from earth's erupting volcanoes for the period of 2000 to 2014. *Geophysical Research Letters*, *42*, 282–289. https://doi.org/10.1002/2014GL061997

Xu, Y., Koper, K. D., & Burlacu, R. (2017). Lakes as a source of short-period (0.5–2 s) microseisms. *Journal of Geophysical Research: Solid Earth*, *122*, 8241–8256. https://doi.org/10.1002/2017JB014808

Zhu, H. (2018). High vp/vs ratio in the crust and uppermost mantle beneath volcanoes in the central and eastern anatolia. *Geophysical Journal International*, *214*. https://doi.org/10.1093/GJI/GGY253

Zhu, W., & Beroza, G. C. (2019). Phasenet: A deep-neural-network-based seismic arrival-time picking method. *Geophysical Journal International*, *216*(1), 261–273.

Appendix A

Localisation du trémor

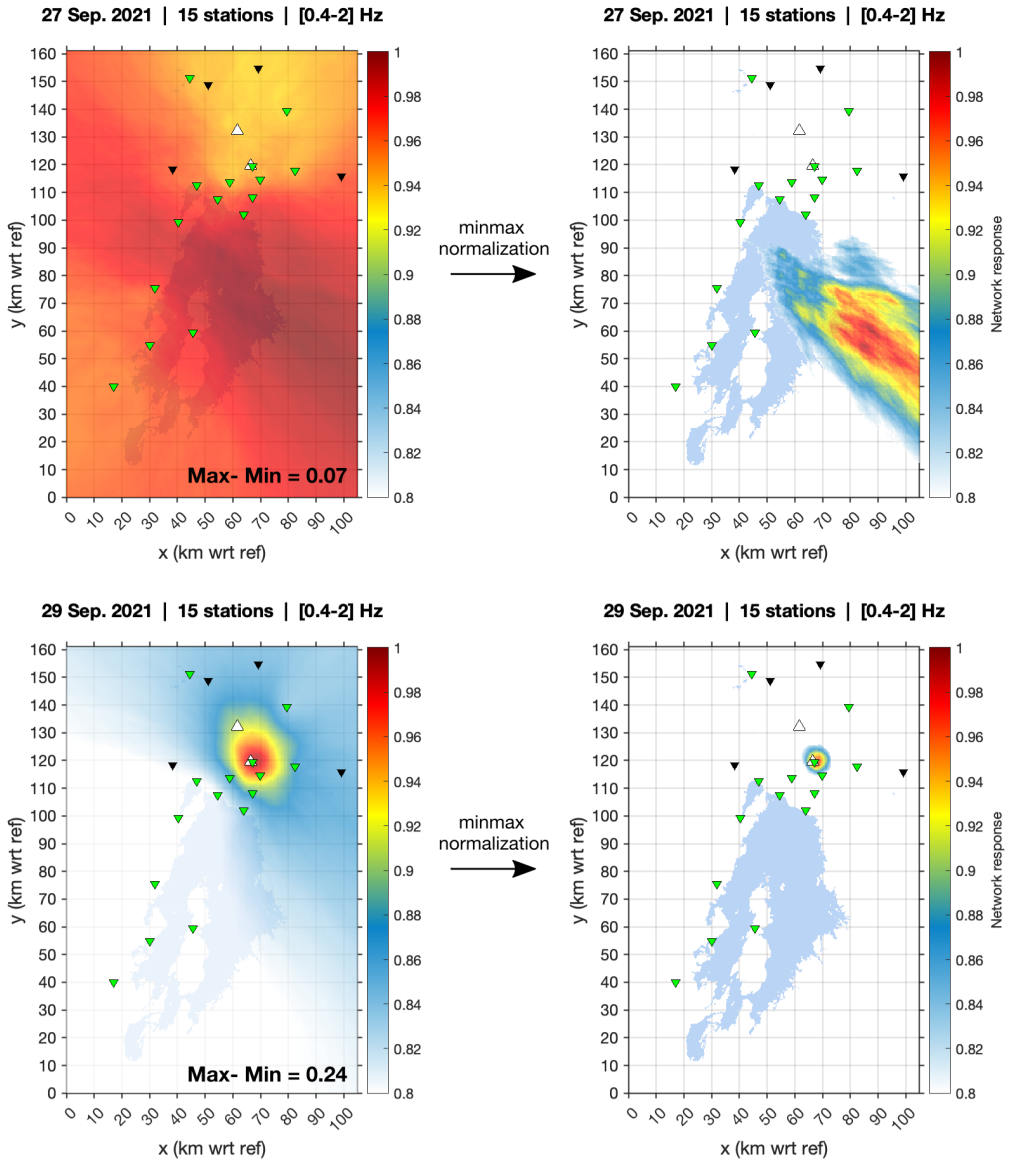

FIGURE A.1: Exemples de "Network response 2D" (longitude-latitude): En haut, sans source trémor apparente (le 27 septembre 2021); en bas, avec une source trémor claire au Nyiragongo le 29 septembre 2021. Les cartes sur la gauche sont les cartes obtenues par somme (stack) des NCFs. Après normalisation par le maximum, le point de la grille égale à 1 indique la source la plus probable. L'écart entre le maximum et le minimum (Max-Min) permet d'identifier si ce maximum fait du sens en terme de point source. C'est le cas pour le 29 septembre (en bas) mais pas pour le 27 septembre (en haut). Pour une meilleure visualisation des maxima entre différentes journées, chaque carte peut être mis à l'échelle entre 0 et 1 (cartes de droite), ce qui est appelé "minmax normalization". Ce sont ces dernières cartes qui sont représentées dans le chapitre 2

Appendix B

Comparison between Bonjer/Bram, iasp91 and Kivu 1D models

B.1 Bonjer/Bram model

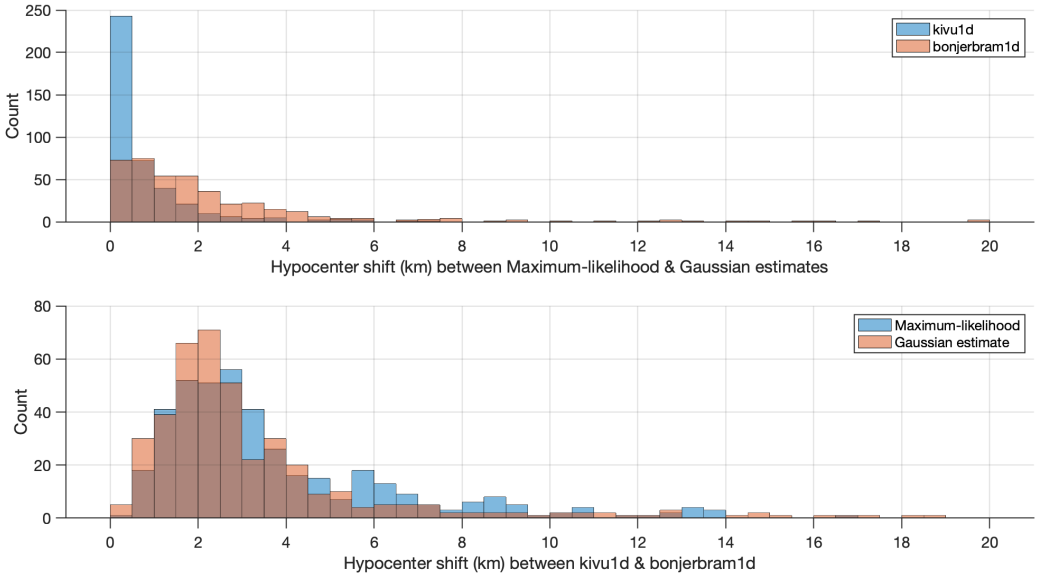

FIGURE B.1: **(Top)** Histograms showing the hypocenter shift (in km) between the MaxL and Gaussian solutions using the Kivu 1D model (blue) and Bonjer/Bram model (red). **(Bottom)** Hypocenter shift between both models for MaxL solutions (blue) and Gaussian estimates (red).

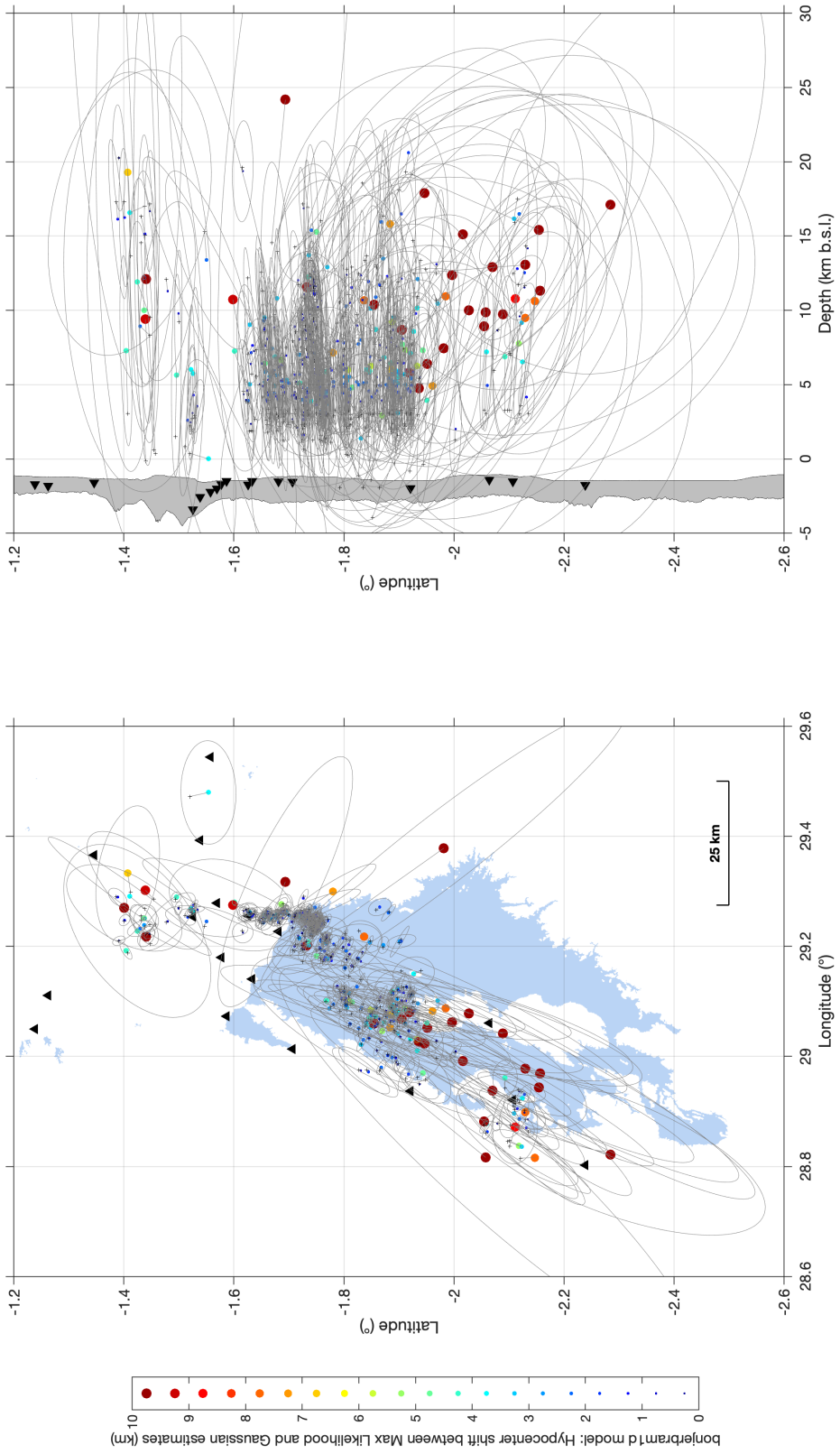

FIGURE B.2: Using the Bonjer/Bram model, comparison between computed MaxL (black crosses) and Gaussian solutions (colored circles) obtained with NonLinLoc for 410 events. The color scale corresponds to the distance (in km) between both solutions (clipped at 10 km).

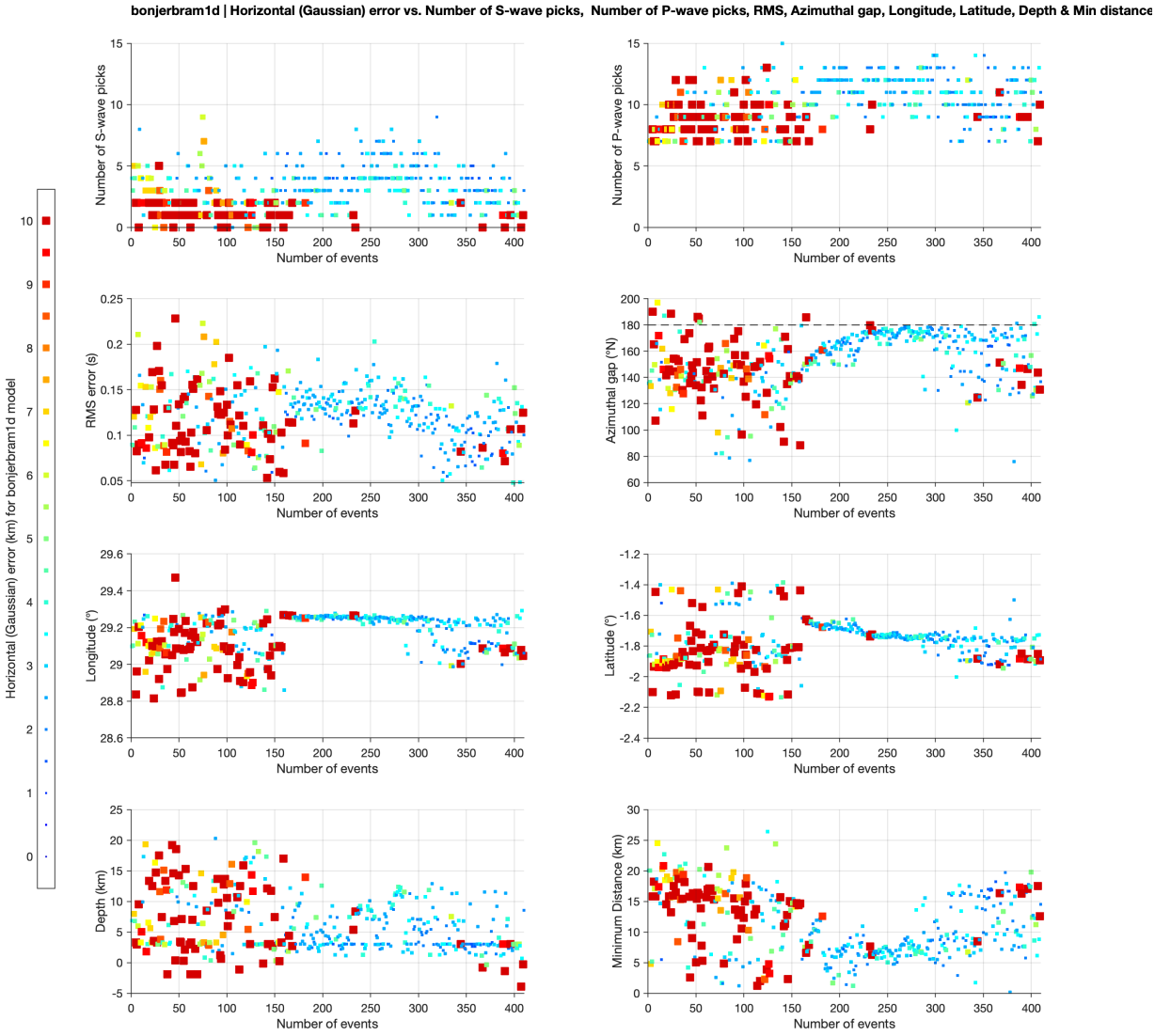

FIGURE B.3: Using the Bonjer/Bram model, computed maximum horizontal (Gaussian) error MaxERH (in km) for 410 events as a function of number of S-wave picks, number of P-wave picks, RMS error, azimuthal gap, longitude, latitude, depth and minimum distance to the seismic stations. Marker size and colors are proportional to MaxERH. The color scale ranges between 0 and 10 km (i.e., values exceeding 10 km are set to 10 km).

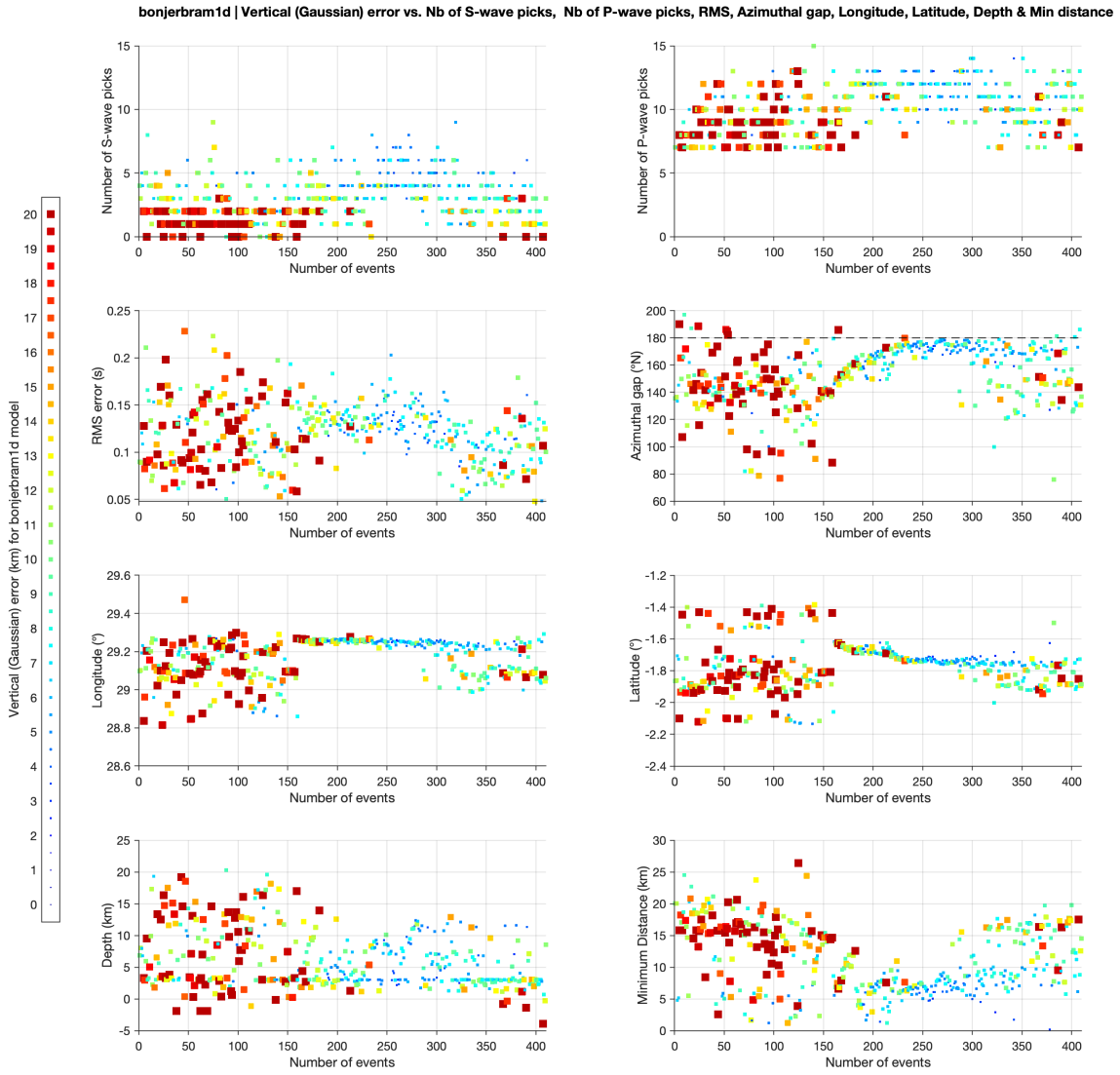

FIGURE B.4: Using the Bonjer/Bram model, computed maximum vertical (Gaussian) error MaxERZ (in km) for 410 events as a function of number of S-wave picks, number of P-wave picks, RMS error, azimuthal gap, longitude, latitude, depth and minimum distance to the seismic stations. Marker size and colors are proportional to MaxERZ. Note that the range of the color scale is twice the one used for MaxERH (0 to 20 km).

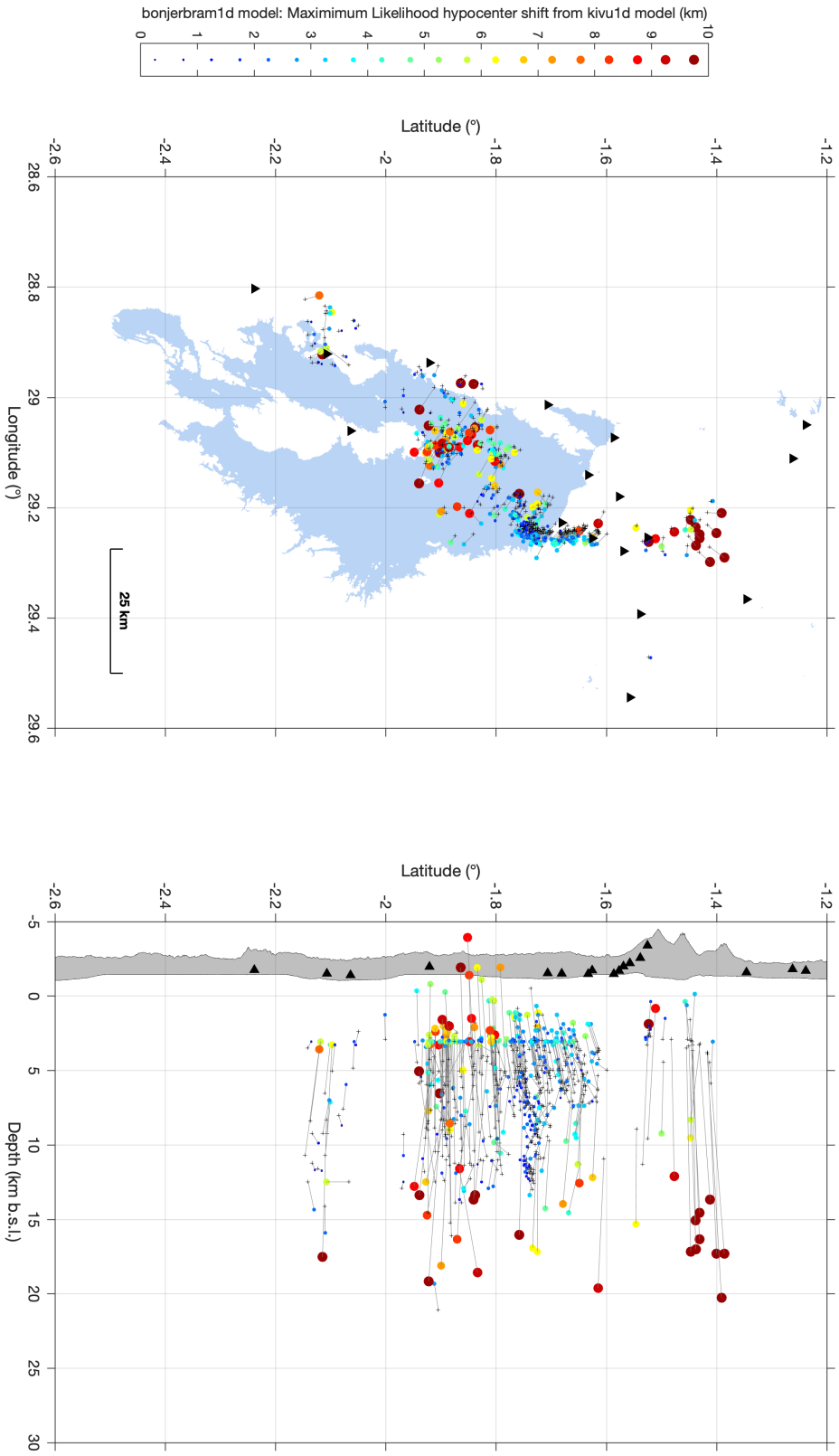

FIGURE B.5: Distance (in km) between MaxL solutions obtained with the Kivu 1D model (black crosses) and the Mavonga et al. (2010) model (colored circles). The color scale corresponds to the distance (in km) between both solutions (clipped at 10 km).

B.2 iasp91 model

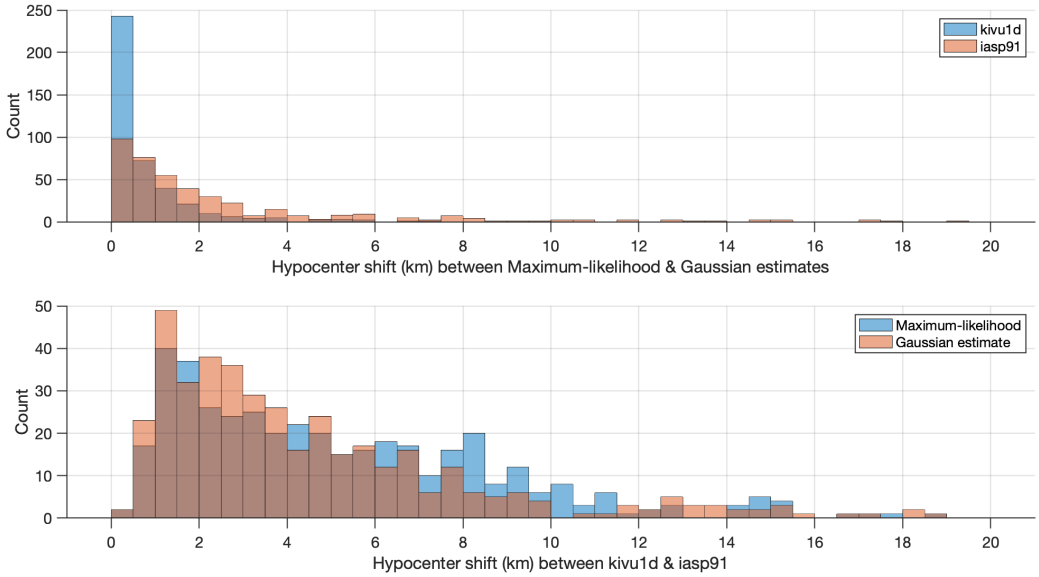

FIGURE B.6: **(Top)** Histograms showing the hypocenter shift (in km) between the MaxL and Gaussian solutions using the Kivu 1D model (blue) and iasp91 (red). **(Bottom)** Hypocenter shift between both models for MaxL solutions (blue) and Gaussian estimates (red).

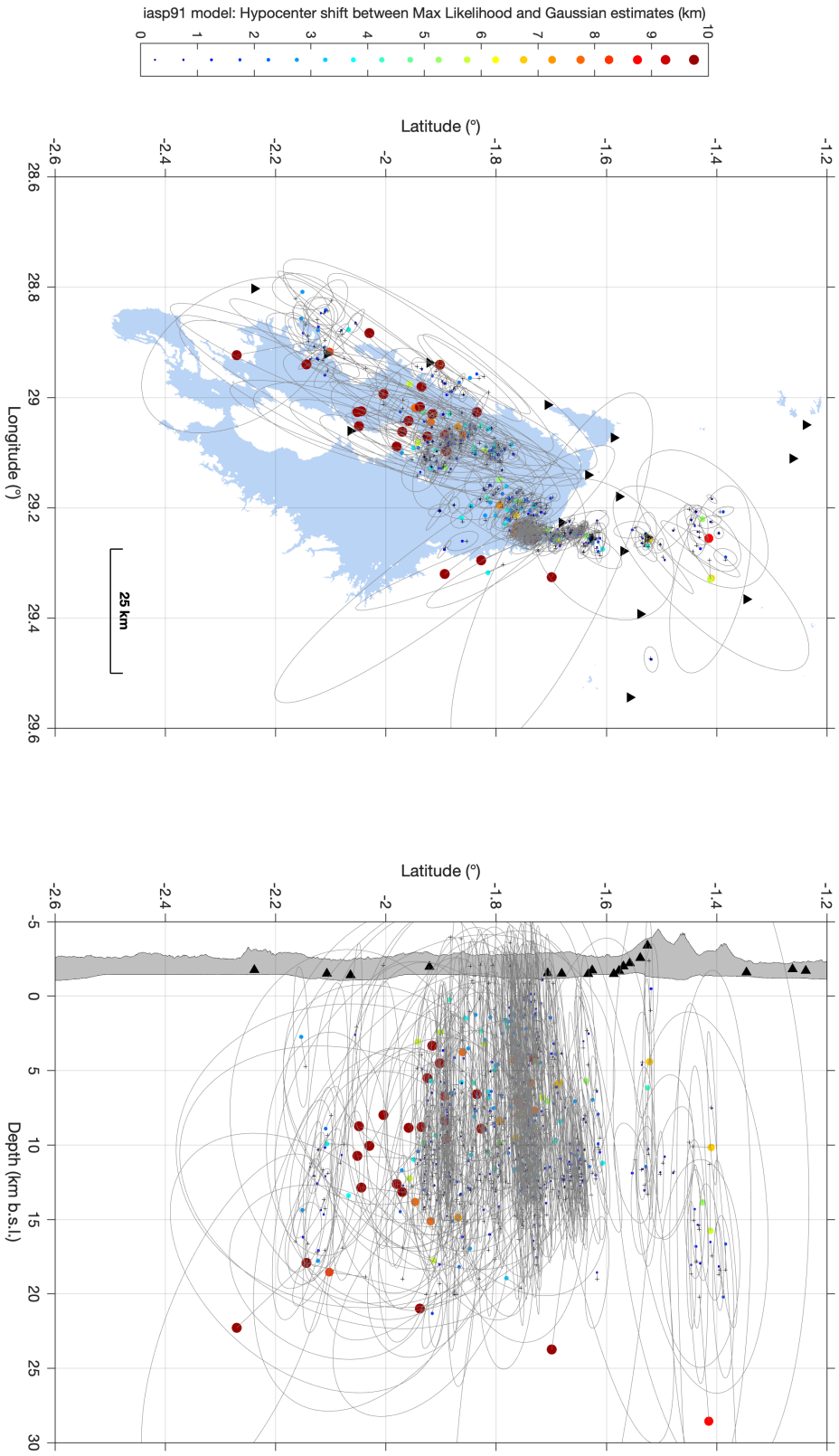

FIGURE B.7: Using the iasp91 model, comparison between computed MaxL (black crosses) and Gaussian solutions (colored circles) obtained with NonLinLoc for 410 events. The color scale corresponds to the distance (in km) between both solutions (clipped at 10 km).

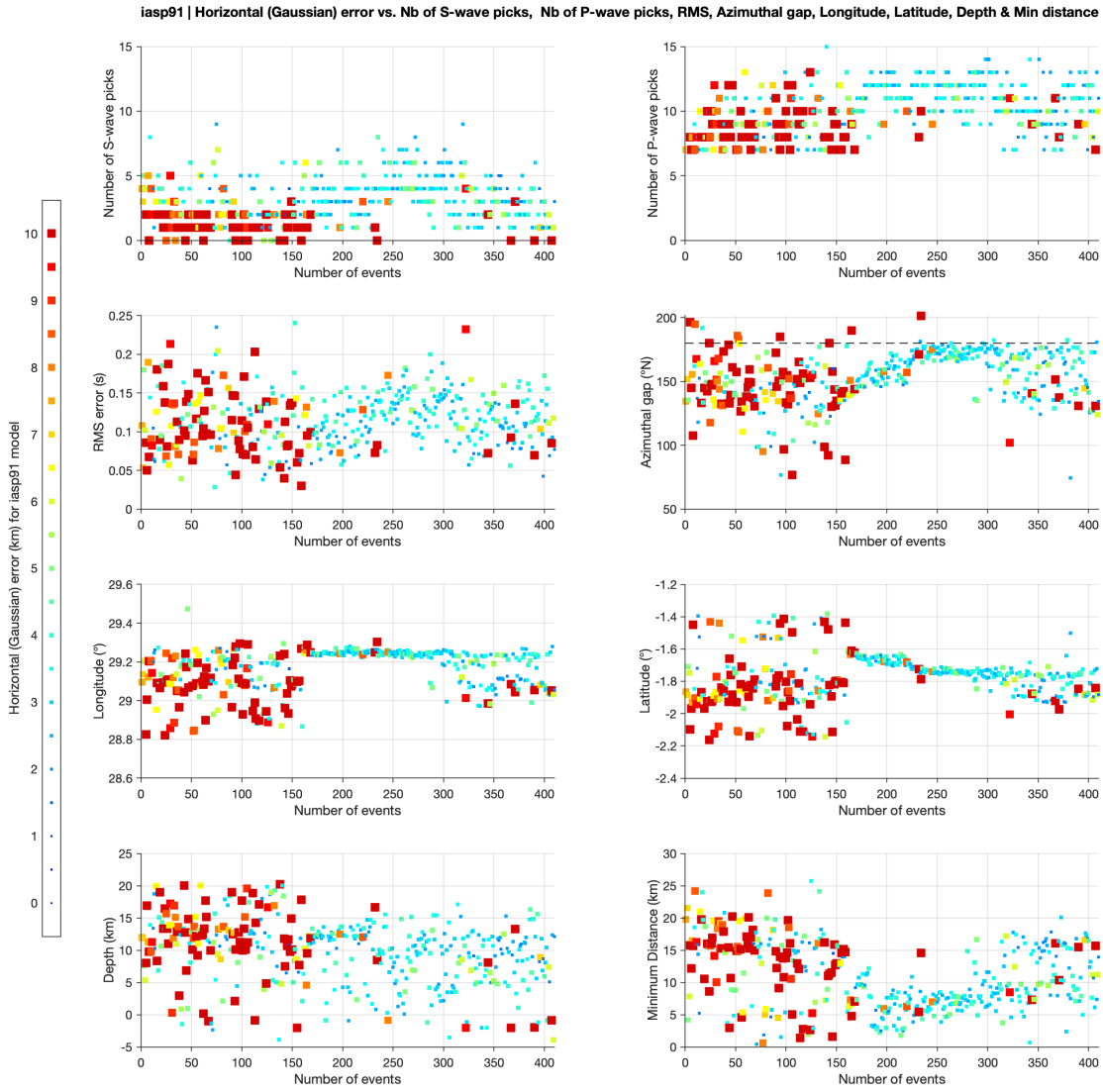

FIGURE B.8: Using the iasp91 model, computed maximum horizontal (Gaussian) error MaxERH (in km) for 410 events as a function of number of S-wave picks, number of P-wave picks, RMS error, azimuthal gap, longitude, latitude, depth and minimum distance to the seismic stations. Marker size and colors are proportional to MaxERH. The color scale ranges between 0 and 10 km (i.e., values exceeding 10 km are set to 10 km).

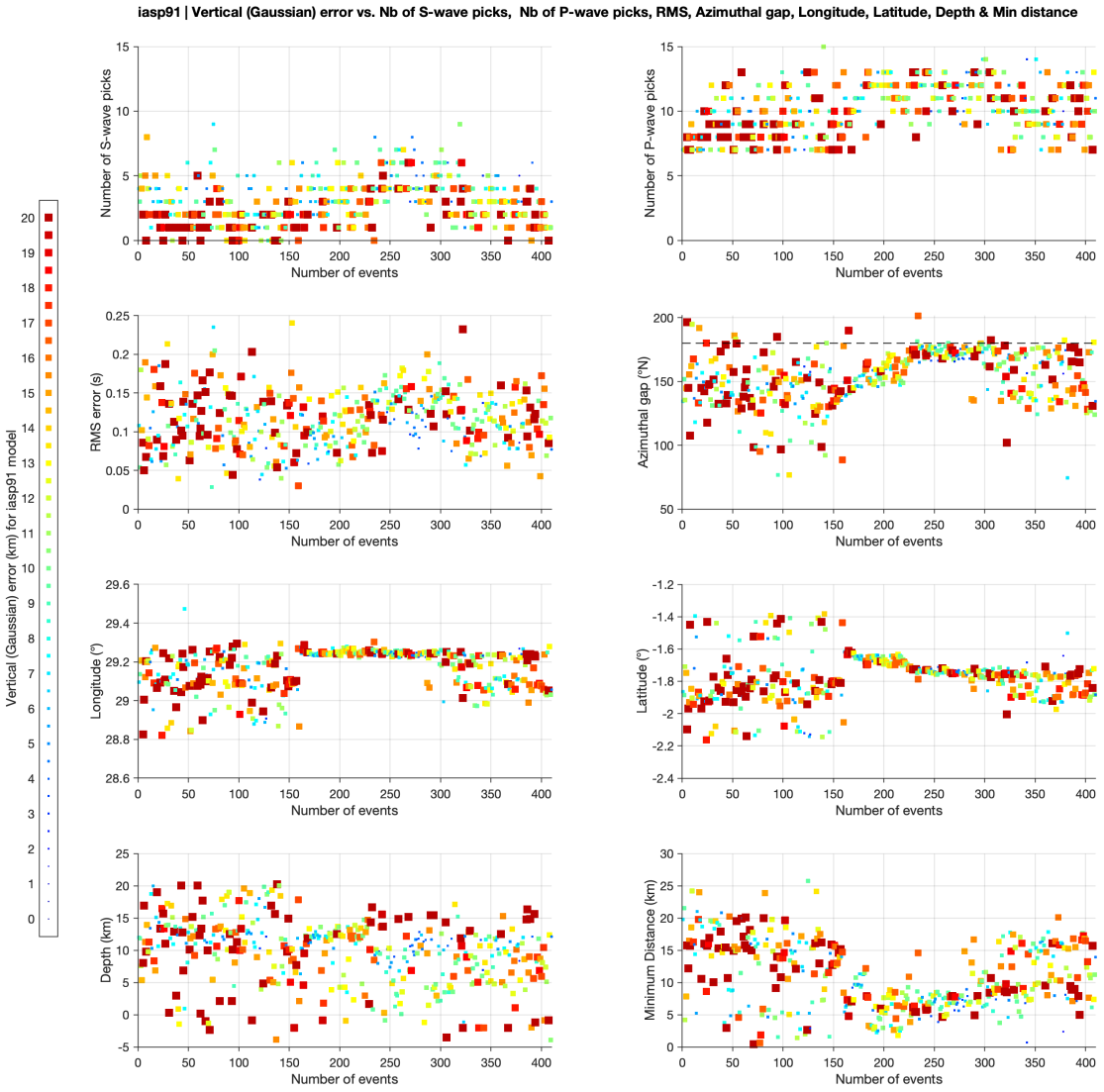

FIGURE B.9: Using the iasp91 model, computed maximum vertical (Gaussian) error MaxERZ (in km) for 410 events as a function of number of S-wave picks, number of P-wave picks, RMS error, azimuthal gap, longitude, latitude, depth and minimum distance to the seismic stations. Marker size and colors are proportional to MaxERZ. Note that the range of the color scale is twice the one used for MaxERH (0 to 20 km).

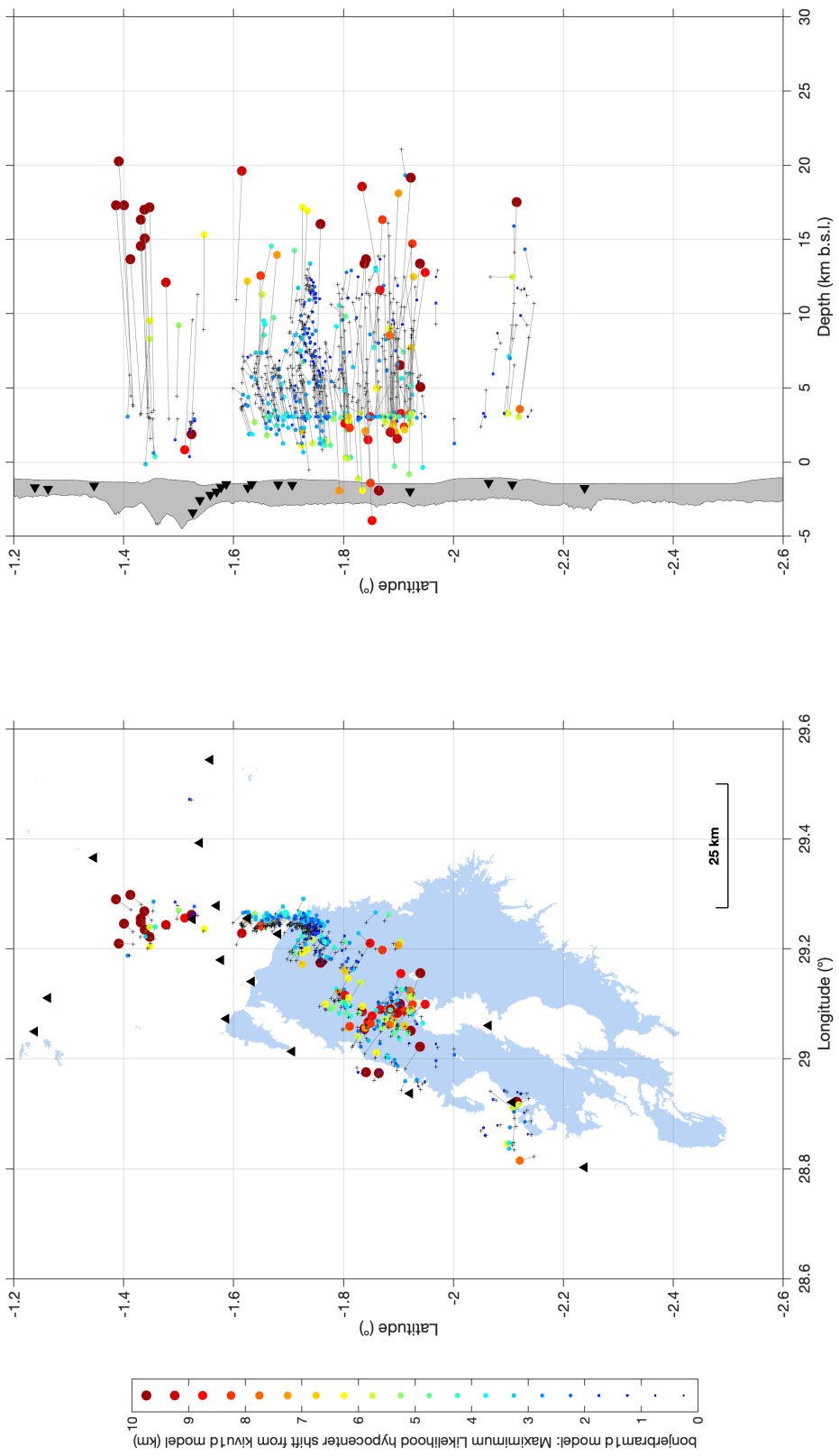

FIGURE B.10: Distance (in km) between MaxL solutions obtained with the Kivu 1D model (black crosses) and the iasp91 model (colored circles). The color scale corresponds to the distance (in km) between both solutions (clipped at 10 km).

B.3 Kivu 1D model without P-wave station delays

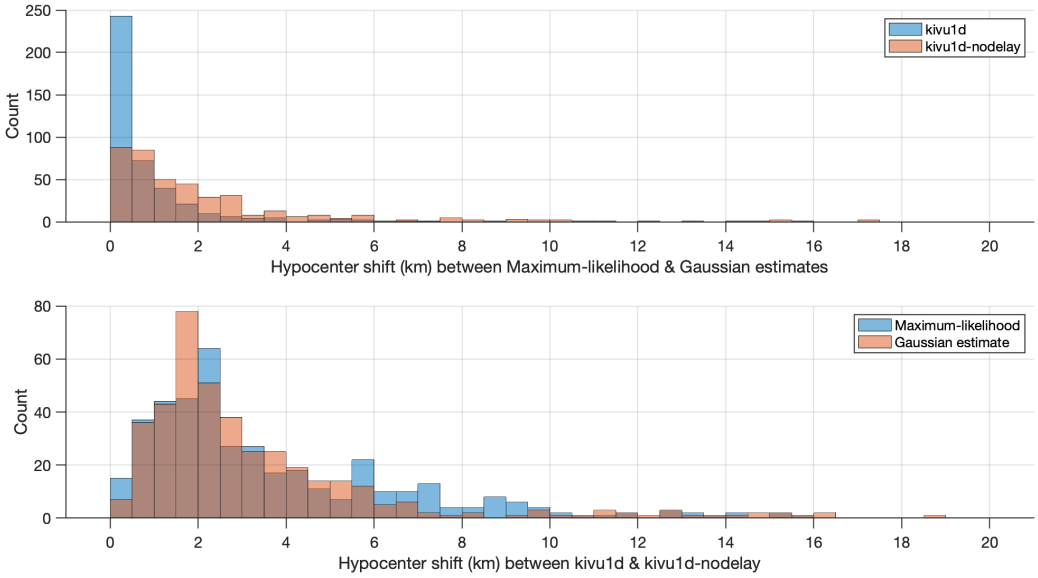

FIGURE B.11: **(Top)** Histograms showing the hypocenter shift (in km) between the MaxL and Gaussian solutions using the Kivu 1D model (blue) and the Kivu 1D model without P-wave station delays (red). **(Bottom)** Hypocenter shift between both models for MaxL solutions (blue) and Gaussian estimates (red).

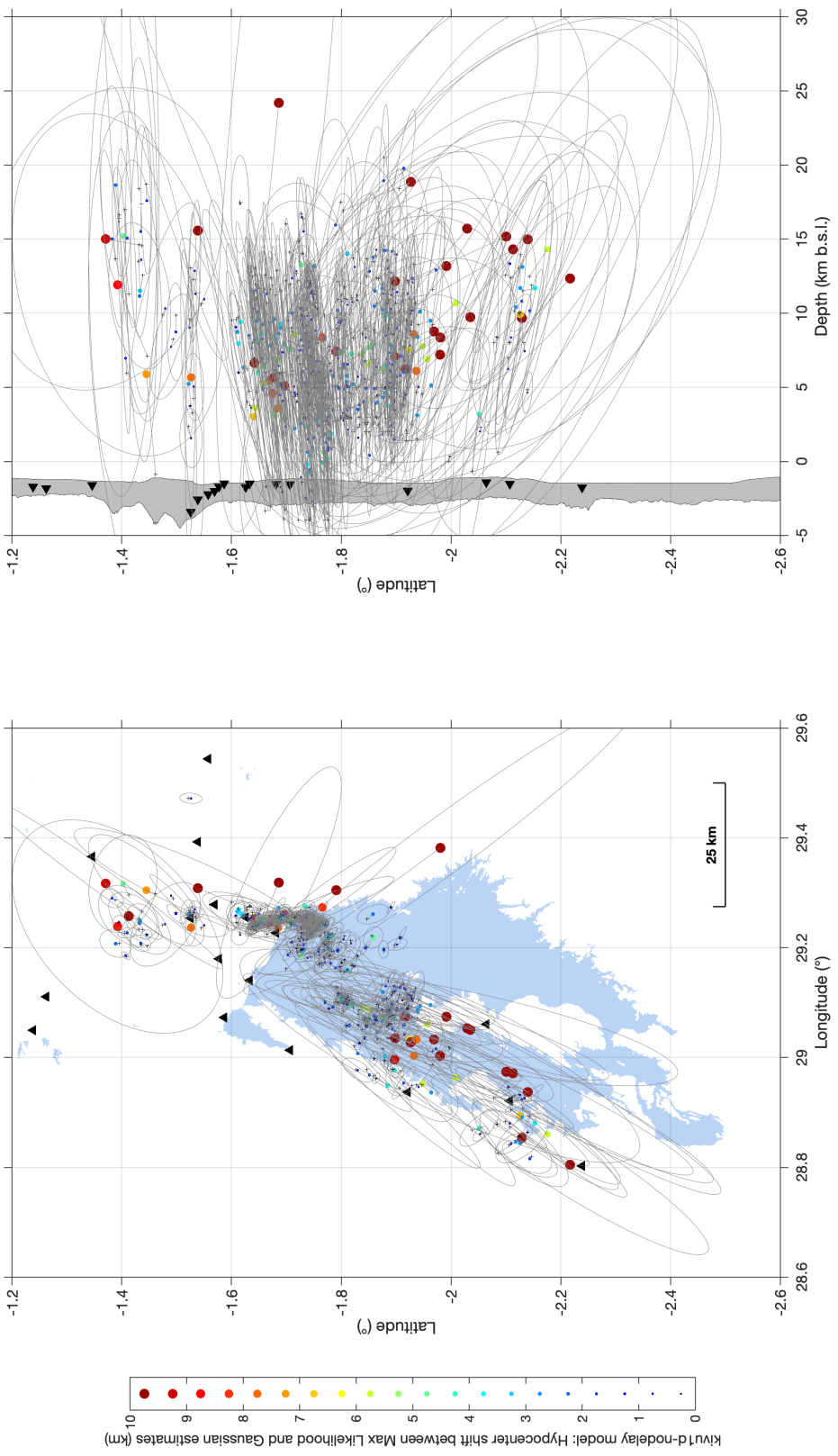

FIGURE B.12: Using the Kivu 1D model without P-wave station delays, comparison between computed MaxL (black crosses) and Gaussian solutions (colored circles) obtained with NonLinLoc for 410 events. The color scale corresponds to the distance (in km) between both solutions (clipped at 10 km).

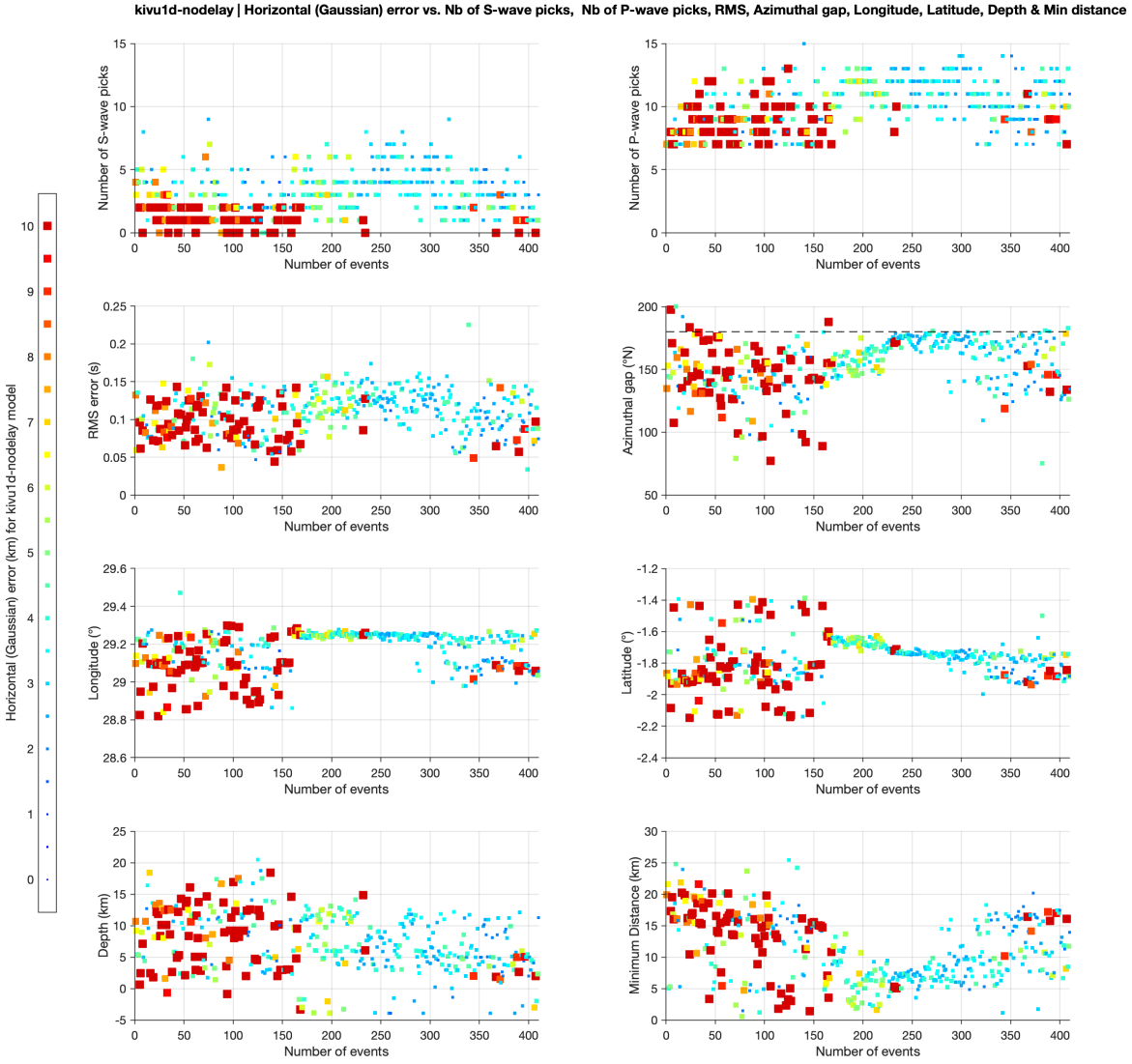

FIGURE B.13: Using the Kivu 1D model without P-wave station delays, computed maximum horizontal (Gaussian) error MaxERH (in km) for 410 events as a function of number of S-wave picks, number of P-wave picks, RMS error, azimuthal gap, longitude, latitude, depth and minimum distance to the seismic stations. Marker size and colors are proportional to MaxERH. The color scale ranges between 0 and 10 km (i.e., values exceeding 10 km are set to 10 km).

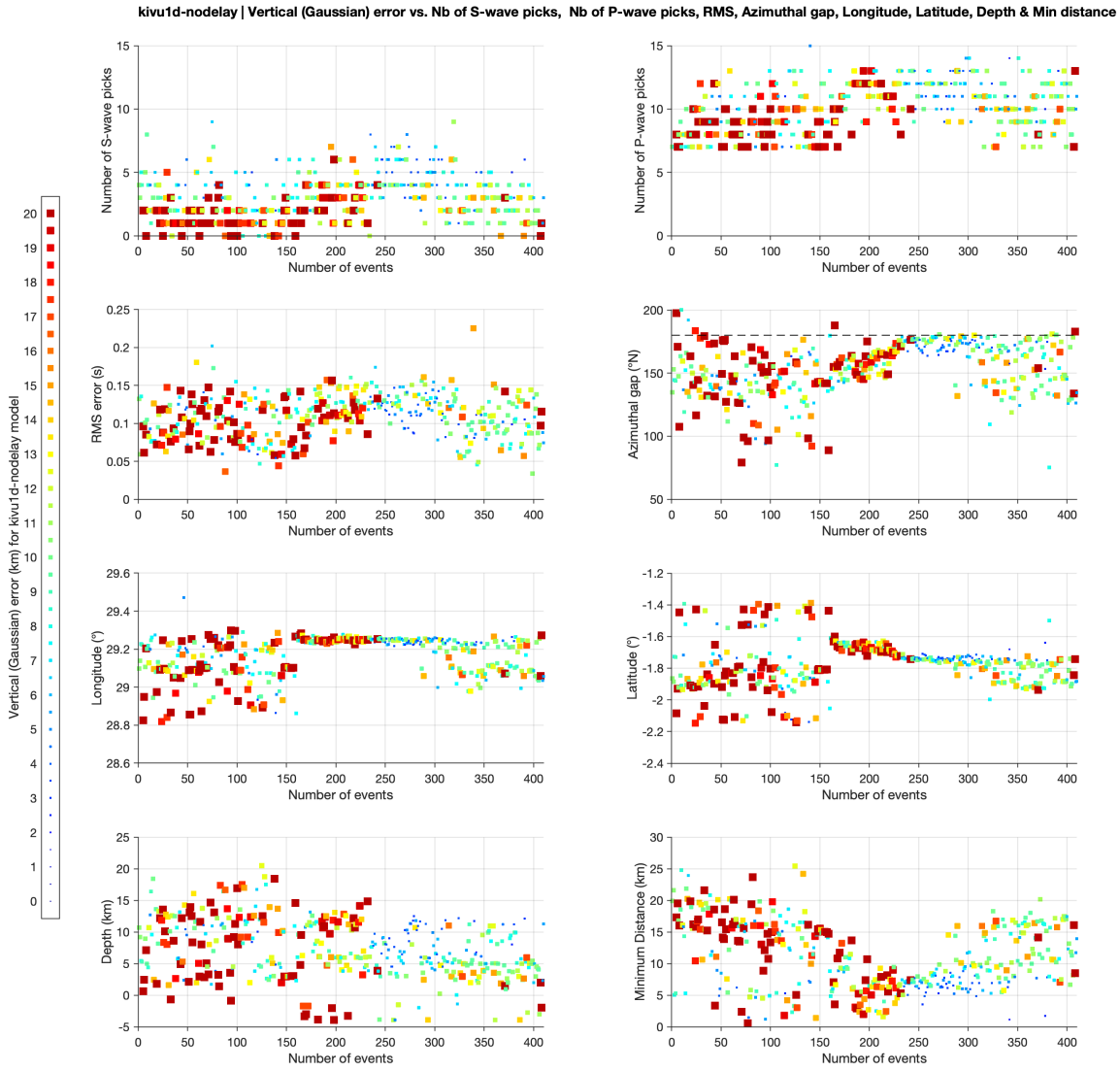

FIGURE B.14: Using the Kivu 1D model without P-wave station delays, computed maximum vertical (Gaussian) error MaxERZ (in km) for 410 events as a function of number of S-wave picks, number of P-wave picks, RMS error, azimuthal gap, longitude, latitude, depth and minimum distance to the seismic stations. Marker size and colors are proportional to MaxERZ. Note that the range of the color scale is twice the one used for MaxERH (0 to 20 km).

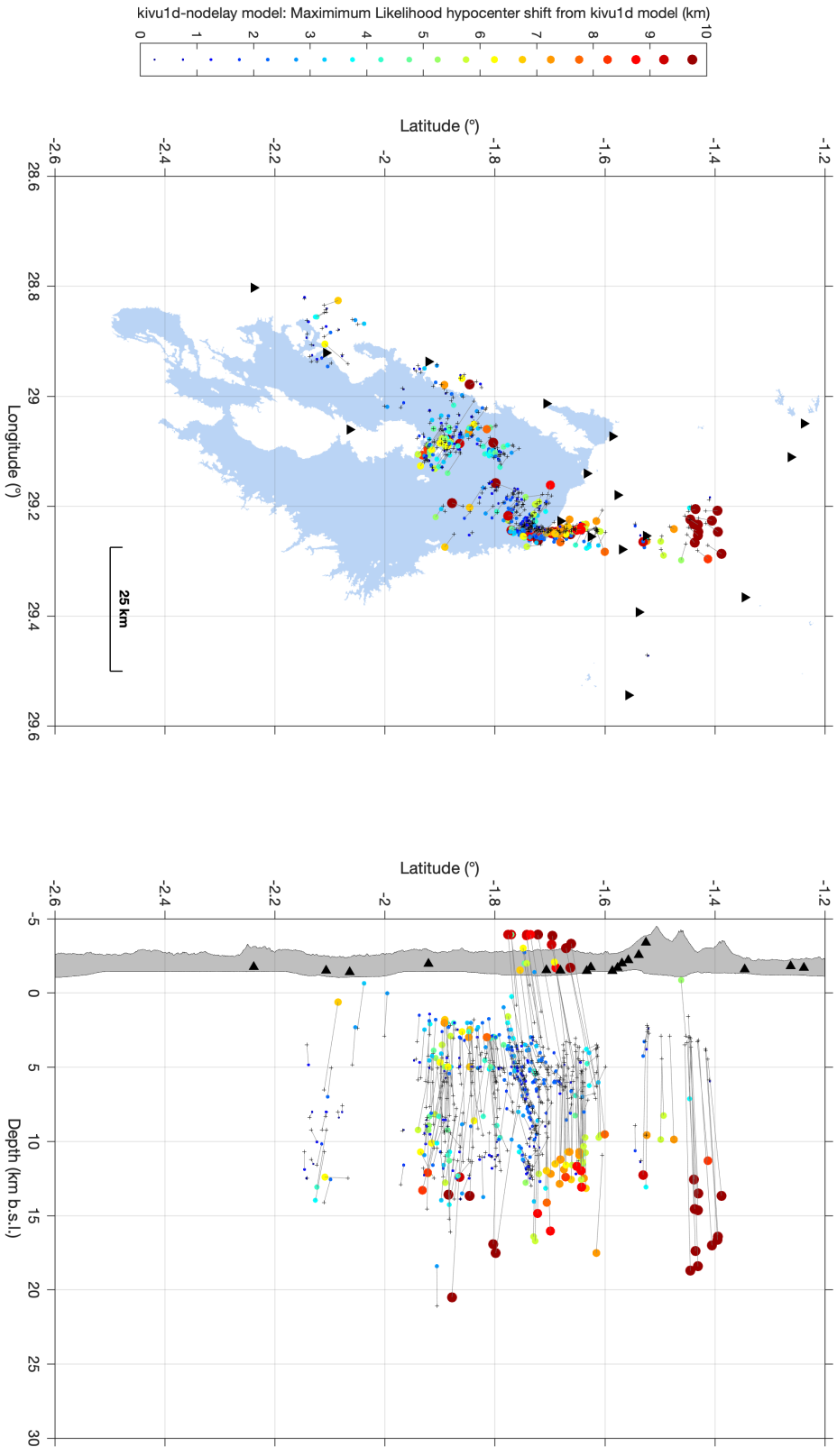

FIGURE B.15: Distance (in km) between MaxL solutions obtained with the Kivu 1D model (black crosses) and the Kivu 1D model without P-wave station delays (colored circles). The color scale corresponds to the distance (in km) between both solutions (clipped at 10 km).

B.4 Kivu 1D model without S-phase observations

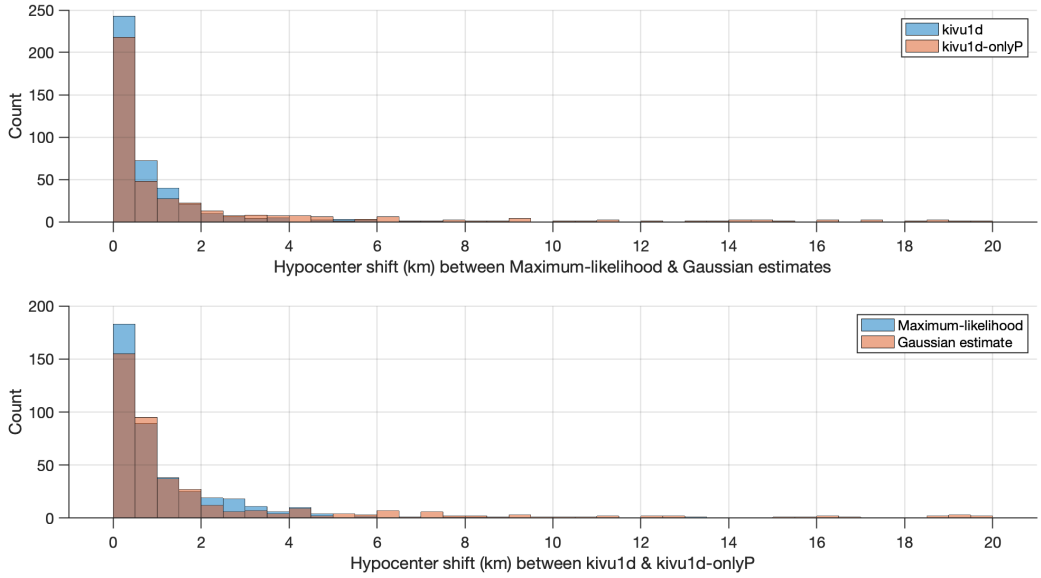

FIGURE B.16: **(Top)** Histograms showing the hypocenter shift (in km) between the MaxL and Gaussian solutions using the Kivu 1D model (blue) and the Kivu 1D model without S-phase observation (red). **(Bottom)** Hypocenter shift between both models for MaxL solutions (blue) and Gaussian estimates (red).

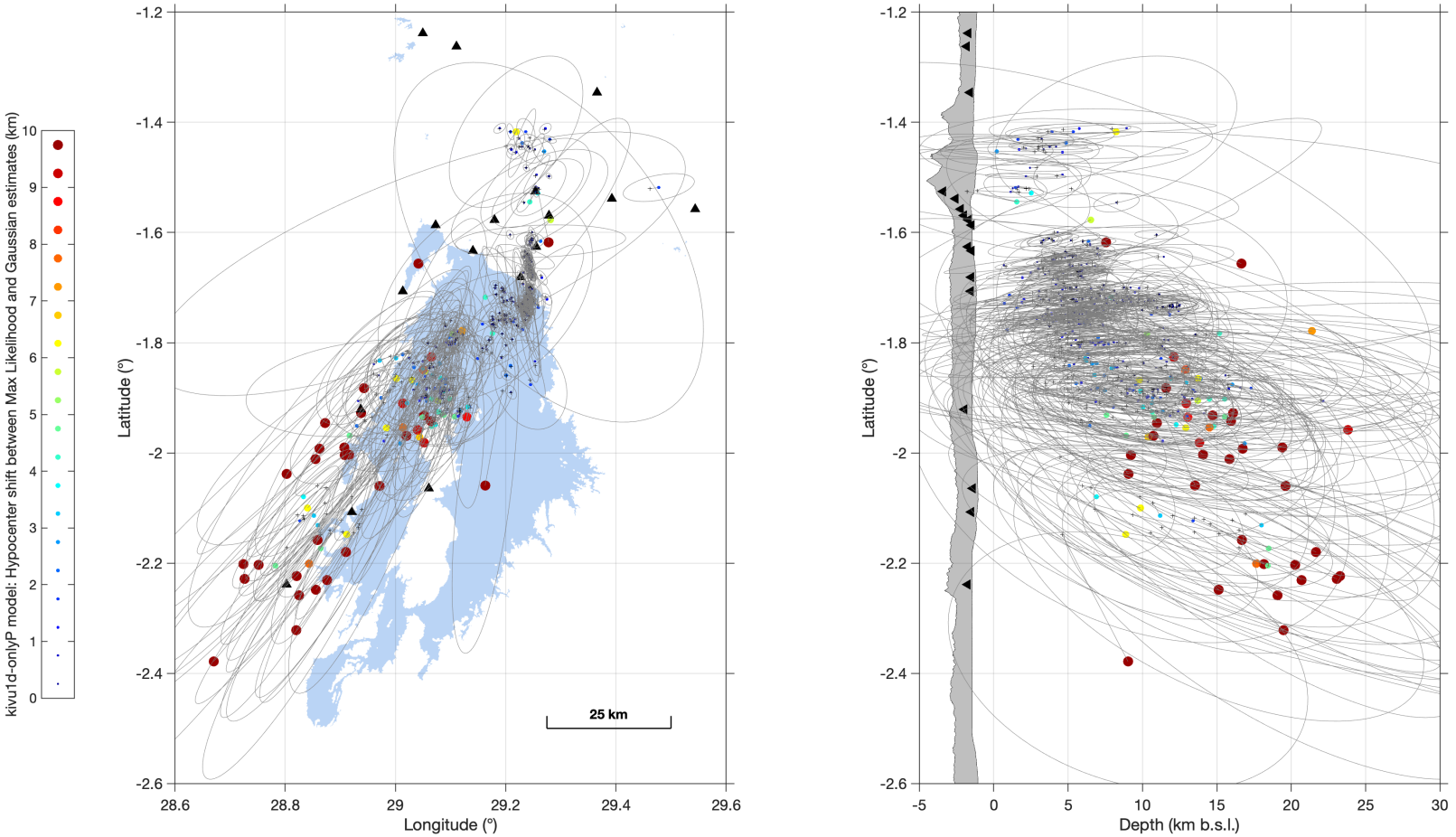

FIGURE B.17: Using the Kivu 1D model without S-phase observations, comparison between computed MaxL (black crosses) and Gaussian solutions (colored circles) obtained with NonLinLoc for 410 events. The color scale corresponds to the distance (in km) between both solutions (clipped at 10 km).

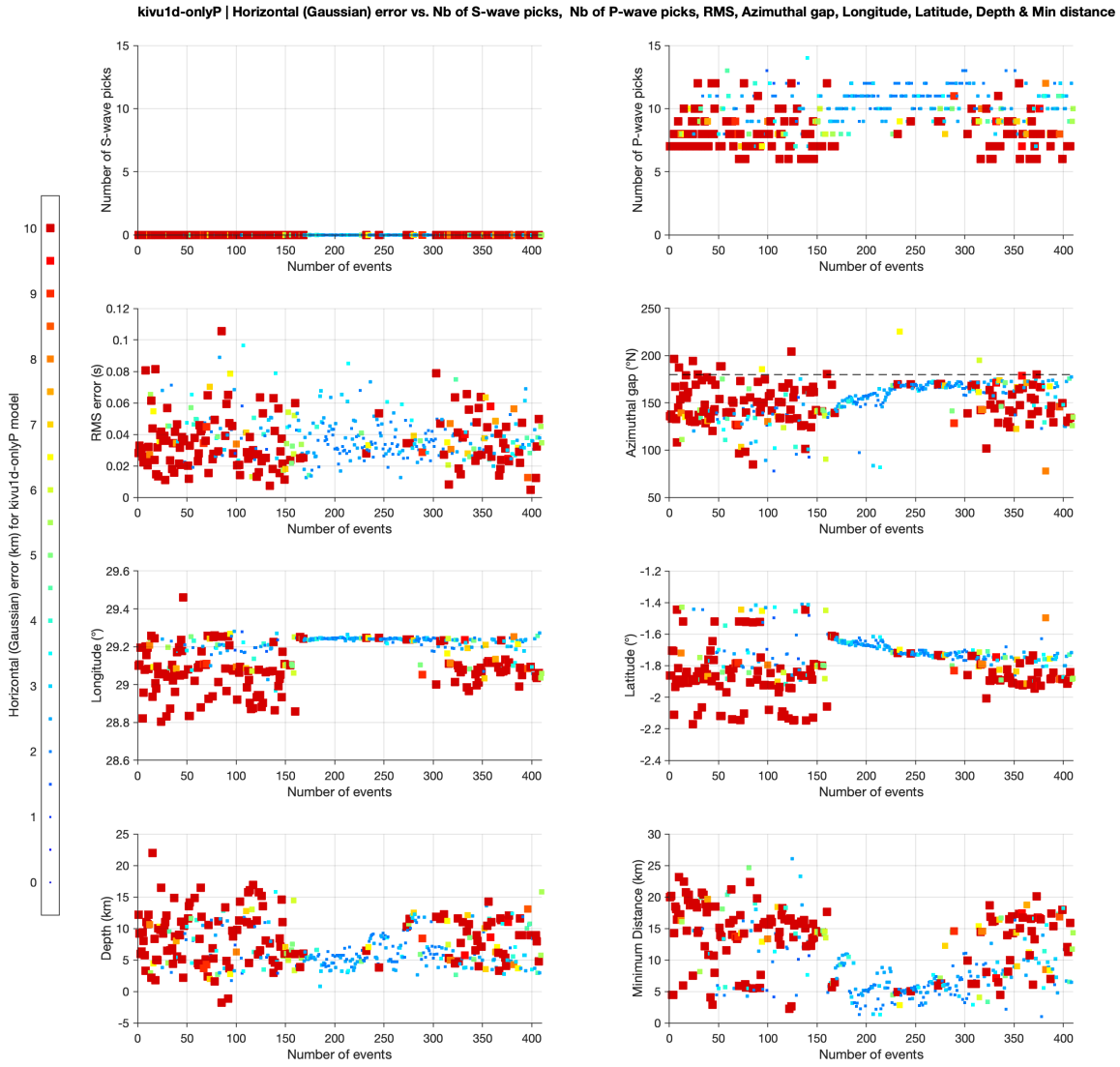

FIGURE B.18: Using the Kivu 1D model without S-phase observation, computed maximum horizontal (Gaussian) error MaxERH (in km) for 410 events as a function of number of S-wave picks, number of P-wave picks, RMS error, azimuthal gap, longitude, latitude, depth and minimum distance to the seismic stations. Marker size and colors are proportional to MaxERH. The color scale ranges between 0 and 10 km (i.e., values exceeding 10 km are set to 10 km).

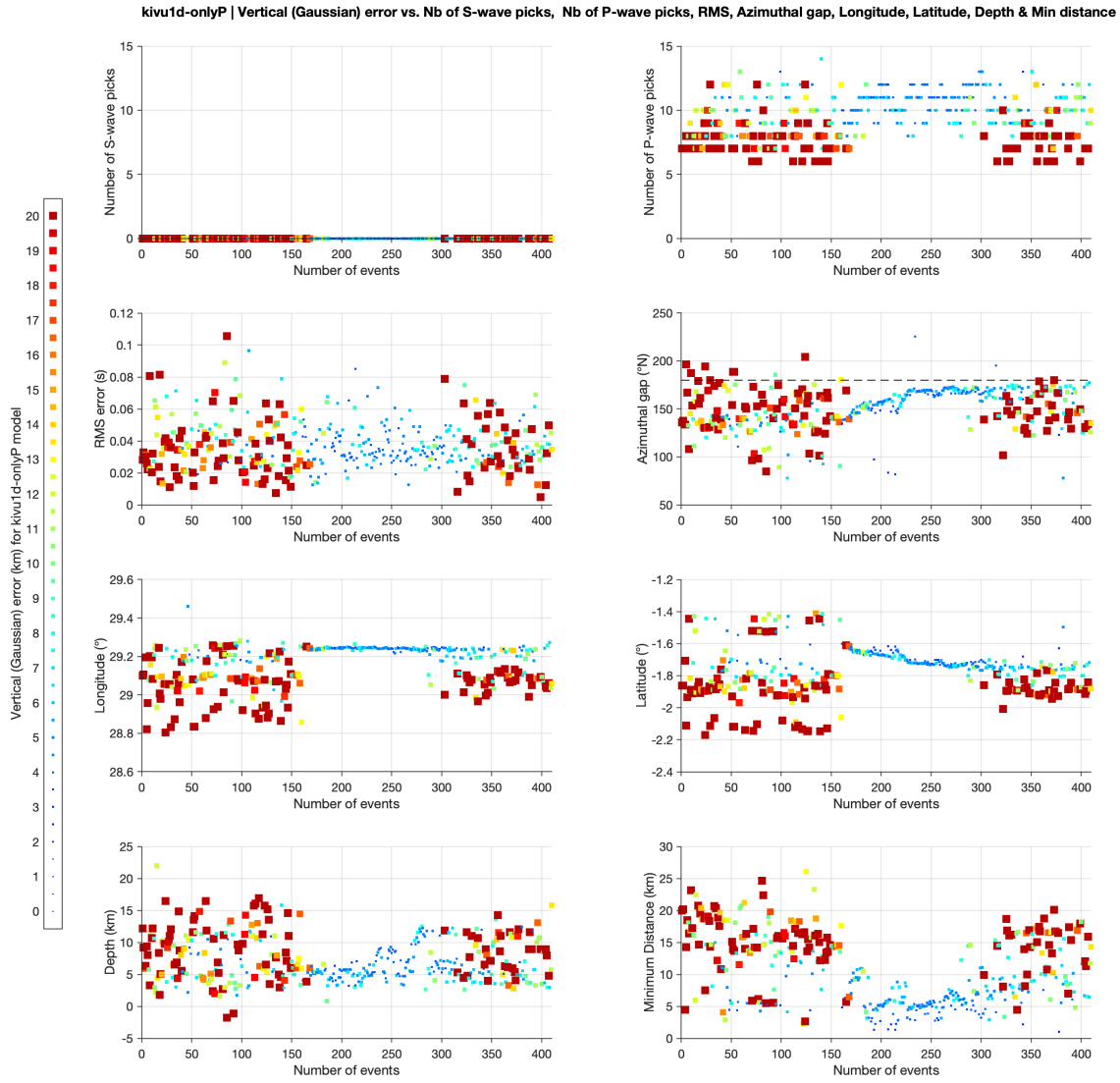

FIGURE B.19: Using the Kivu 1D model without S-phase observation, computed maximum vertical (Gaussian) error MaxERZ (in km) for 410 events as a function of number of S-wave picks, number of P-wave picks, RMS error, azimuthal gap, longitude, latitude, depth and minimum distance to the seismic stations. Marker size and colors are proportional to MaxERZ. Note that the range of the color scale is twice the one used for MaxERH (0 to 20 km).

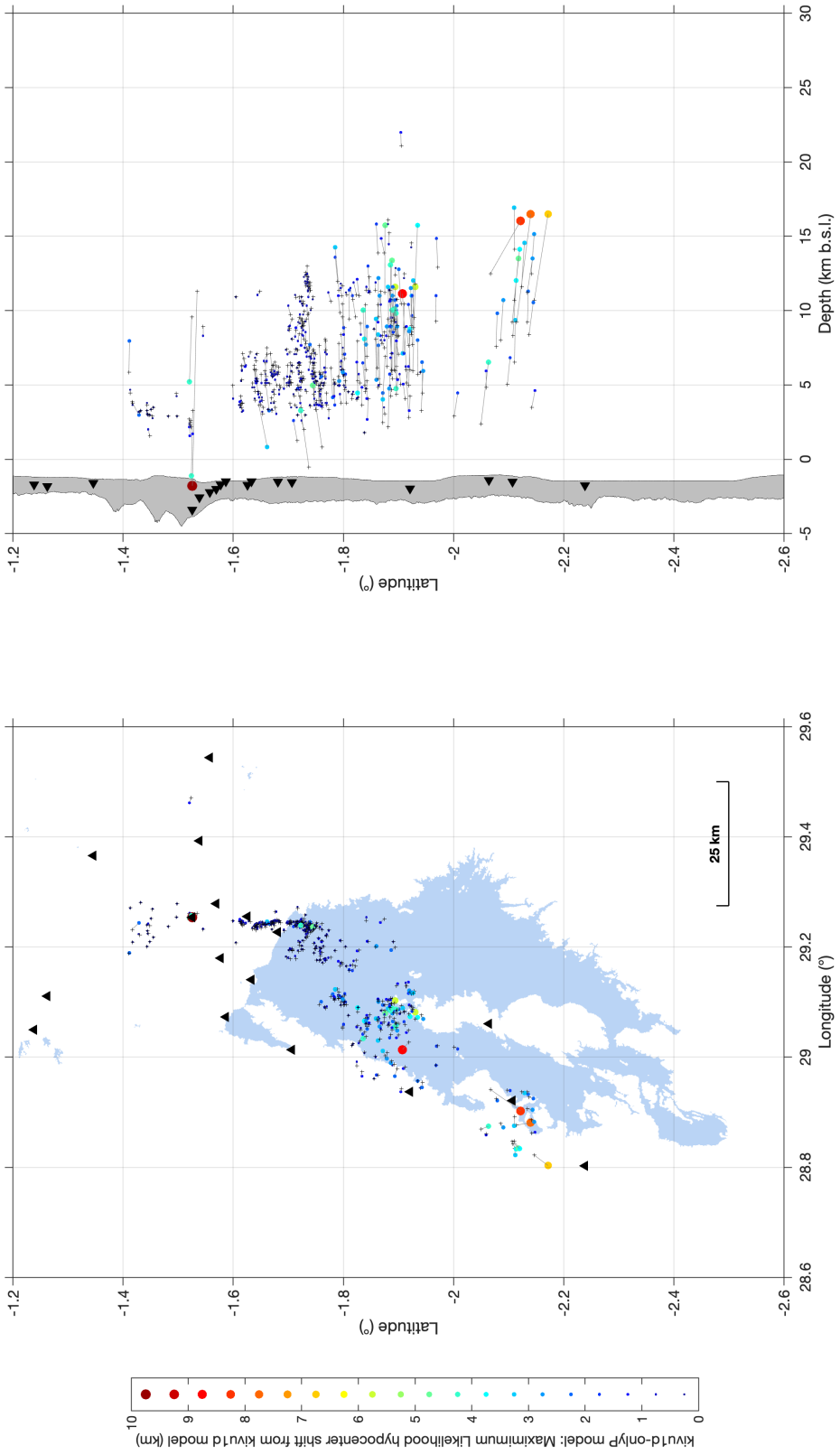

FIGURE B.20: Distance (in km) between MaxL solutions obtained with the Kivu 1D model (black crosses) and the Kivu 1D model without S-phase observation (colored circles). The color scale corresponds to the distance (in km) between both solutions (clipped at 10 km).

Appendix C

Daily seismicity at Nyiragongo without repetitive events

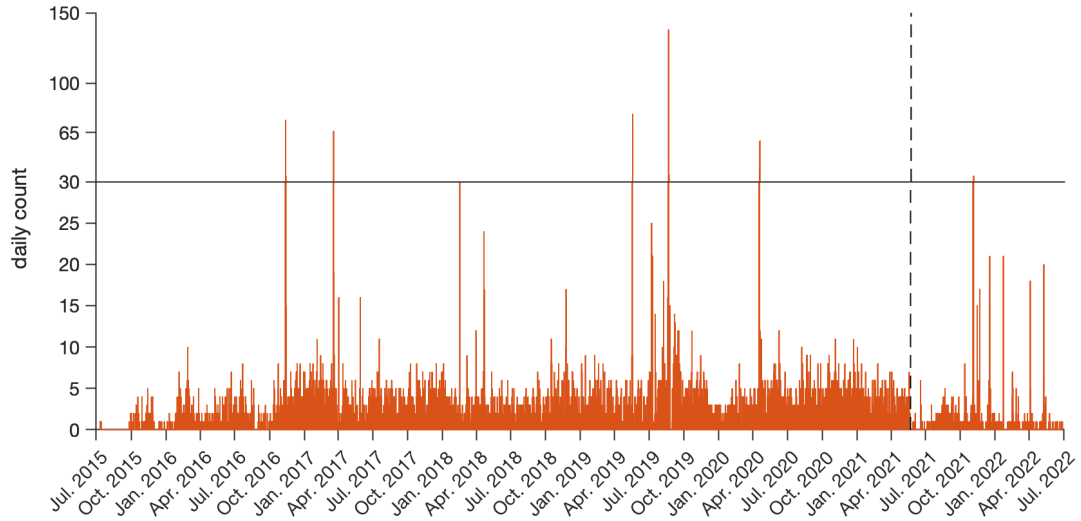

FIGURE C.1: Histogram of daily seismicity at Nyiragongo at intermediate depth (7.5 - 15 km b.s.l.) after filtering out repetitive events. Repetitive events were first detected by template matching at KBTI station using a 3-component master event and catalog events occuring at the same time (+/- 10 s) were then removed. The black dashed line is the eruption on 22 May 2021

Appendix D

Monitoring seismic velocity changes based on ambient noise

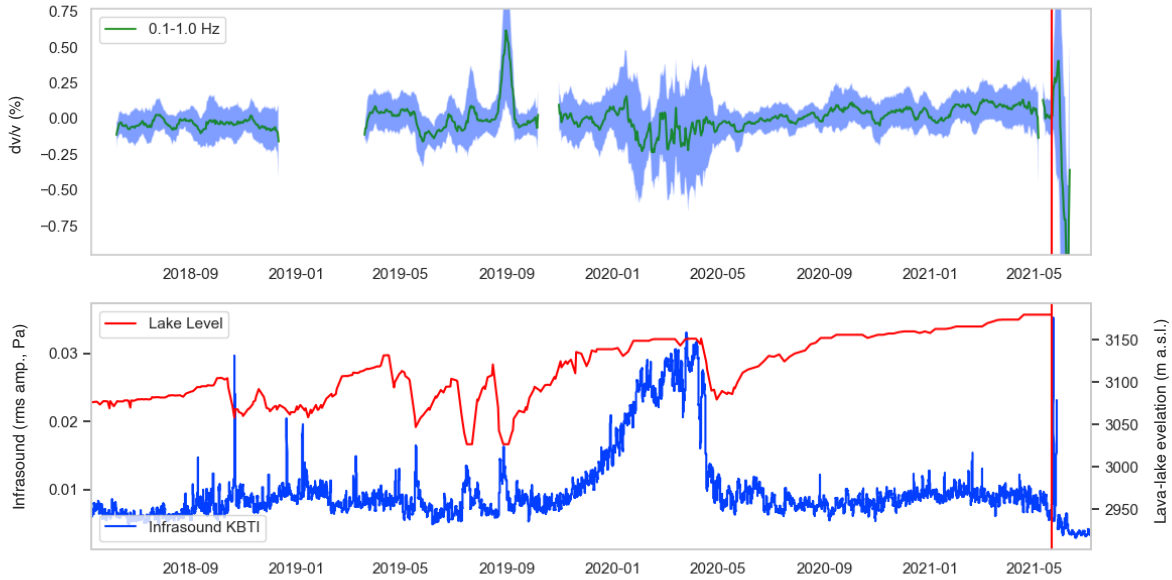

FIGURE D.1: (Up) Relative apparent seismic velocity changes (dv/v in %; green curve) measured using the NYI-RSY station pair between 2018 and 2022. The dv/v are estimated in the 0.1-1 Hz frequency range using a reference stack covering the entire time period. The 1-day dv/v results are smoothed using 10-day rolling median. We applied the same smoothing procedure to draw the error (in blue). (Bottom) Lava-lake level (in red) and acoustic amplitude at KBTI (10-min RMS level) filtered between 0.4 and 2 Hz. These time series are the same than plotted in Chapter 2.